UNIVERSIDADE D
COIMBRA

Susana Figueiredo e Silva

TIME-GATED FLUORESCENCE LIFETIME MICROSCOPY METHODS AND INSTRUMENTATION FOR METABOLIC IMAGING

Tese no âmbito do Doutoramento em Engenharia Biomédica, orientada pelo Professor Doutor António Miguel Lino Santos Morgado e apresentada ao Departamento de Física da Faculdade de Ciências e Tecnologia da Universidade de Coimbra.

Agosto de 2018

Department of Physics

TIME-GATED FLUORESCENCE LIFETIME MICROSCOPY METHODS AND INSTRUMENTATION FOR METABOLIC IMAGING

Susana Figueiredo e Silva

Thesis submitted to the PhD in Biomedical Engineering supervised by Professor António Miguel Lino Santos Morgado and presented to the Department of Physics of the Faculty of Sciences and Technology of the University of Coimbra.

August 2018

UNIVERSIDADE D
COIMBRA

Departamento de Física

MÉTODOS E INSTRUMENTAÇÃO DE MICROSCOPIA DE TEMPO DE VIDA DE FLUORESCÊNCIA "TIME-GATED" PARA IMAGIOLOGIA METABÓLICA

Susana Figueiredo e Silva

Tese no âmbito do Doutoramento em Engenharia Biomédica orientada pelo Professor Doutor António Miguel Lino Santos Morgado e apresentada ao Departamento de Física da Faculdade de Ciência e Tecnologia da Universidade de Coimbra.

Agosto de 2018

UNIVERSIDADE D
COIMBRA

Ao meu Tio Paulo e ao meu Avô Albino

Abstract

Time-Gated fluorescence lifetime imaging microscopy (FLIM) is a microscopy technique where fluorescence decay curves are acquired by opening a series of time windows delayed from the excitation pulse. The analysis of these fluorescence decays results in images where the pixel value is a fluorescence lifetime. This technique has a wide range of applications, including biological and biomedical functional imaging. Metabolic imaging, where the images are obtained from the autofluorescence of metabolic coenzymes and correspond to maps of cell metabolism, is an example.

In this project, we develop a wide-field Time-Gated fluorescence lifetime microscope suitable for one-photon excitation of FAD fluorescence and evaluated its performance and its suitability to metabolic imaging of thick biological samples such as the cornea. The project also included the evaluation of Structured Illumination Microscopy (SIM) methods for optical sectioning and the assessment of the accuracy and precision limits of the Rapid Lifetime Determination (RLD) algorithms that compute the decay parameters and the ratio used as metabolic indicator. This was done through computer simulations on a model of the time-gated microscope, with accurate noise modelling and accounting for the measured instruments response function (IRF), in conditions imposed by *in vivo* imaging acquisition (total counts lower than 10^4, no frame summing).

Throughout this report, we show the developed instrument has timing and optical performance comparable to similar implementations found in the literature and complies with the requirements to measure FAD emission in cells. We successfully implemented SIM in the instrument, obtaining the desired out-of-focus background rejection with well-known test samples. We also verified that the SIM techniques did not affect the accuracy of the measured lifetime but degraded their precision.

The evaluation of the RLD performance defined an optimal region for FAD fluorescence lifetime accuracy and precision: gate separations around 1800 ps and low camera gains (1.05 or 2.41). In this region, the accuracy of the shorter lifetime (τ_1) is always better than 10% but the precision error is near 20%. For the longer lifetime (τ_2) both the accuracy and the precision errors are smaller (< 5% and <10%, respectively). The accuracy of the fractional contributions α_1 and α_2 and of the metabolic ratio α_2/α_1 remains rather stable for gains $k' \leq 2.41$ and gate separations $\Delta t > 1000$ ps, with a ratio accuracy error around 15%. However, the ratio precision is always worse than 10%. Our results also demonstrate that both the accuracy and the precision associated to the metabolic ratio not only depend on the adopted windowing scheme, but also on the nominal value of the ratio: higher values of metabolic ratio will have worse precision and better accuracy. Moreover,

no gate separation offers measurement performance independent of the ratio value being measured, although, for any ratio value, its precision is stable for gate separations between 1500 and 2500 ps. Applications where the range of expected ratio values lies between 0.25 and 1.22 yield a precision error between 13.5% and 25%.

A new version of RLD algorithm for single-exponential decays is presented. This version accounts for the effect of the IRF of the microscope in the measurement accuracy by deconvoluting the IRF from the acquired data. The algorithm uses an iterative reconvolution scheme and results in large improvements of lifetime accuracy for short lifetimes.

Concerning the application to whole cornea imaging, we conclude that the techniques used in the time-gated microscope are unable to obtain cell metabolic images based on FAD fluorescence decays. SIM optical sectioning is extremely challenging on this type of sample due to their large thickness and transparent nature that prevent an adequate contrast of the structured pattern projected in the sample. This made impossible to obtain effective optical sections of corneal layers and cell structures. We were able to acquire fluorescence images from epithelial and endothelial cells, but, due to the lack of optical sectioning, the contributions from the out-of-focus layers degraded considerable the image quality.

In conclusion, the wide-field one-photon excitation approach to FAD fluorescence lifetime metabolic microscopy of the cornea is not viable. Despite this negative outcome, this work resulted in a fully functional time gated fluorescence lifetime microscope and allowed to test the limits of the RLD algorithms in the demanding conditions of low count images as well as to accomplish a thorough evaluation of the performance of time-gate fluorescence lifetime microscopy in the imaging of thick transparent samples.

Keywords: Time-Gated, fluorescence lifetime, instrumentation, metabolic imaging, rapid lifetime determination (RLD), FAD, cornea

Resumo

A microscopia de tempo-de-vida de fluorescência Time-Gated é uma técnica de microscopia onde as curvas de decaimento de fluorescência são adquiridas através da abertura de uma série de janelas temporais (gates)com um determinado atraso em relação ao pulso de excitação. A análise destas curvas de fluorescência resulta em imagens cujos valores dos pixéis são tempos de vida de fluorescência. Existe uma grande variedade de aplicações para esta técnica, incluindo imagiologia funcional em aplicações biológicas e biomédicas. Um exemplo é a imagiologia metabólica, técnica onde as imagens são obtidas através do sinal de autofluorescência proveniente de co-enzimas metabólicas e correspondem ao metabolismo da célula.

Neste projecto, um microscópio de tempo de vida de fluorescência Time-Gated de campo inteiro com excitação por um fotão da fluorescência do FAD foi desenvolvido e o seu desempenho e aplicabilidade em imagiologia metabólica de amostras biológicas espessas como a córnea foi avaliado. Técnicas de microscopia de iluminação estruturada (SIM) foram implementadas e avaliadas, bem como uma análise dos limites de exactidão e precisão dos algoritmos de determinação rápida do tempo-de-vida (RLD), que calculam os parâmetros do decaimento e o rácio usado como indicador metabólico. Esta análise foi feita através de simulações computacionais do modelo de aquisição do microscópio Time-Gated com um modelo de ruído exacto e tendo em conta as medidas da função de resposta do instrumento (IRF) nas condições impostas pelas aquisições de imagens *in vivo* (número de contagens de fotões total inferior a 10^4 sem soma de frames).

Ao longo deste documento, demonstramos que o instrumento desenvolvido apresenta performances óptica e temporal comparáveis com outras implementações semelhantes descritas na literatura, e está em conformidade com os requisitos necessários para medir a emissão de fluorescência do FAD nas células. A técnicas de SIM foram implementadas com sucesso, conseguindo atingir a supressão do fundo fora de foco desejada em amostras de testes bem conhecidas. Também verificámos que estas técnicas de iluminação estruturada não afectam a exactidão das medidas de tempo-de-vida, mas degradam a sua precisão.

A avaliação da performance do RLD definiu uma região óptima para a exactidão e precisão do tempo-de-vida de fluorescência do FAD: separações entre gates de 1800 ps e baixos ganhos na câmara (1.05 ou 2.41). Nesta região a exactidão do tempo-de-vida mais curto (τ_1) é sempre melhor que 10%, mas o erro de precisão está perto de 20%. Para o tempo de vida mais longo (τ_2) tanto os erros de exactidão como de precisão são mais baixos (< 5% e <10%, respectivamente). A exactidão nas contribuições fraccionais α_1 e α_2 e do rácio metabólico α_2/α_1 mantém-se estável para ganhos $k' \leq 2.41$ e para separações de gate $\Delta t > 1000$ ps, com um erro de exactidão no rácio próximo

de 15%. No entanto, a precisão no rácio é sempre pior que 10%. Os nossos resultados demonstram que tanto a exactidão como a precisão associadas ao rácio metabólico não dependem apenas do esquema de gate adoptado, mas também no valor nominal do próprio rácio: valores mais altos de rácio metabólico têm piores precisões e melhores exactidões. Além disso, não existe um valor de separação de gate que ofereça medidas de performance independentes do valor do rácio a ser medido, mesmo que, para qualquer valor de rácio, a precisão seja estável para separações de gate entre 1500 e 2500 ps. Para aplicações onde os valores esperados do rácio variêm entre 0.25 e 1.22, o erro de precisão está entre 13.5% e 25%.

Uma nova versão do algoritmo de RLD para decaimentos mono-exponenciais é apresentada. Esta versão tem em conta o efeito da IRF do microscópio na medida da exactidão, através da sua desconvolução nas medidas adquiridas. O algoritmo usa um esquema de reconvolução iterativo, o que resulta em fortes melhorias na exactidão de medidas de tempos-de-vida curtos.

Em relação às aplicações para imagiologia de córneas inteiras, concluiu-se que as técnicas usadas no microscópio time-gated não são capazes de obter imagens metabólicas baseadas nos decaimentos de fluorescência do FAD. O seccionamento óptico através de SIM é bastante difícil neste tipo de amostra, uma vez que a sua espessura e transparência impedem a obtenção de um contraste do padrão projectado na amostra adequado. Isto fez com que fosse impossível obter secções ópticas efectivas das camadas da córnea e das suas estruturas. Foram adquiridas algumas imagens de fluorescência das células do epitélio e do endotélio, mas, devido à falta de seccionamento óptico, as contribuições das camadas fora de foco deterioraram consideravelmente a qualidade da imagem.

Para concluir, usar microscopia de campo inteiro através de excitação por um fotão para imagiologia metabólica baseado em FAD na córnea não é uma solução viável. Apesar disso, deste trabalho resultou um microscópio de tempo de vida de fluorescência time-gated completamente funcional que permitiu testar os limites dos algoritmos RLD em condições difíceis de baixo número de contagens. Mais ainda, também foi possível conseguir uma avaliação extensa da sua performance em imagiologia de amostras espessas e transparentes.

Palavras-chave: Time-Gated, tempo-de-vida de fluorescência, instrumentação, imagiologia metabólica, determinação rápida do tempo-de-vida (RLD), FAD, córnea

Agradecimentos

No final desta longa maratona chamada doutoramento quero agradecer às pessoas que de uma maneira ou de outra foram fundamentais para a sua concretização:

Ao meu orientador, Professor Miguel Morgado, que me lançou o desafio da realização deste projecto e para o qual disponibilizou apoio, conselhos científicos e críticas construtivas que foram essenciais para a conclusão do mesmo. Mais ainda, a sua calma e paciência foram essenciais para me ajudarem a ultrapassar todas as dificuldades que foram surgindo neste longo percurso do Doutoramento, mantendo a luz ao fundo do túnel que por vezes parecia ainda mais ténue que a fluorescência que queríamos detectar. Obrigada Professor.

Ao serviço de oftalmologia do Hospital Universitário de Coimbra pela cedência do material necessário, em especial à Professora Maria João Quadrado.

A todos os elementos e ex-elementos da equipa de investigação onde este projecto foi inserido. Um agradecimento especial ao Professor José Paulo Domingues e ao Professor Rui Bernardes por toda a disponibilidade demonstrada quando com eles discuti as minhas dúvidas e dificuldades. Fica também um agradecimento especial à Ana Batista que, mesmo estando longe, foi sempre uma colega e amiga disponível para esclarecer dúvidas e ultrapassar os desafios impostos pelo projecto.

Aos amigos:

À Marlene, "Doutora das Farmácias", por toda a ajuda nos laboratórios de química e, acima de tudo, por ser a amiga de todos os dias durante o desenvolvimento deste projecto.

À minha "prima" Rute, por toda a paciência, conselhos, disponibilidade e amizade demonstrados durante a realização deste trabalho e desde que é minha amiga.

Ao Tiago, pela amizade, por me motivar a nunca desistir e também por todas as boleias dadas de e para o aeroporto.

À minha homónima favorita pelas frases de incentivo, pela palavra amiga constante e por estar sempre disponível para me ajudar em tudo o que preciso.

Ao Luís, por ser um amigo bem-disposto e preocupado, pela paciência em aturar as minhas queixas e pelo tempo dedicado a algumas revisões da tese.

À Ana, pelos almoços em Coimbra e pelas conversas sem fim durante os mesmos.

Ao Zé, que, apesar de me derreter a paciência, tem sempre uma palavra amiga quando é necessário.

Ao Pedro, ao Aníbal e ao Diogo, pela amizade e pela prontidão em me ajudarem em tudo o que fosse necessário.

À Inês, que, apesar de estar anos sem a ver, continua a ser a boa amiga de sempre.

A todos os amigos “Pxinxos e Txufas” que, estando longe ou perto, me deram força e motivação para continuar o projecto e trazê-lo a bom porto.

À Sara e à Cristina, as amigas de sempre que me acompanharam e apoiaram em mais uma etapa da minha vida.

Um agradecimento especial a toda a família que sempre me deu educação, carinho e condições necessárias para chegar até aqui.

Aos meus avós, São e Fernando, os meus segundos pais, que me dão todos os mimos do mundo e que tanto ajudaram na minha educação e conquistas até hoje, acreditando em mim mais que ninguém.

Por último, mas em lugar de destaque, aos meus pais, Maria Alvarina e António Egídio, os impulsionadores da realização deste doutoramento, os pilares da minha vida e grandes responsáveis pela minha existência e por tudo o que consegui até hoje.

A todos o meu Muito Obrigada!

This project was supported by FCT Projects PTDC/SAU-ENB/122128/2010 and PEST-C/SAU/UI3282/2013 and Compete Programs FCOMP-01-0124-FEDER-021163 and FCOMP-01-0124-FEDER-037299

Contents

List of Figures

List of Tables

Acronyms List

ADC – Analog-to-Digital Converter

ADP – Adenosine Diphosphate

ATP – Adenosine Triphosphate

CCD – Charged-Coupled Device

CFD – Constant Function Discriminator

CMOS – Complementary Metal-Oxide Semiconductor

DMD – Digital Micromirror Device

FAD – Flavin Adenine Dinucleotide

FLIM – Fluorescence Lifetime Imaging Microscopy

FMN – Flavin Mono-Nucleotide

GOI – Gated Optical Intensifier

HiLo – “High”-“Low”

HRI – High Rate Intensifier

IRF – Instrument Response Function

MCP – Microchannel plate

NADH – Nicotinamide Adenine Dinucleotide

PGA – Programmable Gate Array

PMT – Photomultiplier Tube

RLD – Rapid Lifetime Determination

RME – Relative Mean Error

RSD – Relative Standard Deviation

SIM – Structured Illumination Microscopy

SR – SIM – Super-Resolution Structured Illumination Microscopy

TC – Total Counts

TCSPC – Time-Correlated Single-Photon Counting

TG – Time-Gated

Introduction

A. Context and motivation of this study.

This study stems from the research activities on corneal imaging, carried out at the Instrumentation Group of the former Institute for Life Sciences and Biomedical Imaging (IBILI) during the past 15 years. This research group that since long has a focus on the development of instrumentation and methods to evaluate ocular function (Cunha-Vaz, Domingues and Correia, 2000; Schwartz *et al.*, 2008; Domingues, Branco and Morgado, 2010), began its research activities on corneal imaging by developing methods for quantitative corneal confocal microscopy (Popper *et al.*, 2004). These methods were applied with success in the evaluation of the impact of systemic metabolic diseases on corneal tissues, starting the group's interest in corneal function. Those studies were the first to report that diabetic patients exhibit lower densities of basal epithelial cells (Quadrado *et al.*, 2006) and sub-basal nerves (Popper *et al.*, 2005) densities even for short diabetes duration. Work progressed to the development of corneal nerves morphometric analysis algorithms for assessing peripheral nerve damage and repair on peripheral diabetic neuropathy (Ferreira, Morgado and Silva, 2010; Otel *et al.*, 2013). The research project concerning diabetic peripheral neuropathy early diagnosis and follow-up through *in vivo* automatic analysis of corneal nerves morphology was funded by Fundação para a Ciência e Tecnologia (FCT - Project PTDC/SAU-BEB/104183/2008). It was in the framework of this research project that I started my research activities on the Instrumentation Group.

The idea of evaluating corneal metabolism at cell level using fluorescence lifetime techniques is quite old in the group. However, it was necessary a long period of time to obtain the funds and equipment required for exploring it. The motivation for implementing this idea was simple. Corneal diseases are the second major cause of blindness worldwide, according to the World Health Organization. Being the major refractive component of the optics of the eye, the cornea is fundamental to visual acuity. Therefore, corneal pathologies can induce severe visual impairment. Moreover, being a highly innervated tissue, corneal diseases cause severe pain and discomfort. and, eventually lead to blindness. So, it is easy to understand that non-invasive methods for early detection of corneal pathologies can have a large impact on the monitoring and management of patients and contribute to prevent disease progression to irreversible conditions.

The corneal imaging modalities currently used in clinical practice, such as the standard slit-lamp imaging or the newer modalities of corneal confocal microscopy and anterior segment optical coherence tomography, are structural imaging modalities. Although they are contributing greatly to improve the knowledge on corneal pathophysiology and the standards of clinical practice, the

clinicians still require an imaging tool capable of detecting the very early signs of cell dysfunction. In other words, a functional imaging modality with cell-level resolution could have a deep impact on understanding the mechanisms causing corneal diseases, on the detection of disease signs at very early stages and, ultimately, on the patients' prognosis. Fluorescence lifetime metabolic imaging microscopy has the potential of fulfilling this need.

The first efforts of the Instrumentation Group for pursuing the development of fluorescence lifetime metabolic imaging microscopy came with competitive proposal for acquiring scientific equipment (CONQ-REEQ/665/2005). This proposal was awarded by FCT allowing the acquisition of the gated intensified CCD camera and of the time-correlated single photon counting microscope that were used in this project. Still, it was only much recently, that was possible to present a scientific project proposal fully dedicated to fluorescence lifetime metabolic imaging (PTDC/SAU-ENB/122128/2010). This proposal was funded by FCT and resulted in a project that took place between May 2012 and August 2018 that setup the basis and constituted the initial phases of the work that I present in this thesis.

This research proposal comprised the development and evaluation of two different approaches for implementing fluorescence lifetime metabolic imaging microscopy, both having the cornea as final application:

Using multiphoton imaging techniques, namely two-photon excitation and second harmonic generation, with serial pixel imaging using laser scanning excitation and time-correlated single photon counting detection.

Using one-photon excitation with parallel, wide-field imaging and time-gated detection through an intensified camera.

The first approach offered greater promise due to the inherent optical sectioning of multiphoton imaging, the use of safer infrared wavelengths and the possibility of exciting both NAD(P)H and FAD fluorescence with the same laser source. However, there were concerns on the safety of the high peak radiant powers required by multiphoton excitation and on the very high cost of lasers capable of emitting pulses with a few tenths of femtoseconds. As the Instrumentation Group didn't have the resources to implement this approach, a research collaboration was established with the group of Professor Karsten König in the University of Saarland (Saarbrücken, Germany) and a PhD student moved to Germany to carry out the project. The work done was very successful, achieving functional imaging of all corneal layers, although restricted, so far, to *ex vivo* samples (Batista *et al.*, 2016; Batista, 2018; Batista, Hans G. Breunig, *et al.*, 2018; Batista, Hans Georg Breunig, *et al.*, 2018a).

The second approach, which I pursued in this work, could use much less expensive picosecond diode lasers and was considered safe for in vivo ocular imaging, due to the results already obtained in time-resolved fluorescence imaging of the retina by the group of Prof. Dietrich Schweitzer (Schweitzer *et al.*, 2004a). However, there were high concerns on the possibility of obtaining optical sectioning on a thick transparent tissue, on the suitability of Rapid Lifetime Determination algorithms for obtaining the decay parameters with adequate accuracy and precision and on obtaining an adequate signal using only FAD fluorescence. Relying on NAD(P)H fluorescence was not considered since one-photon excitation of this metabolic co-factor implies ultraviolet radiation that was deemed unsafe for in vivo ocular imaging, due to its phototoxicity.

This was the context and motivation that lead to the research project that resulted in the research work presented in this thesis. The work I did resulted in the overall conclusion that the one-photon approach to fluorescence lifetime metabolic imaging microscopy of the cornea is not viable. Despite this negative outcome, this work allowed to develop a fully-functional time-gated fluorescence lifetime microscope, to test the limits of the RLD algorithms in the demanding conditions of low-count images posed by the requirements of *in vivo* acquisition, and to present a thorough evaluation of the performance of time-gated fluorescence lifetime microscopy in the imaging of thick transparent samples. Moreover, the time-gated solution proposed exhibit optical performance compared to similar implementations, which indicates that it could be applied to other types of biological samples.

B. Objectives

The main objective of this project was to evaluate the performance and adequacy of the wide-field time-gated fluorescence lifetime microscopy technique for the metabolic assessment of thick tissues (like the cornea) in conditions compatible with *in vivo* image acquisition.

For accomplishing this main objective, it was necessary to define the following intermediate objectives:

To design, setup and characterize a time-gated fluorescence lifetime microscope for wide field imaging of FAD fluorescence.

To evaluate the performance of optical sectioning methods for widefield microscopy and their impact on the determination of fluorescence lifetime decays.

To determine the limits of accuracy and precision of the Rapid Lifetime Determination algorithms in conditions compatible with the properties of the developed microscope and the requirements of *in vivo* image acquisition (total counts lower than 10^4; no frame summing).

C. Thesis structure

Given the objectives presented and the work developed during the course of this project, we organized this thesis in 8 different chapters: 3 regarding the state of the art of the used techniques. 4 chapters presenting our studies - one regarding the description of the developed time-gated microscope, other containing information about its optical and timing performance, another focused on the accuracy and precision of the Rapid Lifetime Determination (RLD) algorithm and finally one regarding its application in corneal tissues – and the final eighth chapter dedicated to the final conclusions and discussion.

In the first chapter of this thesis, we describe the metabolism of a cell and the particular role played by the co-enzymes FAD and NADH. We present the basics behind metabolic imaging and give some examples of its successful application in biology and medicine.

In the second chapter, the working principle of Time-Domain FLIM techniques is analyzed with a greater focus on the Time-Gated technique. An evolution of this technique since its arrival until today is reported along with some examples of biological applications. The issue of optical sectioning is also addressed, and the concept of structured illumination microscopy is introduced. Two methods of SIM are presented: “3-phase approach” and “HiLo”.

Chapter 3 is focused on the problem of determining the fluorescence decay parameters (lifetimes and fractional contribution). Here we present the most standard methods to determine these parameters and successfully fit the fluorescence decay curves acquired with time-domain techniques. The basic principle behind RLD is also presented.

The description of the developed microscope is made in Chapter 4. All optical and electronical components used are described along with the layouts of the final optical setups.

The evaluation of the time-gated microscope in terms of optical and timing characteristics is described in Chapter 5. All the tests performed to evaluate and compare the microscope with similar implementations are described along with the results obtained. HiLo influence on lifetime determination is also addressed.

Chapter 6 includes all the work regarding simulations to evaluate the accuracy and precision of the RLD algorithms. Different results are presented going from the validation of the simulations against experimental measurements on the fluorescent solutions, to their application to our target case: low photon counts with enlarged IRF and an accurate noise model.

Chapter 7 concerns the attempts to image animal corneas. An introduction to corneal structures and to what was expected to image is made and then the results obtained with our microscope are presented.

Finally, in Chapter 8, we present the final conclusions and an overall discussion of the results obtained during this project.

D. List of Contributions

Papers in international journals and proceedings:

Susana F. Silva, José Paulo Domingues, and António Miguel Morgado, Precision and accuracy of double-exponential decay measurements in time-gated imaging systems using rapid lifetime determination. Meas. Sci. Technol. (in submission) 2018

Susana F. Silva, José Paulo Domingues, and António Miguel Morgado, Accurate Rapid Lifetime Determination on Time-Gated FLIM Microscopy with Optical Sectioning, Journal of Healthcare Engineering, vol. 2018, Article ID 1371386, 7 pages, 2018. doi:10.1155/2018/1371386

Susana F. Silva; Ana Batista; José Paulo Domingues; Maria João Quadrado and António Miguel Morgado, Time-gated FLIM microscope for corneal metabolic imaging, Proc. SPIE 9712, Multiphoton Microscopy in the Biomedical Sciences XVI, 97122C (March 14, 2016); doi:10.1117/12.2214182; http://dx.doi.org/10.1117/12.2214182

Susana F. Silva, Ana Batista, Olga C. Castejón, Maria João Quadrado, José Paulo Domingues, Miguel Morgado, Development of a time-gated fluorescence lifetime microscope for in vivo corneal metabolic imaging. Proc. SPIE 9537, Clinical and Biomedical Spectroscopy and Imaging IV, 953709 (July 15, 2015); doi:10.1117/12.2183945.

Ana Batista, Susana F. Silva, José Paulo Domingues, António Miguel Morgado, Fluorescence Lifetime Based Corneal Metabolic Imaging, Procedia Technology, 17, 2014, 281-288, http://dx.doi.org/10.1016/j.protcy.2014.10.238.

Other conference papers:

Silva, S.F., Batista, A., Domingues, J.P., Quadrado, M.J., Morgado, M., Fluorescence lifetime microscope for corneal metabolic imaging, Proceedings of 2015 IEEE 4th Portuguese Meeting in Bioengineering (ENBENG), 26-28 Feb. 2015, doi: 10.1109/ENBENG.2015.7088878

Batista, A.; Silva, S.F.; Domingues, J.P.; Morgado, A.M., Corneal metabolic imaging by FAD autofluorescence lifetime, Proceedings of 2013 IEEE 3rd Portuguese Meeting in Bioengineering (ENBENG), 20-23 Feb. 2013, doi: 10.1109/ENBENG.2013.6518396

Chapter 1 Tissue Metabolic Assessment by Fluorescence Imaging

A. Cell Metabolism

Eukaryotic cells comprise numerous organelles and a great diversity of chemical networks to provide the basic conditions for living systems to exist. One of the most important processes occurring within a cell is the metabolism, defined as "the sum of all chemical changes that take place in a cell through which energy and basic components are provided for essential processes, including the synthesis of new molecules and the breakdown and removal of others" (National Cancer Institute, 2017). As the definition suggests, energy is an essential component for any metabolic process to occur. In eukaryotic cells, energy is made available by the production and consumption of a specific molecule, adenosine triphosphate (ATP), a coenzyme that acts as an energy carrier in cells' metabolic processes. Different type of substrates can generate the production of ATP such as carbohydrates, lipids or proteins. Glucose is considered the primary source of energy to a cell since it maximizes the production of ATP. To produce ATP, glucose can be consumed in two different ways: anaerobically through a process called glycolysis or, more efficiently, aerobically through cellular respiration (Cooper and Hausman, 2007). These processes compound chains of chemical reactions in which a great diversity of molecules is present. Glycolysis is the first step in ATP production and is common to both aerobic and anaerobic pathways (Cooper and Hausman, 2007). It occurs in the cytoplasm and corresponds to the conversion of a molecule of glucose into pyruvate. During this chain of chemical events, two molecules of ATP are produced while two molecules of NAD^+ are reduced to NADH (nicotine adenine dinucleotide) (Cooper and Hausman, 2007; Georgakoudi and Quinn, 2012a). The final product of glycolysis, pyruvate, can follow two different paths, depending on the presence or absence of oxygen (O_2). When following the aerobic pathway, pyruvate enters the mitochondrial matrix and experiments the network of events that compound oxidative phosphorylation and the electron transport chain. Immediately after entering the mitochondria, it is converted in Acetyl-CoA, a molecule that will trigger the citric acid cycle (also known as Krebs cycle) giving rise to the production of more ATP molecules. The conversion of pyruvate into Acetyl-CoA is called pyruvate decarboxylation. During this process, a molecule of FAD (flavin adenine dinucleotide) is reduced to $FADH_2$, while a molecule of NAD^+ is reduced to NADH –Figure 1.1 (Georgakoudi and Quinn, 2012a).

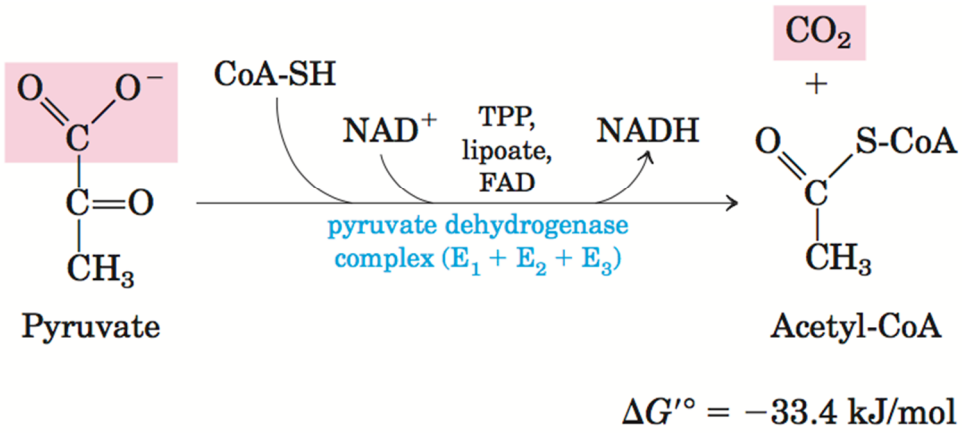

Figure 1.1 - Chemical reaction that transforms pyruvate into Acetyl-CoA with the conversion of one molecule of NAD^+ into NADH (Nelson and Cox, 2005)**.**

The citric acid cycle is the process that follows in the cellular aerobic respiration. It starts with one molecule of Acetyl-CoA, produced either by pyruvate decarboxylation or through the catabolic reactions of other substrates such as lipids or proteins. Acetyl-CoA prompts the Krebs cycle, which is composed by a series of chemical reactions that can be divided in different steps, as shown by Figure 1.2. Briefly, during the overall cycle, 3 molecules of NAD^+ are reduced to NADH and one molecule of FAD is reduced to $FADH_2$. Moreover, the cycle generates two molecules of ATP for each molecule of Acetyl-CoA that enters it. At this point, each glucose molecule yields 4 molecules of ATP, considering the ATP molecules already produced during glycolysis (Cooper and Hausman, 2007).

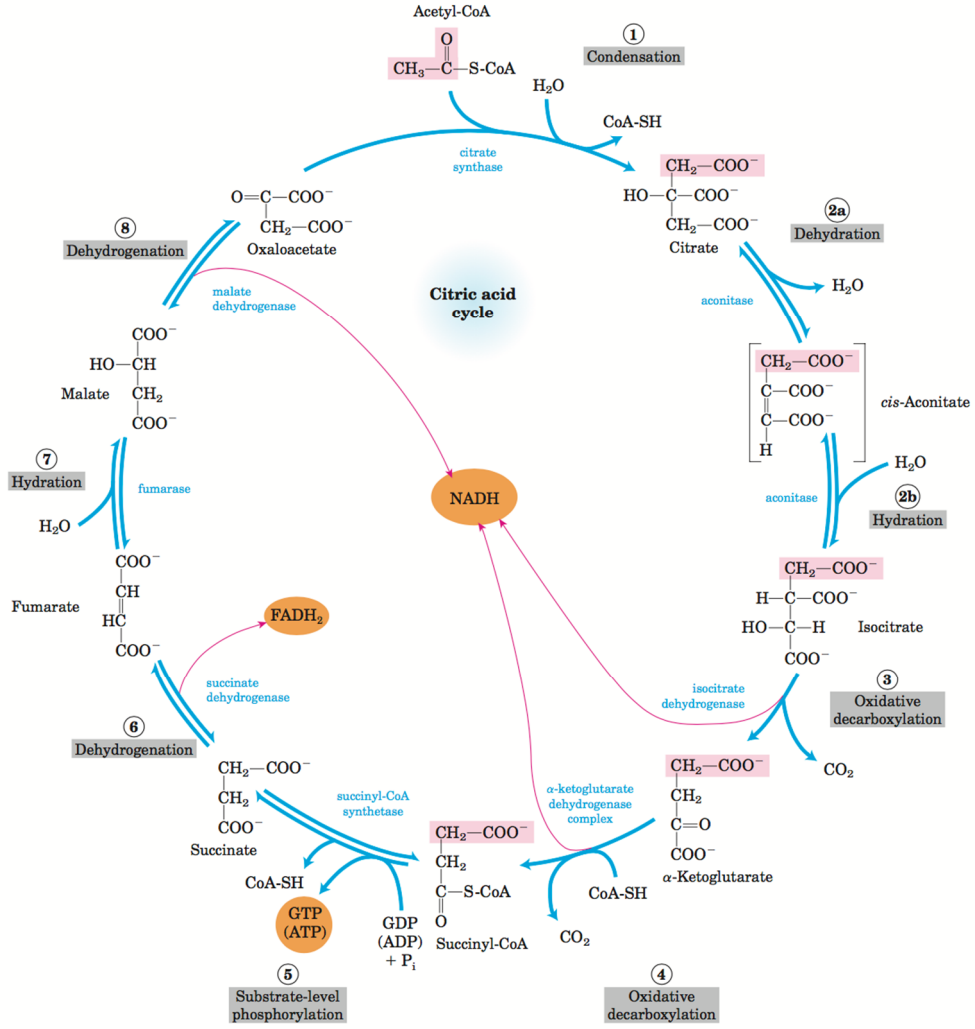

Figure 1.2 - Schematic representation of the citric acid cycle, summing up the main reactions that occur within and the conversions of NAD^+ to NADH and FAD to $FADH_2$ (Nelson and Cox, 2005).

Mitochondrial NADH and $FADH_2$ (originated during the citric acid cycle) will serve as donors of electrons for other oxidation-reduction reactions that occur within the cell. In aerobic conditions, these molecules will donate electrons in the electron transport chain, where most ATP molecules are produced. These reactions that lead to the production of more molecules of ATP from ADP are very energy-yielding and, for a better use of this energy, they should occur gradually. This explains the existence of the electron transport chain, which is a cellular mechanism composed of five complexes and placed in the inner mitochondrial membrane. It is responsible for gradually monitoring the process of electron donation from both NADH and $FADH_2$ to the reduction of O_2 to H_2O. and the consequent generation of more ATP molecules, as schematized in Figure 1.3 and in Figure 1.4.

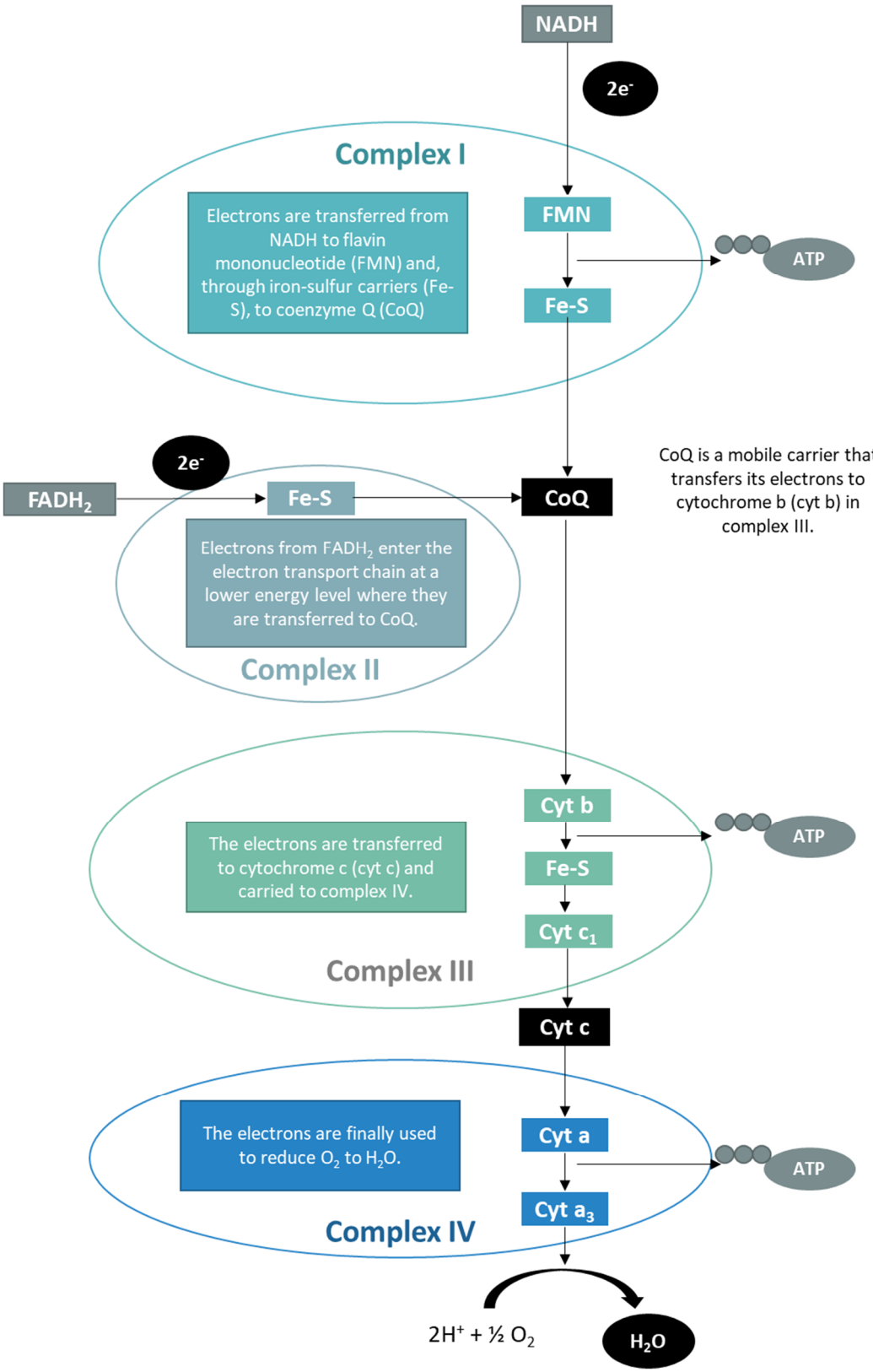

Figure 1.3 - Schematic representation of the first four complexes that compound the electron transport chain and the main molecule conversions which occur within it adapted from (Cooper and Hausman, 2007)**.**

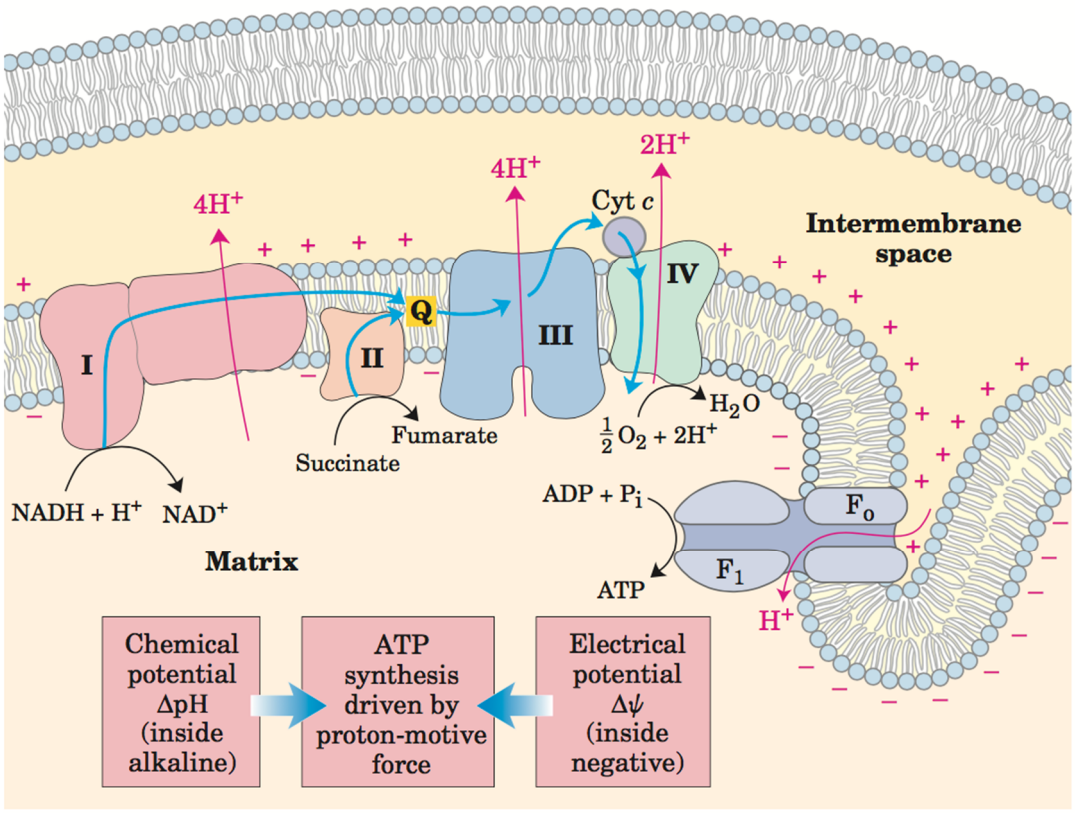

Figure 1.4 - The electron transport chain (Nelson and Cox, 2005).

Electron donation by NADH and $FADH_2$ involves different complexes of the electron transport chain. Complex I handles the reception of the electrons transported by NADH, where NADH is again oxidized to NAD^+ by donating two electrons to flavin mononucleotide (FMN). FMN will then donate these electrons through an iron-sulfur carrier to coenzyme Q (CoQ), also known as ubiquinone. During this process, enough free energy is harvested, and four protons are pumped into the intermembrane space, leaving the inner matrix negatively charged. CoQ will serve as electron transporter in the complex III, where electrons are first transferred to cytochrome b and, again, through an iron-sulfur carrier to cytochrome c. Once more, enough free energy is made available in this process, which will lead to the pump of four more protons into the mitochondrial intermembrane space, and to an increase in the negative charge of the inner mitochondrial matrix. Cytochrome c will in turn transport electrons to complex IV. Here, the electrons are finally transferred to O_2 while enough energy is freed to pump two other protons to the intermembrane space (Cooper and Hausman, 2007).

On the other hand, $FADH_2$ origins from the Krebs cycle intermediate succinate and its reduction only occurs at the complex II of the electron transport chain. During this reduction reaction, $FADH_2$ will donate 2 electrons to CoQ. However, the free energy associated to these reactions is not enough to pump any protons to the outside of the inner matrix space, which means that $FADH_2$

reduction reactions are not as productive as NADH reduction reactions. Proton pumping to the intermembrane space only occurs on the next complexes, similarly to what happens with the electrons originated on the NADH converted in complex I (Cooper and Hausman, 2007).

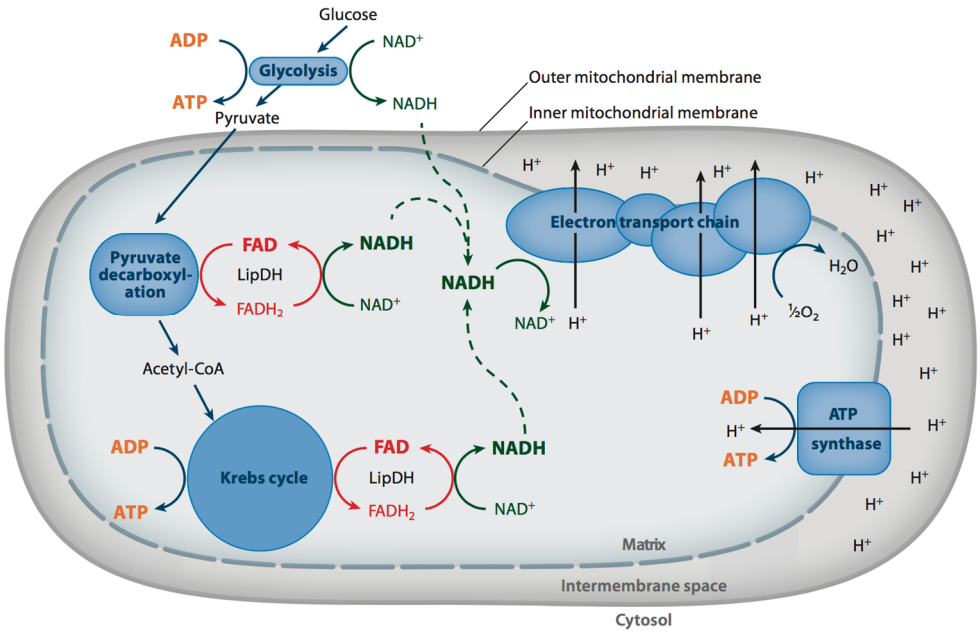

Figure 1.5 – Schematic representation of all the processes involved in the cellular respiration and the conversion of glucose into ATP molecules, with special focus to the locations where NADH and FAD conversions occur. (Georgakoudi and Quinn, 2012a).

A final complex is present at the electron transport chain – Complex V. Before describing it, it is necessary to underline that the mechanism of ATP production at the electron transport chain is different from the one that happens during glycolysis and Krebs cycle. During these processes, due to the high energy-yielding reactions occurring, a high-energy phosphate is transferred directly to ADP from another substrate. On the contrary, during the electron transport chain, the free energy present will lead to the generation of the proton gradient across the inner mitochondrial membrane. This proton gradient stores the energy freed during the different transport stages and it will be used by the Complex V, also known as ATP – synthase, to favorably couple the flow of protons across the membrane. As the protons flow back into the inner space of the mitochondria, more molecules of ATP are synthesized (Cooper and Hausman, 2007; Georgakoudi and Quinn, 2012a).

B. NADH and FAD fluorescence on tissue metabolic assessment

As stated in the previous section, the important role of the co-enzymes NADH and FAD is easy to understand. Besides their importance, these two molecules also have a very important feature: some of their protein conformations are capable of emitting fluorescence under the right conditions. This fact allowed the application of different optomechanical techniques to assess them and try to correlate their fluorescent properties with the metabolic state of a cell or tissue. NADH is fluorescent in the reduced redox state while FAD only fluoresces in the oxidized redox state (Georgakoudi and Quinn, 2012a). Their fluorescence excitation spectrums are depicted in Figure 1.6 and Figure 1.7. Due to this difference in the oxidized states and fluorescence emission, a ratio, obtained by dividing the FAD fluorescence intensity by the sum of NADH and FAD fluorescence intensities, is a good approximation of the mitochondrial matrix space redox ratio (Equation (1.1)). Therefore, it is commonly named optical redox ratio (Chance and Lieberman, 1978; Chance *et al.*, 1979; Skala and Ramanujam, 2010).

$$Redox\ Ratio = \frac{[FAD]}{[FAD] + [NADH]} \tag{1.1}$$

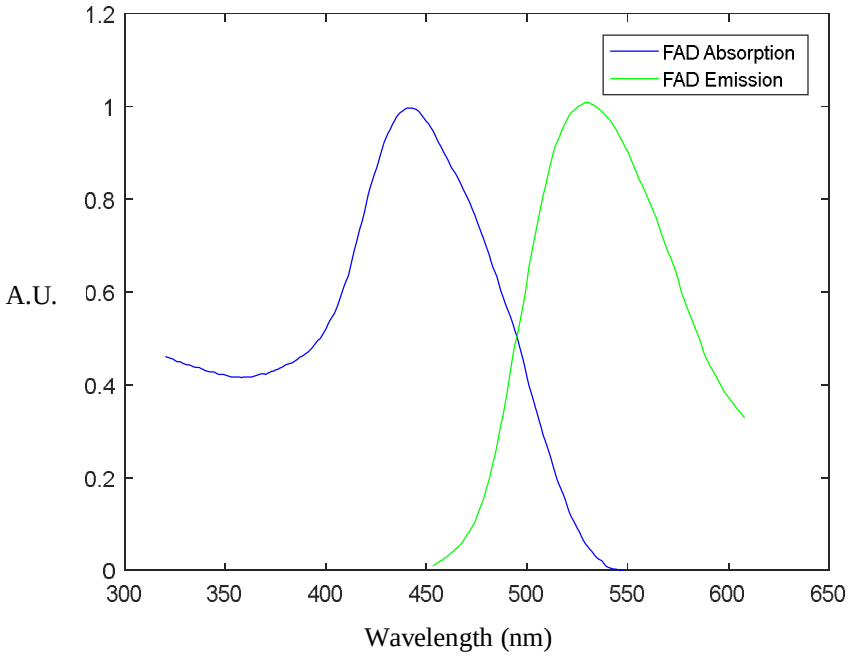

Figure 1.6 – Fluorescence excitation and emission spectrums of FAD (OIA, 2011)**.**

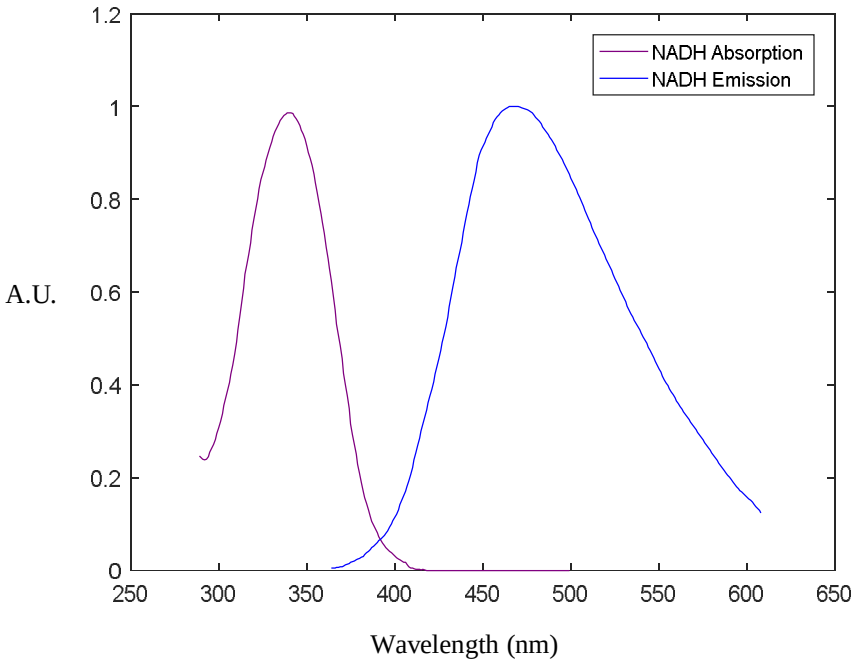

Figure 1.7 – Fluorescence excitation and emission spectrums of NADH (OIA, 2011).

The optical metabolic ratio can be very important in evaluating the metabolic state of a cell through non-invasive methods. From this value different conclusions can be inferred about the cell metabolic states and, in a more systemic view, correlate it with diseases and alterations in animal/human tissues and organs. Considering this, assessment of redox ratios has become a quite popular technique in biological research during the last decades. Among many other causes for changes in the values of this ratio, one of the most importance is the noticeable difference between aerobic and anaerobic ATP production. This difference was first noticed by Chance et al (Chance *et al.*, 1962, 1979; Chance and Lieberman, 1978) during the decades of 1960-1970. In the presence of O_2, a healthy and completely differentiated mammalian cell, with a high demand for ATP production, favors the oxidative phosphorylation metabolic pathway. Therefore, during the electron transport chain there is a high demand for NADH to be oxidized into NAD^+ to trigger the proton flux system. This tends to reduce the concentration of NADH within the mitochondria while, at the same time, increasing the oxidation of $FADH_2$ to FAD and thereby the FAD concentration. This situation increases the optical redox ratio, since the fluorescence intensity of NADH decreases and the FAD fluorescence signal increases. When O_2 is absent from the cell, the electron transport chain is inhibited and the anaerobic metabolism mechanisms that occur outside the mitochondria are favored. This leads to an increase in the cytosolic NADH via glycolysis while mitochondrial NADH also increases due to a reduced demand of the electron transport chain to oxidize it to NAD^+. At the same time, $FADH_2$ accumulates in the mitochondria while FAD concentration is reduced (Georgakoudi and Quinn, 2012b) leading to a reduction in the redox ratio. This phenomenon can also happen in the presence of O_2, mainly when cell

proliferation occurs. As mentioned, during glycolysis, besides pyruvate, other sub-products are generated, which are essential to other metabolic processes occurring when a cell proliferates. This favors the ATP production through glycolysis and anaerobic pathways over oxidative phosphorylation, resulting in similar behaviors in FAD and NADH concentrations to those observed when O_2 is absent from the cell. This phenomenon is of great interest in the cancer research field. It is known that cancer cells are in constant proliferation, so, it is expected that glycolysis is highly favored when compared to oxidative phosphorylation. Therefore, optical measurements of redox ratio can be a good indicator of the presence of cancer cells, even at an early stage (Skala, Riching, Bird, *et al.*, 2007). Different studies have been conducted to relate changes on the redox ratio with the presence of cancer cells (Skala, Riching, Bird, *et al.*, 2007; Bueno *et al.*, 2011), and there is a tendency to observe a reduced redox ratio in cancer cells when compared to healthy cells, a result that is mainly attributed to the higher rate of glycolysis in cancer and to reduced oxidative phosphorylation.

Not all fluorescence signal from NADH and FAD is directly connected with glycolysis and oxidative phosphorylation. In the case of NADH, there is a small portion of the fluorescence signal that is attributed to the presence of nicotinamide adenine dinucleotide phosphate (NAD(P)H), a molecule used as an electron carrier in anabolic pathways and that is only present in the cytosol. Distinguishing NADH from NAD(P)H with just spectral discrimination is not an easy task, since their fluorescence spectra are very similar. Moreover, NADH exists in at least two different conformations. Cytosolic NADH exists as a free molecule while mitochondrial NADH is bound to a protein called malate-dehydrogenase. Spectrally, fluorescence from these two conformations cannot be easily distinguished. However, these two conformations have very distinct fluorescence lifetimes, making possible to separate them through a fluorescence lifetime imaging system. Cytosolic NADH (free) has typically a short lifetime in the sub nanosecond range, while protein bound and mitochondrial NADH has a longer value, reported to be around 2 ns (Georgakoudi and Quinn, 2012a).

Similarly, FAD fluorescence intensity is not related to the total concentration of FAD in a cell. FAD is more commonly found bound to proteins called flavoproteins. The great majority of these proteins quench the FAD fluorescence, through its binding site, making impossible its detection by an imaging system. However, there is an exception: FAD bound to lipoamide dehydrogenase (LipDH), which is a complex that reduces NADH, is responsible for 50% of the total fluorescence signal associated with FAD. The fluorescence emission of this complex is quenched in the presence of NAD^+, and due to that, its fluorescence lifetime is reported as a short component in the sub nanosecond range. The remaining 50% of the FAD fluorescence emitted by a cell is equally distributed by the electron transfer flavoprotein and the FAD that is reducible only by the dithionite and is not related to cell metabolism (Georgakoudi and Quinn, 2012a). Again, similarly

to what happens with NADH, fluorescence lifetime can help in distinguishing between FAD associated with flavoproteins and free FAD. In this case, free FAD presents a larger lifetime component, also around 2 to 3 ns.

Due to these consistent differences in the fluorescence lifetime values between free and protein bound forms of NADH and FAD, a new ratio has been proposed to evaluate metabolic processes within a cell, through non-invasive optical methods: the free to protein-bound ratio, which is defined as the ratio between the relative amounts of the free and protein-bound components of the molecule being analyzed (Lakowicz *et al.*, 1992; Schneckenburger and König, 1992). Information given by this ratio is also a promising method to evaluate the metabolic processes of a cell, since it can give a more detailed insight on the biochemical properties of the mentioned co-factors (Lakowicz *et al.*, 1992). When combined with the "traditional" redox ratio, the overall characterization of the cell metabolism is improved. As with the "traditional" optical redox ratio, the free to protein bound ratio is also very dependent on which networks are active in metabolic processes of a cell. Particularly, it is stated that the free to protein bound ratio of flavins (FAD) is dependent on the function of the respiratory chain (Schneckenburger and König, 1992).

In 2014, Walsh et al (Walsh *et al.*, 2014) proposed a new index to evaluate metabolism based on metabolic imaging: optical metabolic imaging (OMI) index. This ratio, given by Equation (1.2), combines the information from the redox ratio and NADH and FAD fluorescence lifetimes to give a metric to correlate with the metabolic state of a cell or tissue. It is a linear combination of the mean-normalized redox ratio and the mean-normalized lifetimes of NAD(P)H and FAD.

$$OMI\ Index = \frac{RR_i}{\langle RR \rangle} + \frac{NAD(P)H\tau_{mi}}{\langle NAD(P)H\tau_m \rangle} - \frac{FAD\tau_{mi}}{\langle FAD\tau_m \rangle} \quad (1.2)$$

Differences in both redox and free to protein bound ratios associated with NADH and FAD fluorescence lifetime have already been demonstrated for a wide range of biological samples and proposed as a promising diagnostic method to identify a great variety of neoplastic diseases such as breast, head and neck cancers (Bird *et al.*, 2005; Walsh *et al.*, 2013; Shah *et al.*, 2014). Moreover, the application of fluorescence lifetime analysis as a diagnostic technique is already a reality in the field of dermatology, with different commercial equipment already available to help in the diagnosis of different skin diseases (Koenig, 2012). Fluorescence lifetime analysis based only on NAD(P)H fluorescence is more commonly found than studies based only on FAD or on the combination of the fluorescence decay information of the two co-factors. This can be explained by a greater concentration of NAD(P)H in cells since, as mentioned, it exists in both cytoplasm and mitochondria and also by the higher fluorescence probability (quantum yield)

attributed to NADH. Metabolic perturbations and their influence on NAD(P)H fluorescence lifetime have been reported in cells treated with metabolic inhibitors, which inhibit glycolysis and/or oxidative phosphorylation, such as cyanide (Bird *et al.*, 2005; Walsh *et al.*, 2013; Shah *et al.*, 2014) or cobalt chloride (Schneckenburger *et al.*, 2004) For instance, when cyanide was used to induce the inhibition of the electron transport chain in both breast and oral mucosa, it was found a decrease in the mean lifetime of NAD(P)H, meaning that the free-protein contribution of NAD(P)H increased in the cell. Moreover, when oxidative phosphorylation is inhibited, with cobalt chloride ($CoCl_2$) treatment in MCF10A cells and with rotenone treatment in BKEz-7 endothelial cells from calf aorta, an increase in the fluorescence lifetime of protein-bound NAD(P)H is observed together with a decrease in the relative amount of this conformation (Schneckenburger *et al.*, 2004).

OMI Index was introduced as a resource to study the effect of cancer drug treatments on sub-populations of cells. Since this is a relatively new parameter in the field, only a few authors have used this index to assess the metabolism of cells. Examples of the use of this index are directly related to the assessment of drug response in cancer treatments. Through that, it is possible to assess cancer cells metabolism and verify if the drug has effect or not in them (Walsh *et al.*, 2014; Walsh and Skala, 2015; Sharick *et al.*, 2018)

During the last years our group has collaborated with the research group of Prof Karsten König in the University of Saarland, Saarbrücken, Germany on the development of metabolic imaging of ocular tissues, particularly, the cornea using multiphoton excitation techniques. Metabolic imaging was successful applied to *ex-vivo* porcine corneas (Batista *et al.*, 2016) where metabolic images based on FAD and NADH fluorescence were acquired. Following this work, corneal metabolic imaging was studied as a method to assess the condition of corneas for transplantation (Batista, Hans Georg Breunig, *et al.*, 2018a). Moreover, multiphoton metabolic imaging was also used to understand the cell metabolic changes occurring in some corneal diseases (Batista, Hans Georg Breunig, *et al.*, 2018b). A more detailed study of *ex-vivo* porcine ocular tissues was also conducted (Batista, Hans G. Breunig, *et al.*, 2018).

Chapter 2 Fluorescence Lifetime Imaging Microscopy Instrumentation Methods

A. Fluorescence and Fluorescence Lifetime

Fluorescence is a luminescent process characterized by the spontaneous emission of light from an excited molecular entity with retention of spin multiplicity (Braslavsky, 2007), (Mycek and Pogue, 2003). This phenomenon can be easily understood through a simplified version of a Jablonski diagram (Jablonski, 1935) demonstrated in Figure 2.1. Upon light absorption by a given molecule, electrons from the most external layer are excited from ground state (S_0) to the first (S_1) or higher (S_2) excited states depending on the absorbed photon energy $h\nu_a$. The electron in the excited state maintains its spin-pairing to the second electron in the ground-state orbital. Immediately after excitation, the molecule undergoes fast relaxation to the lowest vibrational state of the first excited electronic level (internal conversion). However, to maintain the thermal equilibrium, the molecule tends to return to its 'original' non-excited state. Several processes can occur during the return to the ground state. One of them is fluorescence, a radiative decay process characterized by the emission of a photon with lower energy than the absorbed one. This effect is known as Stoke's shift and was first demonstrated by Sir George Stokes in 1852 (Stokes, 1852). Fluorescence emission is typically characterized by the return of the electrons in the lowest energy state of S_1 to a higher excited ground state level S_0, reaching quickly after thermal equilibrium (Lakowicz, 2006a). The equivalent energy associated with fluorescence emission is described by Equation (2.1), where h is the Planck's constant and υ_F is the frequency of the light. The return to ground state can occur through other processes, radiative or non-radiative. Here we focus on the fluorescent effect since it allows the characterization of different processes and is highly used in biological applications.

$$E = h\upsilon_F \tag{2.1}$$

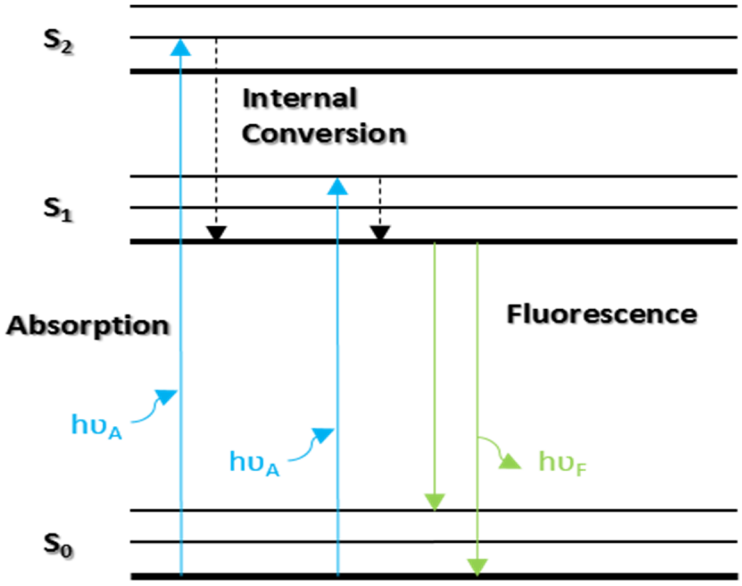

Figure 2.1 – Simplified version of Jablosnki Diagram (adapted from (Lakowicz, 2006a)**).**

Given the retention of the spin pairing between excited and grounded electrons, the process of fluorescence is very fast, occurring generally in the nanosecond or picosecond range. (Lakowicz, 2006a). Thus, an intrinsic parameter of each molecule, fluorescence lifetime (τ) can be defined as the average time between the molecule excitation and the return to the ground state or, in other words, as the average time the molecule stays in its excited state prior to its return to the ground state (Lakowicz, 2006a) (Periasamy *et al.*, 1996). This value is theoretically defined as the inverse of the sum of the rate constants for all excited state depopulation processes and described by Equation (2.2), where k_r and k_{nr} are the radiative and non-radiative rate constants, respectively (Suhling *et al.*, 2015).

$$\tau = \frac{1}{k_r + k_{nr}} \tag{2.2}$$

Fluorescence lifetime is related to another intrinsic parameter of each fluorophore called quantum yield through Equation (2.3), where τ_0 is the radiative or natural lifetime.

$$\phi = \frac{\tau}{\tau_0} = \frac{k_r}{k_r + k_{nr}} = \frac{1}{1 + (k_{nr}/k_r)} \tag{2.3}$$

Quantum yield (ϕ) is defined as the ratio between the number of emitted photons and the number of absorbed photons. Brighter fluorescent molecules exhibit greater quantum yields (Suhling *et al.*, 2015).

The fluorescent intensity decay curve of a given fluorophore corresponds to the electron depopulation of the excited state. Considering that N is the number of fluorophore molecules that populate the excited state S_1, dN can be defined as the number of excited fluorophores returning to the ground electronic level in the instant dt – Equation (2.4).

$$dN = (k_r + k_{nr})N(t)dt \tag{2.4}$$

By integrating Equation (2.4) and considering the relation of lifetime with radiative and non-radiative rate constants described in Equation (2.2), the fluorescence intensity decay profile $I(t)$ is described by Equation (2.5) where $I(t)$ is proportional to $N(t)$.

$$I(t) = I_0 e^{\frac{-t}{\tau}} \tag{2.5}$$

Equation (2.5) represents the ideal fluorescence decay where only one lifetime exists. However, when mixtures of fluorophores or multiple states of fluorophore species arising from interactions with the local environment are considered, the fluorescence decay profile is more complex. As an example, this happens when autofluorescence from biological tissues is measured. These complex decays are represented by Equation (2.6) and they are simply the sum of different exponential decays with different lifetimes (τ_n) and pre-exponential amplitude factors (I_n) (Marcu, French and Elson, 2014).

$$I(t) = \sum_{i=1}^{N} I_n e^{\frac{-t}{\tau_n}} \tag{2.6}$$

B. Instrumentation

The first instrument to measure the decay time of fluorescent molecules was reported in 1858 by the French physicist Eduard Becquerel. By using sun as the light source, he developed a "phosphoroscope" which was comprised of two rotating disks with four windows positioned in

such a way that did not line up - Figure 2.2. By placing uranyl salts (sample) between the disks, he was able to measure time intervals as short as 10^{-4} s (Becquerel, 1867). Following Becquerel work, in 1899, Abraham and Lemoine, benefiting from Kerr cells studies (Kerr, 1875), introduced the concepts of light modulation and phase which allowed measuring intervals of time nearly 100,000 times shorter than Becquerel's "phosphoroscope" (Abraham and Lemoine, 1899, 1900). The application of these concepts was only successfully concluded in 1921 by Robert Wood who was able to measure time intervals as short as 10^{-7} s (Wood, 1921). The first nanosecond lifetime measurements were demonstrated by the Argentinian physicist Raman Enrique Gaviola in the 1920s. He developed an instrument named "Fluorometer" which was based on principles from both Becquerel's" phosphoroscope" and Abraham-Lemoire experiments. He established the principles of modern fluorescence lifetime spectroscopy and he was also the first to demonstrate that lifetimes depend on the molecular species and on their local environment (Gaviola, 1926). Despite this rapid growing in the late 19th century and early 20th century, it was only in 1957 that the first time-domain implementation was reported. Seymour S. Brody reported on an instrument that used a hydrogen flash lamp and a high-speed oscilloscope to measure fluorescence lifetimes in the order of microseconds (Brody, 1957; Marcu, French and Elson, 2014).

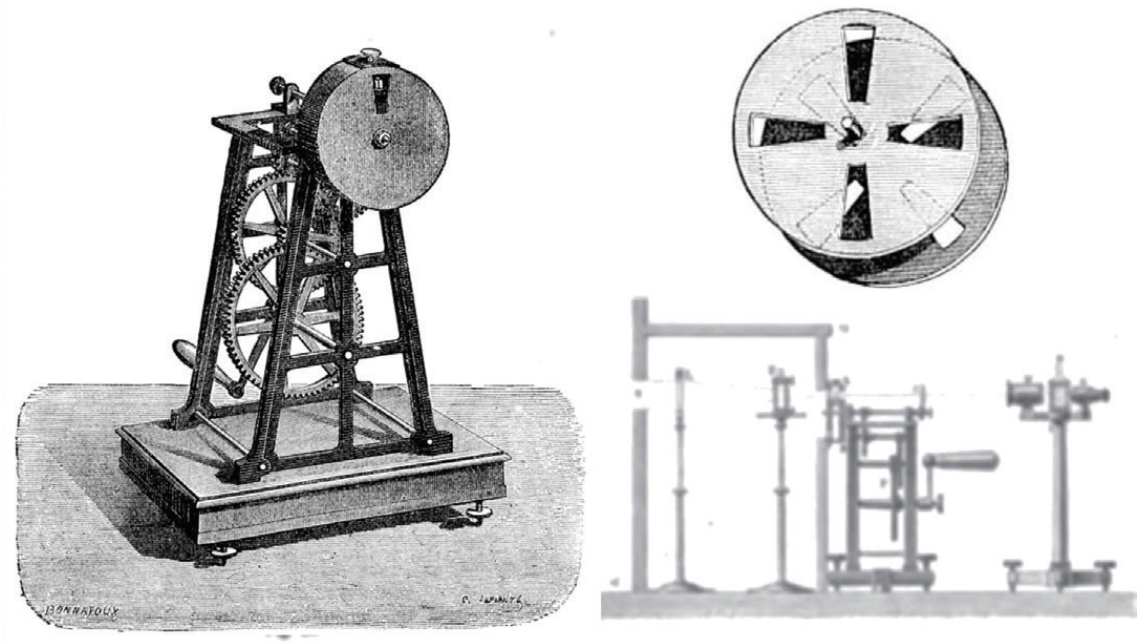

Figure 2.2 – Eduard Becquerel phosphoroscope (Marcu, French and Elson, 2014)**.**

Nowadays, and after more than 150 years of development, the instrumentation available can be grouped in Time- and Frequency-Domains. Frequency-domain makes use of modulated light sources and modulated detection while Time-Domain techniques rely on a pulsed light source and a direct measurement of the fluorescence signal emitted as a function of time. This can be seen as an advantage over frequency-based techniques since the lifetime can be directly estimated. Time-

Domain Fluorescence Lifetime Imaging Microscopy (FLIM) is quite popular among the scientific community and, in general, can be divided in two main techniques: Time-Correlated-Single-Photon-Counting (TCSPC) and Time-Gated. In the next sections, the working principle behind each one of them is described and examples of their biological applications are given.

1. Time-Gated FLIM

In the last decade of the 20th century, the advent of microchannel plates led to the development of a Time-Domain technique called Time-Gated FLIM. As Figure 2.3 points out, the fluorescence decay profile of a given molecule is measured by opening and time-scanning a series of "time windows", commonly called gates, and acquiring fluorescence photons during a defined interval. An image corresponding to each scanned gate is acquired and a fluorescence intensity decay profile can be rebuilt by plotting the photon counts versus the time of acquisition.

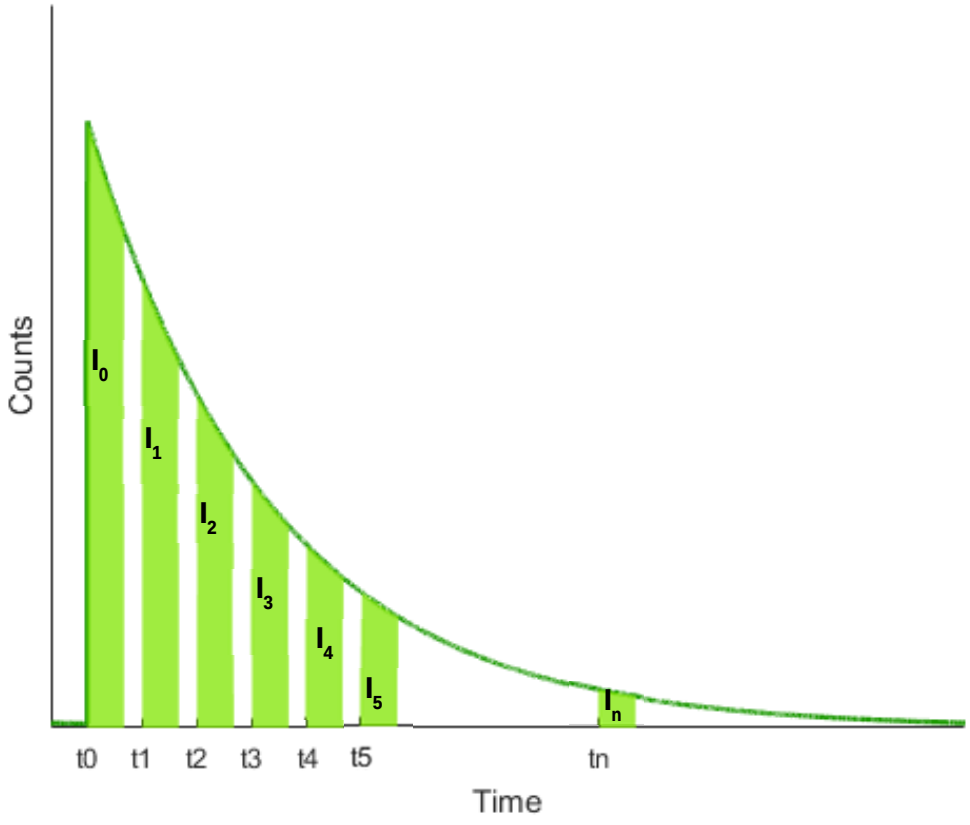

Figure 2.3 – Principle of Time-Gated Fluorescence Lifetime Measurement.

The first implementations of Time-Gated FLIM date back to 1993 when Cubeddu et al (Cubeddu, Taroni and Valentini, 1993) and Oida et al (Oida, Sako and Kusumi, 1993) reported on the first

time-domain fluorescence lifetime acquisition systems based on microchannel plates (MCP) electron multipliers. These devices placed between a photocathode and a phosphor screen constitute the gate optical intensifier (GOI) which is one of the key components to perform Time-Gated FLIM. By applying a gating voltage to the photocathode, the GOI will convert the fluorescence photons, collected by an imaging system, into electrons. Through the scheme presented in Figure 2.4, the processes inside a GOI can be easily understood. The duration of the gating voltage defines the gate width, and therefore the number of photons collected by the GOI. Electrons leaving the photocathode are then multiplied according to the voltage applied to the MCP (MCP voltage) which will define the gain introduced. When leaving the MCP, the accelerated electrons will strike the phosphor screen and be reconverted into photons through a phosphorescence process - Figure 2.5. These devices are typically coated by aluminum layers to direct the converted photons to the CCD direction and therefore increase the number of photons detected (Marcu, French and Elson, 2014; Stanford Computer Optics, 2018a).

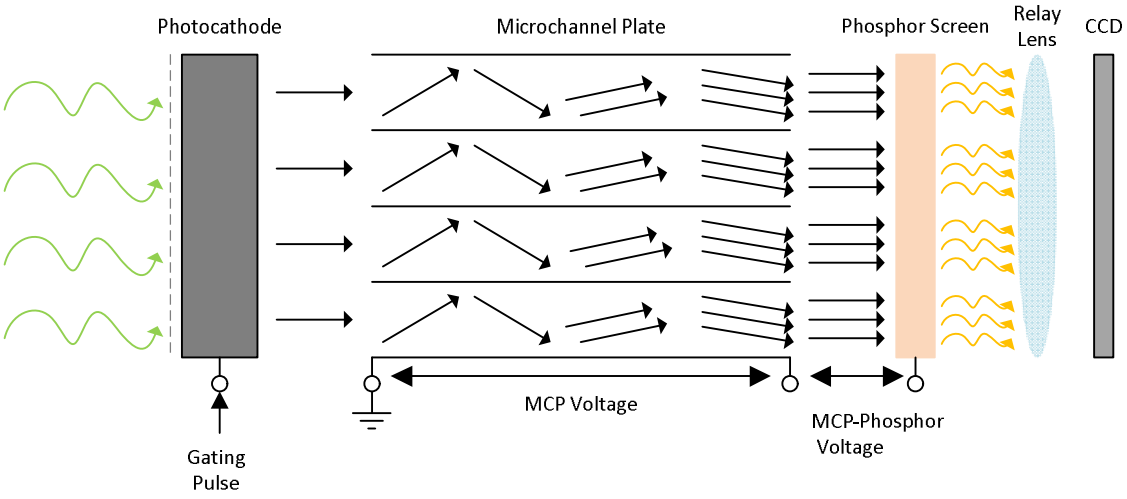

Figure 2.4 – Working principle of a gated optical intensifier (GOI). Photocathode, Microchannel plate and phosphor screen compose this system whose main task is to collect and multiply photons coming from an optical system prior placed and relay them to the CCD.

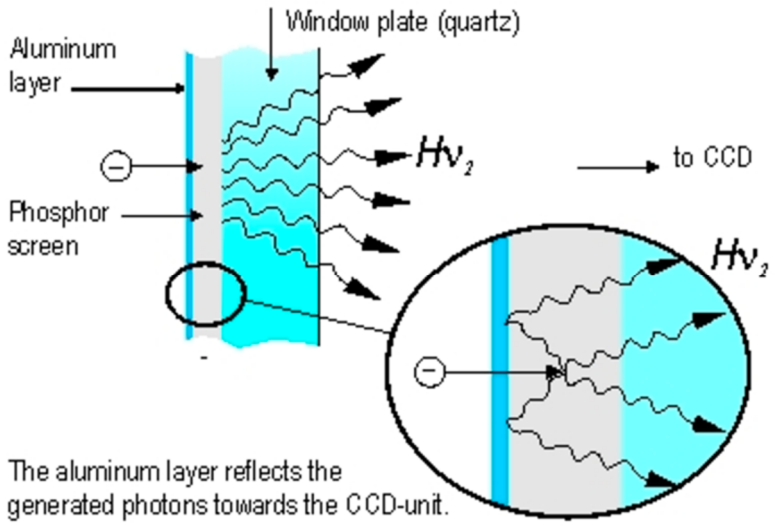

Figure 2.5 – Phosphor screen basic working principle (Stanford Computer Optics, 2018b)**.**

GOIs can work either in low-rate or high-rate repetition schemes. When working in a low repetition scheme, narrower gates (less than 100 ps) can be obtained, but the repetition rates are limited to a few kHz. High-rate repetition GOIs are typically named High-Rate-Intensifiers (HRI) and allow repetition rates in the order of MHz, which can be an advantage to measure shorter lifetimes. The main difference between these two types of devices lies in the place where the gating voltage is applied. While in HRI the gating voltage is low and applied directly to the photocathode, in GOI it is applied to a mesh placed in front of it. Spatial resolution is compromised with HRI due to the reduced proximity focusing. (Webb *et al.*, 2002).

Other devices are fundamental to build a Time-Gated system. The main one is the illumination system. Since this is a Time-Domain technique, a pulsed light source is required. The specifications of this device, mainly its pulse repetition frequency and its pulse width, will limit the timing properties of the Time-Gated system. Light source will provide the trigger to the entire Time-Gated detection system, which should be synchronous to the light pulse event. As explained, this technique is based on the acquisition of a series of images during the fluorescence decay of a given sample. To achieve that, the system needs to know when it should open the gate and acquire the signal, i.e., when to apply the gating voltage to photocathode inside the GOI/HRI. For that, the basic concept is to delay the trigger signal provided by the light source. This can be accomplished by passing the trigger signal through a user controllable delay generator, which will send the delayed trigger to the HRI and control when the gate is opened. If the trigger is synchronous to the light pulse event, the user can control when the images are acquired during the fluorescence time decay. The resolution of these systems is currently in the order of

picoseconds, allowing the measurement of fluorescence decay curves with lifetimes in the range of nano- and picoseconds (Webb *et al.*, 2002; Marcu, French and Elson, 2014).

The last three key components of a Time-Gated system are the CCD, which will ultimately record the fluorescence image, the computer with a frame-grabber installed where all the devices are controlled and the image is digitized and the imaging system, which can be a microscope, an endoscope or other optical system for collecting the fluorescence photons before they reach the GOI (Cole *et al.*, 2001). Figure 2.6 summarizes the main components and the connections required to successfully obtain a Time-Gated Fluorescence Acquisition System.

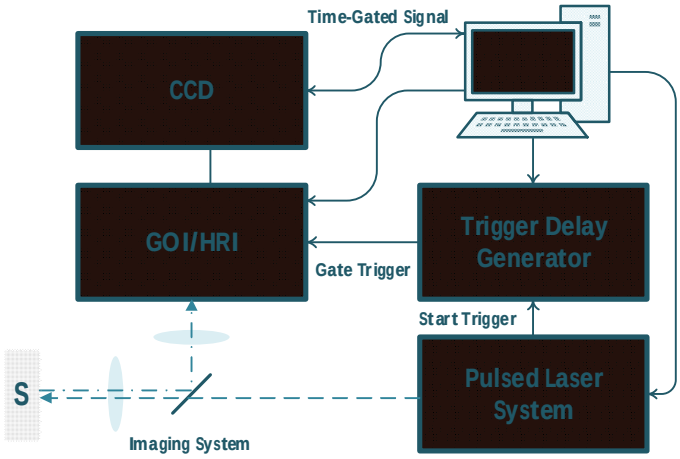

Figure 2.6 – General setup for a Time-Gated fluorescence lifetime acquisition system.

Being a real detection system, data acquired through a Time-Gated system has not an ideal response and noise is an important aspect to take into consideration. Contrarily to what happens in other Time-Domain FLIM systems, the noise characterization of Time-Gated detection is not ruled only by Poisson statistics. In an attempt to better characterize these systems, McGinty et al (McGinty *et al.*, 2009) studied a typical Time-Gated system and concluded that the dominant source of noise follows a Poisson distribution, but an excess noise term that is dependent on the characteristics of the GOI/HRI is added.

The noise distribution can be better understood by reviewing the process of photon multiplication that takes place in GOI/HRI. A photon reaching the photocathode of the GOI is converted in an electron and multiplied proportionally to the voltage applied to the MCP. The resultant electrons are converted in photons in the phosphor screen before reaching the CCD. Thus, the mean signal acquired by the CCD ($\bar{I}$) will just be the result of the multiplication of a gain function k by the number of photons S_{ph} reaching the photocathode during a gate, as described by Equation (2.7).

$$\bar{I} = kS_{ph} \tag{2.7}$$

This gain function k is proportional to several features of the GOI/HRI system, as Equation (2.8) suggests, where G_{MCP} is the MCP average gain, η_p the quantum efficiency of the phosphor screen, T the transmission efficiency of the coupling optics and η_{CCD} the quantum efficiency of the CCD.

$$k \sim G_{MCP} \cdot \eta_p \cdot T \cdot \eta_{CCD} \tag{2.8}$$

The standard deviation ∇ associated with the mean CCD signal collected can be obtained through Equation (2.9) where ∇_{CCD} is the noise associated with the CCD, typically readout noise. From that, it can be concluded that the variance in the signal collected is dependent on the number of photons reaching the photocathode during a gate, the gain applied to the MCP and as mentioned, the readout noise of the CCD.

$$\nabla_I{}^2 = S_{ph}\nabla_k{}^2 + k^2\nabla_{S_{ph}}{}^2 + \nabla_{CCD}^2 \tag{2.9}$$

Equation (2.9) summarizes the different sources of noise possible in this type of systems. The first term describes the variance of the gain function k, the second term is the noise associated with the photoelectron statistics and finally the variance associated with the readout noise of the CCD is the last term.

Assuming that the detected photons are ruled only by Poisson statistics, $\nabla_{S_{ph}}^2 = S_{ph}$, Equation (2.9) can be rewritten into Equation (2.10) where E is an excess noise factor and A, the variance of the gain k, is considered constant. A, E and k can be determined for different gain voltages by fitting linear and quadratic functions to plots of the mean CCD signal and the square of the standard deviation (variance) respectively as a function of the number of detected photons.

$$\nabla_I^2 = AS_{ph}^2 + k^2 E S_{ph} + \nabla_{CCD}^2 \tag{2.10}$$

From Equation (2.10), it can be concluded that when the system is shot-noise limited $E = 1$ and A and ∇_{CCD} are 0. However, according to the experiments reported by McGinty et al, this ideal

situation does not occur in Time-Gated systems. The authors proved that, when working with a low MCP voltage, noise is ruled by Poisson statistics with an excess noise factor E which decreases with increasing MCP gain. This means that in such conditions the factor A is 0 and Equation (2.10) can be simplified into Equation (2.11).

$$\nabla_I^2 = k^2 E S_{ph} + \nabla_{CCD}^2 \tag{2.11}$$

When working with very high MCP voltages the additional noise factor A increases and affects the noise distribution. The system no longer follows a Poisson distribution. The decrease of the excess noise factor is different from what happens in the conventional photomultiplier tubes. This can be explained by the differences in the gain mechanism between these detectors such as the angle of incidence during the electron-wall interaction (Eberhardt, 1979).

Time-Gated FLIM has been used in a variety of biological and biomedical applications. Benefiting from systems such as microscopes, endoscopes or simple wide-field lenses, endogenous and exogenous FLIM-based contrast has been reported throughout the years. In fact, the first TG-FLIM implementations, which date back to 1993, were demonstrated in biological samples. Cubeddu et al (Cubeddu, Taroni and Valentini, 1993) aimed to create a method to detect tumors, particularly murine fibrosarcoma, when rats were administrated with injections of photosensitizers such as HpD (hematoporphyrin derivative) and phthalocyanines. By illuminating the affected tumor area with the specific excitation wavelength for each photosensitizer, the authors could acquire fluorescence images in which the tumor area was highly contrasted. In this application, the main goal of the authors was not to create a lifetime map of the affected area, but to have a method for distinguishing the autofluorescence of the tissue from the fluorescence of the photosensitizer. This was only possible due to the long lifetime associated with the photosensitizer, which allowed the acquisition of an image several nanoseconds after the excitation pulse, giving enough time for the tissue autofluorescence to extinguish. Later on, in 1995, the same group extended their work and used the same instrument setup to acquire lifetime maps corresponding to the fluorescence of HpD by opening two gates at 10 and 30 ns after the excitation pulse and processing the data with the Rapid Lifetime Determination method (Cubeddu *et al.*, 1995). Moreover, in 1999 the same setup and methods were again applied, but this time on humans for the detection of skin tumors by measuring the lifetime associated with the accumulation of endogenous Proptoporphyrin IX(PpIX) in proliferative tissues upon stimulation through the injection of the Heme precursor δ-aminolevulinic acid.

Also in 1993, Oida et al (Oida, Sako and Kusumi, 1993) reported on the implementation of a Time-Gated FLIM microscope to observe the extent of fusion of individual endosomes in single cells.

Figure 2.7 shows the main components of the microscope built by the group of Oida. Several main modules can be distinguished in this setup: the laser source, which relied on a cavity-dumped mode locked argon ion laser capable of producing pulses with FWHM of 400ps at a rate of 400KHz and central wavelength λ=488 nm; the inverted microscope based on epi-illumination and using a filter wheel to properly select the wavelengths for imaging; the nanosecond gate system containing the same basic elements that are still used nowadays to set up a Time-Gated system: a pulse delay generator, a gate driver, a photocathode, a MCP and a cooled CCD. This detection system was capable of producing gates as narrow as 2.5 ns at a repetition rate of 500 kHz. The cooled CCD camera was connected to a computer for digitizing the signals, processing the images and controlling the entire system. With this system, the authors obtained lifetime maps on a pixel-by-pixel basis and identified intracellular fusion of endosomes at different times.

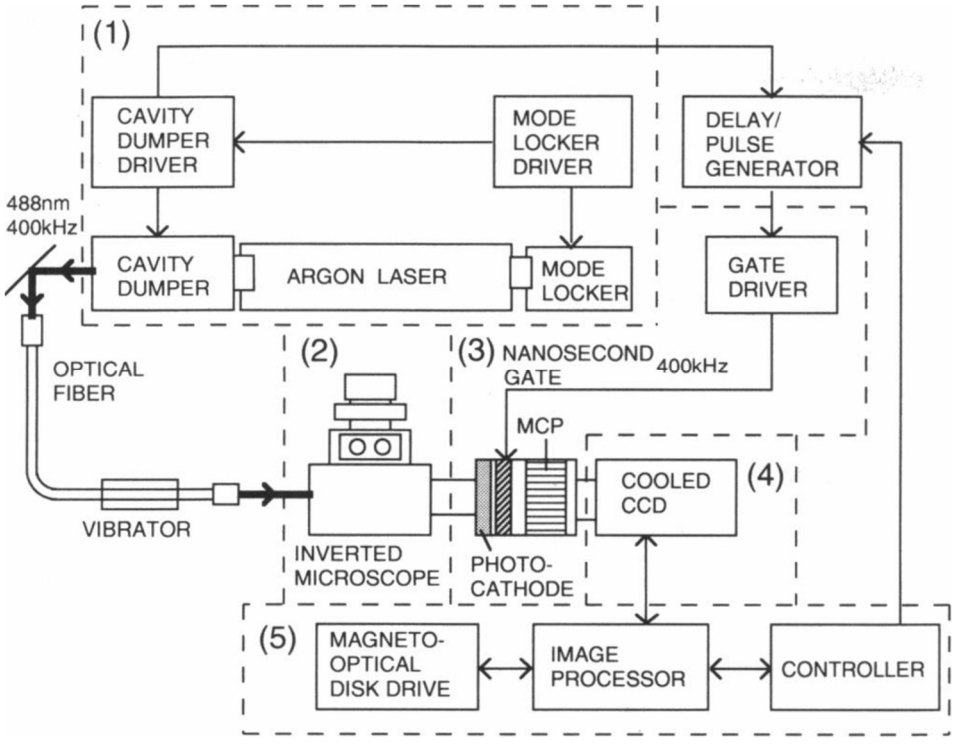

Figure 2.7 - System setup of a Time-Gated FLIM Microscope for detection of individual liposomes in cells (Oida, Sako and Kusumi, 1993)**.**

The instrument setups already mentioned were the first to be demonstrated and thereby their characteristics, when compared to modern technology, were quite limited. In 1998, K. Dowling (Dowling *et al.*, 1998) and his collaborators demonstrated the first instrument capable of resolving lifetimes differences as small as 10 ps, while providing a time response of less than 100 ps.

Approximately 10 ps duration pulses at 415 nm were delivered to excite a sample through a wide-field imaging system with a commercial Ti:Sapphire laser amplified by a home-built CR:LISAF regenerative amplifier. The detection system was based on a GOI with a time response (minimum gate width) around 90 ps and a delay generator, capable of scanning the fluorescence emission profile in steps of 25 ps connected to a CCD camera. The acquired data series were processed with a nonlinear least-squares fitting algorithm. To demonstrate the fluorescence lifetime imaging capacities of these systems, the authors imaged solutions of Coumarin 314 in ethanol, DASPI in a mixture of ethanol and glycerol and isolated biological samples of collagen and elastin. Based on this setup, the first structured illumination time domain fluorescence lifetime imaging microscope was reported in 2000 (Cole *et al.*, 2001). The system was based on a similar light source to that used in K. Dowling et al 1998, but this time an HRI could work at higher frequencies (in the order of MHz). The imaging system was based on an inverted epifluorescence microscope. Optical sectioning with widefield illumination was provided by a structured illumination microscopy. Structured illumination microscopy, which was first introduced in 1997 (Neil, Juskaitis and Wilson, 1997), will be further detailed in this thesis. With this optical setup, the authors could create FLIM maps of simple samples such as fluorescence stained cottons fibers and fluorescence microspheres with better axial resolution and less out-of-focus noise degrading the quality of the final lifetime image.

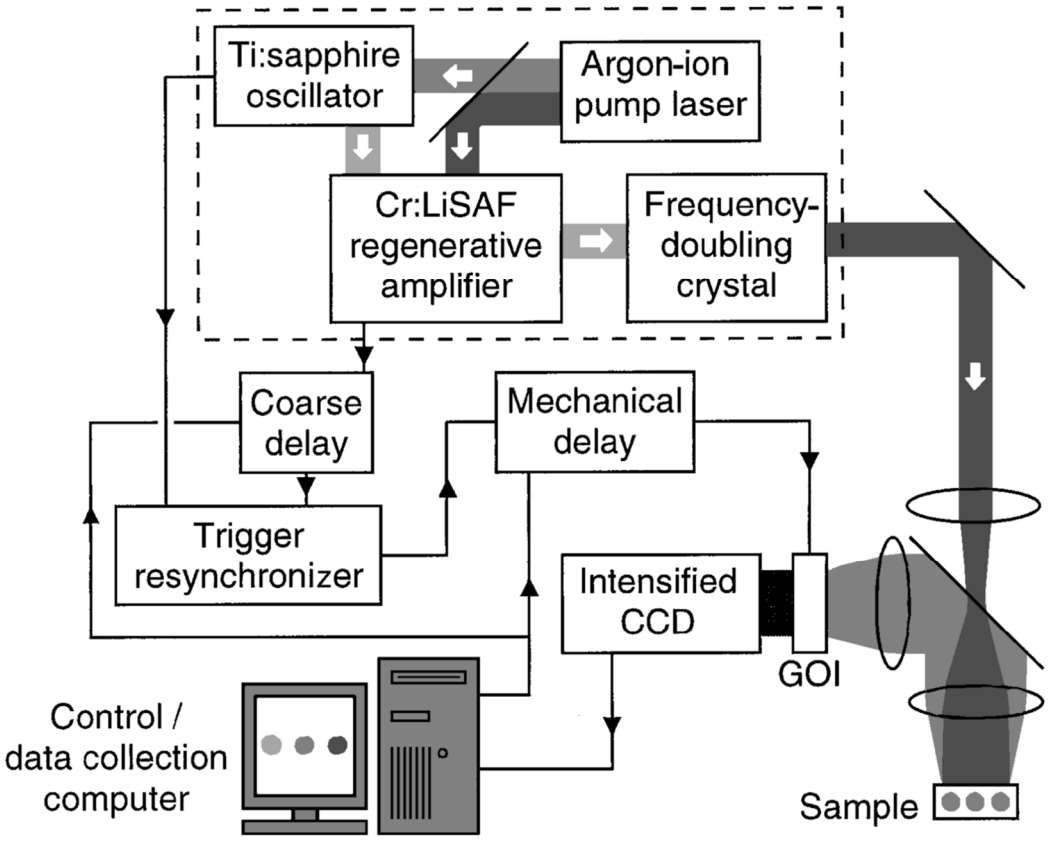

Figure 2.8 – Dowling et al instrument setup (Dowling *et al.*, 1998)**.**

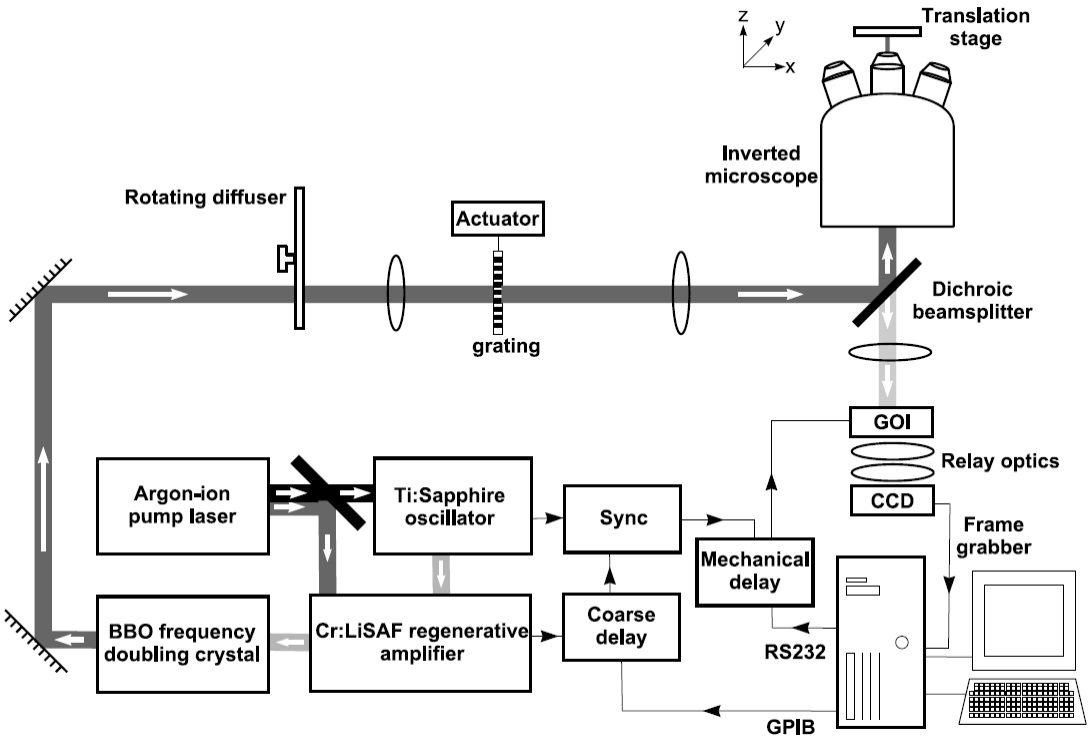

Figure 2.9 – Webb et al (Webb *et al.*, 2002)**microscope setup where it can be seen the structured illumination components in the illumination path of the microscope.**

In 2002, Elson et al (Elson *et al.*, 2002) demonstrated a multi-spectral Time-Gated FLIM. The TG instrument was quite similar to the examples previously demonstrated, with a GOI capable of generating gates as narrow as 90 ps and a laser source based on a home-built diode-pumped Cr:LISAF oscillator/amplifier system capable of generating 100fs pulses at 80 MHz. Here, structured illumination was also used to provide optical sectioning. However, the main difference in this application lies in the ability to image different wavelengths in the same shot. By placing a multispectral imager before the GOI (Elson *et al.*, 2002), the fluorescence from the sample could be acquired in the same image at two different wavelengths. This way, the lifetime maps of different spectrally-resolved components could be simultaneously acquired in a faster way, without the need for multiple exposures. The instrument was tested by imaging a freshly extracted piece of rat heart. By using different sets of filters, fluorescence intensity and lifetime maps of this sample could be acquired for different spectrums. A schematic representation of this instrument is depicted in Figure 2.10.

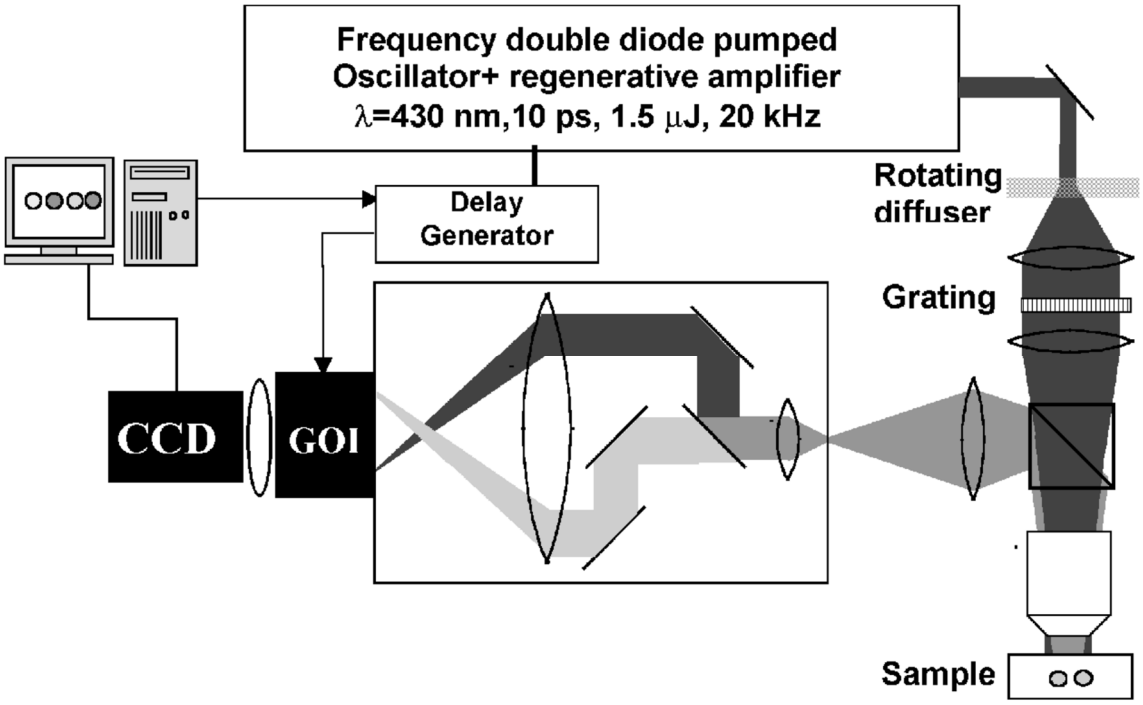

Figure 2.10 – Schematic representation of the multispectral optical sectioning Time-Gated FLIM microscope reported by Elson et al in 2002 (Elson *et al.*, 2002)**.**

One of the main disadvantages inherent to Time-Gated FLIM is the possibility of sample movement during the acquisitions of the series of images. This phenomenon, very common in *in vivo* applications can cause artifacts in the lifetime image and lead to poor lifetime fitting. In order to avoid this problem, an alternative approach to TG-FLIM was introduced in 2004 (Elson *et al.*, 2004). Using a segmented gated optical intensifier (SGOI) in conjunction with a four-channel optical intensity splitter, a single-shot wide-field fluorescence lifetime map could be demonstrated. This SGOI system, represented in Figure 2.11 consists of a typical gated optical intensifier, like those described before, with a photocathode, a MCP and a phosphor screen. However, its distinctive characteristic lies in the photocathode since it is split into quadrants by resistive sections. This provides four channels that can be gated at different delays times as long as the gate width is constrained to a single value. The four-channel optical intensity splitter is placed in front of the SGOI and relays four sub-images of the sample under inspection onto each of the quadrant. The main advantage of FLIM is the acquisition speed, particularly when using Rapid Lifetime Determination (RLD) methods.

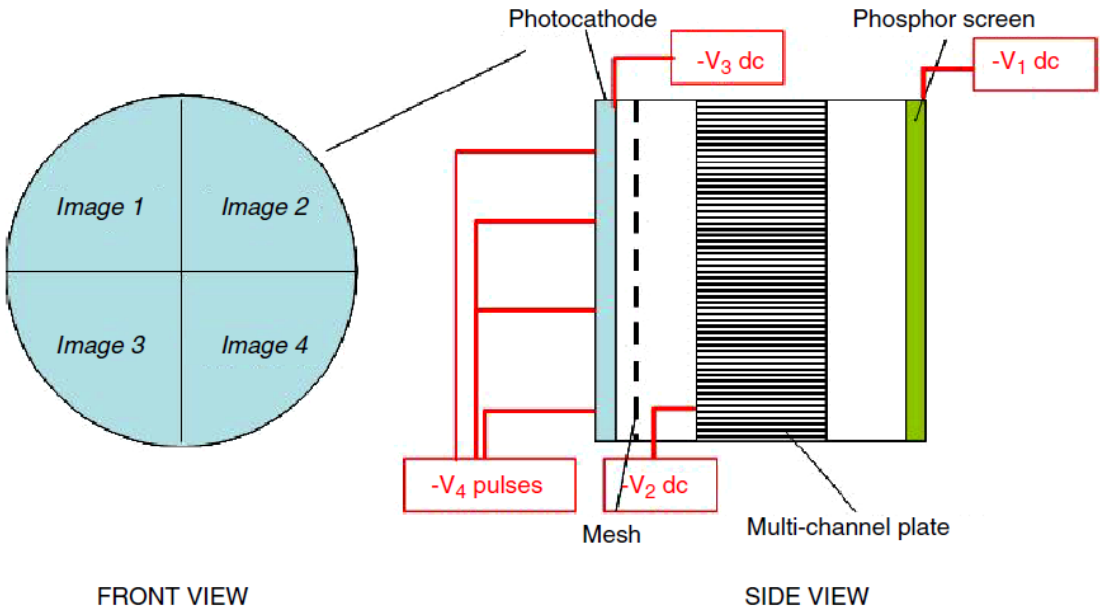

Figure 2.11 – Schematic representation of the four-channel segmented GOI used for single-shot FLIM by Elson et al (Elson *et al.*, 2004)**.**

Despite not being the most widespread Time-Domain FLIM method, Time-Gated FLIM throughout the years has been applied as the acquisition system in a great variety of biological applications. Studies on different types of cancer have been reported whether based in endogenous or exogenous fluorophore excitation with single or multiphoton light sources (Straub and Hell, 1998; Lévêque-Fort *et al.*, 2004). Some examples of these reports are the measurement of time-resolved autofluorescence from fixed breast cancer samples (Tadrous *et al.*, 2003), studies on the time-resolved spectra of gliomas to improve the tumor margin definition and enhance brain tumor diagnosis (Marcu *et al.*, 2004), an endoscopic FLIM apparatus to diagnose glioblastoma multiform intraoperatively (Sun *et al.*, 2010). the development of a device to detect oral carcinoma by tissue autofluorescence at λ=334nm ((Sun *et al.*, 2009) and the study of the potential of TG-FLIM to obtain contrast between basal cell carcinomas and surrounding uninvolved skin (Galletly *et al.*, 2008). The application of TG-FLIM is not limited to cancer. There are also reports in the area of cardiovascular diagnostics (Marcu, 2010) where it allows the characterization and diagnosis of atherosclerotic plaques.

2. Time-Correlated-Single-Photon-Counting (TCSPC)

Time-Correlated-Single-Photon-Counting (TCSPC) is the other time-domain technique in FLIM. This technique shares the direct fluorescence decay measurement in time with the Time-Gated

technique. However very significant differences can be found in the system setup and the data acquisition process.

Based on the fact that the detection of a photon in a particular signal period upon light excitation is a relatively unlikely event, the working principle of TCSPC assumes that detecting more than one photon per excitation pulse is a very rare event and therefore can be neglected. In this condition, it can be shown that the histogram of the arrival times of the first fluorescence photon corresponds to the fluorescence decay profile of the sample (Lakowicz, 2006b). The light source of this type of systems is similar to those used in Time-Gated, a short-pulsed source with a defined pulsing frequency is used to excite the sample and to synchronize the whole system. The fluorescent emitted photon is then detected through a photodetector, such as photomultiplier tube (PMT), a MCP or a single photon avalanche diode (SPAD) (Wahl, 2014), and fast electronics are used to register its arrival time. This process is continuously repeated during a certain interval of time until a histogram of the events (number of photons emitted) versus detection time is created (Becker, 2005). TCSPC was developed based on the method of "Delayed Coincidence" used in nuclear physics to determine the lifetime of unstable nuclei (Becker, 2015). The first reported applications of such technique on the detection of the shape of light pulses date back to 1961 (Bollinger and Thomas, 1961) , but it was only in the 1970's that the technique was first applied to the spectroscopy of excited molecules (Cova, Bertolaccini and Bussolati, 1973; Lewis *et al.*, 1973; Leskovar *et al.*, 1976).

The classical working principle of TCSPC is described in Figure 2.12 and in Figure 2.13. Two photodetectors are used to detect the excitation light pulse and emitted photons. Each photodetector is linked to a constant function discriminator (CFD) which mark very precisely the arrival time of the pulses. Both CFDs are linked to a time-to-amplitude converter which generates a voltage ramp that increases linearly with time on the nanosecond timescale. In the classical TCSPC approach the first photodetector detects the excitation pulse and sends a start signal to the TAC. The second photodetector will then register the pulse from the single detected photon and send a stop signal to the TAC. So, the voltage at the TAC output will be proportional to the time delay between the excitation and the emission signals. A programmable gain amplifier (PGA) is connected to the TAC and is used to amplify its output voltage. An analog-to-digital converter (ADC) digitizes the signal and its samples are stored and processed. A window discriminator (WD) can be placed after the PGA to restrict the signal to a given range of amplitudes, i.e. range of time intervals. This process of detection is constantly repeated with a pulsed-light source to obtain the histogram of the arrival times of the first photon of fluorescence (Becker, 2005; Lakowicz, 2006b).

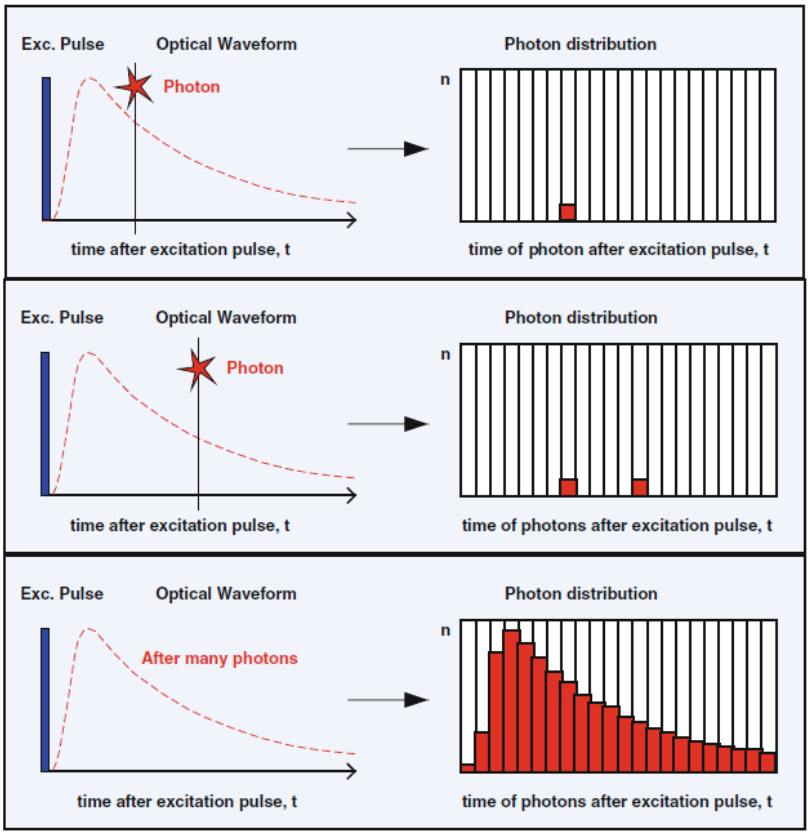

Figure 2.12 – Classical TCSPC waveform detection and building (Becker, 2015).

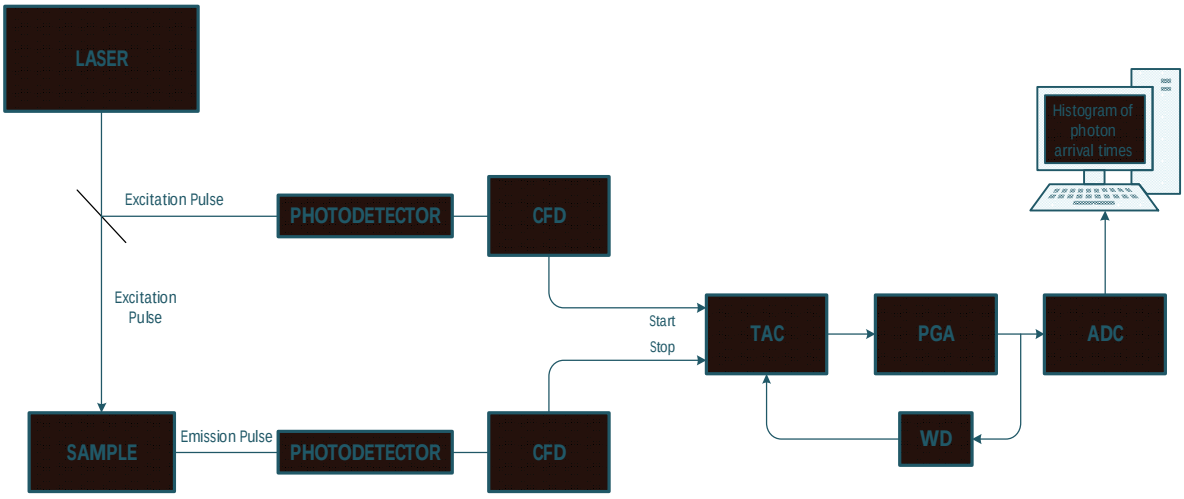

Figure 2.13 - Classical TCSPC working principle, adapted from (Becker, 2005).

The classical TCSPC method described above was the first to be implemented. However, with the development of higher-frequency pulsed lasers sources, a revised approach to the classical TCSPC approach had to be introduced. Before each start pulse, the TAC needs to be reset to 0 and this introduces a delay between the stop signal and the consequent start signal, slowing the entire signal acquisition process. To avoid this, the reverse-mode TCSPS is applied in modern

TCSPC devices - Figure 2.14 (Kinoshita, Ohta and Kushida, 1981; van Resandt, Vogel and Provencher, 1982).

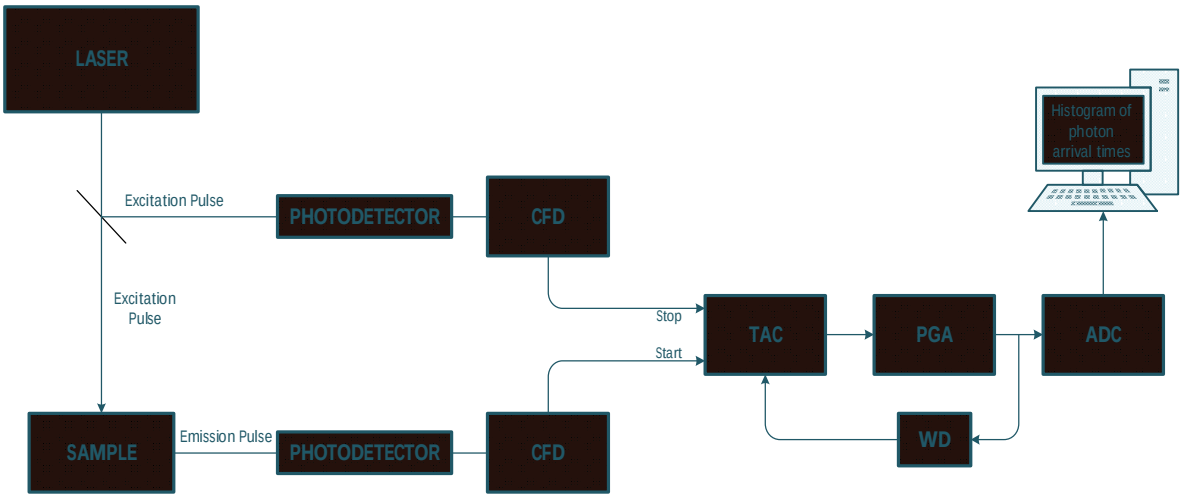

Figure 2.14 - Reversed TCSPC working principle, adapted from (Becker, 2005)**.**

The main difference between the reverse-mode and the classical TCSPC is the start and stop signals. In the reverse mode, the start signal is given by the detected single photon event while the stop signal is given by the detection of the delayed excitation pulse. The introduction of this approach is based on the fact that the emission signals occur about 1 time per 100 excitation pulses. This way the TAC lead time does not slow down the acquisition process, giving the TAC enough time to be reset to 0 before detecting another event (Becker, 2005).

The classical and reverse mode TCSPC implementations allow the recording of the fluorescence intensity versus time, which means that this method only gives direct access to two-dimensional data (photon counting versus time). However, if each photon distribution over time was to be varied along other parameters, one should obtain a multi-dimensional distribution of a TCSPC acquisition. Despite this, obtaining such multi-dimensional data by only varying the other parameters and still counting photons with either the classical or reverse-mode TCSPC, would result in a considerably long and in some cases impractical acquisition process, since for each parameter varied, the system would have to wait until the entire photon vs time distribution was completely acquired. In order to speed up this process, in 1993. Becker&Hickl (Becker, 1993) introduced the concept of multi-dimensional TCSPC in which the photon density is not only recorded as a function of time, but also as a function of other physical parameters that may interest the user. These can include spatial coordinates, which are used to obtain lifetime images, excitation and emission wavelength or polarization state of light. Multi-dimensional TCSPC is the approach most commonly used in modern TCSPC and results in large number of optical waveforms for different combination of parameters. Its main advantage is that it can be executed even when these parameters under inspection vary at faster rates than the photon detection

(Becker, 2015). In this type of implementation, the time after excitation of each detected photon is stored together with the value of the additional parameters under inspection at the moment of the photon detection. This way there is no need to wait until the entire waveform is complete to change the additional parameter value. As in the classical method, a multi-dimensional waveform can be built by repetitively exciting the sample, as exemplified in Figure 2.15

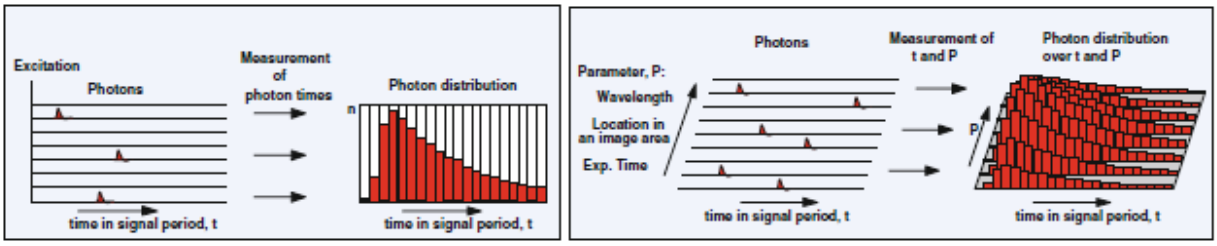

Figure 2.15 – Classical TCSPC waveform building vs Multi-Dimensional TCSPC waveform building. In multi-dimensional approach, a waveform per parameter varied is acquired (Becker, 2015)**.**

Multi-dimensional TCSPC is currently a commercial technique widely spread throughout the world. Becker and Hickl and Picoquant are two of the main manufacturers of this type of instruments. Due to this, there are innumerous reports of fluorescence lifetime imaging in biological samples whether based on exogenous fluorescent labeling (Knemeyer, Marme and Sauer, 2000; van Zandvoort *et al.*, 2002; Lakowicz, 2006a) or using endogenous molecules (Schweitzer *et al.*, 2004b). A special case of endogenous fluorescence is that of the metabolic cofactors NADH and FAD which have important roles on the metabolic process of the cell, particularly in the Krebs' Cycle. They are known to present different fluorescence lifetimes when bound or unbound to proteins. Using this information, they have been the object of study in different cells and tissues since their fractional lifetime contributions to the fluorescence decay can be used to evaluate with minimal invasion the metabolic process of cells or tissues (Bird *et al.*, 2005; Skala, Riching, Bird, *et al.*, 2007; Skala, Riching, Gendron-Fitzpatrick, *et al.*, 2007; Chorvat and Chorvatova, 2009; Ghukasyan and Kao, 2009).

TCSPC is the most suitable technique to be used with multiphoton microscopy. Almost all applications of multiphoton microscopy cited in Chapter 1 of this thesis use this type of acquisition technique.

C. Structured Illumination Methods

Optical sectioning in wide-field microscopy has always presented itself as a challenge when imaging thick specimens. When using conventional microscopy, the rules of diffraction limits described by Abbe in the 19th century apply. Due to that, when imaging thick fluorescent or light-scattering samples, light emitted or reflected by these specimens comes not only from the focal plane but also from out-of-focus planes that are as well illuminated, as described by Figure 2.16. The illumination takes the form of a cone which size is dependent on the depth of field of the used imaging lens (normally an objective). The depth of field of an objective is directly dependent on its numerical aperture (*NA*). Due to that, the image quality in wide-field microscopy is very reduced since the instrument cannot distinguish between sections of the thick specimen, retaining the contribution of light from out-of-focus planes and presenting, mainly, very low contrast.

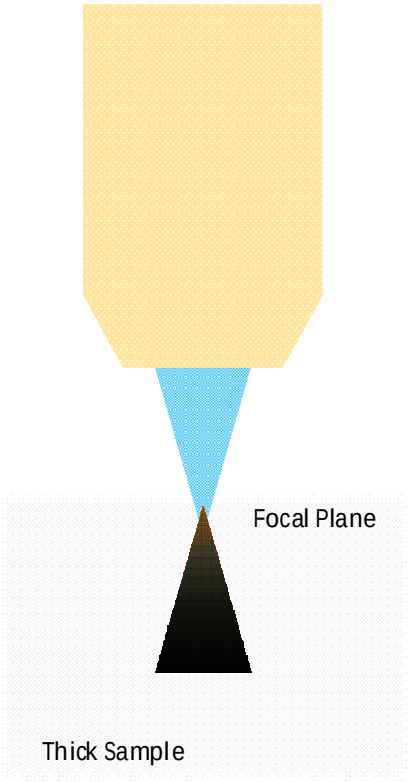

Figure 2.16 - Effect of depth of field in conventional wide-field microscopy.

Confocal microscopy is the most popular and widespread alternative to wide-field microscopy. However, this is a scanning technique (not wide-field) and the image is constructed on a pixel by pixel basis, which can turn the image acquisition process quite slow. During the last two decades, several approaches have been developed to achieve optical sectioning with wide-field microscopy and present a viable alternative to confocal microscopy. Neil et al in 1997 (Neil, Juskaitis and Wilson, 1997), Gustafsson (Gustafsson *et al.*, 2008) and Mertz in 2008 (Lim, Chu and Mertz,

2008) are examples of authors that demonstrated methods to achieve optical sectioning in wide-field microscopy without the need of point-scanning and with results comparable to those obtained with confocal microscopy. All these methods are englobed in a category called Structured Illumination Microscopy (SIM) whose main objective is to achieve optical sectioning and, in some cases, improvements on lateral resolution beyond the diffraction limits (Gustafsson *et al.*, 2008), through wide-field microscopy techniques.

Neil and Mertz approaches to structured illumination are only focused on obtaining optical sectioning and therefore no more than 3 images are required to achieve it. Gustafsson's approach, on the other way, is known for also improving the lateral resolution by a factor of two beyond the diffraction limit. To do so, a greater number of images is necessary. To the current project, the main goal of using SIM is to achieve optical sectioning and, due to that, only Neil and Mertz approaches are presented in detail.

1. 3-Phase Approach

As mentioned, this structured illumination technique was first demonstrated by Neil et al in 1997 (Neil, Juskaitis and Wilson, 1997). Aiming to create a viable alternative to confocal microscopy using wide-field microscopy, their approach comes from analyzing the weak transfer function associated with wide-field microscopes. By doing so, they concluded that it is only the zero spatial frequency that does not attenuate with defocus. So, the goal was to create a method that would be able to eliminate this component while maintaining the information that is in focus. For that, they suggested the superimposition of a single-frequency sinusoidal pattern onto the focal plane of the objective. Thus, only the parts of the object that were in focus would appear super-imposed with the sinusoidal pattern. However, only one image would not solve the problem, as the out-of-focus light would still appear and, worse than in conventional case, the image would retain the imposed sinusoidal frequency. So, the authors demonstrated that by using 3 images acquired with the same spatial pattern frequency, but with phase differences of $2\pi/3$ (120º) between each one, the projected pattern would be eliminated, and a sectioned image would be obtained.

In other words, by acquiring I_1 (ϕ_0=0º), I_2 (ϕ_0=120º) and I_3 (ϕ_0=240º), the sectioned image I_p could be obtained by applying Equation (2.12).

$$I_p = [(I_1 - I_2)^2 + (I_1 - I_3)^2 + (I_2 - I_3)^2]^{1/2} \quad (2.12)$$

Furthermore, the conventional image (I_0) can also be recovered by taking the average of the 3 acquired images – Equation (2.13).

$$I_0 = \frac{I_1 + I_2 + I_3}{3} \tag{2.13}$$

The process can be easily understandable by the scheme depicted in Figure 2.17.

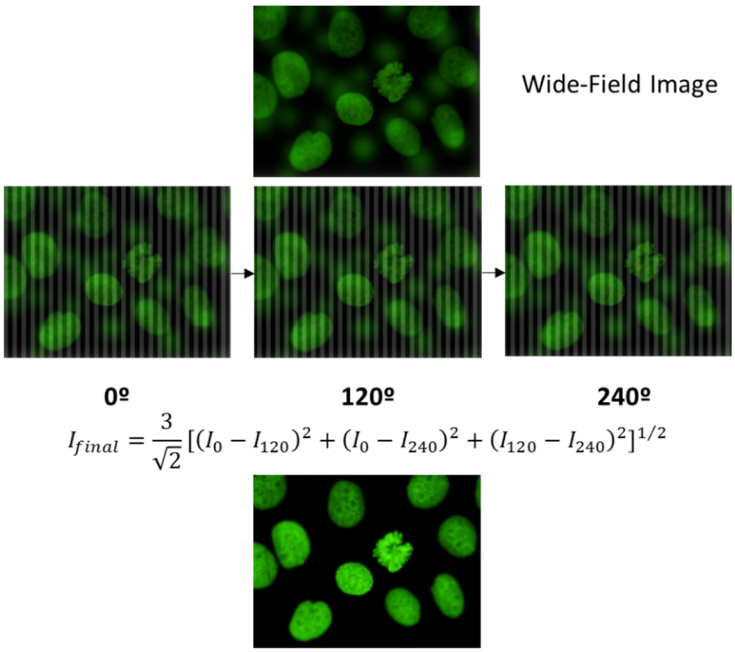

Figure 2.17 - Schematic demonstration of 3-phase approach structured illumination microscopy process.

The optical sectioning quality of this technique is directly related to the spatial frequency of the pattern projected. Higher frequencies will yield greater optical sectioning power, being the maximum limit the case in that normalized frequency ($\tilde{v}$) is 1. The normalized axial intensity response of the microscope is given by Equations (2.14) - (2.16). It is obviously dependent on the normalized frequency $\tilde{v}$, which is given by Equation (1.18) where f_g and f_t are the focal lengths of the lenses imaging the grating onto the sample and the tube lens focal length, respectively, M and NA are the magnification and numerical aperture of the microscope objective used, respectively.

$$I_p(u) = \left| \frac{2J_1\left[u\tilde{v}\left(1-\frac{\tilde{v}}{2}\right)\right]}{\left[u\tilde{v}\left(1-\frac{\tilde{v}}{2}\right)\right]} \right|^2 \tag{2.14}$$

$$\tilde{\upsilon} = \frac{f_g \lambda M \upsilon}{(NA) f_t} \tag{2.15}$$

$$u = \left(\frac{8\pi}{\lambda}\right) z n \sin^2\left(\sin^{-1}\frac{(NA)}{n}/2\right) \tag{2.16}$$

The method, despite being simple, has some drawbacks that can reduce its performance. In 2001, Cole et al (Cole *et al.*, 2001), reviewed the most common issues that can affect the perfect recovery of an optical sectioned image. These problems have as main effect the appearance, in the final image, of first or higher order pattern residuals which are superimposed to valuable image information. For each one of them, the authors also proposed a solution that would minimize or even eliminate these problems.

When imaging fluorescence samples, fluorescence bleaching can occur, reducing the amount of fluorescence signal collected by the microscope and recorded by the CCD. The three images required by SIM are not acquired simultaneously, but successively on time. This, together with fluctuations on the light source, can cause oscillations in the mean intensity signal between the 3-phase shifted images. To minimize this problem, authors suggest the normalization of each patterned image by maximum mean of the three images. Another very common problem associated with some implementations of SIM are deviations in the effective phase-difference between each acquired image. To successfully apply this algorithm, it is essential that the pattern phase shift between the three images is as close as possible to 120º. Due to physical limitations, exact phase shifts cannot be guaranteed in some SIM implementations, degrading the final image quality. To overcome this, authors suggest that, for each image, the phase associated with fundamental can be estimated by means of Fourier transform. Having the actual phase values, the optical sectioned image can be estimated through an optimized version of Equation (2.12) described in Equation (2.17).

$$I_S = (I_3 - I_1) + j\left[\frac{(I_1 - I_2)}{\tan\left(\frac{\phi_1 - \phi_2}{2}\right)} + \frac{(I_2 - I_3)}{\tan\left(\frac{\phi_2 - \phi_3}{2}\right)}\right] \tag{2.17}$$

Since 1997, the year it was first demonstrated, 3-phase SIM has been used in a great diversity of applications which include, among others, fluorescence and reflectance microscopy. Pattern projection, along with an optimized algorithm to obtain the final image, are key components of SIM. In the original report, pattern projection was achieved by introducing a 40-line/mm one-dimensional grid into the illumination path of a conventional microscope and creating an image of it in the conjugate plane of an infinity-corrected objective. Phase-shifting was possible by moving the pattern with a piezo in saw-tooth fashion synchronized with the CCD frame rate (Neil, Juskaitis and Wilson, 1997) as schematized in .Figure 2.18.

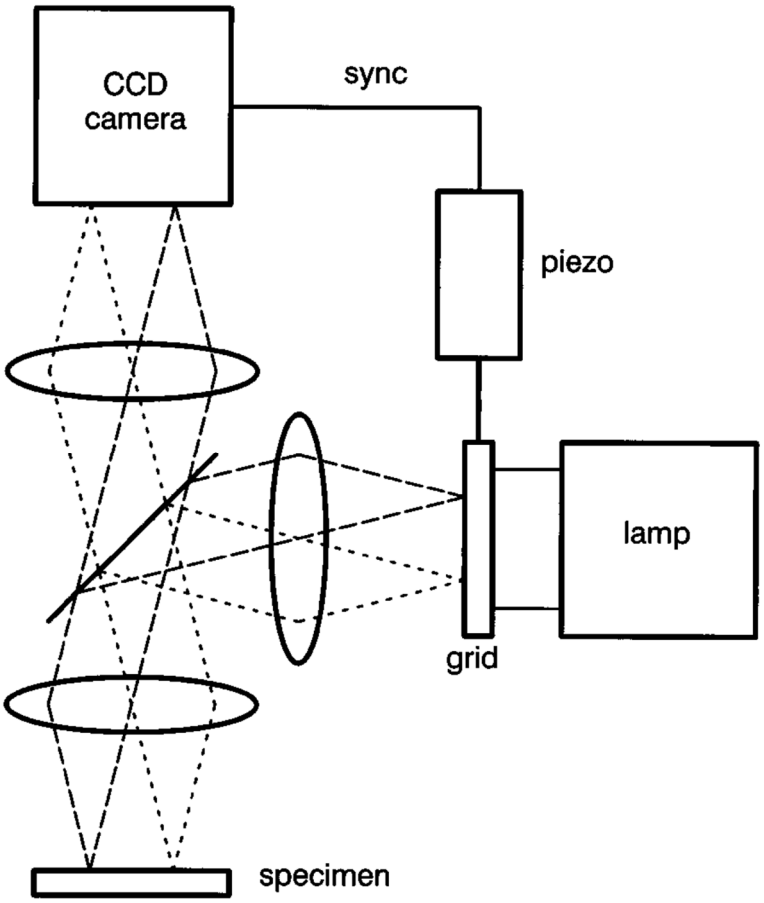

Figure 2.18 – Setup scheme of the first known application of structured illumination microscopy for optical sectioning (Neil, Juskaitis and Wilson, 1997)**.**

This type of implementation was replicated in several microscope setups throughout the years. A Time-Gated microscope with a very similar setup was reported in 2000 by Cole et al (Cole *et al.*, 2000). This classical setup had a few drawbacks that could lead to artifacts in the final image. As said, phase differences between patterned images could suffer from slight mismatches. Moreover, its shifting speed was quite limited, affecting the acquisition frame rate. CCD technology was evolving, and their acquisition frame rates were not followed by the piezo technology used to shift the one-dimensional grid patterns.

Having in mind an increase in acquisition speed and the improvement in pattern phase shifting, Fukano and Miyawaki introduced in 2003 a different concept to integrate SIM in a fluorescence microscope (Fukano and Miyawaki, 2003). With the emerging of digital micromirror devices (DMDs), the authors proposed the replacement of the square grating by this type of device. DMDs were patented by Texas Instruments and are the result of a combination between opto-mechanical and electro-mechanical elements. Each DMD array is comprised by thousands of micromirrors (pixels) which have a bi-stable operation, meaning that they only assume two positions (+ 12º and -12º) according to their "on" or "off" state. Figure 2.6 depicts an unpowered micromirror. The mirror part is attached through a via to a hidden torsional hinge. The mirror bottom is in contact with the spring tips and the two electrodes hold the micromirror in the two possible positions. A dual CMOS memory lies below each micromirror and its two state elements are always complementary. A mirror clocking pulse transfers the dual CMOS memory state to the micromirror, changing its state (Lee, 2013). These devices are usually installed in a microcontroller board with standard interfaces to a personal computer where specific software applications help the user to control which pattern is designed in the DMD surface-

Figure 2.20 shows the setup implemented by Fukano and Miyawaki to use a DMD as a pattern generator for SIM. The generated pattern on the DMD surface is imaged, as before, at the conjugate plane of the microscope objective. However, here, the required patterned phase shifting is provided by changing the state of the micromirrors in the DMD surface, which is a much faster process than translating a physical grating.

This DMD implementation became quite popular throughout the years (Venugopal, Chen and Intes, 2010; Dan *et al.*, 2013; Qian *et al.*, 2015), as the DMD technology developed to denser micromirror arrays and the pattern shifting process became quite faster due to improved DMD-computer communication. Moreover, since the phase shift is digitally generated, phase shifts mismatch from 120º are practically absent, allowing simpler image processing based on the original equation proposed by Neil et al in 1997.

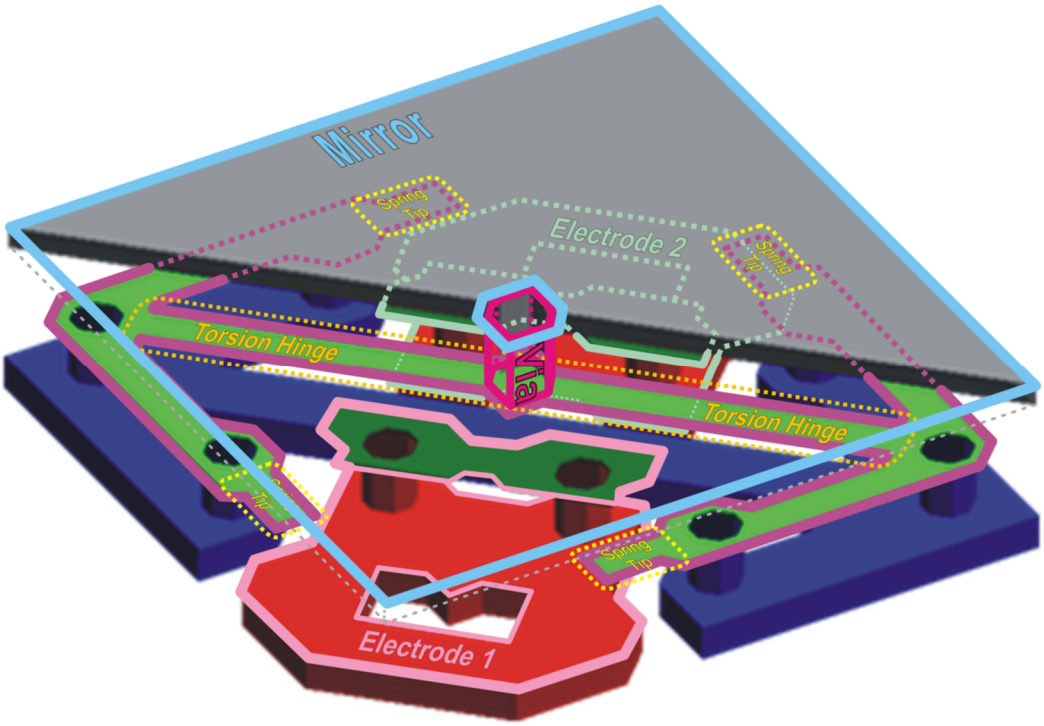

Figure 2.19 – Schematic Representation of a micromirror which corresponds to a pixel on a DMD board (Lee, 2013)**.**

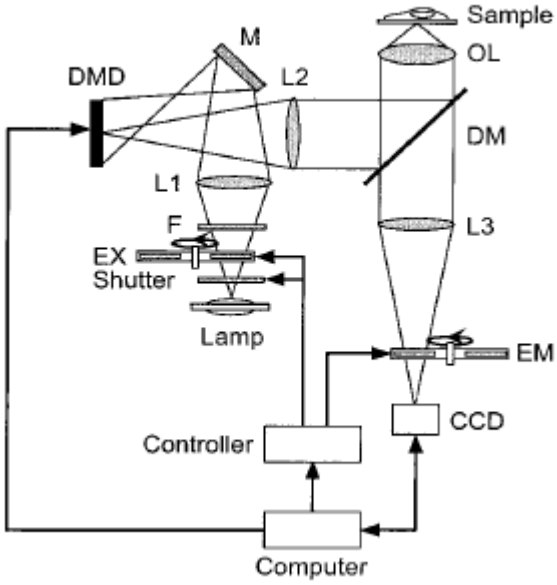

Figure 2.20 – Schematic representation of the first structured illumination microscope using a DMD for pattern generation (Fukano and Miyawaki, 2003)**.**

Another device that can be used to generate the structured illumination pattern is a spatial light modulator (SLM) based on liquid crystal on silicon (LCOS) technology. These systems are the only devices capable of modulating light intensity, phase and polarization at the same time because of polarization rotation and electrically controlled birefringence capacity (ECB). Apart

from this advantage over DMD (which is only capable of modulating light intensity), LCOS SLM have higher pixel resolution making possible to place a high number of pixels on a small panel due to a reflective arrangement given by a silicon back panel (Lazarev *et al.*, 2012). They are mainly applied in super-resolution structured illumination (SR-SIM) instruments due to their ability to act has diffraction gratings. In the first SR-SIM instruments, patterns were generated by light interference from 3 orders of diffraction (-1, 0 and +1) created by a diffraction grating, placed in the illumination path of the microscope, which could be translated and rotated to create the different patterns required by super-resolution image reconstruction (Gustafsson *et al.*, 2008). SLM implementations made this process quite simpler by replacing the diffraction grating and making the pattern generation process much faster (O'Holleran and Shaw, 2014).

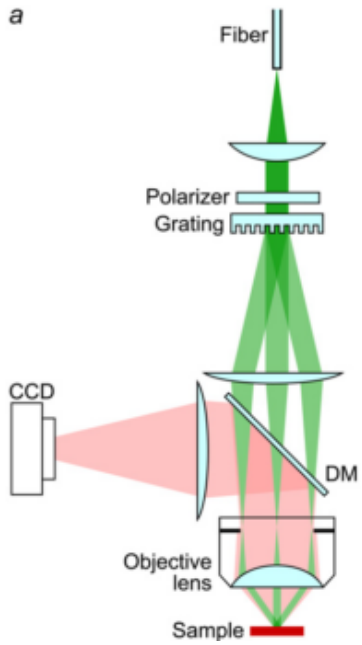

Figure 2.21 - Schematic representation of the structured illumination apparatus for optical sectioning and super-resolution SIM with a diffraction grating (Gustafsson *et al.*, 2008)**.**

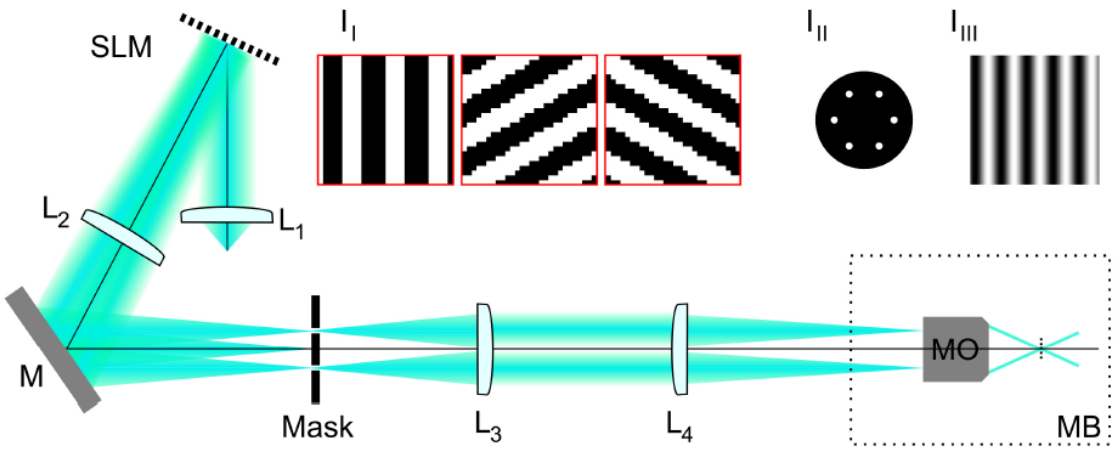

Figure 2.22 – Schematic representation of the microscope setup for optical sectioning and super-resolution SIM with SLM implementation. The diffraction grid was replaced by the SLM. (O'Holleran and Shaw, 2014)

2. HiLo

Considering the limitations previously discussed for 3-phase approach SIM, in 2009 D. Lim et al (Lim, Chu and Mertz, 2008) proposed another method of obtaining optical sectioning through wide-field SIM. Aiming to reduce the phase dependence of the 3-phase method, they demonstrated wide-field optical sectioning based on the acquisition of just two images: one with low-resolution information providing optical sectioning at low spatial frequencies and other with high-resolution information which has optical sectioning for higher spatial frequencies – HiLo microscopy. In this optical sectioning method, the low-resolution image (I_n) corresponds to a wide-field image superimposed with a well-known pattern, while the high-resolution image (I_u) corresponds to a uniform image acquired with a standard wide-field microscope. Different from the 3-phase approach, HiLo microscopy is not limited to sinusoidal pattern superimposition. Instead, in the original paper of D. Lim et al, the authors used a combination of speckle illumination (low-resolution image) and non-speckle illumination (high-resolution image) which can be achieved by placing a diffuser in the illumination path of the wide-field microscope.

These two images are the starting point to obtain an optical sectioned image. The optical sectioning algorithm requires the application of several image processing steps. To start with, and since thick objects have several contributions from out-of-focus light, it is necessary to estimate the local spatial contrast ($C_N(\vec{p})$) of the low-resolution image I_n, through Equation (2.18),

$$C_N(\vec{p}) = \frac{\langle \sigma_n(\vec{p}) \rangle_A}{\langle I_n(\vec{p}) \rangle_A} \tag{2.18}$$

where $\langle \sigma_n(\vec{p}) \rangle_A$ is the standard deviation and $\langle I_n(\vec{p}) \rangle_A$the mean of the images over a region of interest (ROI) of size A. In the ideal case of a thin object this value is 1, since the contrast obtained is not degraded by out-of-focus contributions. In thick samples, $C_N(\vec{p})$ tends to 0 when the out of focus contributions are considered. However, the contrast in the structured image has contributions both from the speckle/pattern and from the object being imaged. So, the contrast inherent to the object does not provide relevant information and we must separate it from the contrast provided by the speckle pattern to obtain optical sectioning. Therefore, I_n and I_u can be rewritten as Equations (2.19) and (2.20).,

$$I_n(\vec{p}) = [\langle O \rangle_A + \delta O(\vec{p})][\langle S \rangle_A + \delta S(\vec{p})] \tag{2.19}$$

$$I_u(\vec{p}) = [\langle O \rangle_A + \delta O(\vec{p})]\langle S \rangle_A \tag{2.20}$$

where $\langle O \rangle_A$ and $\langle S \rangle_A$ arise from both in- and out-of-focus contributions and $\delta O(\vec{p})$ and $\delta O(\vec{p})$ are mainly due to in-focus contributions. $O(\vec{p})$ corresponds to the intensity measured from the actual object with a hypothetical uniform unit illumination and $S(\vec{p})$ is the image intensity obtained when a hypothetical uniform unit object is illuminated with the speckle pattern. Having this, the approximation given by Equation (2.21) can be obtained.

$$C_N{}^2 \approx C_O{}^2 + C_S{}^2 + C_O{}^2 C_S{}^2 \tag{2.21}$$

$C_O{}^2$ and $C_S{}^2$ correspond, respectively, to the contrasts of $O(\vec{p})$ and $S(\vec{p})$ over the resolution area A. $C_O(\vec{p})$ can be estimated by Equation (2.22) and, by applying Equation (2.21), $C_N(\vec{p})$ can be quickly obtained. Therefore, the object independent contrast measure of the relative proportion of $I_u(\vec{p})$ in focus, $C_S(\vec{p})$ can be easily obtained.

$$C_O(\vec{p}) = \frac{\langle \sigma_u(\vec{p}) \rangle_A}{\langle I_u(\vec{p}) \rangle_A} \tag{2.22}$$

A low-resolution version of $I_u(\vec{p})$ can be now obtained simply by multiplying $C_O(\vec{p})$ by the uniform original image $I_u(\vec{p})$ as described by Equation (2.23). This new image $I_{su}(\vec{p})$ will be optically sectioned even for dc frequencies.

$$I_{su}(\vec{p}) = C_s(\vec{p})\langle I_u(\vec{p})\rangle_A \quad (2.23)$$

After obtaining a low-resolution optically sectioned version with coarse-grained speckle pattern of I_u, it is necessary to complement the image with the high-resolution information. For that, a series of transformations and filters should be applied to both the raw uniform image and the raw speckle patterned image.

To start with, it is easier to perform this step in the spatial frequency ($\vec{k}$) domain. So, a fast Fourier transform of the uniform image I_u should be applied – Equation (2.24).

$$\mathcal{I}_u(\vec{k}) = FT[I_u(\vec{p})] \quad (2.24)$$

In the Fourier spectrum of the uniform image, it is known that the out-of-focus contributions are concentrated at the peak that corresponds to $\vec{k} = 0$. So, for $0<k<k_{max}$, the uniform image is already optically sectioned. It is easy to conclude that by applying a high pass filter on the image, only high-resolution optical sectioned information will be retained. This can be accomplished by choosing a filter whose cutoff frequency (k_c) corresponds to ($HP(k_c) = 1/2$), resulting in a new image $\mathcal{I}_{hp}(\vec{k})$ – Equation (2.25).

$$\mathcal{I}_{hp}(\vec{k}) = HP(\vec{k})\mathcal{I}_u(\vec{k}) \quad (2.25)$$

The image in spatial coordinates can be recovered by applying the inverse Fourier transform to $\mathcal{I}_{hp}(\vec{k})$ – Equation (16). $I_{hp}(p)$ will be an optically sectioned high-resolution image of I_u.

$$I_{hp}(\vec{p}) = IFT[\mathcal{I}_{hp}(\vec{k})] \quad (2.26)$$

Finally, it is required to join the low and high-resolution information given by the images $I_{su}(p)$ and $I_{hp}(p)$. For that, it is necessary to limit $I_{su}(p)$ so the information is exactly complementary (in terms of frequency) to that given by $I_{hp}(p)$. So, a low pass filter should be applied to I_{su}(p) with the same cutoff frequency of the high-pass filter applied in the previous step, so that $LP(k)=1-HP(k)$ - Equations (2.27) and (2.28).

$$\mathcal{I}_{su}(\vec{p}) = FT[I_{su}(\vec{p})] \tag{2.27}$$

$$\mathcal{I}_{lp}(\vec{k}) = LP(\vec{k})\mathcal{I}_{su}(\vec{k}) \tag{2.28}$$

A scaling factor, defined by Equation (2.29), must be introduced to guarantee that no effect is present in the transition across $\overrightarrow{k_c}$. This factor is averaged over all angles of $\overrightarrow{k_c}$. Finally, the image fusion is performed either on spatial frequency domain (Equation (2.30)) or in spatial domain (Equation (2.31)), obtaining the final image (I(p)) (Lim, Chu and Mertz, 2008).

$$\eta = \frac{\left|\mathcal{I}_{hp}(\overrightarrow{k_c})\right|}{\left|\mathcal{I}_{lp}(\overrightarrow{k_c})\right|} \tag{2.29}$$

$$\mathcal{I}(\vec{k}) = \eta\mathcal{I}_{lp}(\vec{k}) + \mathcal{I}_{hp}(\vec{k}) \tag{2.30}$$

$$I(\vec{p}) = \eta I_{lp}(\vec{p}) + I_{hp}(\vec{p}) \tag{2.31}$$

This presentation of the HiLo method was based on its original implementation, which used speckle images. However, the authors of the technique also state that it can be applied to other type of patterned images, such as those used in the 3-phase implementation based on the projection of a sinusoidal pattern (Lim, Chu and Mertz, 2008). In fact, based on the possibility that sinusoidal pattern images were also eligible for HiLo processing, a simpler version of the HiLo algorithm was reported by Jerome Mertz and Jinhyun Kim in 2010 (Mertz and Kim, 2010).

Here, and to maintain the nomenclature used by these authors, I_u will be represented by U and I_n by S.

The uniform image can be described as the sum of both in-focus and out-of-focus components and given by Equation (2.32). Since we are considering a sinusoidal patterned image, similarly to the 3-phase method, the image $S(x)$ can be described by an in-focus structured image convolved with a sinusoidal function summed with the out-of-focus contributions that are still present in this image and are meant to be eliminated. Therefore, Equation (2.33) mathematically describes the structured image. This simplified HiLo method can be described using these two equations.

$$U(x) = I_{in}(x) + I_{out}(x) \tag{2.32}$$

$$S(x) = \frac{1}{2}\left[I_{in}(x)\left(1 + Msin(k_g x)\right) + I_{out}(x)\right] \tag{2.33}$$

The first step to remove the out-of-focus contributions is to extract only the in-focus contributions of the patterned image. For that, a simple subtraction correction is applied between the uniform image and a high-pass filtered version of the patterned image to ensure that the subtraction is locally centered about zero. The cutoff frequency used in this filter should be much smaller than the frequency of the superimposed sinusoidal pattern. A new image ($D(x)$) is obtained and corresponds to a partially demodulated image carrying only the pattern and the in-focus contributions of both $U(x)$ and $S(x)$ - Equation (2.34).

$$D(x) = \frac{1}{2}|U(x) - 2S(x)| = I_{in}(x)M\left|\sin(k_g x)\right| \tag{2.34}$$

To remove the patterned information from $D(x)$, a low pass filter with a cutoff frequency smaller but very close to k_g can be applied – Equation (2.35). This is very close to obtain the low pass-filtered version of only the in-focus contributions I_{in}.

$$LP[I_{in}(x)] \approx \frac{\pi}{2M} LP[D(x)] \tag{2.35}$$

Therefore, an image without pattern modulation and with only in-focus contributions can be obtained. However, in this image, the high-resolution components are not present since they are suppressed by the low-pass filter used to remove the pattern. So, to compensate for that, a complementary high-pass filter should be applied to the uniform image to retain the lost high-resolution information. Since, as aforementioned, the out-of-focus information is concentrated on the zero component of Fourier transform spectrum, only in-focus information will be maintained after the high-pass filter – Equation (2.36). To conclude, it is only necessary to combine the low and high-resolution information recovered by this process. An optically sectioned image can be obtained by applying Equation (2.37). The η factor to scale the low-pass filtered image is calculated using the same method described in the previous algorithm and given by Equation (2.29).

$$HP[I_{in}(x)] \approx HP[U(x)] \tag{2.36}$$

$$I_{HiLO}(x) = \eta LP[D(x)] + HP[U(x)] \tag{2.37}$$

This method gives results comparable to the first one described by D. Lim et al in 2008. However, its image processing routine is more direct and faster to implement since no ROI based image processing is required.

HiLo microscopy has already been successfully applied to both fluorescence (Santos *et al.*, 2009; Lim *et al.*, 2011; Muro *et al.*, 2011) and fluorescence lifetime microscopic systems (Dupuis *et al.*, 2013).

Chapter 3 Fluorescence Lifetime Decay Analysis and Lifetime Determination

A. Lifetime Determination Methods

The dynamics of a fluorescence decay process can be mathematically described through different approaches. A simple way to describe it is through the multi-exponential expansion model (Equation (3.1)). The de-excitation of electrons can be described as a first-order differential equation, in which the decay rate of the electrons in the excited state $N(t)$ is proportional to the number of electrons in the excited state and λ is a time constant characterizing the decay rate of the relaxation process. The solution to this first order differential equation is given by Equation (3.2) and since photon emission is proportional to the electronic decay rate, the fluorescence intensity decay curve of a population of a single fluorophore is given by Equation (3.3), where A is the pre-exponential factor and τ is the fluorescence lifetime.

$$\frac{dN(t)}{dt} = -\lambda N(t) \tag{3.1}$$

$$N(t) = N_0 e^{-\frac{t}{\tau}} \tag{3.2}$$

$$F(t) = A\, exp\left(-\frac{t}{\tau}\right) \tag{3.3}$$

If the population under analysis has more than one fluorophore, the different decay rates occurring can be described by a sum of exponential curves and Equation (3.3) is rewritten in Equation (3.4).

$$F(t) = \sum_{i=1}^{M} A_i\, exp\left(-\frac{t}{\tau_i}\right) \tag{3.4}$$

By only considering the mathematical formulation of the fluorescence decay rate given by Equation (3.4), a simple fit to a sum of exponentials should, in theory, be enough to correctly estimate the fluorescence lifetime of a given population of fluorophores. However, in real Time-

Domain systems, fluorescence decay curves acquisition is affected by artifacts that can degrade the fluorescence signal and lead to errors in the estimation of lifetimes, when using a simple multi-exponential fitting. Fortunately, these artifacts are well identified and different methods to overcome them are already published and tested. These distortions are mainly originated on the finite rise-time, width and decay of the excitation laser source; in the scattered light from the excitation source; in excitation photons not entirely blocked by the emission filters; in the limited frequency response of detector and electronics and, when using fiber-optics to deliver excitation light and collect fluorescence emission, in the light dispersion in the optical fiber (Warren *et al.*, 2013; Marcu, French and Elson, 2014). These limitations on the fluorescence decay acquisition can be described through a special curve named Instrument Response Function or Impulse Response Function (IRF), which is specific to each time domain acquisition system.

1. The Instrument Response Function (IRF)

IRF can be defined as "the best approximation to a temporally infinitely short process possible to measure with a given instrument"(Picoquant, 2014). It is also known as "lamp function" which suggests that it is most affected by the time profile of the used excitation source. However, its shape is also highly affected by the other components present in both excitation and emission light paths, as, for example, the time characteristics of the detector used. The fluorescence decay measured with time-domain methods is always the result of the convolution of the IRF with the true fluorescence decay curve.

Considering this, having a way to effectively measure the IRF either through scatter samples or through fluorescent dyes with a well-known ultrashort lifetime is considered an advantage to estimate lifetimes with high accuracy. Knowing the IRF, it is possible to use deconvolution algorithms to remove the instrument artifacts from the true fluorescence decay and obtain very accurate fluorescence lifetime measurements through multi-exponential fits. Throughout the years, different methods of IRF deconvolution have been proposed, published and validated. The most popular are those based on least-squares deconvolution methods and their basic description will be addressed in the following sections. Here, the formulation of least-squares deconvolution presented is based on that described in (Marcu, French and Elson, 2014).

2. Least Squares Deconvolution

As explained, in time-domain systems the acquired fluorescence decay curve is the result of the convolution between the true fluorescence decay curve, $F(t)$, and the IRF of the system, $h(t)$ defined in Equation (3.5).

$$I(t) = h(t) * F(t) \tag{3.5}$$

However, in any time-domain system, the acquired signal is not a continuous but a discretized function. In TCSPC systems this is done through time bins corresponding to the detector channels and, in the case of Time-Gated systems, each bin corresponds to a gate integration. So, for N equally spaced time points, the acquired fluorescence intensity decay curve can be described by Equation (3.6) where $k = 1, 2, \dots, N-1$ and ε_k represents the noise associated with each measurement.

$$y(k) = \sum_{i=0}^{k} F(k-i) \cdot h(k) + \varepsilon_k \tag{3.6}$$

The least-squares deconvolution method assumes that fluorescence decay curves are parameterized by an L-dimensional real vector $c \in \Re^L$. This parameterization can be expressed as a column vector $h(c) = [h(0,c), \dots, h(N-1,c)]^T$ and by defining a measurement data vector $y = [y(0), \dots, y(N-1)]^T$ and a Toeplitz convolution matrix T – Equations (3.7) and (3.8).

$$T = \begin{pmatrix} F(0) & 0 & 0 & \dots & 0 \\ F(1) & F(0) & 0 & \dots & 0 \\ F(2) & F(1) & F(0) & \dots & 0 \\ \vdots & \vdots & \vdots & \ddots & \vdots \\ F(N-1) & F(N-2) & F(N-3) & \dots & F(0) \end{pmatrix} \tag{3.7}$$

$$y = Th(c) + \varepsilon \tag{3.8}$$

Having this, the purpose of least squares deconvolution is to find an estimate for c that minimizes the *generalized* sum of squares error (SSE) represented by Equation (3.9)

.

$$\Omega(c) = \frac{1}{2}(y - Th(c))^T \sum_{\varepsilon}^{-1}(y - Th(c)) \tag{3.9}$$

Considering that in time-domain methods, for a great number of photon counts, noise follows a Poisson distribution, it can be directly estimated by the measured $y(k)$ with $\sum_{\varepsilon} diag\{y\}$.

The estimation of c can be made through different variations of the least-squares deconvolution method: linear and non-linear. On the following sections they are both described.

Linear Least Squares Deconvolution

In linear least-squares deconvolution the minimization of Equation (3.9) is obtained by taking its first derivative with respect to the parameters (Jacobian *J*) equal to 0 – Equation (3.10).

$$J(c) = \frac{\partial \Omega}{\partial c} = \left(\frac{\partial \Omega}{\partial c_1}, \frac{\partial \Omega}{\partial c_2}, \dots, \frac{\partial \Omega}{\partial c_L}\right)^T = 0 \tag{3.10}$$

Considering the model $h(c)$ linear in its parameters – Equation (3.11), where B represents the system matrix specific to the chosen model, and considering that the Jacobian is also linear in c, Equation (3.10) can be redefined as Equation (3.12), from which a closed-form solution to c can be easily obtained - Equation (3.13).

$$h(c) = Bc \tag{3.11}$$

$$B^T T^T \sum_{\varepsilon}^{-1}(y - TBc) = 0 \tag{3.12}$$

$$c = \left(B^T T^T \sum_{\varepsilon}^{-1} TB\right)^{-1} B^T T^T \sum_{\varepsilon}^{-1} y \tag{3.13}$$

Non-Linear Least Squares Deconvolution

When non-linear least-squares deconvolution is considered the Jacobian equation is not linear in the model parameters, which increases the complexity of the problem. A possible solution to this question is to use Newton-type iterative methods (Nocedal and Wright, 1999) which are based on the transformation of Equation (3.10) into a sequence of linear equations. These equations can then be solved iteratively to estimate the value of c that minimizes the SSE.

The parameter c at the m^{th} iteration is designated $c(m)$. So, the first step to find the minimum of c is to take the Taylor expansion of the Jacobian matrix around $c(m)$, given by Equation (3.14).

$$J(c) \approx J\left(c^{(m)}\right) + \frac{\partial J\left(c^{(m)}\right)}{\partial c}\left(c - c^{(m)}\right) \tag{3.14}$$

Now, considering that the derivative of the Jacobian (Hessian matrix $H(m)$) is the second derivative of the generalized SSE equation, $\frac{\partial J}{\partial c}$ can be written as Equation (3.15). Moreover, by considering $J^{(m)} = J(c^{(m)})$ and $H^{(m)} = \frac{\partial J(c^{(m)})}{\partial c}$ and ignoring the non-linear part of Equation (3.14), an updated estimate for c can be found by solving Equation (3.16), which gives the estimated parameter for the *(m+1)* iteration described in Equation (3.17).

$$\frac{\partial J}{\partial c} = \begin{pmatrix} \frac{\partial^2 \Omega}{\partial c_1^2} & \frac{\partial^2 \Omega}{\partial c_1 \partial c_2} & \cdots & \frac{\partial^2 \Omega}{\partial c_1 \partial c_{2L}} \\ \frac{\partial^2 \Omega}{\partial c_2 \partial c_1} & \frac{\partial^2 \Omega}{\partial c_2^2} & \cdots & \frac{\partial^2 \Omega}{\partial c_2 \partial c_L} \\ \vdots & \vdots & \ddots & \vdots \\ \frac{\partial^2 \Omega}{\partial c_L \partial c_1} & \frac{\partial^2 \Omega}{\partial c_L \partial c_2} & \cdots & \frac{\partial^2 \Omega}{\partial c_L^2} \end{pmatrix} \tag{3.15}$$

$$J^{(m)} + H^{(m)}\left(c - c^{(m)}\right) = 0 \tag{3.16}$$

$$c^{(m+1)} = c^{(m)} - (H^{(m)})^{-1} J^{(m)} \tag{3.17}$$

The Jacobian and Hessian matrices are described in Equations (3.18) and (3.19) where ***I*** denotates the identity matrix and ⊗ the Kronecker product.

$$J^{(m)} = -\left(\frac{\partial h\left(c^{(m)}\right)}{\partial c}\right)^{T} T^{T} S_{e}^{-1}\left(y - Th\left(c^{(m)}\right)\right) \tag{3.18}$$

$$\begin{aligned} H^{(m)} = &-\left(y - Th(c^{(m)})\right)^{T} \sum_{\varepsilon}^{-1} T \otimes I \left(\frac{\partial^{2} h\left(c^{(m)}\right)}{\partial c \partial c'}\right)^{T} \\ &-\left(\frac{\partial h(c^{(m)})}{\partial c}\right)^{T} T^{T} \sum_{\varepsilon}^{-1} T \left(\frac{\partial h(c^{(m)})}{\partial c}\right) \end{aligned} \tag{3.19}$$

Moreover, the first and second derivative of the intensity decay function with respect to the model parameters is given by Equations (3.20), (3.21) and (3.22) for $i = 1, 2, \ldots, L$.

$$\frac{\partial h(c)}{\partial c} = \begin{pmatrix} \frac{\partial h(t_1;c)}{\partial c_1} & \frac{\partial h(t_1;c)}{\partial c_2} & \cdots & \frac{\partial h(t_1;c)}{\partial c_L} \\ \frac{\partial h(t_2;c)}{\partial c_1} & \frac{\partial h(t_2;c)}{\partial c_2} & \cdots & \frac{\partial h(t_2;c)}{\partial c_L} \\ \vdots & \vdots & \ddots & \vdots \\ \frac{\partial h(t_N;c)}{\partial c_1} & \frac{\partial h(t_N;c)}{\partial c_2} & \cdots & \frac{\partial h(t_N;c)}{\partial c_L} \end{pmatrix} \tag{3.20}$$

$$\frac{\partial^{2} h(c)}{\partial c \partial c'} = \left(\frac{\partial^{2} h(c)}{\partial c \partial c_1}, \ldots, \frac{\partial^{2} h(c)}{\partial c \partial c_L}\right) \tag{3.21}$$

$$\frac{\partial^{2} h(c)}{\partial c \partial c_i} = \begin{pmatrix} \frac{\partial^{2} h(t_1;c)}{\partial c_1 \partial c_i} & \frac{\partial^{2} h(t_1;c)}{\partial c_2 \partial c_i} & \cdots & \frac{\partial^{2} h(t_1;c)}{\partial c_L \partial c_i} \\ \frac{\partial^{2} h(t_1;c)}{\partial c_1 \partial c_i} & \frac{\partial^{2} h(t_2;c)}{\partial c_2 \partial c_i} & \cdots & \frac{\partial^{2} h(t_2;c)}{\partial c_L \partial c_i} \\ \vdots & \vdots & \ddots & \vdots \\ \frac{\partial^{2} h(t_N;c)}{\partial c_1 \partial c_i} & \frac{\partial^{2} h(t_N;c)}{\partial c_2 \partial c_i} & \cdots & \frac{\partial^{2} h(t_N;c)}{\partial c_L \partial c_i} \end{pmatrix} \tag{3.22}$$

To avoid the direct calculation of the Hessian matrix, which involves second derivatives, the Hessian matrix is often approximated as described in Equation (3.23), changing Equation (3.17) to Equation (3.24). This Gaussian-Newton method is summarized in the flowchart represented in Figure 3.1.

$$H = J^{T} J \tag{3.23}$$

$$c^{(m+1)} = c^{(m)} - (J^{(m)T}J^{(m)-1}J^{(m)} \quad (3.24)$$

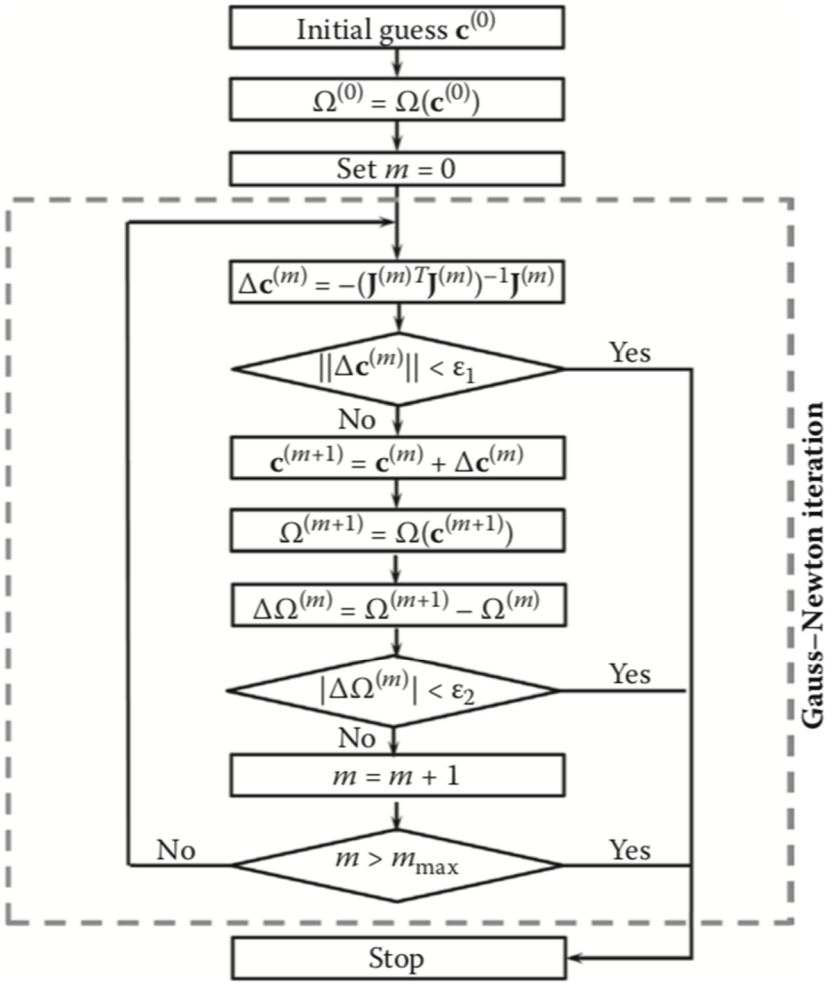

Figure 3.1 - Fluxogram of Gauss-Newton method in non-linear LSD (Marcu, French and Elson, 2014)**.**

3. Rapid Global Fitting Method

In 2013, Warren et al (Warren *et al.*, 2013) proposed a different variation of least-squares deconvolution for fitting large fluorescence lifetime datasets acquired with time-domain methods and suitable for both TCSPC and Time-Gated. This new approach was based on separable nonlinear least square algorithm and on variable projection techniques that had been already described by Golub and Pereyra (Golub and Pereyra, 2003) and using analytical derivatives as suggested by TIMP (Laptenok *et al.*, 2007) to guarantee convergence (Christensen, Hurn and

Lindsay, 2008). These authors developed an open-source software suit (FLIMfit) dedicated to different aspects of lifetime analysis, including different possibilities of decay deconvolution through a separated acquisition of the IRF. The software is also capable of accounting for some additional parameters that may affect the fluorescence decay measurement such as stray light, scattered excitation light and time-varying noise background.

The method that describes the fluorescence decay dynamics is slightly different from that presented in the beginning of this chapter. Here, the fluorescence decay curve for a single-lifetime fluorophore population excited by a train of light impulses is given by Equation (3.25), where $H(t)$ corresponds to the Heaviside function, T is the period of the light pulses reaching the fluorophores and τ is the fluorescence lifetime.

$$D(\tau,t) = \left[H(t) + \frac{1}{\exp\left(\frac{T}{\tau}\right) - 1}\right] \exp\left(-\frac{t}{\tau}\right) \tag{3.25}$$

The influence of the IRF is then given by the convolution of the scattered IRF $g_i(t)$ with the decay function $D(t,\tau)$ – Equation (3.26). This model also accounts for the special case when the IRF is acquired with a known fluorescence sample. In this case, the reference lifetime of the IRF enters the equation and changes the convolution to that present in Equation (3.27).

$$\widetilde{D}(\tau,t) = g_I(t) * D(\tau,t) \tag{3.26}$$

$$\begin{aligned}\widetilde{D}_R(\tau,t) &= g_R(t) * \left[\delta(t) + \left(\frac{1}{\tau_R} - \frac{1}{\tau}\right) D(\tau,t)\right] \\ &= g_R(t) + \left(\frac{1}{\tau_R} - \frac{1}{\tau}\right) \widetilde{D}(\tau,t)\end{aligned} \tag{3.27}$$

Finally, for a population where more than on fluorescence lifetime is present, the decay curve is described by Equation (3.28), which is simply the sum of the different mono-exponential curves weighted by an exponential pre-factor A_i.

$$\tilde{I}(T) = \sum_i A_i \tilde{D}(\tau_i, t) \tag{3.28}$$

In the process of fluorescence acquisition, sometimes, light reaching the detector is not only originated on the fluorescence signal being measured. Unwanted contributions can affect the decay signal from mainly three different sources which are: time-independent background such as room light or dark noise from detector and is described by a constant Z, scattered light from the excitation source that is not fully blocked by the emission filter and is described by a contribution S proportional to the IRF and background autofluorescence, particularly present when using IV excitation and can be estimated and accounted for by measuring the time-dependent background fluorescence b(t, W) and included in the model. Having these factors in consideration the model to be fitted takes the form described by Equation (3.29).

$$M(t) = I(t) + Sg(t) + Vb(t) + Z \tag{3.29}$$

Considering that the nonlinear functions present on Equation (3.29) are constant across the dataset, this equation can be rewritten as their linear sum:

$$I^{(s)} = \Phi(\alpha) a^{(s)} \tag{3.30}$$

where $I(s)$ is a vector containing the model decay at sth pixel, α is a vector of nonlinear parameters that are constant across the dataset, $\Phi(\alpha)$ (Equation (3.31)) is a matrix whose columns contain the nonlinear functions included in the model and $a^{(s)}$ (Equation (3.32)) is a vector of linear parameters at the sth pixel.

$$\phi(\alpha) = \begin{bmatrix} \tilde{D}(\tau_1, t_1) & \tilde{D}(\tau_2, t_1) & g(t_1) \\ \vdots & \vdots & \vdots \\ \tilde{D}(\tau_1, t_n) & \tilde{D}(\tau_2, t_n) & g(t_n) \end{bmatrix} \tag{3.31}$$

$$a^{(s)} = \begin{bmatrix} A_1^{(s)} \\ A_2^{(s)} \\ S^{(s)} \end{bmatrix} \tag{3.32}$$

Equations (3.30) to (3.32) describe the fluorescence model in a generalized form, and with that, the weighted residual between the model and data to be minimized can be written as Equation (3.33), where $y_i^{(s)}$ is the decay measured for the sth pixel at the ith time, $\sigma_i^{(s)}$ is the estimated error on the ith measurement and $\Phi_{i,j}(\alpha)$ us the i[th] measurement in j[th] column of $\phi(\alpha)$. Equation (3.33) can be written in matrix form as expressed by Equation (3.34) where $\bar{y}^{(s)}$ is a column vector of the data measured for the s[th] pixel weighted by the estimated error and $\bar{\Phi}(\alpha)$ is the decay matrix weighted by the estimated error.

$$r(\alpha, a) = \sum_{s,i} \left(\frac{y_i^{(s)} - \sum_j \Phi_{i,j}(\alpha) a_j^{(s)}}{\sigma_i^{(s)}} \right)^2 \tag{3.33}$$

$$r(\alpha, a) = \sum_{s} \left\| \bar{y}^{(s)} - \bar{\Phi}(\alpha) a^{(s)} \right\|^2 \tag{3.34}$$

Considering that for a given set of nonlinear parameters, the magnitude of the residual vector is minimized when $a^{(s)} = \bar{\Phi}^{-}(\alpha)\bar{y}^{(s)}$ where $\bar{\Phi}^{-}(\alpha)$ is the symmetric generalized inverse of $\bar{\Phi}(\alpha)$, the linear variables can be eliminated from the residual, turning Equation (3.34) into Equation (3.35), where $(1 - \bar{\Phi}^{-}(\alpha)\bar{\Phi}(\alpha))$ is denoted $P^{\perp}_{\Phi(\alpha)}$ and can be calculated by matrix decomposition of $\bar{\Phi}(\alpha)$ using the QR method.

$$r(\alpha) = \sum_{s} \left\| (1 - \bar{\Phi}^{-}(\alpha)\bar{\Phi}(\alpha))\bar{y}^{(s)} \right\|^2 = \sum_{s} \left\| r_2^{(s)}(\alpha) \right\|^2 \tag{3.35}$$

A different approach from the Gauss-Newton described in the previous section is used to achieve non-linear minimization. Here, this is accomplished by defining Equations (3.35)(3.36)(3.35) with respect to parameters α with a modified Levenberg-Marquart (LM) routine. To calculate the Jacobian matrix given by Equation (3.36), which is obtained by using an approximation of Kauffman.

$$J_j^{(s)} \approx -\left(P^{\perp}_{\Phi(\alpha)} \frac{\partial \bar{\Phi}}{\partial \alpha_j} \bar{\Phi}^{-} \right) \bar{y}^{(s)} = -P^{\perp}_{\Phi(\alpha)} \frac{\partial \bar{\Phi}}{\partial \alpha_j} a^{(s)} \tag{3.36}$$

4. Rapid Lifetime Determination

Rapid Lifetime Determination (RLD) is the name given to the family of algorithms that can be used to estimate fluorescence decay parameters of fluorescence data, including lifetime τ and the pre-exponential factor k with a minimum of data points to perform it. The basics behind these methods were introduced by Ashworth in 1983, in an unpublished paper, particularly for single-exponential fluorescence decays. In 1989, Ballew and Demas (Ballew and Demas, 1989) published the first application of RLD to mono-exponential fluorescence decay data. RLD is very easy to relate with the Time-Gated acquisition method since it is based on integrations of the fluorescence decay curve. Considering a mono exponential fluorescence decay curve given by Equation (3.37) where k is the pre-exponential factor and τ is the fluorescence lifetime. If this curve is divided in two contiguous areas D_0 and D_1, as depicted in Figure 3.2, of width Δt two images are obtained. By applying Equations (3.38) and (3.39), k and τ can be easily estimated.

$$I(t) = k \exp(-\frac{t}{\tau}) \tag{3.37}$$

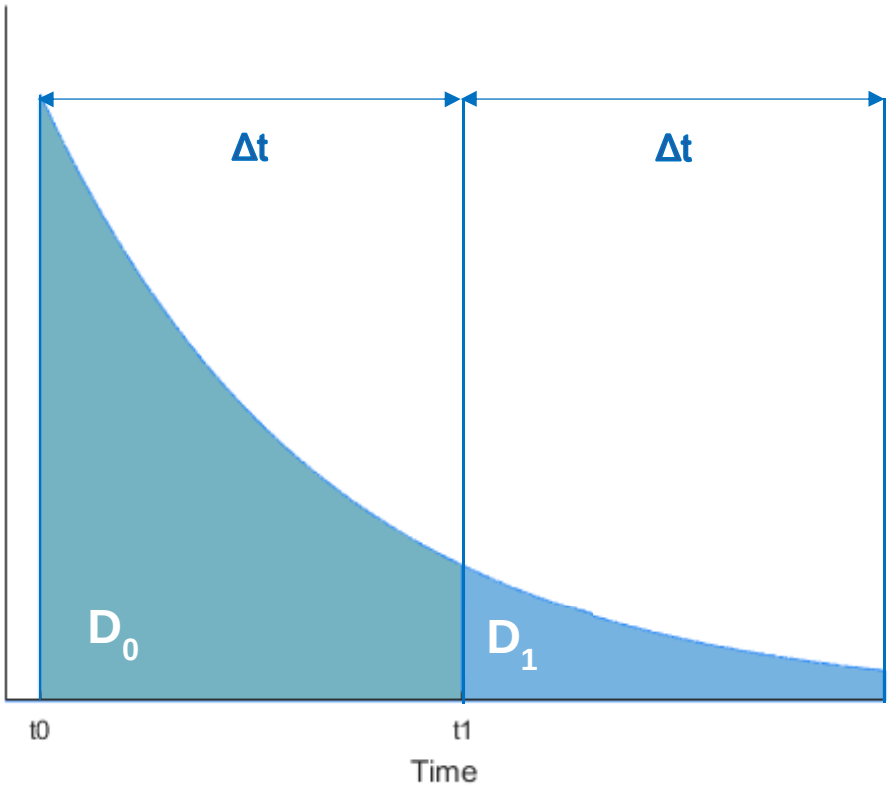

Figure 3.2 – Image acquisition for single-exponential RLD in contiguous gating mode:

$$\tau = \frac{-\Delta t}{\ln(\frac{D_0}{D_1})} \tag{3.38}$$

$$k = \frac{D_0}{\tau(1 - \frac{D_1}{D_0})} \tag{3.39}$$

The algorithm described by Equations (3.38) and (3.39) is the most simple and classical form of RLD and the first to be introduced. Different versions of this methods have reported throughout the years with different gating schemes that are not necessarily contiguous and applications to both mono-exponential and double-exponential decays curves.

The general equations for the application of RLD methods to double-exponential decay curves were introduced by Chang in 2009 (Chang, 2009). A double-exponential decay curve can be defined as a linear combination of two mono-exponential decay curves – Equation (3.40). In this case the number of unknown variables increases to 4: τ_1, τ_2, k_1 and k_2, resulting in a similar minimum number of images/points to solve this problem. This corresponds to 4 integrated areas denominated D_0, D_1, D_2 and D_3. Through Equations (3.41) to (3.50) these 4 unknowns can be obtained. In this case there is no restriction in the gating scheme applied. Different from the classical implementation, the gating scheme can be contiguous, overlapped or gapped depending on the lifetimes under analysis and gate widths available in each system. In these equations g represents the gate width and dt the gate separation.

$$I(t) = k_1 \exp\left(-\frac{t}{\tau_1}\right) + k_2 \exp\left(-\frac{t}{\tau_2}\right) \tag{3.40}$$

$$\tau_1 = \frac{-dt}{\ln(y)} \tag{3.41}$$

$$\tau_2 = \frac{-dt}{\ln(x)} \tag{3.42}$$

$$\alpha_1 = \frac{-(xD_0 - D_1)^2 \ln(y)}{\mathrm{dt}(x^2 D_0 - 2xD_1 + D_2)\left[1 - \left(\frac{xD_1 - D_2}{xD_0 - D_1}\right)^{\frac{g}{dt}}\right]} \tag{3.43}$$

$$\alpha_2 = \frac{-Rln(x)}{\mathrm{dt}(x^2 D_0 - 2xD_1 + D_2)\left[x^{\frac{g}{dt}} - 1\right]} \tag{3.44}$$

$$R = D_1 D_1 - D_2 D_0 \tag{3.45}$$

$$P = -D_1 D_2 + D_3 D_0 \tag{3.46}$$

$$Q = D_2 D_2 - D_3 D_1 \tag{3.47}$$

$$DISC = PP - 4RQ \tag{3.48}$$

$$x = \frac{(-P - \sqrt{DISC})}{2R} \tag{3.49}$$

$$y = \frac{(-P + \sqrt{DISC})}{2R} \tag{3.50}$$

In Chapter 6 of this thesis, a deeper analysis on available RLD algorithms is described, along with the simulations performed to apply these methods to our system.

Chapter 4 System Setup

As described in the Chapter 2 , the development of time-gated FLIM microscope with optical sectioning relies on some essential devices such as the light source, the light modulation system, the acquisition system and the optical components that build up the microscope module. Since the main goal of the developed system is to measure the fluorescence lifetime signal of FAD molecules, some of the characteristics of the system are fixed to the end application. These include, for example, the wavelength of the light source and the gating rate. In the next sections, the main devices that comprise the FLIM microscope will be described.

A. Light Source

The light source of the microscope system is based on a pulsed diode laser system from Picoquant (PicoQuant GmbH, Berlin, Germany). A class 3B laser head (LDH-P-C-440M) with a central wavelength of 440 nm and with a pulsing frequency as high as 40 MHz is managed through a computer controlled multichannel picosecond laser driver (PDL 828 “Sepia II”) - Figure 4.1. The laser head is connected to the picosecond laser driver which is responsible for providing the laser trigger signal synchronous to each laser pulse. The maximum pulsing frequency is set by the laser head, which in this case is 40 MHz. Every time a light pulse is emitted, a synchronized NIM pulse is generated. This NIM signal will serve as the main trigger to the entire acquisition system.

Figure 4.1 – Pulsed Diode Laser System from PicoQuant (PicoQuant, 2016)**.**

Table 4.1 – Pulsed Diode Laser Main Characteristics.

LASER SYSTEM MAIN CHARACTERISTICS	
Central Wavelength	440 nm
Maximum Average Laser Power	22,5 mW
Maximum Pulse Repetition Frequency	40 MHz
Minimum Pulse FWHM	63 ps
Maximum Pulse FWHM	190 ps

The laser power provided by this system is adjustable through the computer interface of the laser driver "Sepia II". The chosen laser power has influence on the pulse shape of the laser beam. If the power provided by the system is set to its maximum value (around 20 mW), the pulse shape and its FWHM will be enlarged. Figure 4.2 depicts this effect.

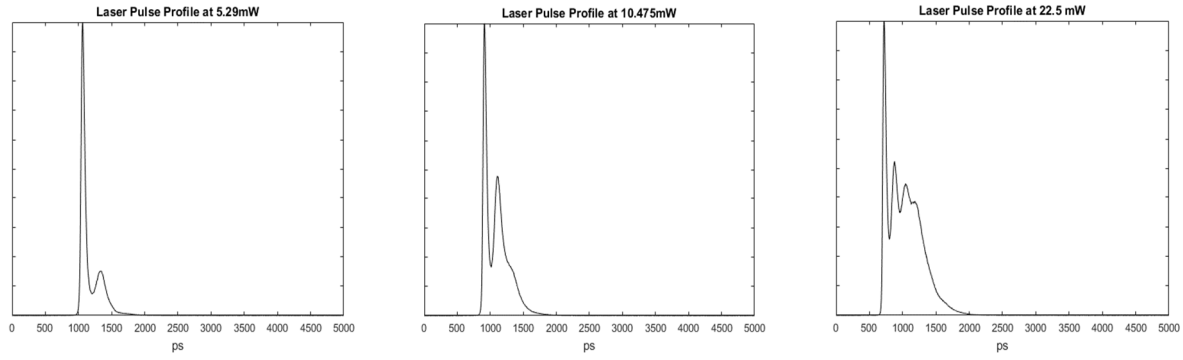

Figure 4.2 – Different laser pulse profiles for different selected laser powers, data provided by PicoQuant.

Handling laser diodes can be quite tricky in what beam shape is concerned. This type of lasers, due to the way they are built, have some characteristics. They are known for their astigmatic, elliptical and large divergent beam output. Fast axis and slow axis are two terms associated with elliptical beams since the divergence in horizontal and vertical directions is not the same. Fast axis is associated with the direction with larger beam divergence and slow axis, the direction with lower divergence angle. Therefore, fast-axis is the direction in which the beam is more enlarged and slow-axis the direction where it is narrower. Laser diodes are also characterized by their linear polarization along the slow axis direction (H. Sun, 2015).

Being laser diode, our light source shares all these characteristics. Figure 4.3 shows the typical elliptical shape of PicoQuant lasers. However, the practical divergence is limited since the beam is already collimated at the exit of the laser head. Table 2.2 summarizes the beam shape

characteristics and the features of the optical components placed in our laser head, as given by the manufacturer.

Table 4.2 – Beam Divergence and Optical Characteristics of the Laser Diode.

BEAM PARAMETERS	
Optics focus length	f = 4.5 mm
Typical divergence with optics	Theta II 0.32mrad; Theta ⊥ 0.11 mrad
Polarization	Linear and perpendicular to the fast axis
Polarization degree	>90%

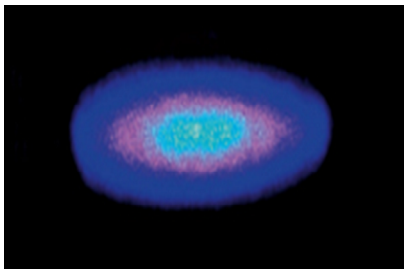

Figure 4.3 – Typical beam shape of a Picoquant diode laser output (PicoQuant, 2016)**.**

B. Time-Gated acquisition system

As described in the previous chapter, the time-gated acquisition system comprises several modules combined to acquire a series of images, each one delayed several tens of picoseconds from the previous one. Four main components are essential to have a Time-Gated system: a delay unit, a GOI and its controller, a CCD and a computer to control the entire system. The system assembled in this work uses a LaVision (LaVision GmbH, Göttngen, Germany) Intensified CCD camera based on an HRI working at rates up to 80 MHz and capable of producing gates as narrow as 200 ps, working together with a delay unit with 1 ps delay resolution and a VGA CCD sensor with 640x480 pixels. A personal computer stores the acquired data and controls the entire system. In the following section, the characteristics of each of these components will be described in detail.

1. HRI Delay Unit

The device responsible for providing the gating scanning instructions is a HRI Delay Unit. Part of the LaVision system, it is an optimized delay scan device for the HRI intensifier controller. It accepts trigger signals (including NIM signals) from 20 to 80 MHz and is controlled by the computer through a RS232 interface. Table 4.3 summarizes the main specifications of this unit. All its user control interface is part of the DaVis software that will described later.

Figure 4.4 – The HRI Delay unit used in the Time-Gated acquisition system (LaVision, 2007b)**.**

Table 4.3- Main specification of the HRI Delay Unit.

HRI DELAY UNIT MAIN CHARACTERISTICS	
Delay Range	0 to 50 ns
Resolution	1 ps
Jitter	<20ps
Delay Error	< 1%
Trigger Thershold Range	-1.5 to +1.5 V
Output	TTL level (almost square wave)
Number of Scan Entries	255

2. High Rate Intensifier (HRI)

The High Rate Intensifier (HRI) is a device composed by two modules: the image intensifier itself and the HRI controller module - Figure 4.5. As earlier described, a photocathode, a MCP and a

phosphor screen are housed inside the HRI. The used HRI, a PicoStar HR, includes a S25 photocathode, a single MCP and a P43 phosphor screen. The photocathode and phosphor screen spectral responses are depicted in Figure 4.6 andFigure 4.7, respectively.

Figure 4.5 - The HRI (PicoStar HR) and HRI Controller Devices included in the LaVision image intensifier system. Our system uses a different CCD from the one attached in this picture (LaVision, 2007b)**.**

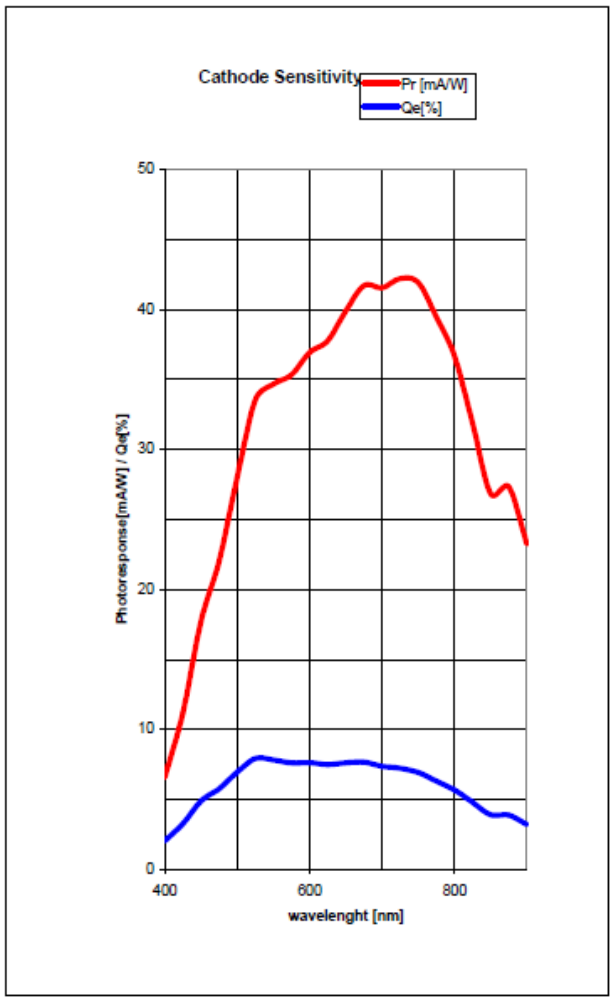

Figure 4.6 - Spectral Response and Quantum Efficiency of the S25 Photocathode installed on the HRI, (from LaVision user's manual.

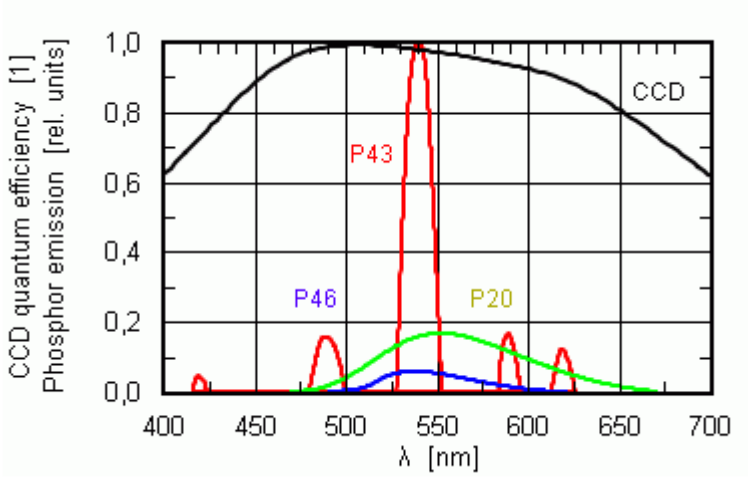

Figure 4.7 - Different Phosphor Screen Spectral Responses. P43 is the one installed in PicoStar HR module (LaVision, 2007a)**.**

The circuit that regulates the main functions of the GOI (intensified gating and gain modulation) is depicted in Figure 4.8. An average pulse (U_{av}) biases the photocathode cathode potential with respect to the MCP voltage input and a negative clamp voltage limits the most negative value of the gate pulse. This way, a careful and stable adjustment of gate widths can be guaranteed (LaVision, 2007b).

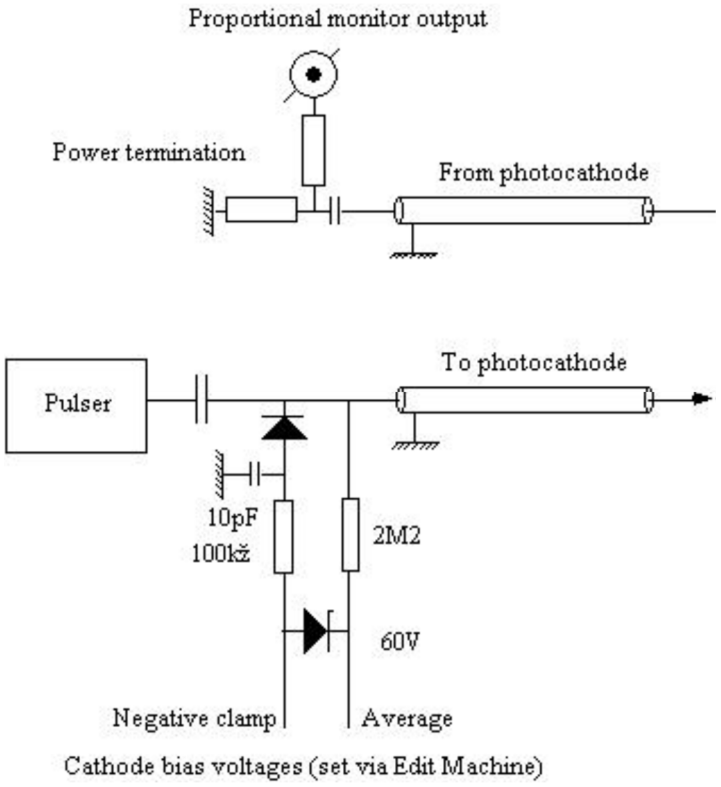

Figure 4.8 – Schematic representation of the circuit that controls the main functions of the GOI (LaVision, 2007b).

Different modes of operation are available to work with the HRI. Through the HRI controller, the user can select between SLAVE, COMB, RF and DC modes. Each has a specific working principle and is responsible for different modes of imaging acquisition. Table 4.4 has a short description of each operating mode available in HRI.

The HRI is connected to a controller unit, which is responsible to handle all the signal control required to guarantee a perfect operation of the image intensifier. This controller unit is divided into 5 main parts, each one with very specific functions. Each of these sections and its main functions are summarized in Table 4.5.

Table 4.4 – Description of each working mode of the Kentech HRI.

SLAVE	• Cathode gate voltage is switched according to the logic input signal. • Low Duty Cycle: 5%; or High Duty Cycle: 50%
COMB	• The trigger signal is routed via an impulse generator so that each transition of the trigger signal produces a narrow gate pulse. • Trigger Rates: 1 MHz to 110 MHz. • Different gate widths are pre-programmed (200, 300, 400, 500, 600, 700, 800, 900, 1000 ps);
DC	• Intensifier is working continuously.
RF	• The intensifier is modulated in response to a sinusoidal RF input. • Modulation Frequency Range: 1 MHz to 1 GHz

Table 4.5 – Description of the 5 units that compound the HRI controller device.

Low Voltage Board	• Provides power for all other sections • Generates logic voltages
High Voltage Tube Bias Supply	• Generates static potentials required for the intensifier tube. • Currents Produced: o Phosphor: 5.8 kV plus MCP voltage o MCP voltages: 260-850V o Cathodes bias average: -50V to +50V. o Cathode bias negative clamp: -50V to + 50 V.
Signal Conditioning	• Allows Mode Selection: SLAVE, COMB, RF, logic or inhibit. • Defines trigger polarity, termination and thresholding. • Allows choice between different pre-programmed COMB gate widths. • Defines RF Gain Control. • Provides TTL Monitor Output Signal. Wide band relays are used to divert the single trigger input to the various parts of the board according to the gate mode.
Cathode Gate Circuit	• Provides impulse outputs for the COMB and logic modes. • Provides linear amplification of the input signal for RF mode.
Internal computer control (TDS 2020 Forth microcontroller based on a Hitachi H8 microprocessor).	• 12-bit DAC control the pulse power supply and signal conditioning modes cards. • Monitors the push buttons, tube temperature, phosphor current ad power supply load.

MCP voltage controls the gain applied in the MCP. This gain is defined as the relationship between the number of counts detected by the CCD per electron reaching the MCP. Gain calibration values provided by the manufacturer are summarized in Table 4.6.

Table 4.6 - Relation between gain in counts per electron and voltage applied to the MCP.

UMCP [V]	GAIN (CNTS/EL)
260	0.01
300	0.02
350	0.06
400	0.17
450	0.43
500	1.05
550	2.41
600	5.2
650	11.1
700	21.6
750	45
800	83
850	140

3. CCD

Another important part of a Time-Gated FLIM architecture is the CCD camera. It is the device responsible for detecting the photons and converting them into digital signals that will be analyzed by the computer. The CCD installed in the system is an Imager Compact from LaVision. This Imager module integrates a 12-bit A/D converter and uses a PCI-Board installed in the computer. The CCD sensor is a VGA type with 640 per 480 pixels and read-out timings varying from 6.8 ms to 24.8 ms, depending on the binning of the CCD. In Table 4.7 its specifications are summarized. Figure 4.9 depicts the spectral profile of the CCD.

Table 4.7 - Imager Compact CCD Specifications.

CCD SPECIFICATIONS	
Number of Pixels	640 (H) x 480 (V)
Pixel Size	9.9 µm x 9.9 µm
Sensor Format	1/2 ‘’
Scan Area	6.3 x 4.8 mm
Full Well Capacity	32.000 e^-
Readout Noise	16 e^-
Scan Rate	16 MHz
Imaging Frequency…	
…at binning mode 1	40 fps
…at binning mode 2	76 fps
…at binning mode 4	140 fps
A/D conversion factor	7 e^-/count
Average Dark Charge @20ºC (per pixel)	< 3 e^-/sec
Spectral Range bandwidth	280… 1000 nm
Non-Linearity (Differential)	<1.5%
Binning Vertical	Factor 1, 2, 4
Binning Horizontal	Factor 1, 2

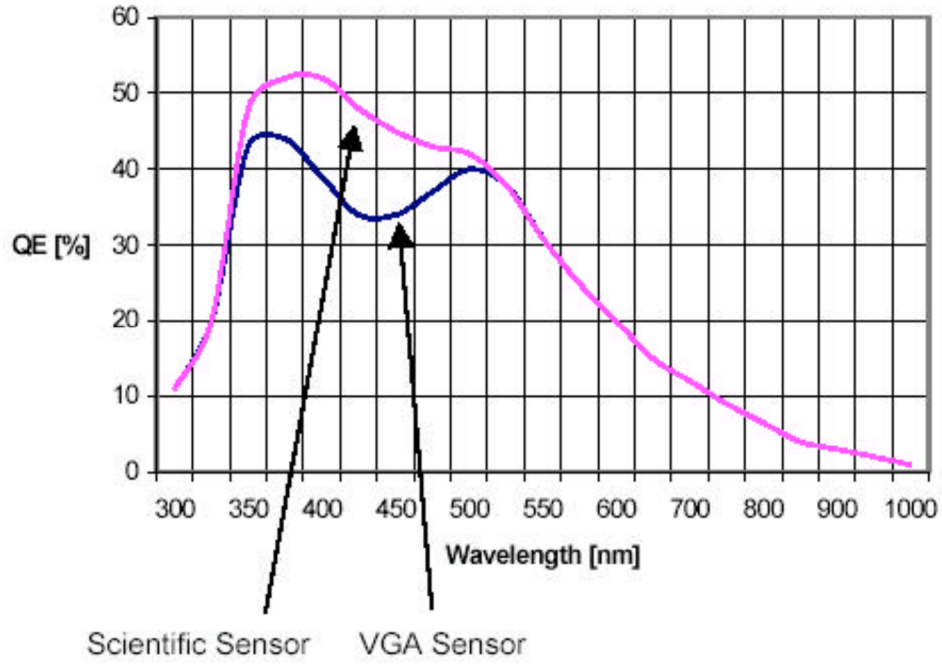

Figure 4.9 – Quantum efficiency of the CCD installed in the system - VGA sensor (LaVision, 2007a)**.**

4. DaVis Software

To easily integrate and control all the devices on the LaVision Time-Gated imaging acquisition system, the manufacturer developed a software application entitled DaVis. The version adequate to this specific system is 7.6. Here, the user can perform all the control actions required for a perfect setup of the HRI, HRI controller, HRI delay units and CCD. The software also offers the possibility of executing a diverse number of image acquisition processes and, after that, image processing such as fluorescence lifetime map calculation.

The first basic operations allowed by the DaVis system are the control of the devices. Upon connection of the system, the software is responsible for analyzing those devices and establishing the last configured system settings. These include, among others, trigger settings for the HRI Delay Unit and the HRI and delay instructions to open the gates. Figure 4.10 shows the user dialogs that allow changings in these configurations according to the specifications of HRI and HRI Delay Unit (HDG).

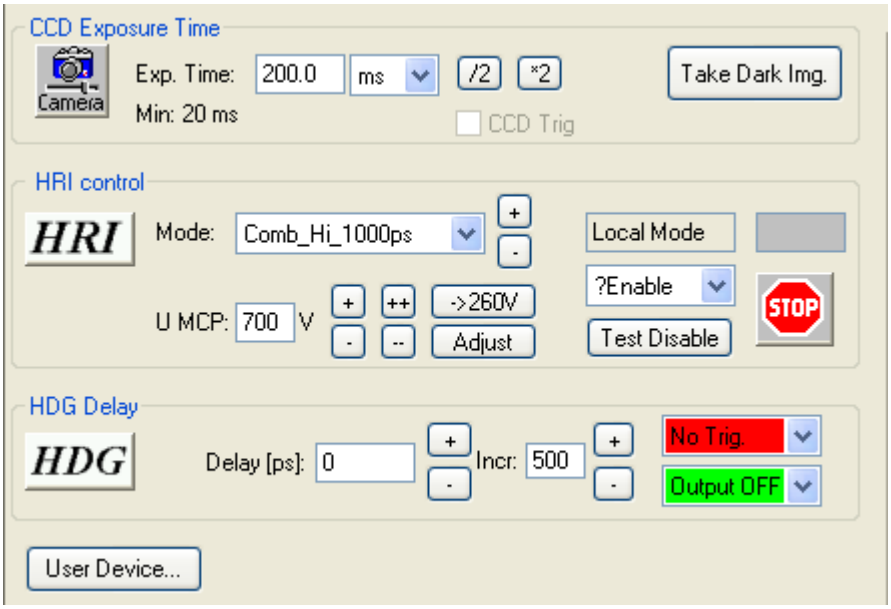

Figure 4.10 - Device Configuration Dialog. Here the user can select the CCD exposure time, the MCP voltage and therefore the gain of the image intensifier and the default HDG delay to open the gate when scanning is not active. The HRI and HDG buttons allow to adjust, trigger settings for these two devices.

In the recording parameters interface, the user must specify the input trigger delays, defining this way when the successive gates will open during the fluorescence decay. The HRI Delay Unit allows 255 scan entries with a resolution of 1 ps between them. Figure 4.11 is a screenshot of this window.

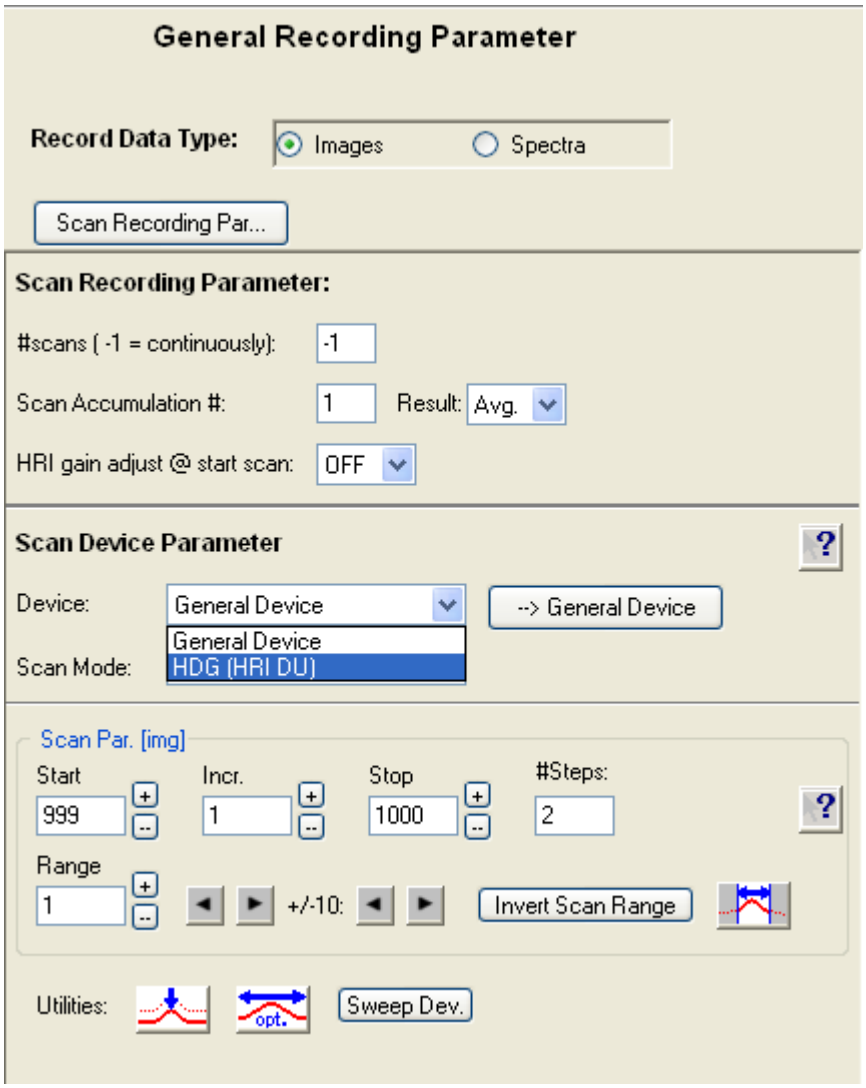

Figure 4.11 – DaVis user interface for defining the timing of each gate.

Image acquisition can be executed in two different modes: by successively scanning gates (the Scan mode), which is the mode used to acquire data for lifetime measurements, or in a continuous way (the Grab mode), where the camera takes a series of images always with the same delay value. This mode can be used, for example, to acquire fluorescence intensity images, a much faster acquisition process. The choice between these acquisition modes is made on a separate tab by either choosing “General Scan Recording Interface” or “General Image Recording Interface” - Figure 4.12.

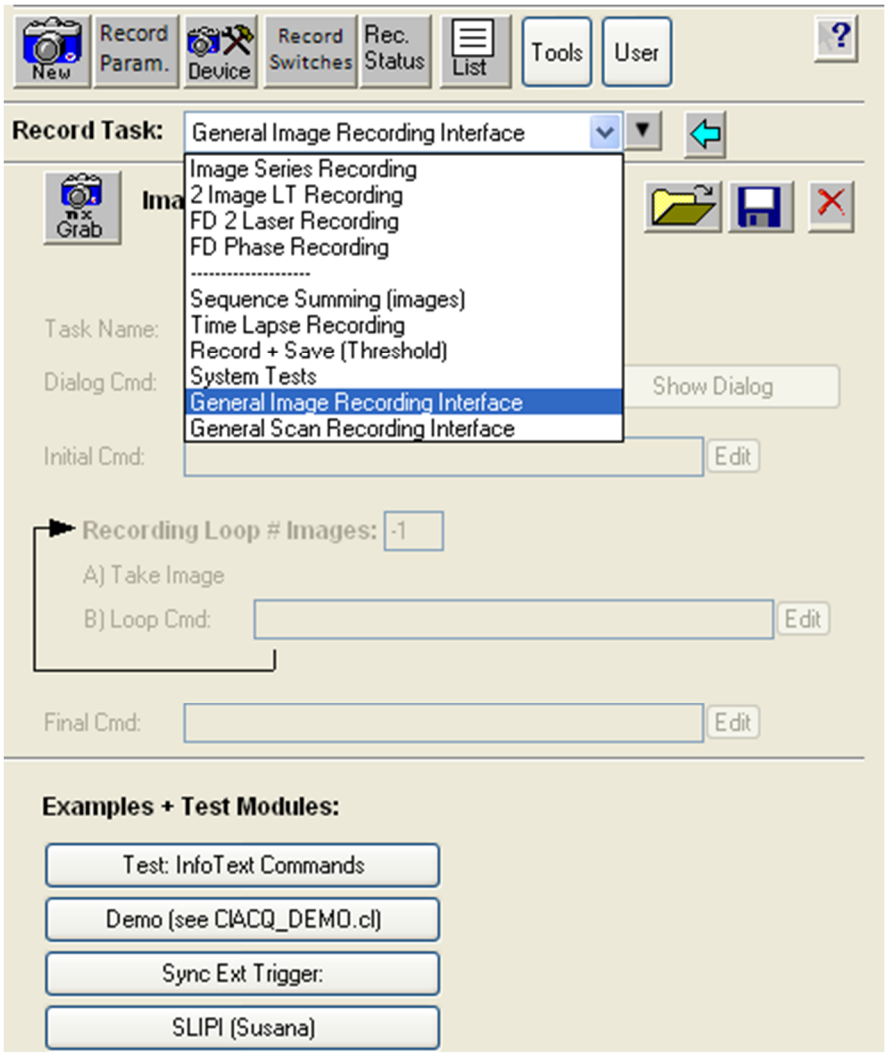

Figure 4.12 – DaVis user interface to choose between "Grab" and "Scan" modes. "Grab" mode is used only to acquire fluorescence intensity images while the "Scan" mode is used to acquire a series of time-gated images to obtain the fluorescence decay profile.

As mentioned, besides imaging acquisition control, DaVis also has features that allow image processing after acquisition. It has a processing mode where fluorescence decay curves can be fitted to single-exponential decay curves based on a non-linear least squares fitting algorithm. This tool also has the capacity to create lifetime maps based on this fitting algorithm. However, it is quite limited since it is not capable of fitting more complex decay curves and therefore, it was not used and will not be described.

C. Digital Micromirror Device (DMD)

The digital micromirror device used is embedded in a system from Texas Instruments (Texas Instruments Inc., Dallas, Texas, USA) called DLP LightCrafter. The original system consists of three subsystems: a light engine, a driver board and a system board. The driver board contains the

LED driver circuits, the DLPC300 DMD Controller, power management circuits and a MSP430 microcontroller, all from Texas instruments. The system board includes a TMS320DM365 digital media processor, a FPGA and several connectors for external inputs. The light engine houses the 606 x 654 diamond pixel 0.3-inch WVGA DMD (DLP3000), along with LEDs and optics for image projection. To use this device in our microscope configuration, the LEDs and optics were removed making possible to illuminate the DMD with the PicoQuant laser and project the formed pattern with custom optics. Figure 4.13 is a schematic representation of the entire DLP architecture.

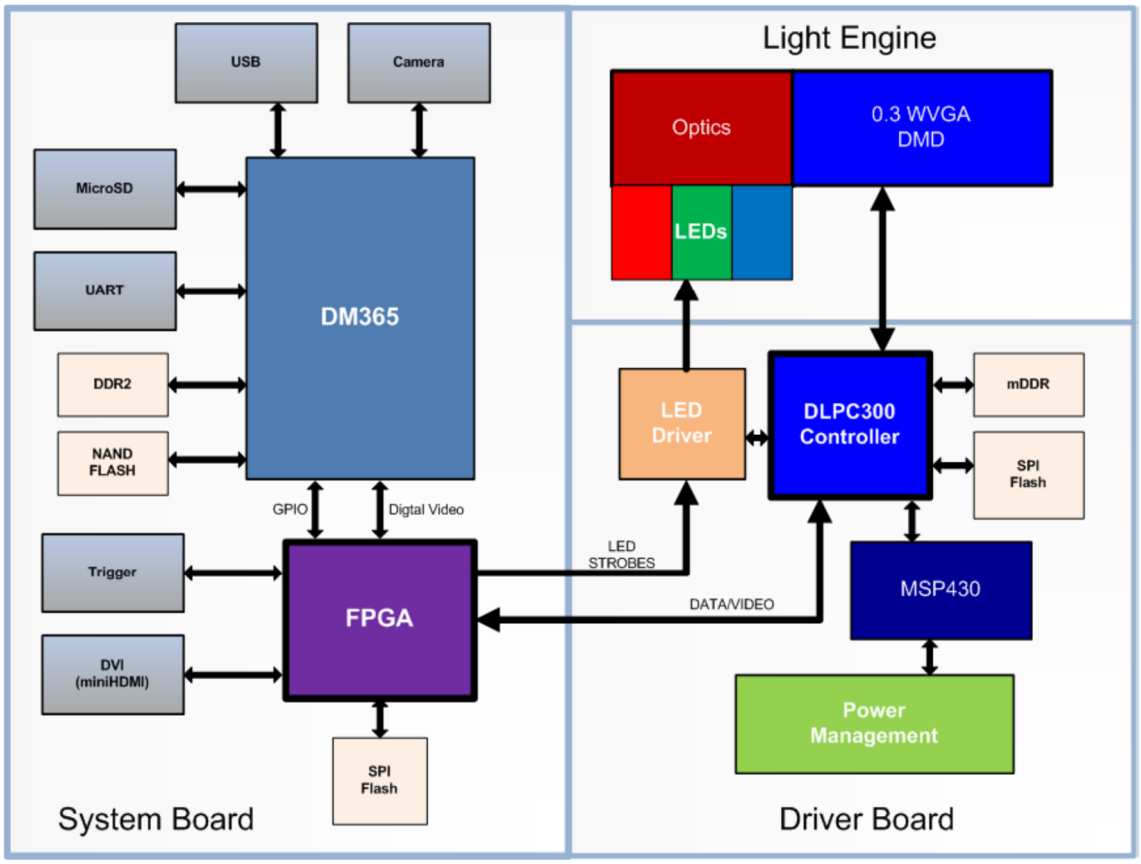

Figure 4.13- Schematic representation of the different sub-systems and connections comprising the DLP LigtCrafter used to create the structured illumination patterns (Texas Instruments, 2012).

As stated, the used DMD is a DLP3000 model. It has 608 x 684 mirrors arranged in a diamond pattern geometry as exemplified in Figure 4.14.

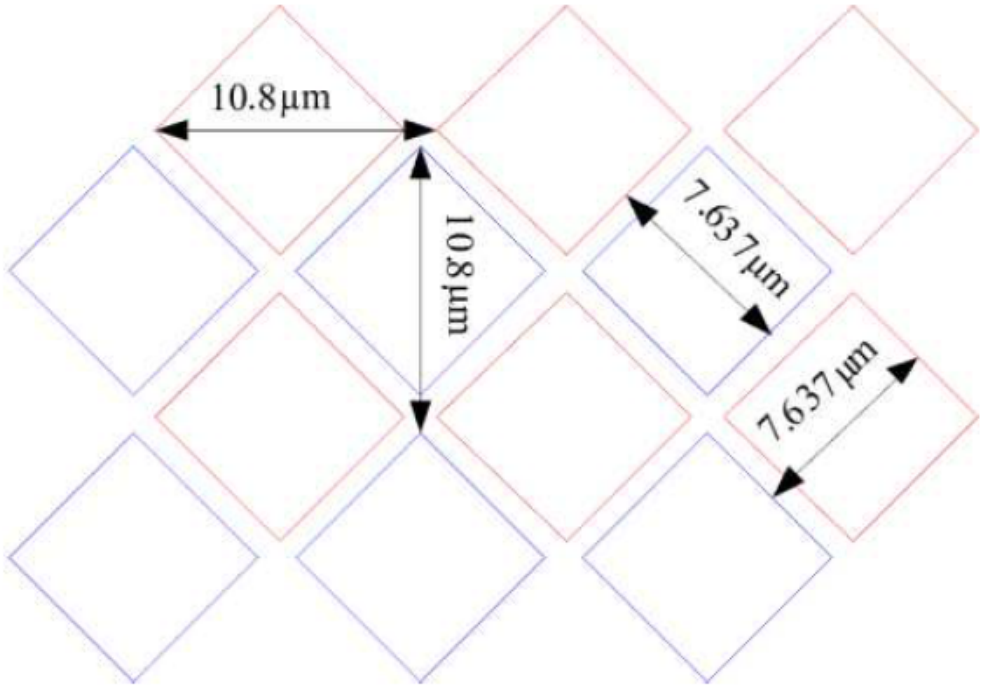

Figure 4.14 – Diamond micromirror arrangement in DLP3000 DMD device (Texas Instruments, 2012).

The DLP LightCrafter is an independent board that can be controlled through a computer via an USB 2.0 connection. The DLP LightCrafter is shipped with a custom developed GUI software, that can be used to establish the connection to the DLP device and also to load the patterns to be shown on the DMD surface. Moreover, it is also provided a C++ based software that allows the user to develop its own application, without having to run every control step through the GUI. For this microscope, this is a very important feature that allows the control to be executed entirely via DaVis software, as explained ahead.

D. Optical Components

Several different optical components are necessary to build a fluorescence microscope using structured illumination. Among the most fundamental, are the microscope objective and the light collecting optics placed before the intensified camera. Other optical components such as dichroic mirrors, filters, beam splitters, mirrors and single and doublet lenses are also essential.

1. Light Collection Optical System

Microscopy requires an imaging system with very low aberration. In our instrument, an adapted commercial infinity-corrected microscope module (C-Mount microscope) is placed before the HRI. This module from Edmund Optics (York, United Kingdom), shown in Figure 4.15, has a tube length of 200 mm and is designed to work with CCD sensors up to 2/3'' in size.

Figure 4.15 – Photograph of the infinity-corrected microscope module installed.

2. Infinity-Corrected Microscope Objective

Infinity-corrected objectives are essential to ease the process of pattern projection and image creation in the HRI. Any infinity-corrected objective can be used with our system. We used four different models from different brands with different characteristics: Olympus Plan N 20x, NA 0.4, Olympus Plan N 40x NA 0.65, Zeiss Achroplan N 40x NA 0.75W and Olympus LUMPlan FLN 60x, NA 1.0W. The last two models are water immersion objectives. Figure 4.16 and Table 4.8 show their main specifications.

Figure 4.16 – Infinity-corrected microscope objectives used with the Time-gated microscope.

Table 4.8 – Infinity-Corrected Objectives main specifications.

	OLYMPUS PLAN N 20X	OLYMPUS PLAN N 40X	ZEISS ACHROPLAN N	OLYMPUS LUMPLANFLN
Magnification	20x	40x	40x	60x
Numerical Aperture	0.4	0.65	0.75	1.0
Working Distance (mm)	1.2	0.6	2.1	2
Field Number (FN)	22	22	Not Specified	26.5
Immersion Liquid	None	None	Water	Water
Cover Glass Thickness (mm)	0.17	0.17	0	0

3. Dichroic Mirrors, Fluorescence Filters and Beam Splitters

Every fluorescence microscope demands the use of filters to separate excitation light from fluorescence light coming from the sample. Usually, a filter cube is used with three elements mounted: an excitation filter, a dichroic mirror and an emission filter. The excitation filter can be either a short-pass filter or a band-pass filter and is used mainly to guarantee that the excitation wavelength is quite restricted to the wavelength desired. The dichroic mirror is a filter that has two types of behavior, above and below a certain cutoff wavelength. Typically, it is installed at 45º degrees to the optical axis and is reflective below the cutoff wavelength while transmitting light above the cutoff wavelength. Finally, the emission filter ensures that there are no reflections contaminating the fluorescence signal. It is usually a long-pass filter or a band-pass filter with spectral transmission adjusted to the fluorescence spectrum we want to detect.

The microscope filters were chosen taking in account that the system was developed to image FAD autofluorescence and that the central wavelength of the installed laser is 443 nm. Thereby, the chosen excitation filter is a hard-coated short-pass Thorlabs (Thorlabs GmbH, Munich, Germany), FESH0450, the dichroic mirror is a Chroma Q505lp and the emission filter is a band-pass Chroma (Chroma Technology Corp, Vermont, USA) HQ535/50m. Their spectral properties are represented in Figure 4.17.

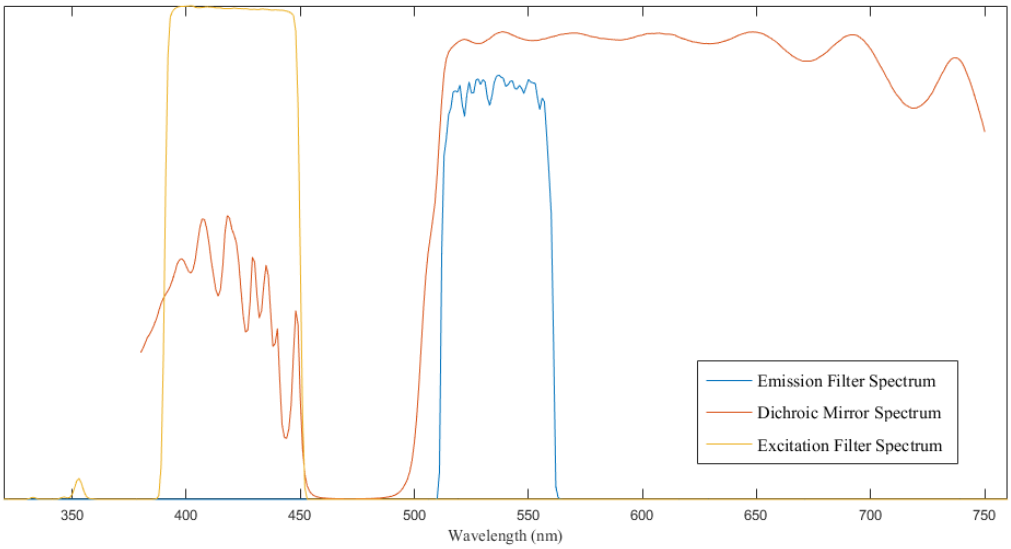

Figure 4.17 – Spectral transmission of the three filters installed in the filter cube. Raw data to build the graphic was collected from manufacturers websites (Thorlabs® and Chroma®).

The microscope is not limited to the fluorescence mode. To operate in reflective mode, the fluorescence filters are removed and replaced by a beam splitter installed in a different cube. The

selected beam splitter is a 50:50 BSW20R from Thorlabs and its spectral reflectance and transmission are represented in Figure 4.18.

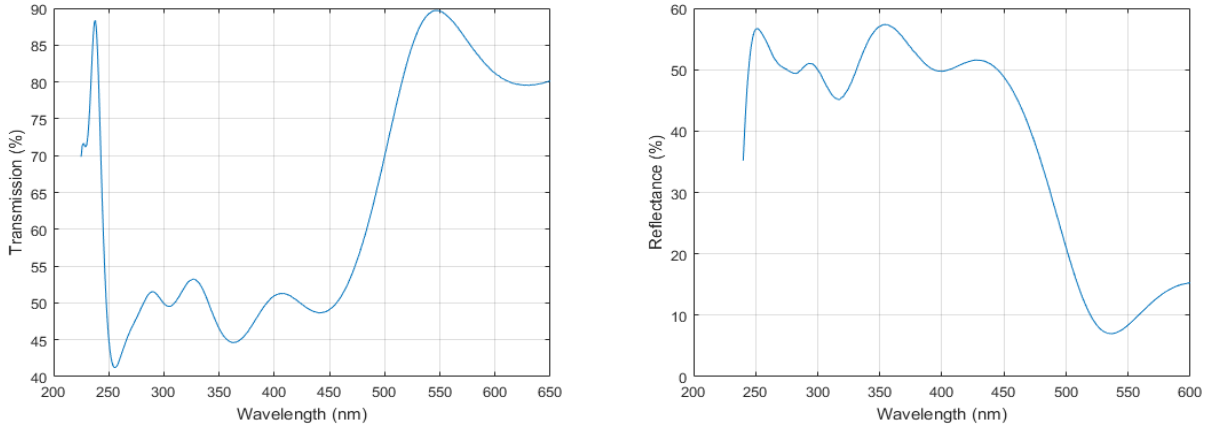

Figure 4.18 – Spectral transmission and reflectance of the BSW20R beam splitter installed for reflective mode.

4. Other Optical Components

Additional optical components are required to project the patterns used to obtain the modulated illumination demanded by the structured illumination technique. During the project, two types of structured illumination were installed: the first was based on the projection of patterns created by the DMD, while the other used the projection of a simple Ronchi Rulling target. The images of both patterns were created on the conjugate plane of the microscope objective, to obtain enough pattern contrast on the sample plane. The used optical components varied between the two configurations. A representation of the illumination optical setup for the first configuration, the DMD implementation, is illustrated on Figure 4.19. Here the laser beam reaches the DMD surface collimated. A dielectric mirror, whose transmission spectrum is depicted in Figure 4.20, reflects the beam coming from the laser into the surface of the DMD, which acts as a two-dimensional diffraction grating giving rise to the projection of a multitude of images of the pattern being defined in the DMD. Right after the DMD, is placed a plano-convex lens with focal distance of 100 mm forming, with another plano-convex lens with focal distance of 150 mm, a Keplerian microscope, whose main function is to augment the DMD pattern about 1.5 x. An iris aperture is placed between these two lenses, to block all the diffraction orders other than the zero order. A dielectric mirror is used just to change the direction of the beam and simplify the spatial optical arrangement. Finally, a 100 mm focal distance doublet lens is used to form the image of the DMD onto the conjugate plane of the objective.

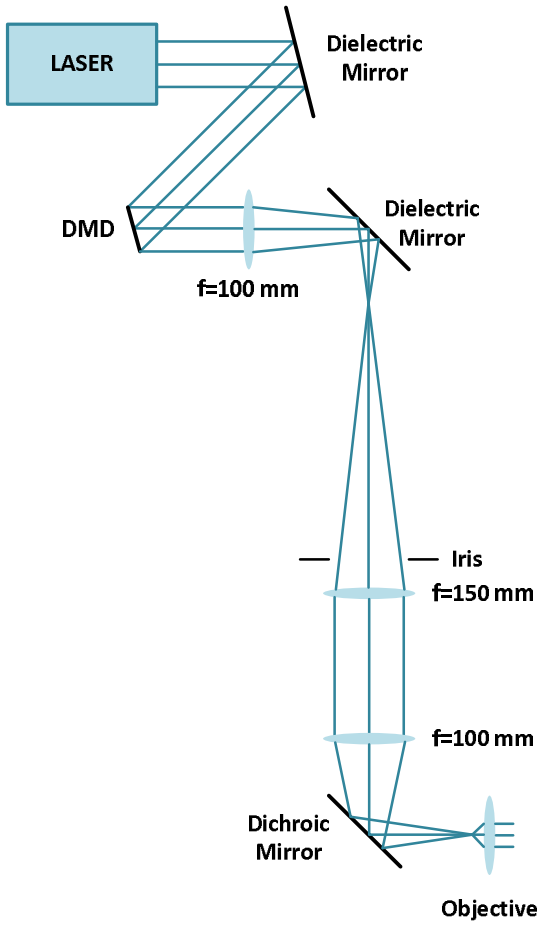

Figure 4.19 – Schematic representation of the illumination optics when the DMD is installed.

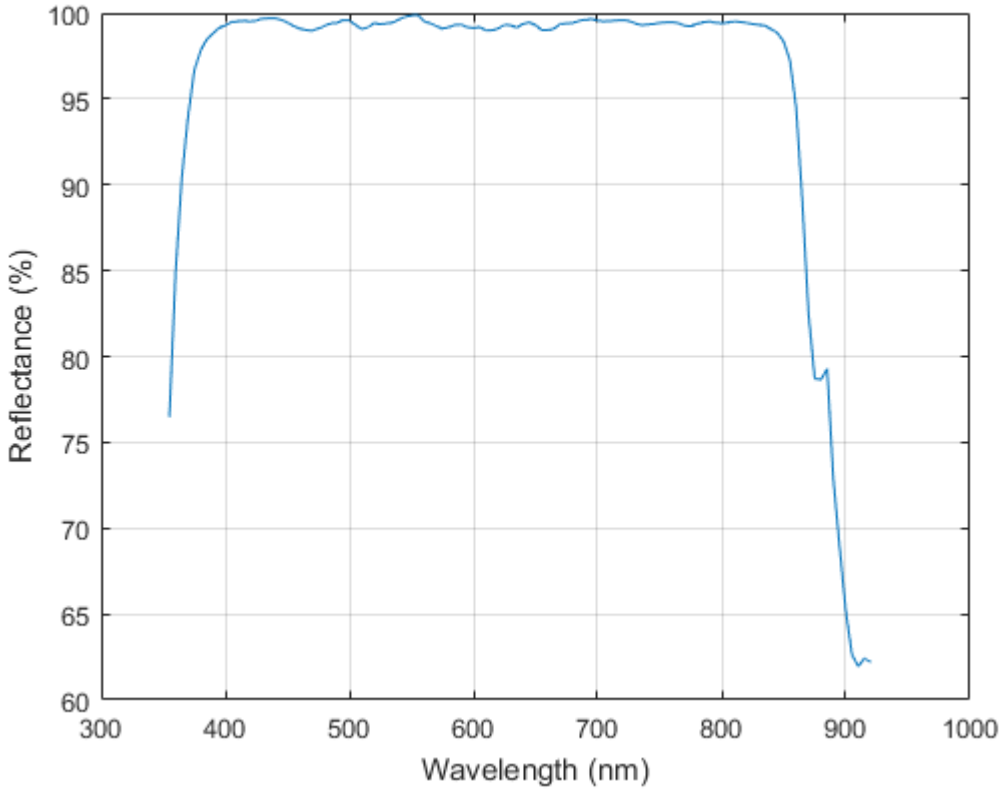

Figure 4.20 – Spectral response of the dielectric mirror installed.

The second microscope configuration is schematized in Figure 4.21. Two main differences are highlighted. First, a cylindrical lenses complex is installed right after the laser head exit to overcome the problem of the small divergence and elliptical shape of the laser beam. This cylindrical complex includes a 50-mm doublet and two cylindrical lenses of 75- and 150-mm focal lengths. Right after the cylindrical lenses complex, the laser beam is focused by a 50-mm doublet lens into the Ronchi ruling pattern plane. Then, two doublet lenses, with focal distances of 150-mm and 100-mm, increase the pattern size and focus it into the conjugate plane of the objective. As in the previous configuration, a dielectric mirror is used just to change the optical direction of the laser beam and to simplify the microscope arrangement.

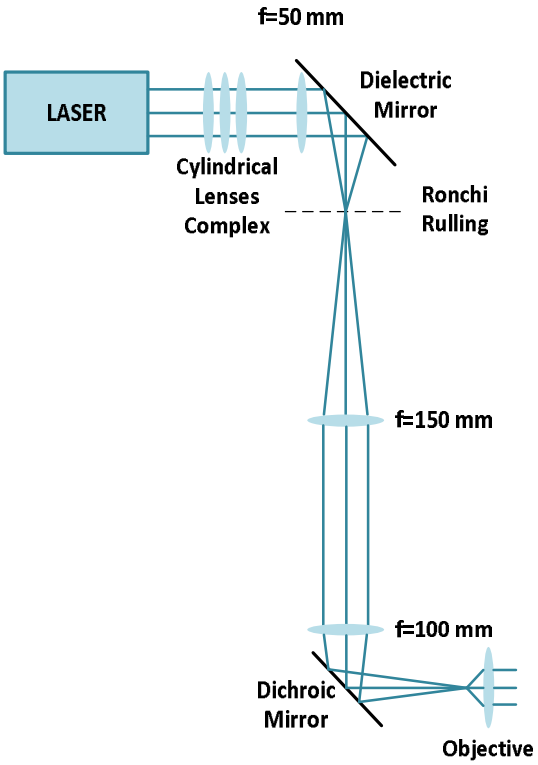

Figure 4.21 – Schematic representation of the illumination path when a Ronchi rulling pattern is installed, replacing the DMD.

Two complete instrument setups were achieved after setting up all the components described throughout this chapter. These are schematized in Figure 4.22 and in Figure 4.23. The main trigger signal is provided by the laser driver and is connected, after passing by an adjustable delay line, to the HRI Delay Unit. Both devices are connected to the computer: the laser driver is controlled via a USB connection and the HRI decay unit through a RS232 connection. The delayed triggers exit the HRI delay unit as TTL signals and are connected to the HRI control unit, which is also controlled by the computer through a RS232 connection. As explained before, the HRI controller establishes the different signal configurations, to provide gating and MCP gain to the CCD. The CCD camera is placed behind the HRI and interfaces with the computer. This configuration is common to both setups of the microscope. On the first setup, the DMD device is also connected to the computer through an USB 2.0 interface.

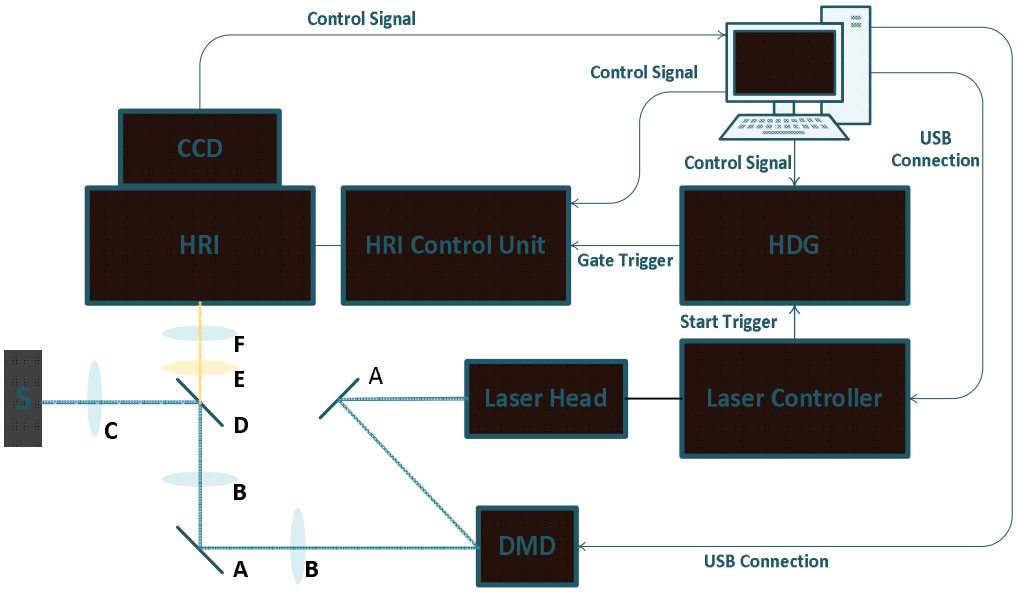

Figure 4.22 – A-Plane Mirror, B – Positive Lens, C – Infinity-Corrected Objective, D – Dichroic Mirror, E – Fluorescence Emission Filter, F – Infinity-Corrected Microscope Module

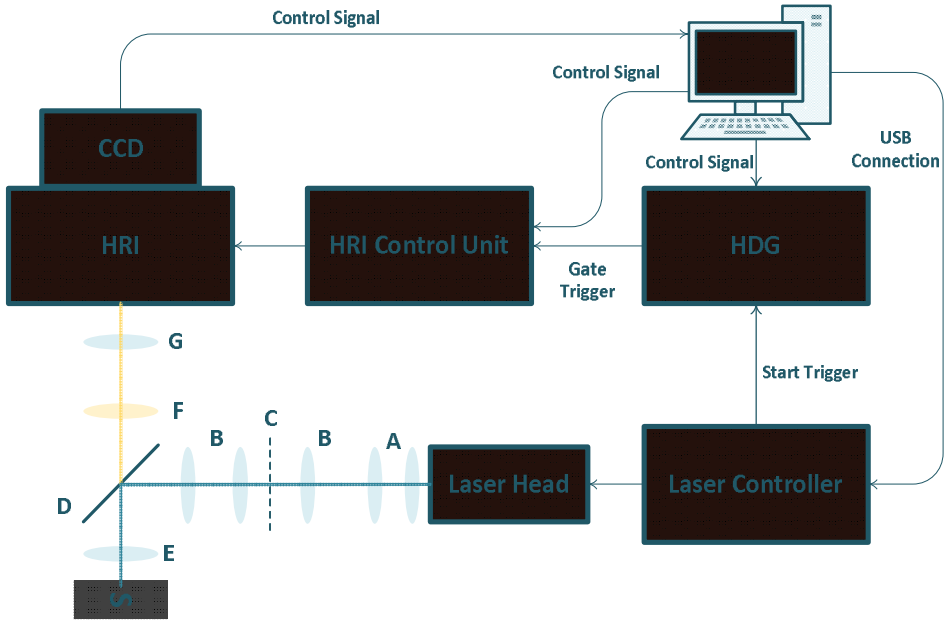

Figure 4.23 – A – Cylindrical Lenses, B – Positive Lens, C – Stripe Pattern, D – Dichroic Mirror. E- Infinity-Corrected Objective, F – Fluorescence Emission Filter, G – Infinity-Corrected Microscope Module.

Chapter 5 System Performance Results

The performance of a fluorescence lifetime imaging microscope is mainly evaluated through its optical and timing characteristics. The optical features of the instrument are directly connected to its imaging quality. They can be evaluated with optical tests very similar to those performed on conventional microscopes. As for the timing properties of the instrument, they limit its capacity to correctly determine the fluorescence lifetime of the molecules under analysis. Throughout this chapter, we will describe both optical and timing tests and their respective results.

A. Optical Parameters Evaluation

The basic optical features to be attended when choosing the proper microscopy imaging system for a specific application are: the field of view, the lateral resolution and the optical sectioning (if the sample has more than a few microns in thickness). In fluorescence microscopy, we also need to consider additional features related to the spectral characteristics of the excited molecules. Considering the requirements set and described in Chapter 4 , several optical parameters were analyzed through different optical tests.

The first parameter measured was the field of view. The field of view of a microscope is defined as the diameter of the image field in millimeters measured at the intermediate image plane (Spring and Davidson, 2017). In this project, we tested four different objectives to obtain a system that could be used with a variety of samples. Due to this, the value of the field of view is not constant: a different value for each used objective is expected. To measure this parameter, a variable line grating resolution target (limit resolution of 250 lp/mm) (Thorlabs GmbH, Munich, Germany) was placed at the focal plane of each objective and the correspondent image was recorded. This measurement was made in both fluorescence and reflectance modes and the results obtained are described in Table 5.1. The target was painted with fluorescent ink for enabling measurement in the fluorescence mode.

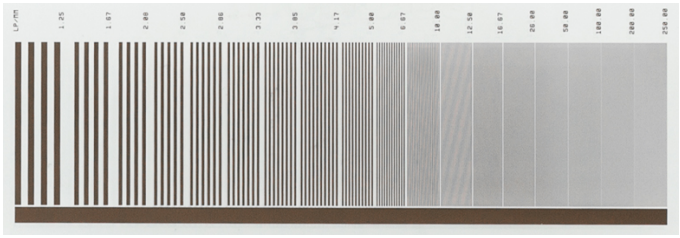

Figure 5.1 - Representation of variable line grating (Thorlabs).

Table 5.1 - Fields of view measured for each microscope objective.

MICROSCOPE OBJECTIVE	FIELD OF VIEW
Olympus 20x	260 x 320 µm
Olympus 40x	176 x 132 µm
Zeiss 40x W	176 x 132 µm
Olympus 60x W	124 x 96 µm

The lateral resolution of a wide-field microscope is, in theory, limited by the laws of diffraction. Lateral resolution is defined as the shortest distance between two points in the specimen plane under that can be distinguished by the observer or by the sensor collecting the image (Michael W. Davidson, 2018). In microscopy, it is often common to distinguish lateral from axial resolution or optical sectioning. Lateral resolution is directly connected to the image acquired on a two-dimensional plane while axial resolution concerns thick specimens and the ability of the microscope to image only sections of it. According to the Rayleigh criterion and Abbe's diffraction limit, lateral resolution is defined by Equation 5.1 where λ is the wavelength of the light in the imaging path (in the case of fluorescence microscopy, it corresponds to the fluorescence emission spectra) and NA is the numerical aperture of the objective.

$$Lateral\ Resolution = \frac{0.61\lambda}{2NA} \tag{5.1}$$

As Equation (5.1) suggests, the lateral resolution limit imposed by diffraction depends on the used objective. The values for the objectives used in this project are summarized in Table 5.2. The wavelength considered to estimate them was the peak emission wavelength of FAD emission spectrum – 530 nm.

Table 5.2 – Estimated Rayleigh lateral resolution limits per microscope objective used, for FAD fluorescence emission.

MICROSCOPE OBJECTIVE	RAYLEIGH LATERAL RESOLUTION LIMIT
Olympus 20x	404.13 nm
Olympus 40x	248.69 nm
Zeiss 40x W	215.53 nm
Olympus 60x W	161.65 nm

In addition to diffraction, there are other physical limitations that can affect the lateral resolution. When the imaging system is based on a CCD sensor, the resolution limit imposed by the pixel and sensor sizes influences the final lateral resolution of the microscopic imaging system and can impose a higher limit than that already described. Imaging systems resolution is often defined in terms of frequency of maximum contrast line pairs per mm (lp/mm). In imaging sensors, the highest resolution is defined by the Nyquist limit, a consequence of the Nyquist sampling theorem. The sensor resolution in mm, also known as the image space resolution, is given by the Equation 5.2:

$$image\ space\ resolution\ \left(\frac{lp}{mm}\right) = \frac{1000}{2 * pixel\ size\ (\mu m)} \tag{5.2}$$

From this relation, it can be concluded that the CCD characteristics are very important in defining the limiting conditions for lateral resolution. They impose the limits in the image space that should be accounted in the object space resolution, the value that really defines what can be distinguished in the object. The relation between image space resolution and object space resolution is given by the magnification of the optical system between the object and the image spaces – Equation 5.3. The magnification of this optical system can be estimated by knowing the focal lengths of the equivalent tube lenses and microscope objective or by dividing the sensor size by the field of view already estimated. Since the intensified CCD system includes unknown optical elements, the effective magnification for each objective used will be estimated by dividing the sensor size by the field of view. With that, the limits of the lateral resolution can be easily estimated by applying Equations (5.3) and (5.4). The results are summarized in Table 5.3.

$$M = \frac{sensor\ size\ (mm)}{field\ of\ view\ (mm)} \tag{5.3}$$

$$object\ space\ resolution = \frac{pixel\ size\ (\mu m)}{M} \tag{5.4}$$

Table 5.3 – CCD limits of object space resolution per microscope objective used.

MICROSCOPE OBJECTIVE	CCD LIMITED OBJECT SPACE RESOLUTION
Olympus 20x	521 nm
Olympus 40x	275 nm
Zeiss 40x W	275 nm
Olympus 60x W	198 nm

The experimental verification of these lateral resolution limits was performed with a similar procedure to that used to estimate the field of view. Again, the variable resolution grating test target was used. The microscope system was able to resolve all the patterns in the used target. So, we can only conclude that lateral resolution is at least 250 lp/mm, the limit of the used test target. With the standard resolution test targets commercially available, it is difficult to test values as low as those estimated and described in Table 5.4.

One of the key development points during the execution of this project was the addition of an optical sectioning method to the widefield microscope that could yield optical sectioning power comparable to that given by commercial confocal systems. For that, as mentioned, two SIM methods were implemented (3-Phase Approach and HiLo), both based on the projection of square/sinusoidal patterns. To estimate their optical sectioning ability, one must recall how the axial point spread function in structured illumination schemes is described. Equations (1.17) - (1.19) give the theoretical normalized axial response for microscopes using this type of illumination. Optical sectioning was analyzed for both implemented methods of SIM and different grating frequencies (υ). The axial response depends on several instrument parameters including microscope objective features, summarized in Table 5.4, physical grating frequencies and focal lengths of grating imaging lenses. Other important parameters include the tube lens focal length, which is always 200 mm and the excitation wavelength, also kept constant at 443 nm. Here, we present results for both implementations. All the other optical parameters measured and presented

so far are similar in both versions. Due to that, this distinction is only made with this feature. Moreover, since the DMD application was developed in an earlier phase of this project, the optical sectioning was only measured using two objectives: the Olympus 20x and the Zeiss 40x.

Table 5.4 – Main characteristics of the microscope objectives used in the developed Time-Gated microscope.

PARAMETER	OLYMPUS 20X	OLYMPUS 40X	ZEISS 40X	OLYMPUS 60X
Magnification	20x	40x	40x	60x
Numerical Aperture	0.4	0.65	0.75	1.0
Refraction Index	1.0	1.0	1.33	1.33

As said in Chapter 2 , the ability to obtain optical sections with both of implemented SIM methods depends on the modulation contrast of the square/sinusoidal projected pattern. It can be estimated by Equations (5.5) to (5.7).

$$I_p(u) = \left| \frac{2J_1\left[u\tilde{v}\left(1-\frac{\tilde{v}}{2}\right)\right]}{\left[u\tilde{v}\left(1-\frac{\tilde{v}}{2}\right)\right]} \right|^2 \tag{5.5}$$

$$\tilde{\upsilon} = \frac{f_g \lambda M \upsilon}{(NA) f_t} \tag{5.6}$$

$$u = \left(\frac{8\pi}{\lambda}\right) z n \sin^2\left(\sin^{-1}\frac{(NA)}{n}/2\right) \tag{5.7}$$

Considering the optical specifications of each objective and of the microscope, already described in the Chapter 5, the theoretical optical sectioning curves could be obtained by applying these equations. They are described in Figure 5.2 and Figure 5.3.

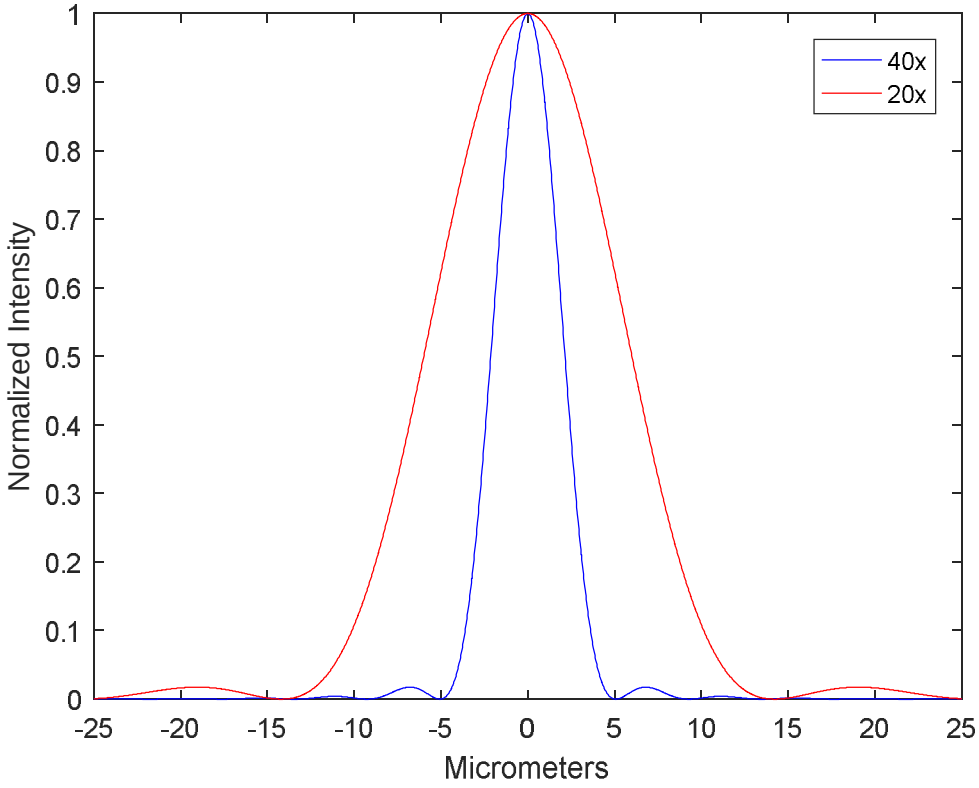

Figure 5.2 - Theoretical optical sectioning estimated for objectives Olympus 20x and Zeiss 40Wx on Equations (5.5) to (5.7) for the 3-phase-apparoach version.

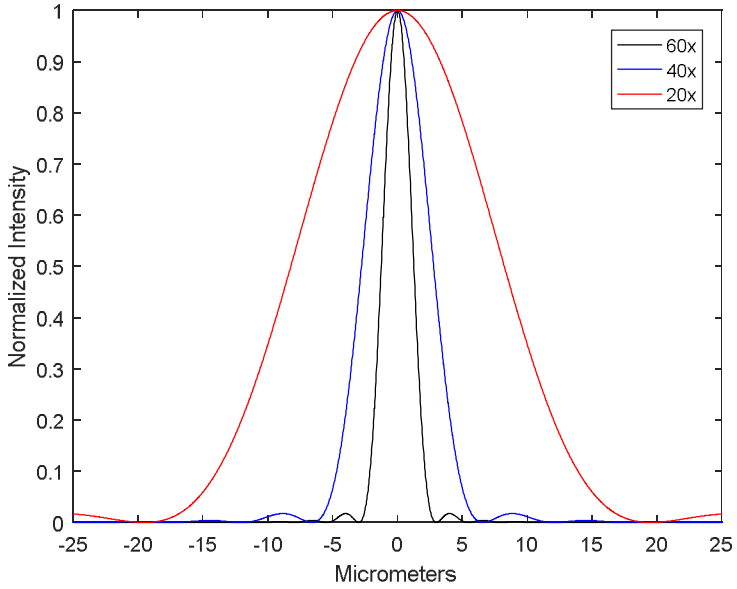

Figure 5.3 – Theoretical and calculated optical sectioning curves based on the optical parameters of the microscope and on Equations (5.5) to (5.7) for the HiLo version.

A special target is required to measure experimentally the optical sectioning. It should be a homogeneous fluorescence sample, thinner than the theoretical axial response of the instrument.

Conventionally, the measurement of optical sectioning would require the axial scanning of this target and the acquisition of a SIM image for each axial step taken. However, there is a simpler way to measure this parameter, which corresponds to the measurement of the modulation depth when the same thin object is axially scanned through the focus of the objective (Webb *et al.*, 2002). For that, modulated images were acquired at different axial steps and the mean of the columns of each of them was obtained, resulting in an intensity profile very similar to a sinusoidal pattern, as depicted in Figure 5.4. By taking the fast-Fourier transform (FFT) of this intensity profile, the dc and the modulation information of the image could be separated, with the former corresponding to the zero-order of the FFT and the latter to the first order. Then, by plotting the intensity of the first order, which is higher when the grating and the fluorescent layer are in conjugate planes of the objective, we can obtain the experimental optical sectioning curve of the microscope. This procedure was applied to the Olympus 20x, Zeiss 40x and Olympus 60x objectives in the case of HiLo microscopy. In the case of the 3-phase approach it was only applied to the Olympus 20x and Zeiss 40x. The experimental plots are depicted in Figure 5.5 for the 3-phase approach and Figure 5.6 for the HiLo. Their FWHM corresponds to the optical sectioning of the microscope for each objective. The obtained values are summarized in Table 5.5 for the 3 phase approach microscope version and in Table 5.6 for the Hilo version.

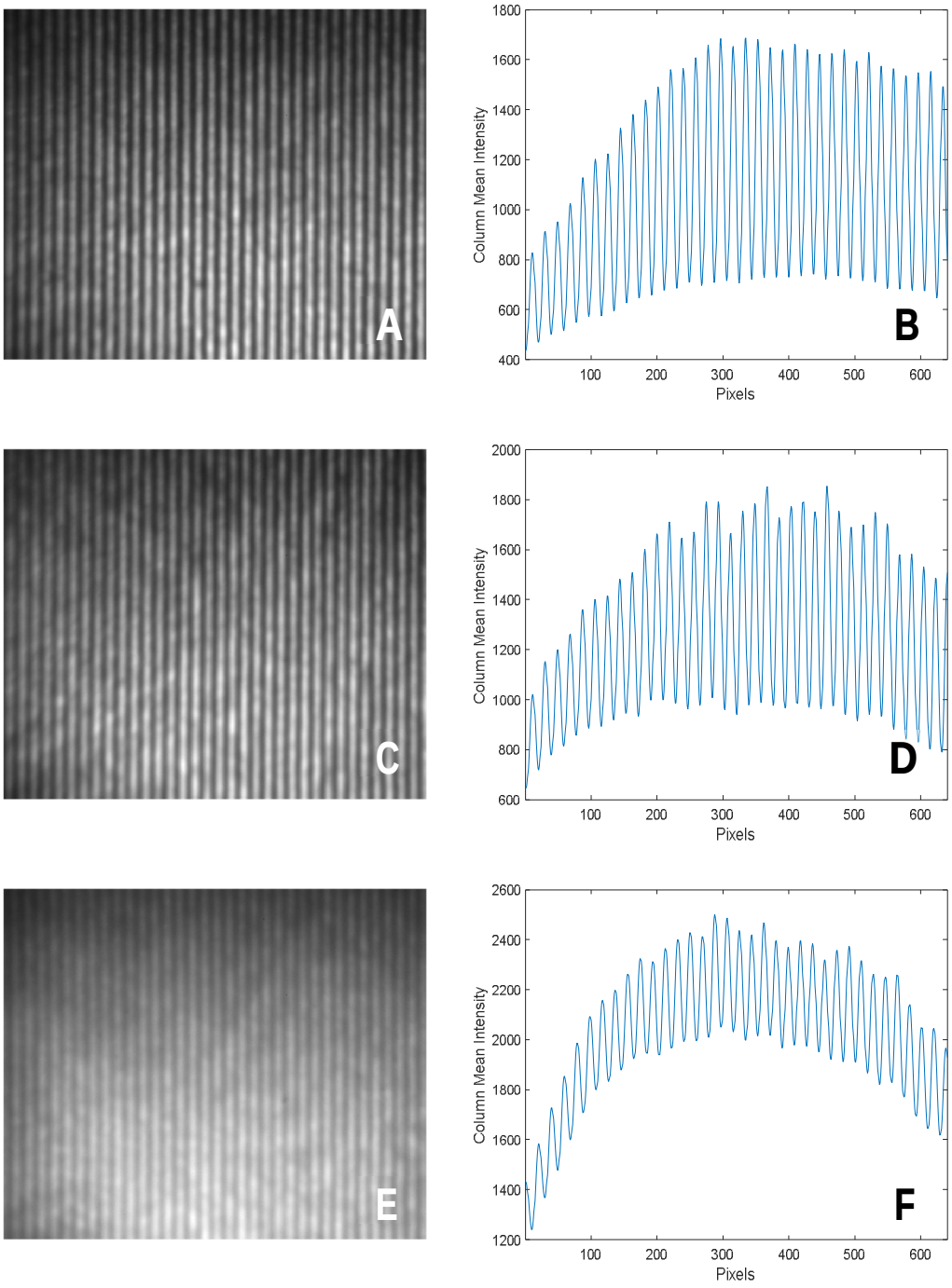

Figure 5.4 – Structured illumination images (A,C,E) and corresponding plot of the mean of the columns acquired with 3 different objectives (B, D, F); A, B – Olympus 20x; C, D – Zeiss 40x, E, F – Olympus 60x. These images were acquired with the HiLo version of the microscope.

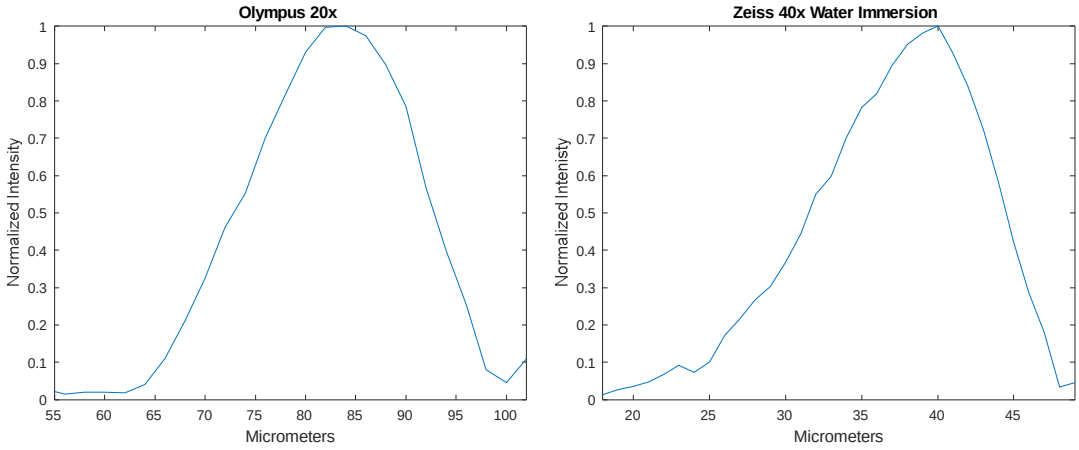

Figure 5.5 - Experimental optical sectioning curves obtained with Olympus 20x and Zeiss 40x objectives for the 3-phase approach version of the microscope-

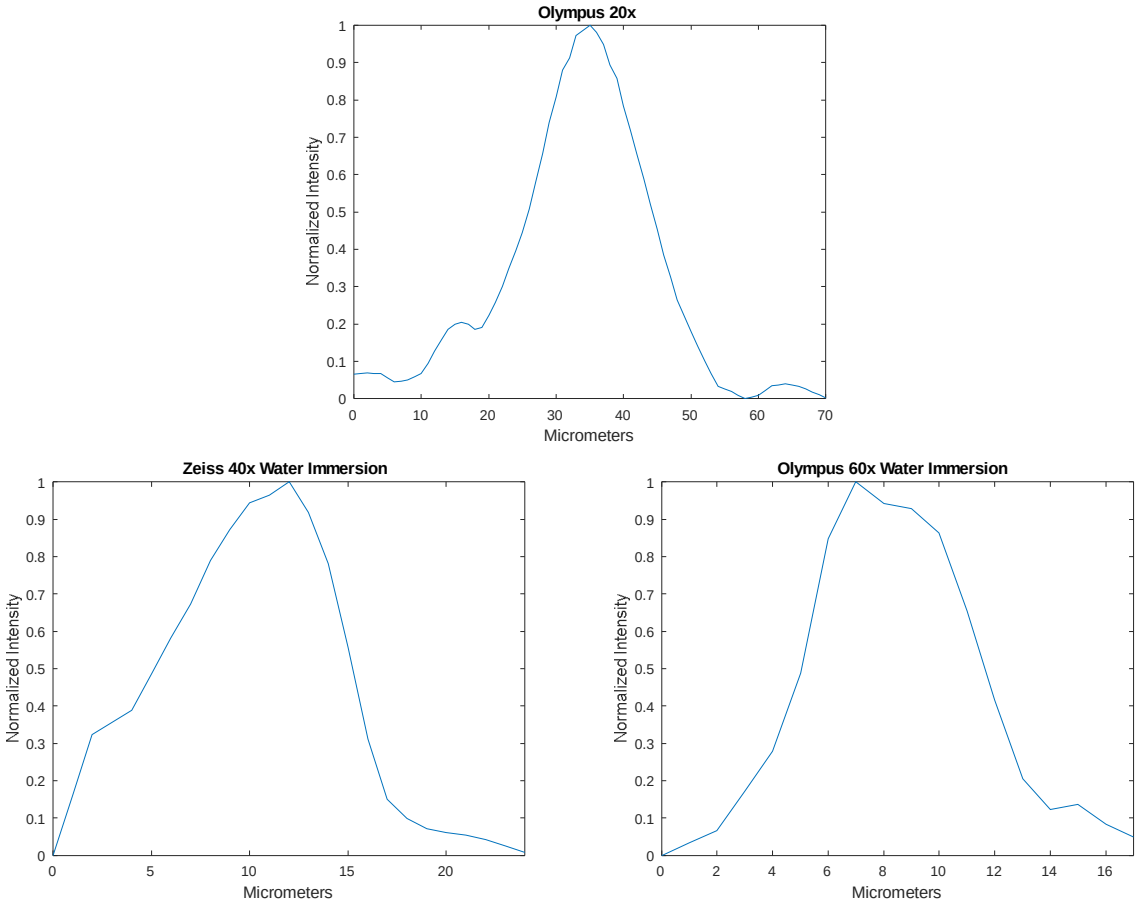

Figure 5.6 – Experimental optical sectioning curves obtained with the 3 different objectives tested for HiLo version of the microscope.

Table 5.5 - Theoretical and experimental values of optical sectioning per used microscope objective with 3 phase approach microscope version.

MICROSCOPE OBJECTIVE	THEORETICAL OPTICAL SECTIONING	EXPERIMENTAL OPTICAL SECTIONING	ABSOLUTE ERROR	ERROR
Olympus 20x	11.7 µm	18.78 ± 0.020 µm	7.08 µm	60.4 %
Zeiss 40x W	4.32 µm	6.91 ± 0.45 µm	2.59 µm	59,95% %

Table 5.6 – Theoretical and experimental values of optical sectioning per microscope objective used with HiLo microscope version.

MICROSCOPE OBJECTIVE	THEORETICAL OPTICAL SECTIONING	EXPERIMENTAL OPTICAL SECTIONING	ABSOLUTE ERROR	ERROR
Olympus 20x	16.46 µm	18.433 ± 0.014 µm	1.973 µm	11.99 %
Zeiss 40x W	5.56 µm	10.022 ± 0.006 µm	4.462 µm	80.26 %
Olympus 60x W	2.5 µm	6.621 ± 0.142 µm	4.121 µm	164.87 %

Deviations are easily observed when comparing the theoretical and the experimental values of optical sectioning. Experimental optical sectioning is higher than the predicted theoretical value, particularly in the water immersion objectives with higher numerical aperture. Different factors can contribute to explain these results: in Equations (5.5) to (5.7) it is assumed that the fluorescence emission wavelength is equal to the excitation wavelength; these same equations do not take into account the presence of the coverslip on the top of the thin layer of the fluorescence ink; and the mechanical resolution of the manual micrometer is too large to accurately measure such low vales of optical sectioning.

From this point on, only the HiLo version of the microscope was used, since, as previously mentioned, fewer images are required to obtain optical sectioning which will decrease the overall acquisition times and sample light exposures. Images of thick, well-known samples were acquired to verify the structured illumination capabilities of the microscope. Two capillaries (Ø = 100 µm) filled with fluorescence solutions and placed one above the other were imaged. With this, we were only able to verify if the out-of-focus contributions in the image were effectively suppressed by the algorithm as shown in Figure 5.7 andFigure 5.8. Plots of profile lines in both wide field and structured illuminated images allow to conclude that the difference between the maximum and

minimum values increases in the structured illuminated image. This confirms that the HiLo algorithm successfully suppresses the out-of-focus contributions.

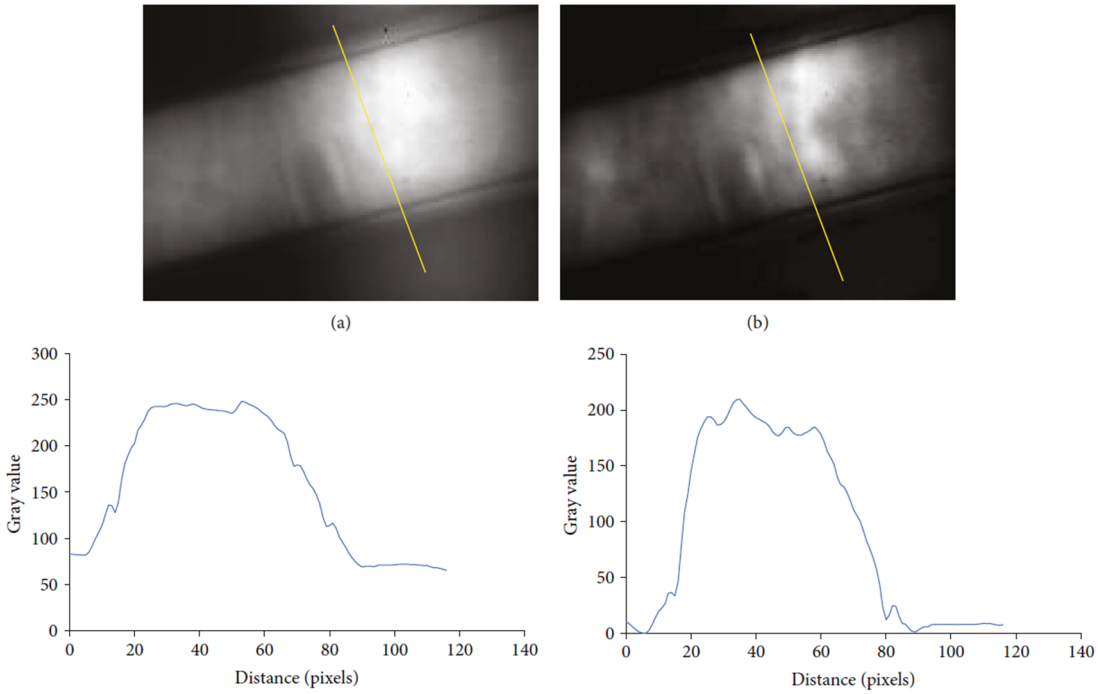

Figure 5.7 - Wide (left) and HiLo (right) fluorescence intensity images of two capillaries filled with Coumarin 153 placed one above the other. On the bottom there are two plots of line profiles to show that optical sectioning improves contrast and reduces out-of focus contributions.

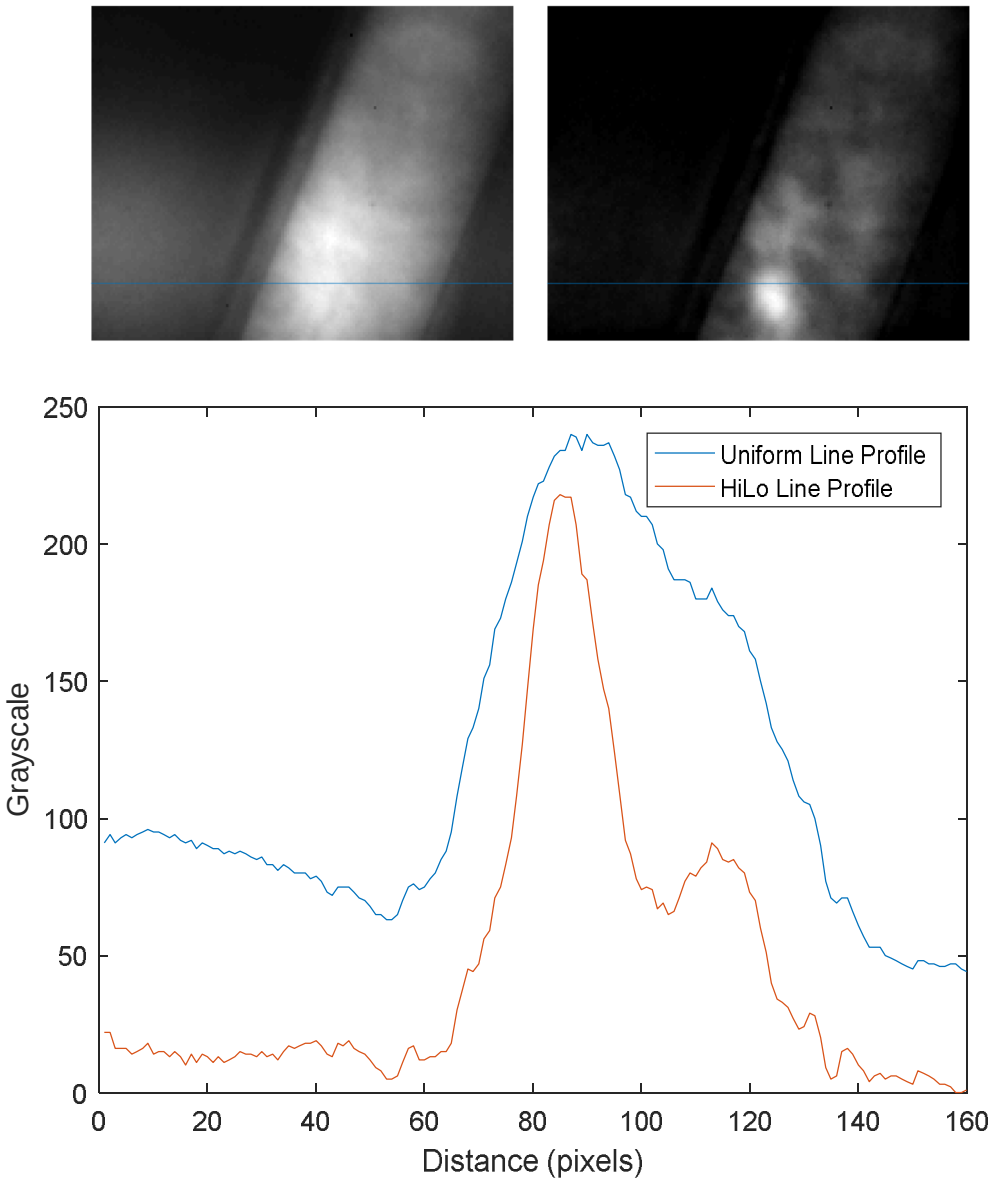

Figure 5.8 – Wide (left) and HiLo (right) fluorescence intensity images of two capillaries filled with Erythrosine B placed one above the other. On the bottom there is a plot of a line profile to show that optical sectioning improves contrast and reduces out-of focus contributions.

In what optical parameters performance are concerned, it can be concluded that the microscope fulfills the requirements defined in the beginning of this project, providing enough field of view, lateral resolution and optical sectioning for the application proposed.

B. Timing Performance

In a fluorescence lifetime microscope, timing characteristics are essential to evaluate the overall performance of the microscope. They limit the capacity to accurately and precisely measure the lifetimes of the molecules excited in a sample. As mentioned in Chapter 3 , the IRF gives the timing characteristics of a time-domain fluorescence lifetime microscope. So, we started by acquiring and evaluating this curve.

The IRF can be acquired both in reflectance and fluorescence mode. However, in this latter mode, it is necessary to use a molecule having a mono-exponential decay with a very-short known fluorescence lifetime. We chose to measure the IRF in the reflectance mode. In a Time-Gated microscope, the scattered light IRF is theoretically described by the convolution of the chosen gate pulse with the intensity pulse of the light source, in our case the picosecond laser. To measure the IRF, a scattering target was placed as sample and neutral density filters were used in the excitation path to avoid CCD saturation. Then, we acquired a timing scan profile for each nominal COMB gate width. The expected FWHM of each of this curve should be close to the nominal value of the COMB mode chosen, since the nominal gate width is always larger than the FWHM of the laser pulse - Figure 5.9.

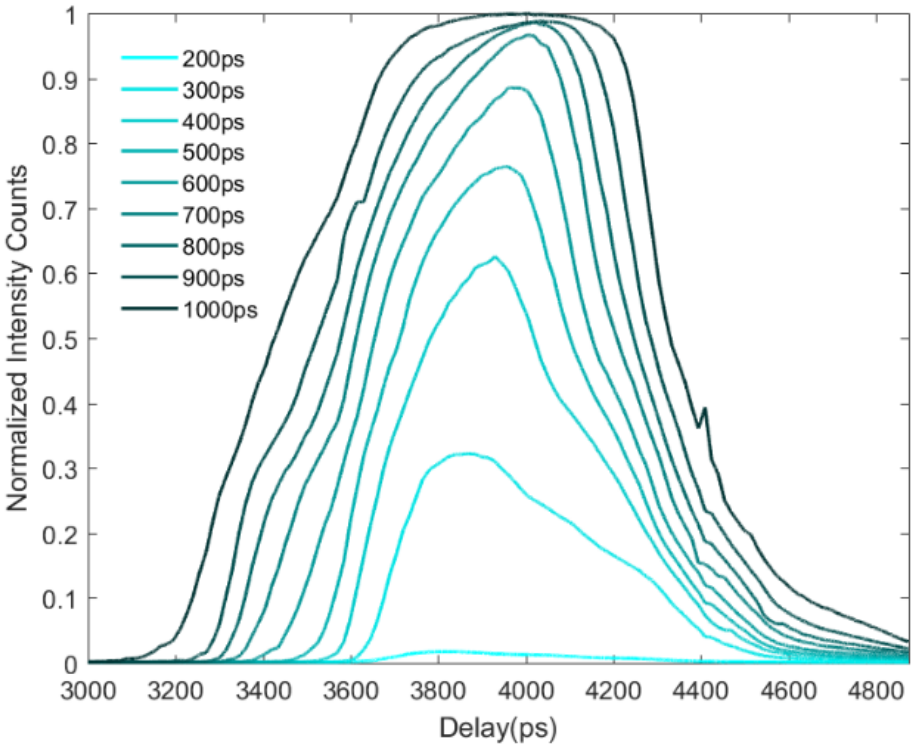

Figure 5.9 – IRF curves obtained in reflectance mode for each COMB mode available in the Time-Gated detection system with laser power set to 12.53 mW.

Having the measured IRF, we could test the timing features of the microscope when measuring fluorescence lifetimes. For that, we chose two different fluorescent dyes with known fluorescence lifetime decay kinetics which, when used with pure solvents, are described by mono-exponential decay curves. Erythrosine B and Coumarin 153, whose fluorescence lifetimes are in the same order of magnitude as FAD fluorescence lifetime components in biological tissues. They were both prepared in a methanol solution and measured in the Time-Gated and TCSPC microscopes. TCSPC was only used as reference to verify the accuracy of the Time-Gated measurement. The lifetime analysis of the data acquired with the Time-Gated microscope was performed with FLIMfit (Warren *et al.*, 2013).

As mentioned, the reference data was obtained by measuring the same solutions on the TCSPC microscope. The acquired signal was then processed with a custom add-on module for Microsoft Excel 97, developed in our research group, which analyses fluorescence lifetime data through a non-linear least-squares fitting procedure. The curves obtained for Erythrosine B and Coumarin 153 in MeOH solutions are depicted in Figure 5.10 and in Figure 5.11, respectively. The measured reference lifetime values and the goodness of both fitting procedures are summarized in Table 5.7.

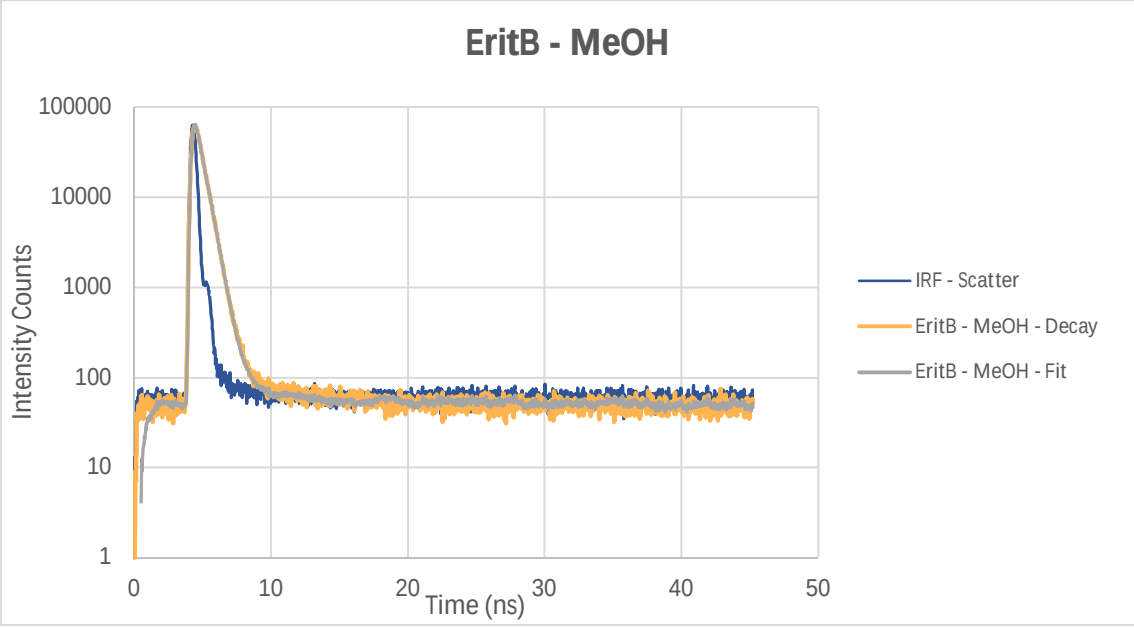

Figure 5.10 - Fluorescence decay curve analysis of an Erythrosine B in MeOH solution acquired with a TCSPC microscope.

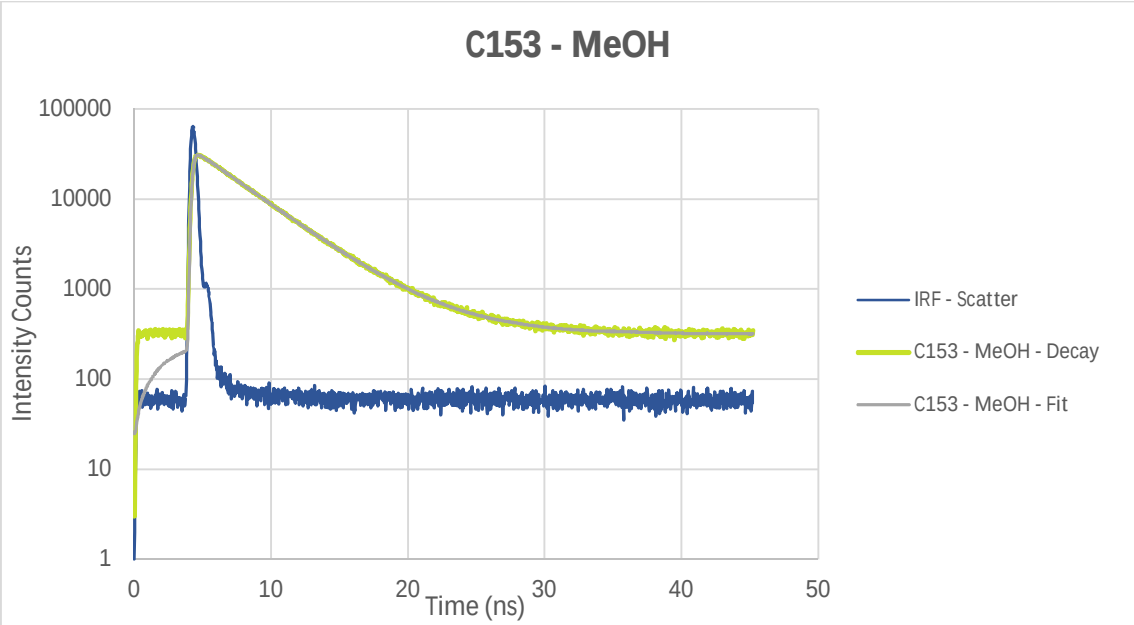

Figure 5.11 – Fluorescence decay curve analysis of a Coumarin 153 in MeOH solution. Acquired with a TCSPC microscope.

The issue of photon efficiency was always a concern during the development of the project. We wanted to maximize the number of photons that reached the CCD without having to rely too much on MCP gain. For that, we only imaged these solutions using the nominal gate of 1000 ps since it maximized the number of photons that reached the CCD.

Table 5.7 - Lifetime results and goodness of fit obtained with TCSPC and Time-Gated.

	Fluorophore (in MeOH)	Lifetime (ns)	Reduced Chi-Sqr
TCSPC	Erythrosine B	0.4906	1.4130
	Coumarin 153	3.9597	1.0568
Time-Gated	Erythrosine B	0.4947	2.1111
	Coumarin 153	3.8688	0.9263

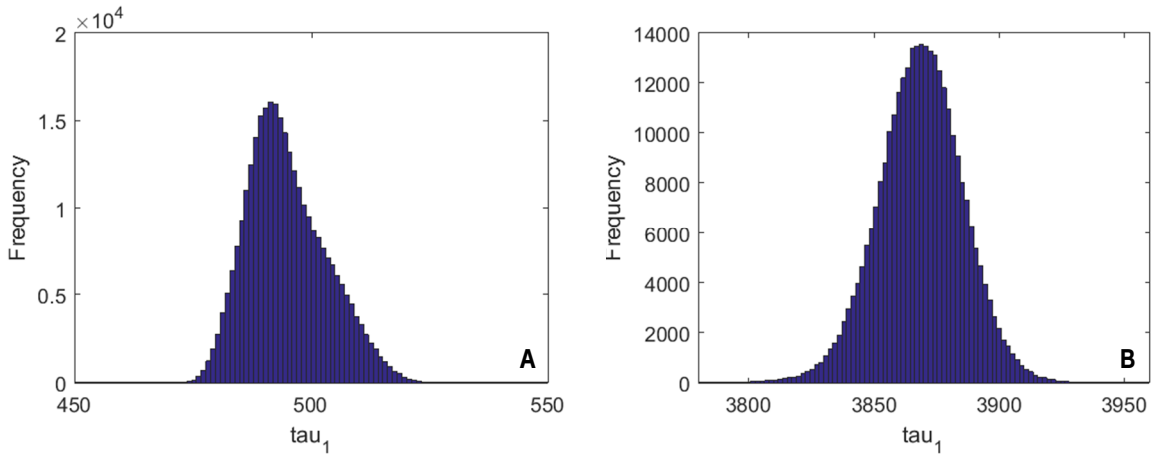

Figure 5.12 – Fluorescence lifetime histograms of A) Erythrosine B in MeOH and B) Coumarin in MeOH solutions.

When comparing the lifetime results between the Time-Gated and the TCSPC microscopes, we can conclude that the Time-Gated microscope measures accurately fluorescence lifetimes within the tested range of values. However, when analyzing the reduced chi-square value, which serves as a reference for the goodness of fit and should be between 0.8 and 1.3 (Morgado, 2003), it is easy to conclude that for the Time-Gated microscope, the quality of measurement for short decay lifetimes is deteriorated, suggesting a lower precision than when using TCSPC. This is an expected result, justified by the noise introduced by the image intensifier. Furthermore, the wavelength of the used laser is not optimized for the excitation and emission spectra of Erythrosine B in MeOH. This, combined with a lower quantum yield, reduces the fluorescence probability and, as consequence, requires longer exposure times and higher CCD gains. These factors can also affect the goodness of fit and contribute to the increased Chi-square value.

Again, capillaries with 100 µm of diameter were filled with the same fluorescent dyes solutions and tested under the microscope. These experiments were done to verify the influence of the structured illumination methods on the accuracy and precision of the lifetime measurement while, at the same time, demonstrating the importance of a sectioning technique on the image quality of fluorescence lifetime maps.

First, the capillaries were filled with Coumarin 153 solution. Two were placed one above the other and the corresponding uniform and modulated images were acquired. The HiLo image was processed using an algorithm written in Matlab®. Since this is a fluorescence decay, a stack of both uniform and modulated images was acquired, resulting in a stack of HiLo images. After the HiLo processing, both uniform and HiLo stacks were analyzed using FLIMfit v 5.0.3 software. The fluorescence maps obtained with the Coumarin 153 in MeOH capillaries are depicted in Figure 5.13.

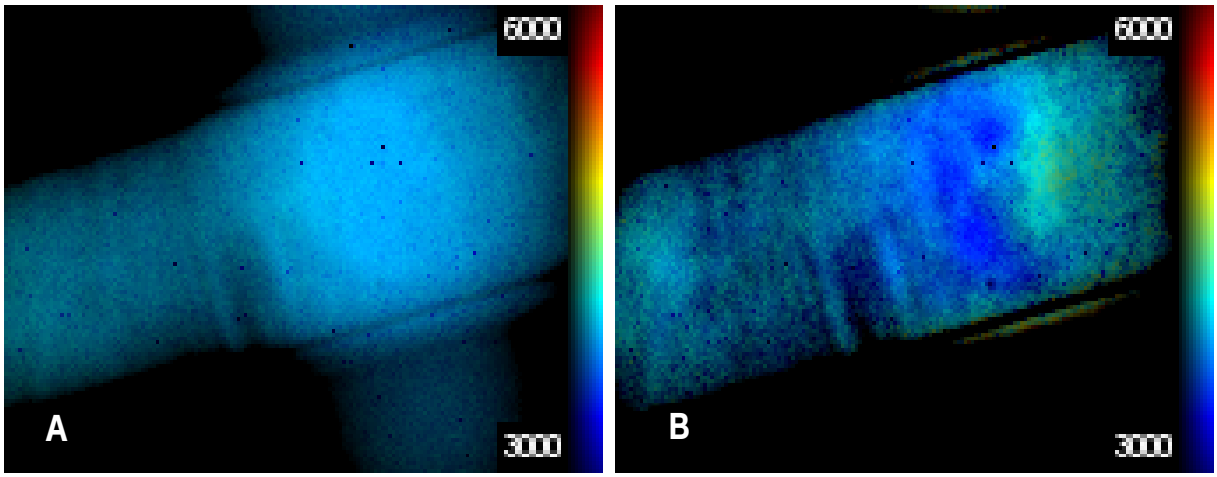

Figure 5.13 - Epi-fluorescence (A) and HiLo (B) fluorescence lifetime maps of a stack of two capillaries filled with Coumarin 153 in MeOH solution and placed one above the other.

By analyzing the fluorescence maps depicted in Figure 5.13, it can be concluded that the lack of optical sectioning affects the quality of the lifetime map, being even more difficult to distinguish between structures in-focus and out-of-focus.

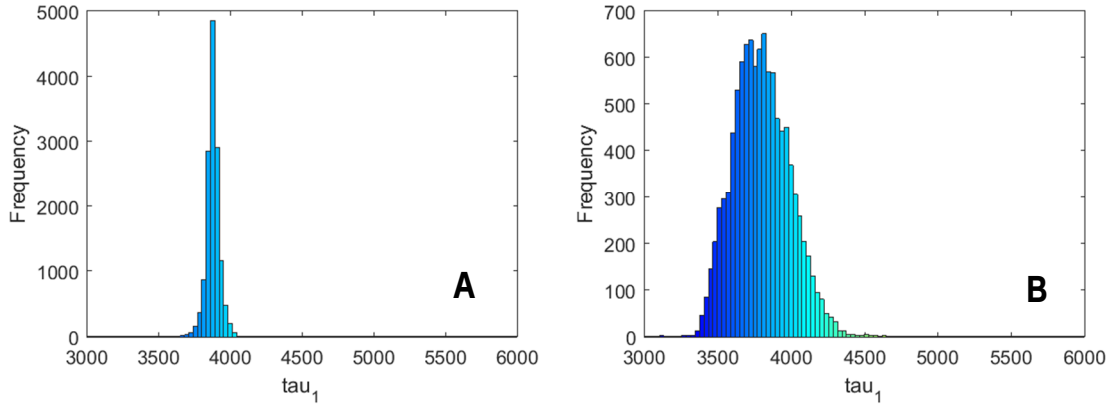

Figure 5.14 -Fluorescence lifetime histograms of epi-florescence (A) and HiLo stacks of two capillaries filled with Coumarin 153 in MeOH solution and placed one above the other.

However, when comparing the lifetime histograms obtained from both maps, it can be concluded that the HiLo processing affects the precision of the lifetime map. The histogram is enlarged. This is proved by the mean and standard deviation measured on the same maps (Table 5.8). While in the epi-fluorescence image, the standard deviation is around 1% of the measured mean value, in the HiLo image, it increases to a value around 5% of the mean value. On the other hand, the mean values measured are comparable, indicating that accuracy is not highly affected by the HiLo processing algorithm. From the reduced chi-square value (higher in the HiLo case), it can also be concluded that the fitting procedure in the HiLo stack is more challenging and the precision of the fitted lifetime is degraded.

Table 5.8 – Lifetime results obtained from the lifetime maps depicted in Figure 5.13.

	MEAN IMAGE LIFETIME (NS)	REDUCED CHI-SQR
Uniform Image	3.8799 +/- 0.0417	1.1147
HiLo Image	3.8541 +/- 0.1522	4.1422

The same experience was repeated, for two capillaries filled with Erythrosine B in MeOH solution. The processed fluorescence lifetime maps are depicted in Figure 5.15.

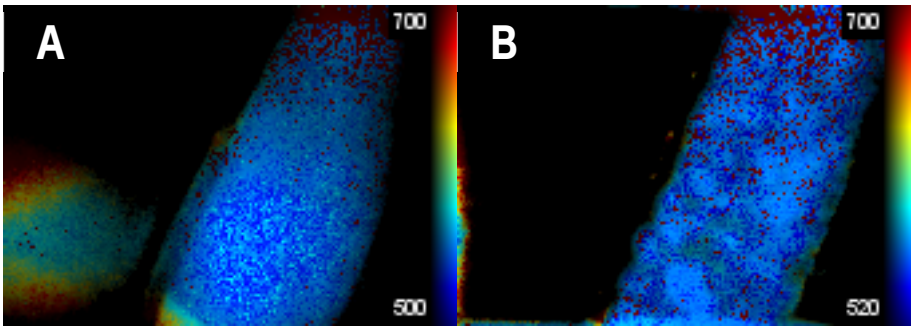

Figure 5.15 - Epi-fluorescence (A) and HiLo (B) fluorescence lifetime maps of a stack of two capillaries filled with Erythrosine B in MeOH solution and placed one above the other.

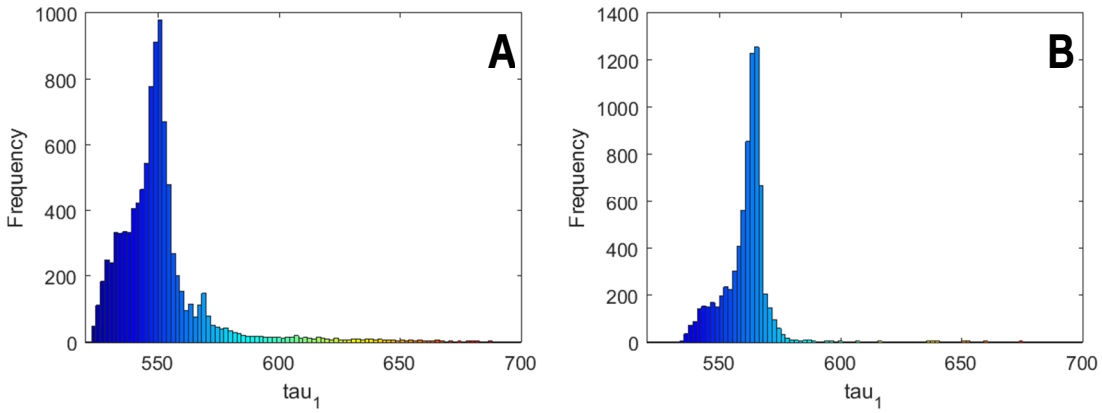

Figure 5.16 - Fluorescence lifetime histograms of epi-florescence (A) and HiLo stacks of two capillaries filled with Erythrosine B in MeOH solution and placed one above the other.

Table 5.9 - – Lifetime results correspondent to the lifetime maps depicted in Figure 5.15.

	MEAN IMAGE LIFETIME (NS)	REDUCED CHI-SQR
Uniform Image	0.6238 +/- 0.2394	29.4710
HiLo Image	0.6760 +/- 0.3317	43.1956

Again, and similarly to what happens with Coumarin 153 in MeOH capillaries, both precision and accuracy are degraded when HiLo optical sectioning is applied to the images. This can happen due to the noisier images obtained with HiLo optical sectioning. So, we need to be careful when using this technique and ensure a high SNR to minimize the effects of the optical sectioning technique in both accuracy and precision.

An analysis of the relation of optical sectioning and fluorescence intensity was performed for better understanding why HiLo processing degrades the fluorescence lifetime maps. Four different images corresponding to different delays (gates) (Figure 5.17 andFigure 5.19) were chosen and intensity profiles along the capillaries were plotted to verify the influence of the signal to noise ratio (SNR) of the fluorescence intensity images on the optical sectioning power .

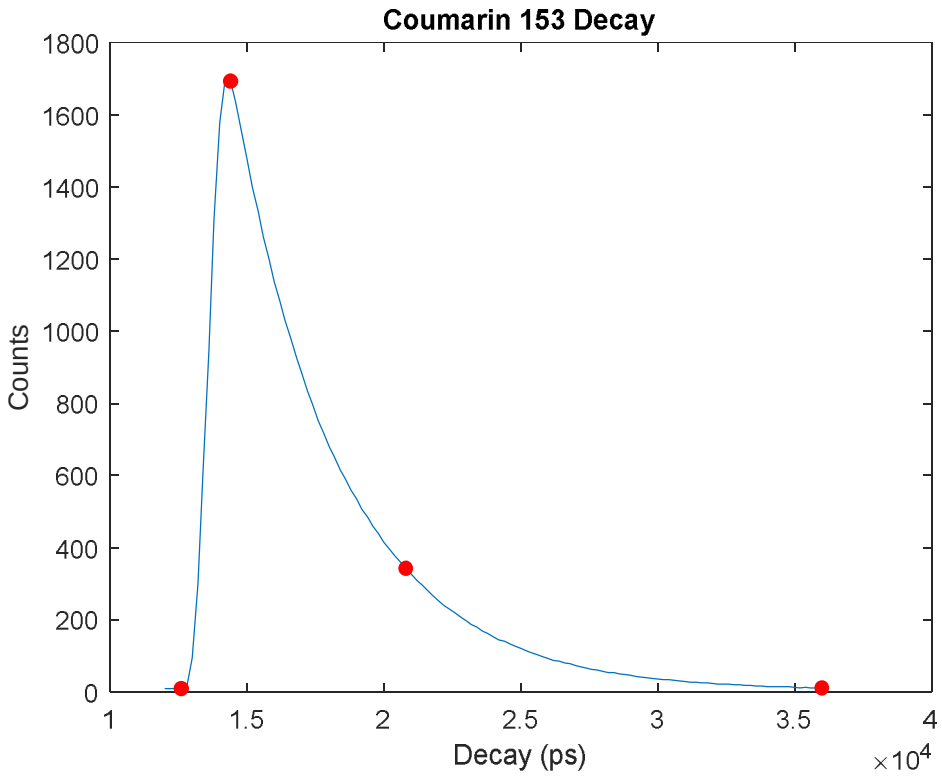

Figure 5.17 – Mean fluorescence decay curve of the stack of images acquired with two capillaries filled with Coumarin 153 in MeOH. The red dots represent the delays used for acquiring the images depicted in Figure 5.18.

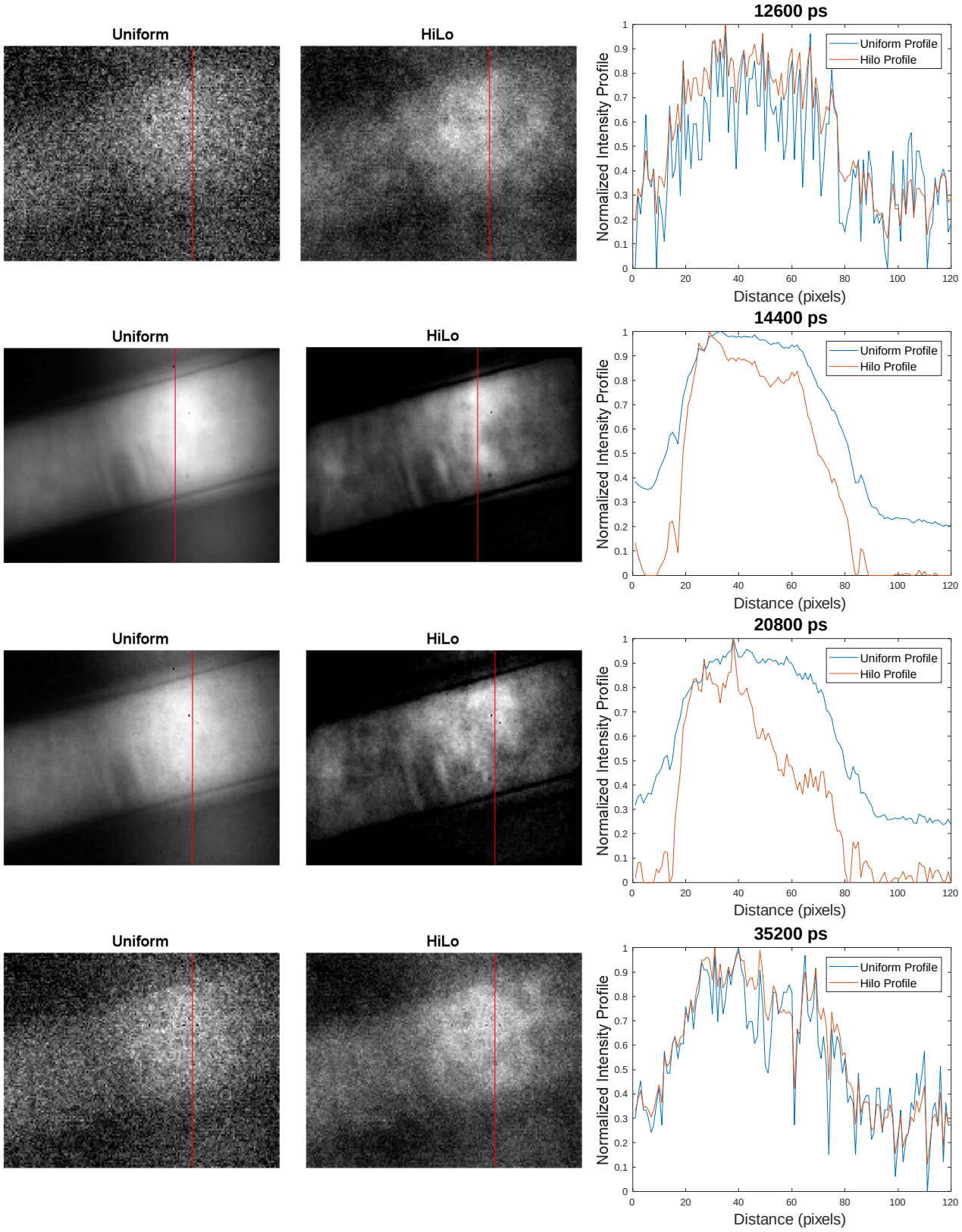

Figure 5.18 - Epi-fluorescence (uniform) and HiLo images of a stack of two capillaries filled with Coumarin 153 in MeOH solutions acquired at different delays and respective section intensity profiles. The delays represented are located at the red spots on the plot depicted in Figure 5.17.

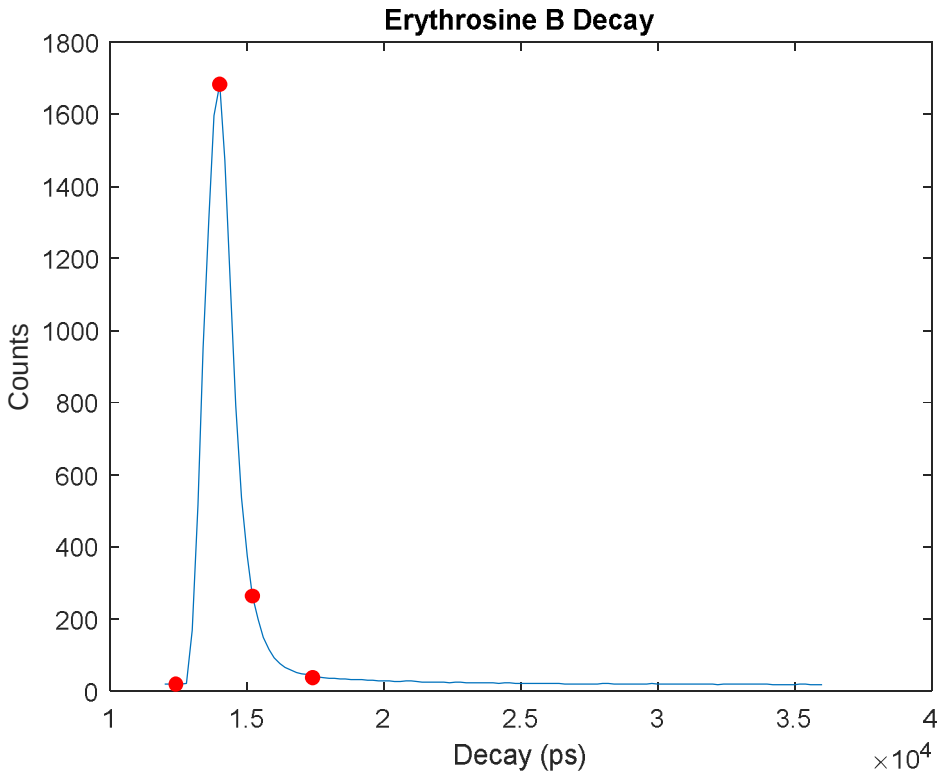

Figure 5.19 - Mean fluorescence decay curve of the stack of images acquired with two capillaries filled with Coumarin 153 in MeOH. The red dots represent the delays used for acquiring the images depicted in Figure 5.20.

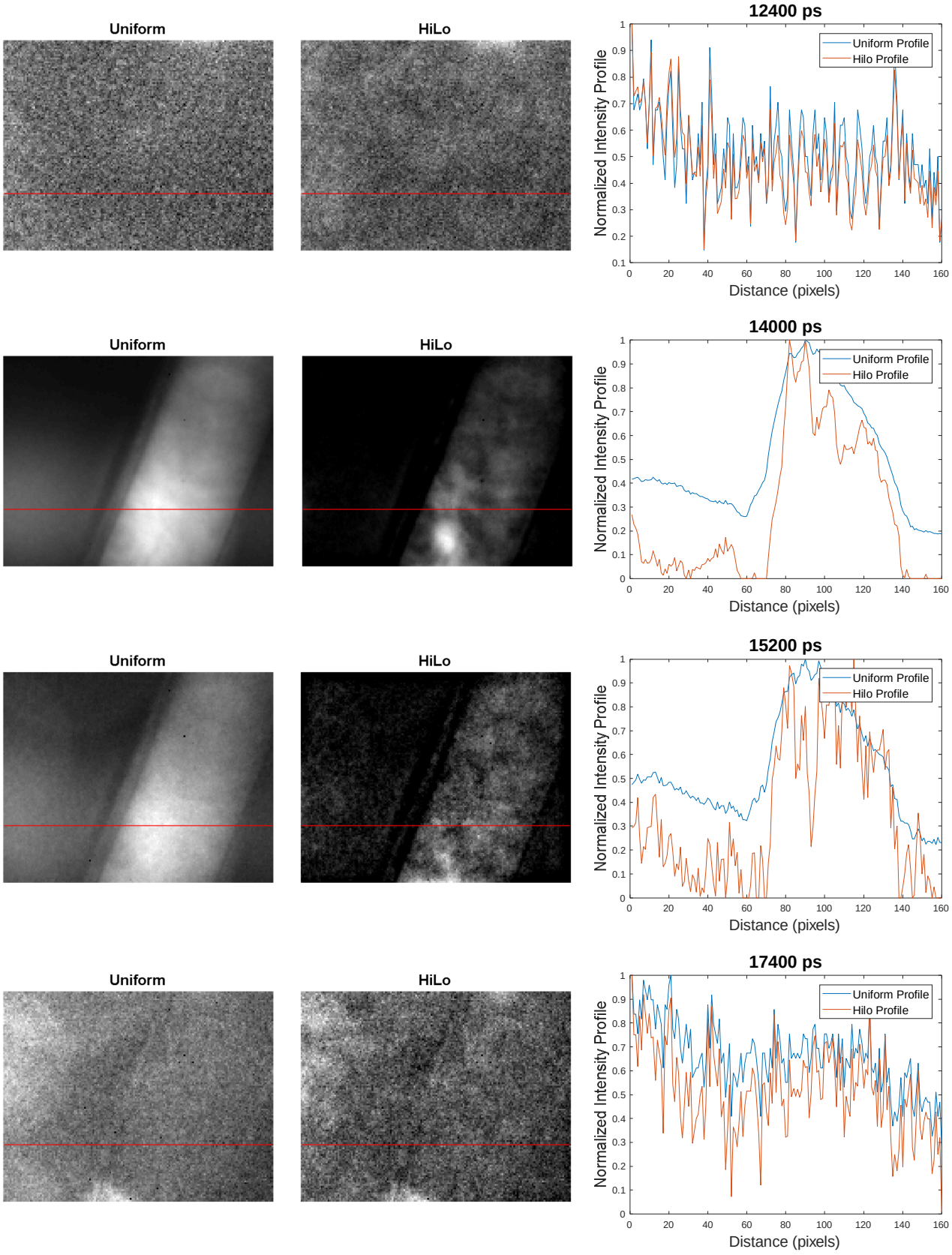

Figure 5.20 – Epi-fluorescence (uniform) and HiLo images of a stack of two capillaries filled with Erythrosine B in MeOH solutions acquired at different delays and respective section intensity profiles. The delays represented are located at the red spots on the plot depicted in Figure 5.19.

When analyzing the fluorescence intensity images taken at different delays for the examples of Erythrosine B and Coumarin 153, it is easy to conclude that HiLo optical sectioning capabilities are highly affected by the signal to noise ratio of the image. The contrast of the sinusoidal pattern in images where the number of counts is almost at the same level as noise is very low, which reduces the optical sectioning capabilities of the algorithm. Because of that, contributions from out-of-focus light are not eliminated and HiLo images are noisier than their corresponding uniform image. This fact contributes to the lower precision of the fluorescence lifetime measurement from the HiLo image which translates into the higher value of chi-square of the corresponding fitting procedures.

The influence of HiLo processing in the presence of two very distinct fluorescence lifetimes was also tested. For that, we used two capillaries of 100 µm: one filled with Erythrosine B and the other with Coumarin 153 (both fluorophore solutions in MeOH). First, they were placed side by side and a set of images was acquired.

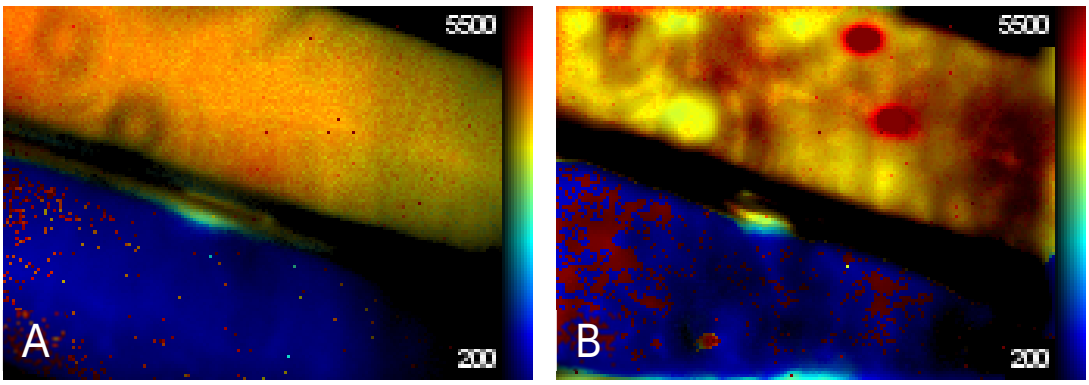

Figure 5.21 – Lifetime maps of the images acquired with two capillaries filled with different solutions and placed side by side in A) widefield and B) HiLo modes.

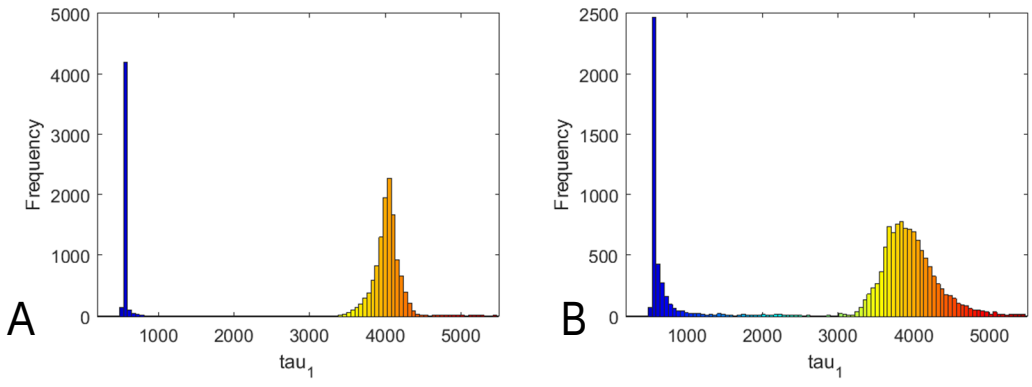

Figure 5.22 – Lifetime histograms correspondent to the lifetime maps depicted in Figure 5.21.

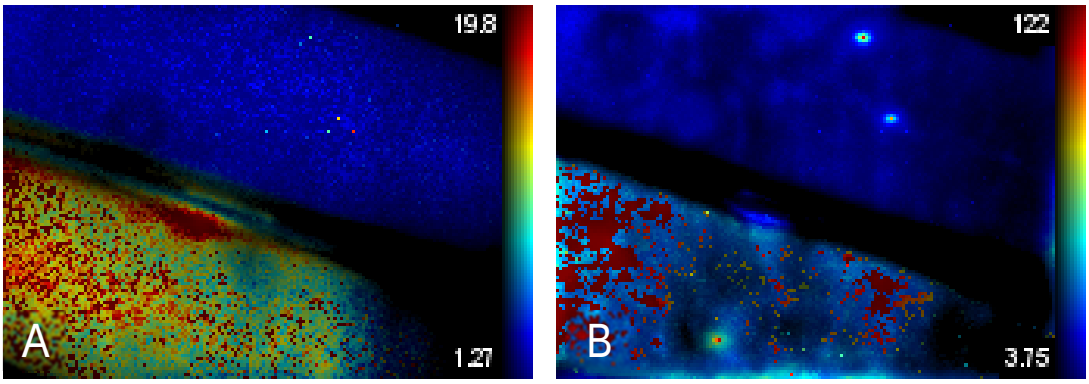

Figure 5.23 – Chi-Sqr maps of the fittings that originated the lifetime maps ad histograms depicted in Figure 5.21 and Figure 5.22.

As with the images of capillaries with isolated solutions, the histogram of lifetimes (Figure 5.22) is enlarged in the HiLo images, confirming that the HiLo processing affects the precision of the lifetime estimation. Figure 5.23 also confirms that the quality of fit is degraded by the HiLo algorithm. From it, it is possible to see that the chi-square values are quite enlarged.

The same two capillaries were then placed one above the other and another stack of images was acquired. The microscope was focused on the top capillary, which was the one filled with Erythrosine B in MeOH solution. Considering that two fluorophores with distinct lifetimes would occupy the same pixel space at different optical sections, we used a two-exponential fitting procedure

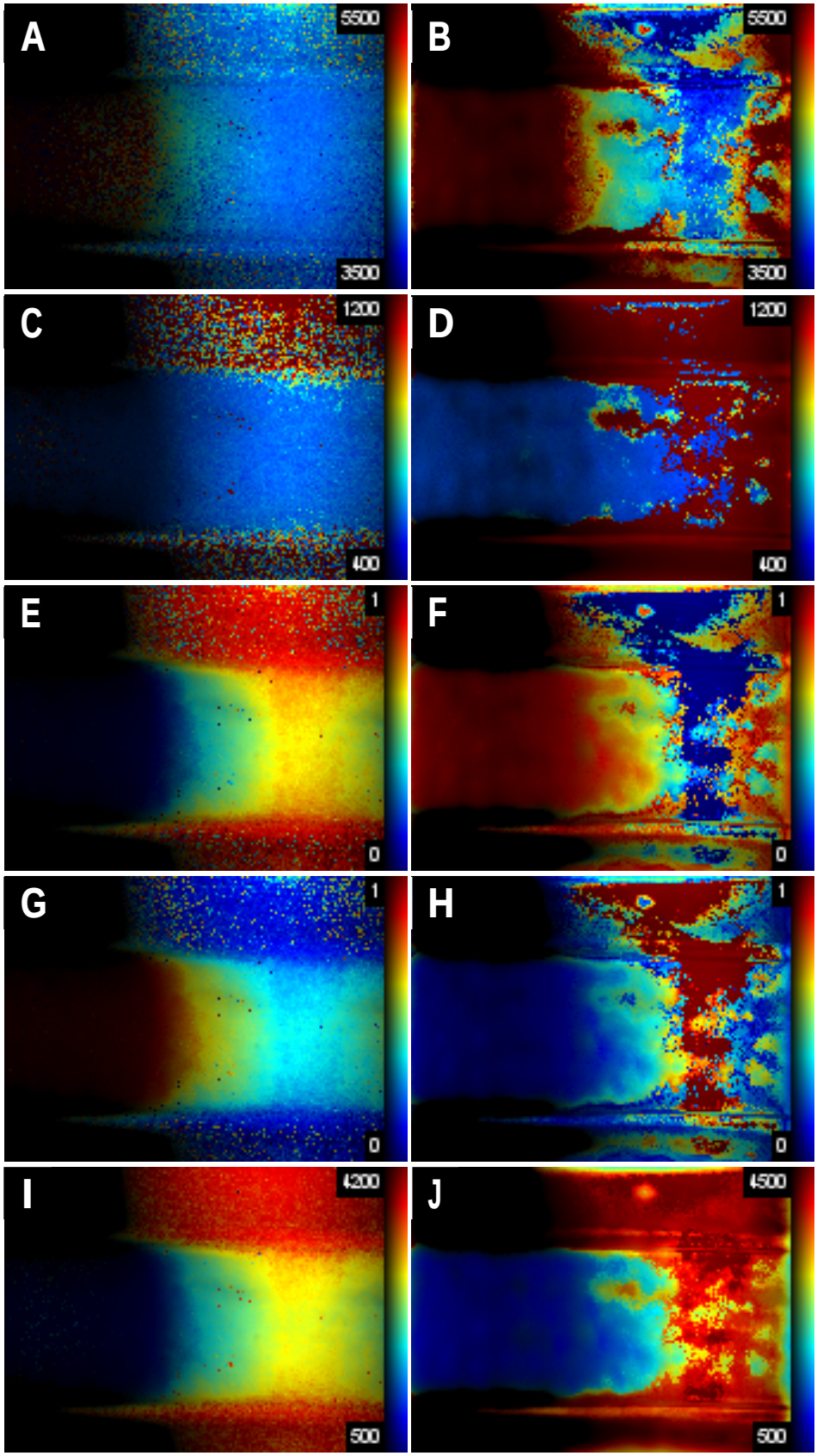

Figure 5.24 – Results from the double-exponential fitting on the stack of images acquired with the two capillaries filled with distinct solutions placed one above the other. A, B – τ_1 map from wide and HiLo images, respectively; C, D – $\tau_2$map from wide and HiLo images, respectively; E, F – α_1 map from wide and HiLo images respectively; G, H – α_2 map from wide and HiLo images respectively; I,J – mean lifetime maps from wide and HiLo images, respectively.

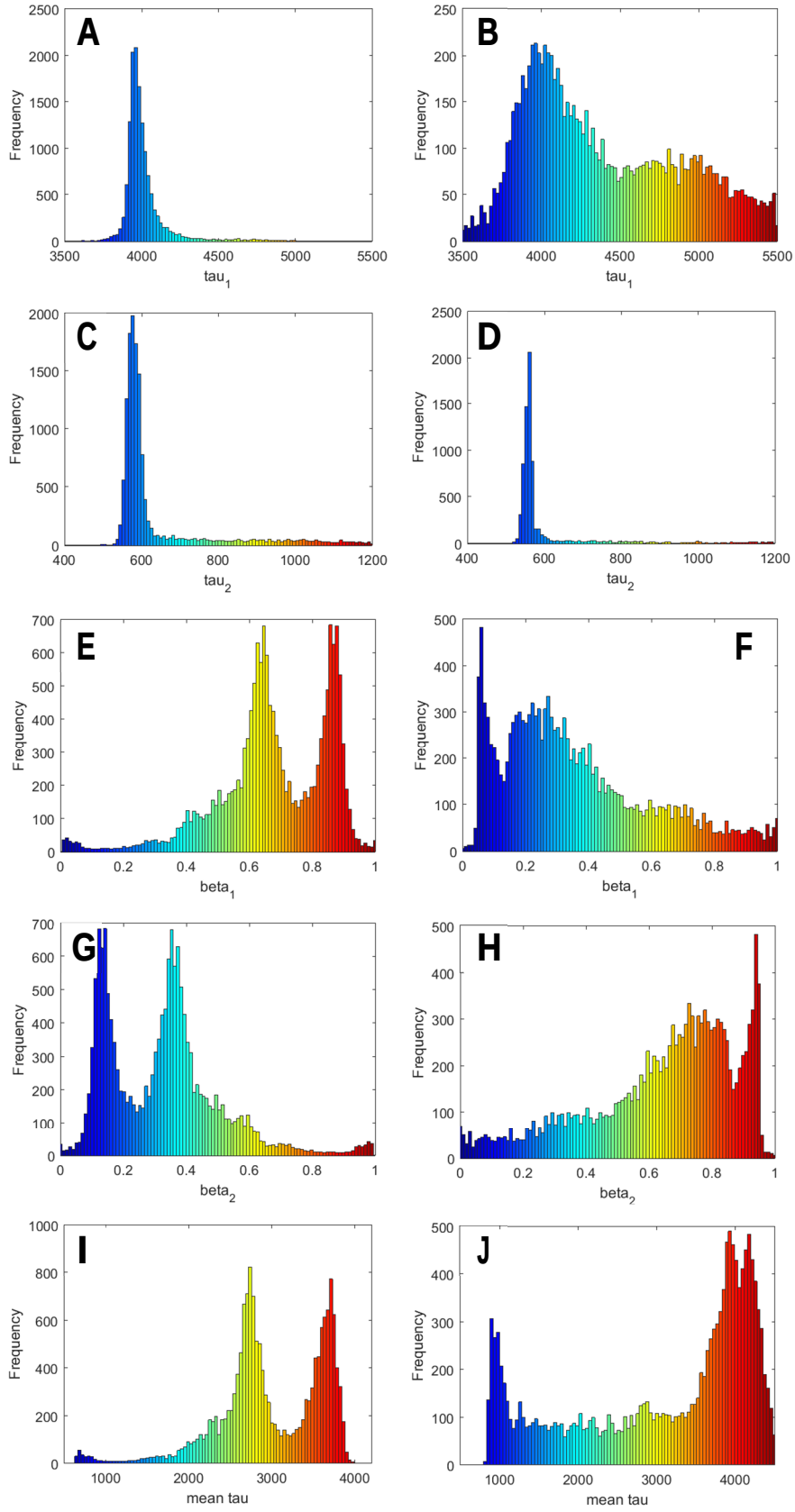

Figure 5.25 – Histograms from the maps depicted in Figure 5.24. A, B – τ_1 histogram from wide and HiLo images, respectively; C, D – τ_2 histogram from wide and HiLo images, respectively; E, F – α_1 histogram from wide and HiLo images respectively; G, H – α_2 histogram from wide and HiLo images respectively; I,J – mean lifetime histograms from wide and HiLo images, respectively.

By analyzing the maps on Figure 5.24 and the histograms present in Figure 5.25, we can conclude that HiLo optical sectioning affects the results of the two-exponential fitting. To begin with, the capillary filled with erythrosine is placed on the horizontal. In the widefield image, due to the lower fluorescence from this fluorophore, when compared to the fluorescence intensity from the out-of-focus contribution of the capillary filled with Coumarin 153, the left part of the focused capillary is barely seen. This situation changes when the HiLo images are considered. In this case, the left parts of the images have more contrast indicating that the HiLo sectioning helps in eliminating background from out-of-focus and in increasing the contrast of the object in focus. However, it is also easy to conclude that the algorithm fails to eliminate the fluorescence coming from the out-of-focus capillary. It was expected that only the lifetimes corresponding to the Erythrosine B would appear in the HiLo sectioning. Although the weight of the lifetimes from Coumarin 153 fluorescence emission is reduced in the HiLo images, as can be seen by the analysis of the α_1 lifetime map and histogram, in the mean lifetime map they still appear, increasing the mean lifetime of the in-focus capillary and being present where no contribution should occur (behind the focused capillary). Moreover, the quality of the fit is decreased in some portions of the image, as can be seen by the chi-square maps depicted in Figure 5.26

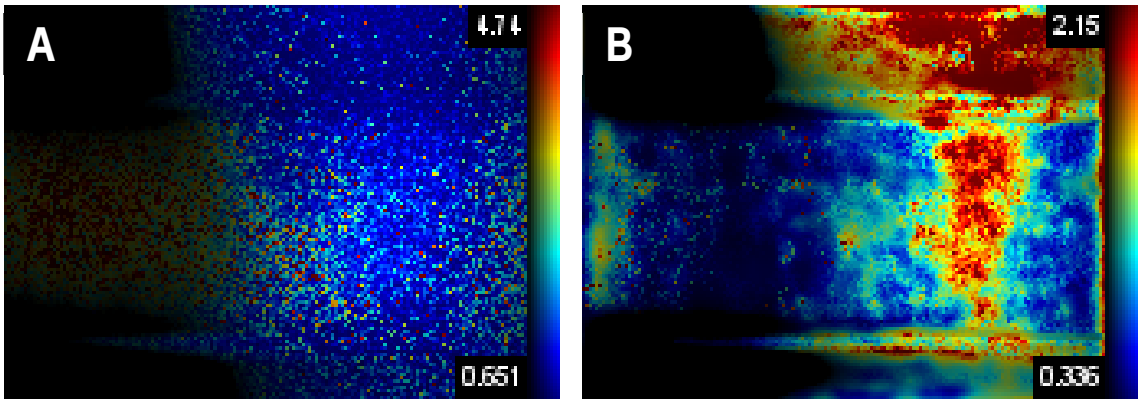

Figure 5.26 – Chi-sqr maps of the wide (A) and HiLo (B) double exponential fittings that give rise to the images and histograms depicted in Figure 5.24 and I Figure 5.25.

To conclude, HiLo optical sectioning is not perfect when applied with lifetime fitting since the precision of the results and the quality of the fitting are slightly degraded. However, it seems to be a good solution to remove the out-of-focus contributions, at least when they have lower fluorescence intensity than the components in focus.

Chapter 6 Accuracy and Precision in RLD Algorithms

A. Introduction

As already mentioned, one of the goals of this work was to evaluate the accuracy and precision of the Rapid Lifetime Determination (RLD) algorithms in determining fluorescence decay parameters and metabolic ratios, i.e ratios to build metabolic images. RLD is a quite attractive way of processing fluorescence lifetime data. It uses a small set of images (data) and has low computational complexity. In applications where fast data acquisition is mandatory, like those concerning biological samples affected by photobleaching or *in vivo* clinical measurements, RLD is the algorithm of choice since it only requires the acquisition of two or four images, when dealing with single or double exponential decays respectively. It is also important to mention that RLD algorithms are the perfect match for Time-Gated acquisition systems, due to its relationship with the gate width chosen to acquire the data, as already mentioned in Chapter 3 .

It is of particular interest the evaluation of RLD accuracy and precision in conditions of low number of counts (less than 10^4 total photon counts). In metabolic imaging, the fast acquisition requirement excludes frame summing. Therefore, the dynamic range of the gated intensified CCD camera, which depends on the full well capacity of the CCD camera and on the intensifier gain, limits the number of detected photons. As we are dealing with exponential fluorescence decays only the first image of the acquired set of two or four images can use the full dynamic range of the instrument.

We are also interested in accounting for the effect of the pulsed width of the laser source. This is required when using picosecond pulsed lasers as excitation source, as happens in our instrument. Therefore, our evaluation should be based on the data representing the convolution of the real fluorescence decay profile with the instrument response function (IRF). This function was determined experimentally (see Chapter 3).

As we discussed on Chapter 1 , metabolic assessment through fluorescence lifetime techniques is based on free to protein-bound ratios of metabolic co-factors NADH and FAD. The ratios are given by the ratios of the pre-exponential factors of the double-exponential fluorescence decay. Qualitative metabolic assessment can also be based on the mean fluorescence lifetime, given by Equation (6.1).

$$\tau_m = \frac{\sum_{i=1}^{N} a_i \tau_i}{\sum_{i=1}^{N} a_i}. \quad (6.1)$$

Therefore, the evaluation of the RLD algorithm for metabolic imaging implies knowing the accuracy and precision in determining all the fluorescence decay parameters: the lifetimes and their relative contributions to the decay.

In TG-FLIM the selection of the gating parameters such as gate width (g) and time interval between consecutive gates (Δt) affect the signal-to-noise ratio (SNR) associated with each image and therefore, the accuracy and precision of decay parameters determination. There are several published studies on the evaluation of the precision of the RLD algorithm, with most of them focusing just on single-exponential decays. However, these studies seldom report on accuracy of RLD. Concerning single-exponential decays, Ballew and Demas (Ballew and Demas, 1989, 1991) used Monte Carlo simulations with Poisson noise to study the precision of the classical (contiguous gates) acquisition method and concluded that the method has an optimal precision region with at least 10^4 total photon counts, depending on the ratio values between gate width (g) and lifetime (τ). This region occurs for $\Delta t/\tau$ equal to 2.5 (Ballew and Demas, 1989). The results reported by these authors did not consider the presence of a baseline in the fluorescence decay curves. This was addressed in 1991 when the same group (Ballew and Demas, 1991) reported a different version of RLD. Instead of using just two gates, the decay is divided into three different areas: D_0, D_1 and D_2, described by Equations (6.2) to (6.4). The three unknown parameters (τ - lifetime, A – pre-exponential factor and B - baseline) can then be estimated by applying Equations (6.5) to (6.8).

$$D_0 = \sum_{j=1}^{N/3} d_j \quad (6.2)$$

$$D_1 = \sum_{j=\frac{N}{3}+1}^{2N/3} d_j \quad (6.3)$$

$$D_2 = \sum_{j=2N/3+1}^{N} d_j \quad (6.4)$$

$$Y = (D_1 - D_2)/(D_0 - D_1) \tag{6.5}$$

$$\tau = \frac{-\Delta t}{\ln Y} \tag{6.6}$$

$$A = \frac{(D_0 - D_1)\ln Y}{-\Delta t(1 - Y)^2} \tag{6.7}$$

$$B = \left[D_1 - \frac{D_1 - D_2}{1 - \exp(-\frac{\Delta t}{\tau})}\right] \times \frac{1}{\Delta t} \tag{6.8}$$

Again, by using Monte Carlo simulations and considering Poisson noise statistics, the authors found the regions where τ precision is maximized as a function of percentage of B. If B = 0, the optimal region occurs for the condition $\frac{\Delta t}{\tau} = 3$. With the increase of the baseline, a degradation of precision is verified, and the optimal region shifts to lower $\frac{\Delta t}{\tau}$ values. The number of photon counts is a sensitive parameter for τ determination with zero baseline, but this sensitivity decreases when larger values of baseline are considered.

A more generalized version of single-exponential RLD was reported by Chan et al in 2001 (Sing Po Chan *et al.*, 2001). Again, aiming to improve the precision of the method, these authors introduced the mathematical formalism of a more generalized version, still requiring just two gates, but without forcing equal gate widths (g). The first gate (D_0) starts at the beginning of the decay and lasts Δt and the second gate (D_1) starts at $Y\Delta t$ and lasts $Y\Delta t + P\Delta t$. The general expressions for these curve integrals are given by Equations (6.9) and (6.10), where Y and P are the adjustable coefficients for the integration intervals. If $Y = P = 1$, this generalized RLD method becomes the classical contiguous RLD. On the other hand, if $Y \neq P$ and $P = 1$, the method is transformed into the family of noncontiguous methods that include the overlapped case.

$$D_0 = \int_0^{\Delta t} A\, exp\left(\frac{-t}{\tau}\right) dt \tag{6.9}$$

$$D_1 = \int_{Y\Delta t}^{Y\Delta t + P\Delta t} A\, exp\left(\frac{-t}{\tau}\right) dt \tag{6.10}$$

Given these expressions, the ratio between the two images is given by Equation (6.11) with $R = \Delta t/\tau$.

$$\frac{D_1}{D_0} = \frac{\exp(-R(P+Y) - \exp(-YR)}{\exp(-R) - 1} \tag{6.11}$$

If $P \neq 1$, R cannot be isolated and τ cannot be obtained in closed form, but R and τ can be rapidly calculated by solving Equation (6.11) through an iterative Newton-Raphson method. Once more, the efficiency of this generalized RLD method was assessed through Monte Carlos simulations with the addition of Poisson noise, obtaining the best parameters of P and Y, $(P = 12, Y = 0.25)$. These values were compared with other versions of RLD: the classical contiguous approach $(P = 1, Y = 1)$ (P=1, Y=1), the 50% overlap $(P = 1, Y = 0.5)$, a nonadjacent and non-overlapping scheme with a long second interval $(P = 12, Y = 1.5)$, a 100% overlapping with a long second integration $(P = 12, Y = 0)$ and contiguous intervals with a long second integration period $(P = 12, Y = 1)$. They concluded that their optimized approach gave the best precision, even at small $\Delta t/\tau$ values and with almost no degradation in performance up to $\Delta t/\tau$ equal to 10. The optimized values of Y and P are translated into a gating overlap of 75% and D_1 having a width between $4\ \Delta t/\tau$ and $12\ \Delta t/\tau$.

In 2010, Chang and Mycek (Chang and Mycek, 2010) evaluated optimal gating schemes for single-exponential lifetime analysis with both Monte-Carlo simulations and analytical solutions. At the same time, they studied the effect of the combination of these optimal gating schemes with Total Variation denoising algorithms to improve the precision and acquisition speed in time-gated acquisition of biological samples. The authors considered just Poisson noise fixed by the lifetime determination to 4 gates (Equation (6.12) with N=4) and used as optimization parameter the Relative Standard Deviation (RSD), defined as the ratio between the standard deviation and the mean value of a given decay parameter (in the single-exponential decay case, the fluorescence lifetime). Despite obtaining different results between the two simulation methods, both converged to optimum values of gate width and gate spacing, which are, generally, $g \geq 3\tau$ and $\Delta t \approx 0.75\ \tau$.

$$\tau_p = \frac{N\left(\sum t_i^2\right) - \left(\sum t_i\right)^2}{N\sum t_t ln(I_{i,p}) - \left(\sum t_i\right)\left(\sum ln\left(I_{i,p}\right)\right)} \tag{6.12}$$

Sharman et al (Sharman *et al.*, 1999), were the first to report on double-exponential RLD. The authors presented analytical expressions for contiguous gating scheme ($g = \Delta t$) and 50%

overlapping gating condition ($g = 2\Delta t$), for the cases when the lifetimes are known and when all four decay parameters are unknown. They also used closed form solutions for overlap = 25 % and 75 %. It was found that the overlapping RLD has comparable or superior performance to the contiguous RLD methods, presenting larger regions of comparable RSD, meaning that the overlapping RLD is less stringent in terms of measurement conditions. The authors verified that precision degrades as the two lifetimes approach became closer. Reasonable overall precisions require that τ_2/τ_1 should be at least 2 and ideally 3 or 4. The precision reaches a minimum for $\Delta t/\tau_1 > 2$, best for $\alpha_1/\alpha_2 > 1$.

More recently, Ching-wei Chang on his PhD thesis (Chang, 2009) developed the general closed form solutions for double-exponential RLD with arbitrary overlap (see Equations 3.40 to 3.50) and used them to evaluate the precision of the RLD method.

Monte Carlo simulations were performed to study the behavior of RSD for different τ_2/τ_1 (from 1 to 20 with increment equal to 1) and α_1/α_2 (from 0.1 to 100 in 0.1 steps) ratios. The constant $\log_{10}(g/\Delta t)$ varied from 0.1 to 1 with a step value of 0.1 and $\log_{10}(g/\tau_1)$ varied from 1 to 1.4 with increments of 0.2. The total counts were high: 10^6.

This study provided several interesting conclusions regarding the optimal conditions of double-exponential RLD. Firstly, with the number of total counts (TC) and gate separation/overlap Δt fixed, increasing α_1/α_2 results in a larger gate width to maintain the optimal conditions. Additionally, when the ratio α_1/α_2 increases, a longer gate coverage is required. This can be explained by the dimmer longer-lifetime component that needs a larger gating record, to be distinguished from the short-lifetime component. The same behavior is observed when τ_2/τ_1 is decreased and α_1/α_2 is fixed, since the longer-lifetime component becomes more overlapped with the shorter-lifetime component making the long-life tail more crucial for distinction. This RLD method is also quite sensible to the total number of counts, maintaining the relation between precision and $(TC)^{1/2}$ already reported in other studies. Please note that the parameter TC refers to the sum of the values of the pixels with the same spatial coordinates across the four images. However, for small values of TC, longer gating can be used to achieve lower values of RSD. Finally, the authors also report that their results suggest that the separation between gates Δt has a greater effect on RSD than the value of gate width g. This indicates that the choice of gate separation/overlap is more critical than the choice of gate width.

A common point to all the studies based on RLD is that *a-priori* knowledge of the expected lifetime under analysis is necessary to define the optimal parameters of acquisition for maximizing the SNR and, consequently, the precision of the measurements. This is certainly a handicap of the method particularly when analyzing *in vivo* biological samples using endogenous fluorophores. Although the fluorescent species may depend only on the type of tissue being

analyzed, their lifetimes are modulated by their dynamic microenvironment. At best, we can predict the range of fluorescence lifetimes expected, based on the type of sample and on the spectral characteristics of the instrument.

B. Error analysis of RLD performance on double-exponential decays

1. Methods

Simulations were performed to evaluate the accuracy and precision of the RLD method when used to analyze data acquired with the time-gated fluorescence lifetime microscope developed by us. A sample representative of FAD fluorescence was simulated by generating 100x100 data arrays for each of the four decay parameters (lifetimes and pre-exponential factors). Each element of these arrays was generated following experimental data from the epithelium of the porcine cornea, measured by two-photon excitation FLIM in a joint project involving our research group (Batista *et al.*, 2016) The used values are presented in Table.6.1.

Table.6.1 – FAD decay parameters measured with a multiphoton TCSPC system (Batista *et al.*, 2016)**.**

T_1 [NS]	T_2 [NS]	A_1 (%)	A_2 (%)	FREE TO PROTEIN-BOUND RATIO
0.55 ± 0.07	2.47 ± 0.89	65.0 ± 8.3	35 ± 8.3	0.56 ± 0.19

The fluorescence decay curve was then simulated following the formalism described by Warren et al (Warren *et al.*, 2013) and given by Equation (6.13), where $H(m)$ is the value of the Heaviside function for the m^{th} time step and T is the period to the train of excitation laser pulses. N is a parameter used to control the total number of counts on the decay curve. This way, from the sample arrays and using a time step of 1 ps, we obtained a volume of 25000 data arrays of 100x100 elements, where the element (i, j) of the m^{th} array is the value of the decay curve corresponding to the decay parameters of the (i, j) coordinates of the sample, for the m^{th} time step.

$$I(m) = N\left\{\left[H(m) + \frac{1}{\exp\left(T/\tau_1\right)}\right] k_1 \exp\left(-\frac{m}{\tau_1}\right) + \left[H(m) + \frac{1}{\exp\left(T/\tau_2\right)}\right] k_2 \exp\left(-\frac{m}{\tau_2}\right)\right\}, \quad (6.13)$$

Ideally, the gate signal provided by the system should be a square pulse. In fact, this never happens. Moreover, considering the high width of the pico-second laser (63 to 100 ps depending on the laser power), the resulting IRF of the system, which corresponds to the convolution between the laser excitation pulse and the gate signal, presents a shape different from the ideal square pulse expected that is used in the published studies on RLD precision. Here, we decided to account for the effect of the non-ideal IRF on the application of RLD algorithms. The gating signal was included in the simulation by convolving the data volume representing the fluorescence decay data with a vector corresponding to the ideal square gate pulse or to a real gating profile measured by imaging a scattering sample in the reflectance mode of the instrument. Examples of gating curves used in the simulations are presented in Figure.6.1.

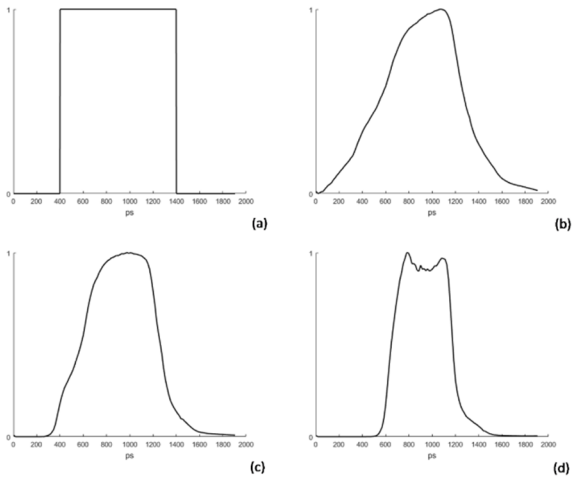

Figure.6.1 – Examples of gating profiles used in the simulation: a) ideal gating profile – width of 1000 ps; b) gating profile for a nominal width of 1000 ps with a laser power of 100 %; c) nominal width: 800 ps, laser power level: 90 %; d) nominal width: 500 ps, laser power level: 80 %.

The next step in the simulation concerned noise. As previously mentioned, Time-Gated systems are not ruled only by Poisson statistics inherent to photon detection. So, in our simulation we have considered the noise factors described by McGinty et al (McGinty *et al.*, 2009), previously reported in this document and described by Equation (6.14), where k is the number of electrons in the CCD per detected photon, a value that depends on the image intensifier voltage, E is the excess noise factor, N_{ph} is the number of detected photons, σ_k is the standard deviation associated

with fluctuations in the conversion constant k and σ_{CCD} is the noise associated with CCD, namely readout noise and dark current noise.

$$\sigma_I^2 = k^2 E N_{ph} + \sigma_k^2 N_{ph}^2 + \sigma_{CCD}^2, \quad (6.14)$$

Considering the specifications of our system, the noise related to fluctuations in the k constant was discarded since it is only relevant in instruments capable of delivering high MCP voltages. In regard to CCD noise, we just considered the readout noise ($\sigma_{CCD_{rd}}$), which, as stated previously on Table 4.7, is equal to 16 electrons, a value that corresponds to 2.28 counts at the output of the camera ADC (the A/D conversion factor is 7 electrons per count – see Table 4.7). Therefore, the image variance (noise) is reduced to Equation (6.15)

$$\sigma_I^2 = k^2 E N_{ph} + \sigma_{CCDrd}^2 = \eta^2 k'^2 E N_{ph} + \sigma_{CCDrd}^2, \quad (6.15)$$

where η is the quantum efficiency of the camera S25 photocathode, which was already presented in Figure 4.6 (a value $\eta = 0.08$ was used in the simulations). The factor k corresponds to the gain in counts per electron and was measured for the different MCP voltages by the manufacturer of the gated intensified camera (LaVision, 2007a). The excess noise factor E was calculated by interpolating the values presented by McGinty et al for a similar camera (McGinty *et al.*, 2009). These values are listed in Table 6.2.

Table 6.2 – Gain and Excess noise factors of the developed Time-Gated system.

MCP VOLTAGE (V)	K (COUNTS /ELECTRON)	E
500	1.05	2.203
550	2.41	1.842
600	5.20	1.653
650	11.1	1.461
700	21.6	1.315
750	45.0	1.158

To obtain reliable simulations, the windowing schemes were setup so that the beginning of the first integration window is close to the peak of the decay curve. This fact was confirmed by simulating a Poisson noise limited decay with average values $\tau_1 = 550\,ps$; $\tau_2 = 2470\,ps$; $\alpha_1 = 0.65$; $\alpha_2 = 0.35$ representative of flavins fluorescence, and evaluating the accuracy of the values of these parameters obtained with the RLD method, for several shifts between the decay peak and the beginning of the first integration window, while keeping both g and Δt constant. This evaluation was performed for both contiguous and 50% overlapped windowing schemes. If the decay peak is far from the beginning of the first integration window, the accuracy of all measured decay parameters degrades greatly. This can be seen in Figure 6.2, where the variation of the relative mean error (RME) on the value of the free to bound protein ratio, caused by changing the location of the integration windows, is presented. The relative mean error for a given decay parameter is defined by Equation (6.16).

$$RME(\%) = \frac{|mean\ value - correct\ value|}{correct\ value} \times 100, \tag{6.16}$$

Therefore, all simulations using the actual gating profiles of the image intensifier were carefully set up, assuring that the accuracy of the measured decay parameters is not degraded by improper location of the RLD integration windows in relation to the decay peak.

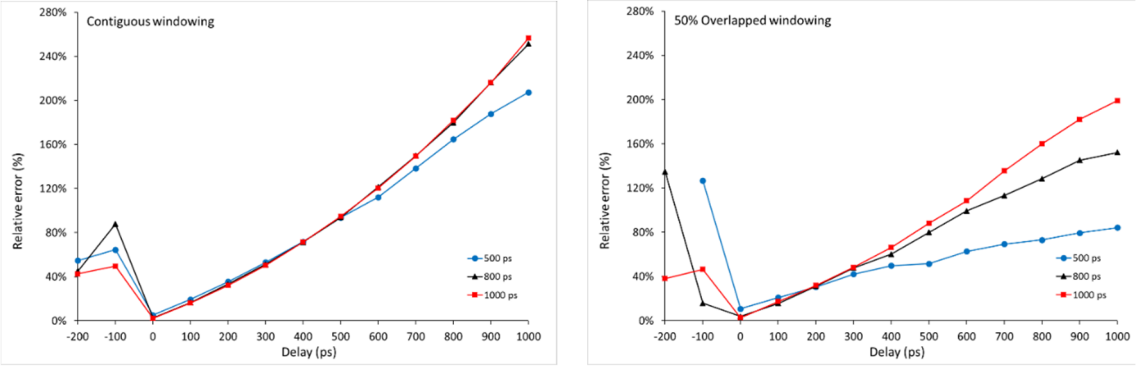

Figure 6.2 - – Accuracy in the value of the free to protein-bound ratio for different delays between the start of the first integration window and the peak of the decay curve. The accuracy values are presented as percent errors for the contiguous and the 50% overlapped windowing schemes. Total counts of the decay curves were kept slightly above 106. For continuous windowing the best accuracy values are 2.35%, 2.50% and 5.19% for nominal gate widths of 1000, 800 and 500 ps, respectively. For overlapped windowing the best accuracy values are 2.69%, 3.87% and 10.81%, respectively.

The simulation algorithm was validated against images from samples with double-exponential fluorescence decay, acquired with the developed time-gated fluorescence lifetime microscope. The samples were a mixture of two standard fluorophores in a solution of methanol (MeOH): Erythrosine B and Coumarin 153. Both dyes were purchased from Sigma Aldrich (Darmstadt, Germany). The reagent methanol was of analytical grade (Labbox Labware Barcelona, Spain). Individual solutions of each dye were prepared with concentration of 1 µM and their fluorescence decays, acquired with the Time-Gated microscope, were fitted to a mono-exponential decay using FLIMfit software (Warren et al, 2013), an open-source software for analysis of Time-Gated data. Fluorescence lifetime for Erythrosine B in methanol was measured to be 469.24 ± 7.37 ps, while for Coumarin 153 was measured to be 3.94 ± 0.02 ns. These values were confirmed using a TCSPC fluorescence lifetime microscope (MicroTime 100, PicoQuant GmbH, Berlin, Germany).

From those solutions, we prepared a mixture of the two fluorophores. 90% of the mixture volume was from Erythrosine B and 10% was from Coumarin 153. Time-Gated microscope nominal gate width was set to 1000 ps and laser to 90% of its power. MCP gain was varied between 1.05 and 45 counts/electron. Measurements were made on 5 solution samples. RLD analysis was performed at each gain setting. Reference values were obtained using FLIMfit with datasets of 232 images acquired with the time-gated microscope for k =1.05. The time-shift between each image of the datasets was 100 ps. Since Coumarin 153 quantum yield is higher than that of Erythrosine B, the fractional contribution (α_1) of this fluorophore was expected to be lower than 0.9. This was confirmed by the measured reference values: τ_1 = 519.32 ps; τ_2 = 4118.11 ps; α_1 = 0.873; α_2 = 0.127. The reference ratio is, therefore, equal to 0.145.

C. Results and Discussion

The simulations we performed can be divided in two sets: those concerning a total number of counts higher than 10^4 and those where TC is in the range of 10^3. The first set was done to show the limits of the RLD algorithm both in shot noise limited conditions (that is when we consider as only noise source the Poisson noise inherent to photon detection) and in conditions replicating the developed instrument. Although these simulations are not representative of the operational conditions intended for the time-gated fluorescence lifetime microscope, they are useful to illustrate the expected performance in settings where high levels of TC are obtainable, either by frame summing or by using high values of pixel binning.

The second set is representative of the operational conditions intended for the developed instrument. As already discussed, it is fundamental to reduce the irradiation time for biological samples or *in vivo* clinical applications, a requirement that precludes the use of frame summing. As the camera ADC has a resolution of 12-bits, pixel values higher than 4096 cannot occur. Taking in consideration the fluorescence lifetimes associated with NADH and FAD, we conclude that TC will always be lower than 10^4 in a real experiment performed according to the requirements for metabolic imaging in biological samples.

1. Validation of the Simulations

For validation purposes, we ran simulations of a fluorophore system with a double exponential decay with parameters equal to the reference values measured for the mixture Erythrosine B and Coumarin 153 in Methanol ($\tau_1 = 519.32\,ps$; $\tau_2 = 4118.11\,ps$; $\alpha_1 = 0.873$; $\alpha_2 = 0.127$). Figure 6.3 presents the comparison between τ_1, τ_2, and α_2/α_1 ratio obtained from simulated and experimental data, using the RLD algorithm, for three different values of Δt (1, 2 and 3 times the gate width).

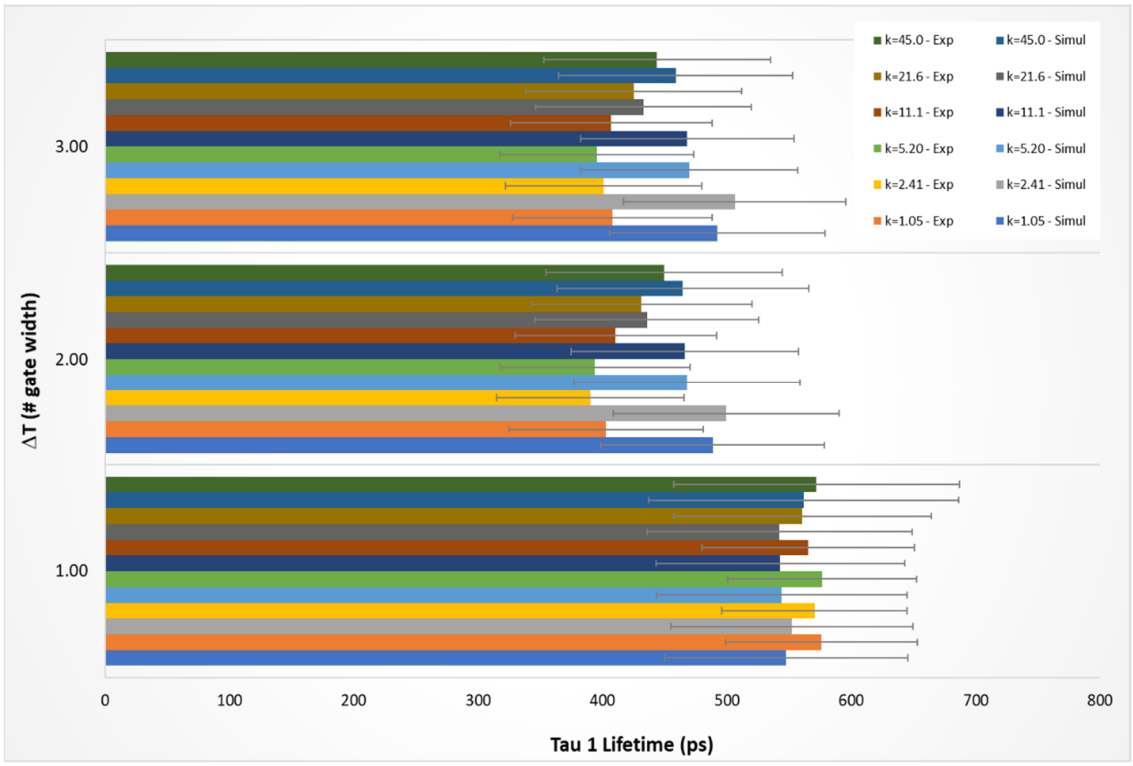
k=45.0 - Exp
k=45.0 - Simul
k=21.6 - Exp
k=21.6 - Simul
k=11.1 - Exp
k=11.1 - Simul
k=5.20 - Exp
k=5.20 - Simul
k=2.41 - Exp
k=2.41 - Simul
k=1.05 - Exp
k=1.05 - Simul
3.00
2.00
1.00
ΔT (# gate width)
0
100
200
300
400
500
600
700
800
Tau 1 Lifetime (ps)

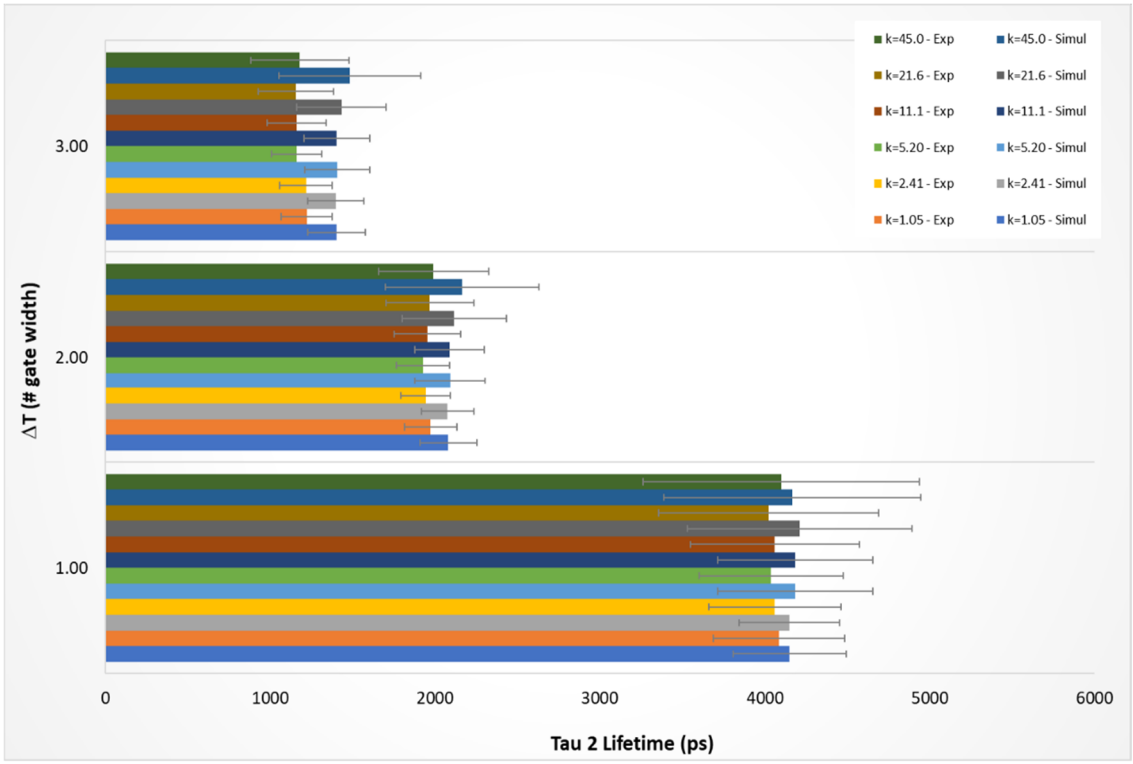
k=45.0 - Exp
k=45.0 - Simul
k=21.6 - Exp
k=21.6 - Simul
k=11.1 - Exp
k=11.1 - Simul
k=5.20 - Exp
k=5.20 - Simul
k=2.41 - Exp
k=2.41 - Simul
k=1.05 - Exp
k=1.05 - Simul
3.00
2.00
1.00
ΔT (# gate width)
0
1000
2000
3000
4000
5000
6000
Tau 2 Lifetime (ps)

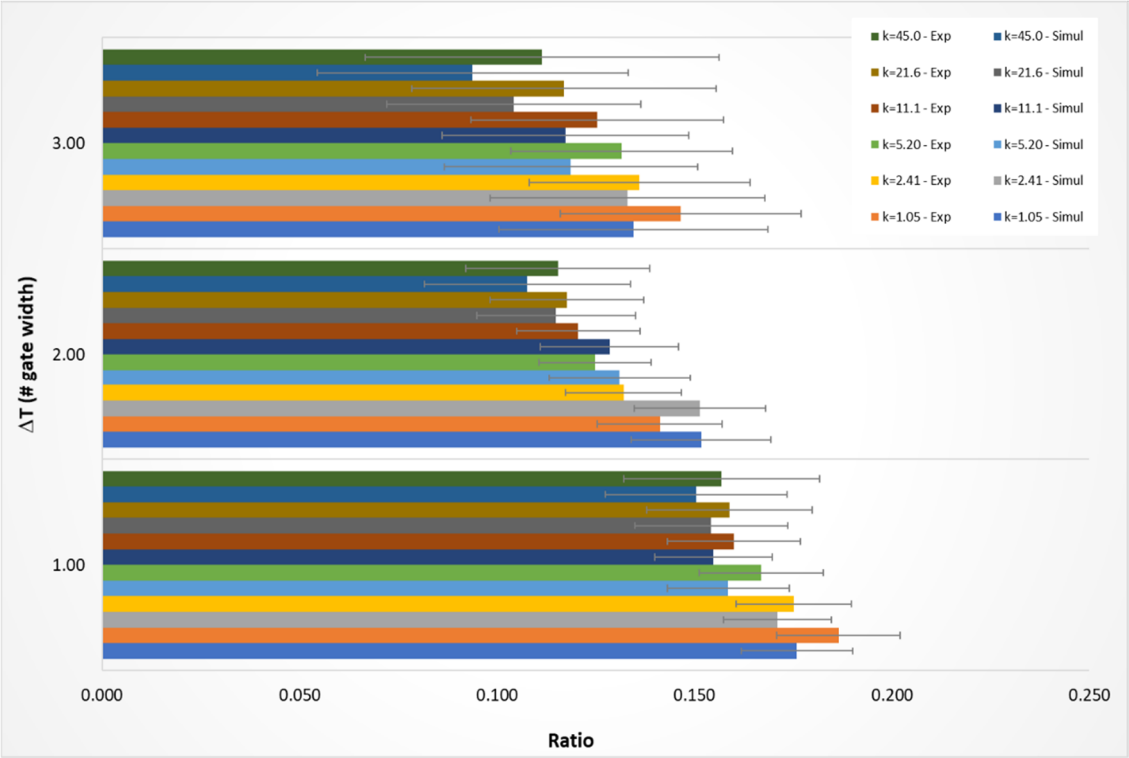

Figure 6.3 – Comparison between the mean values of the decay parameters τ1, τ2 and α2/α1 ratio, obtained from simulated and experimental data using the RLD algorithm. Results are presented for three values of Δt (1, 2 and 3 times the gate width). Error bars correspond to ± SD (standard deviation)

The graphs of Figure 6.3 do not reveal significant differences between simulation and experimental results for corresponding parameters, for any of the three windowing schemes tested. This was confirmed by applying the t-test between simulation and experimental samples of a given parameter. No statistically significant differences were found.

2. TC higher than 10^4: Poisson noise limited images

We analyzed the impact of the total photon count on the accuracy and precision of the decay parameters measured by the RLD method. In this analysis, we used data arrays with just Poisson noise added, meaning that the parameters k and E of Equation (6.15) were kept equal to the unity and the CCD readout noise is not considered. Simulations were performed for contiguous and 50% overlap windowing schemes, using gating profiles corresponding to the three nominal widths and laser power levels of 100%, 90% and 80%.

In these simulations, we choose to introduce variability in the parameters' arrays representing the sample, used to generate the data volume. Instead of creating 100x100 arrays of constant value for each of the four decay parameters, each element of these arrays was generated following a

normal distribution with mean and standard deviation given by the FAD experimental values presented in Table.6.1.

Figure 6.4 illustrates the variations in the accuracy of RLD calculated free to protein-bound ratio, given by the relative mean error (RME).

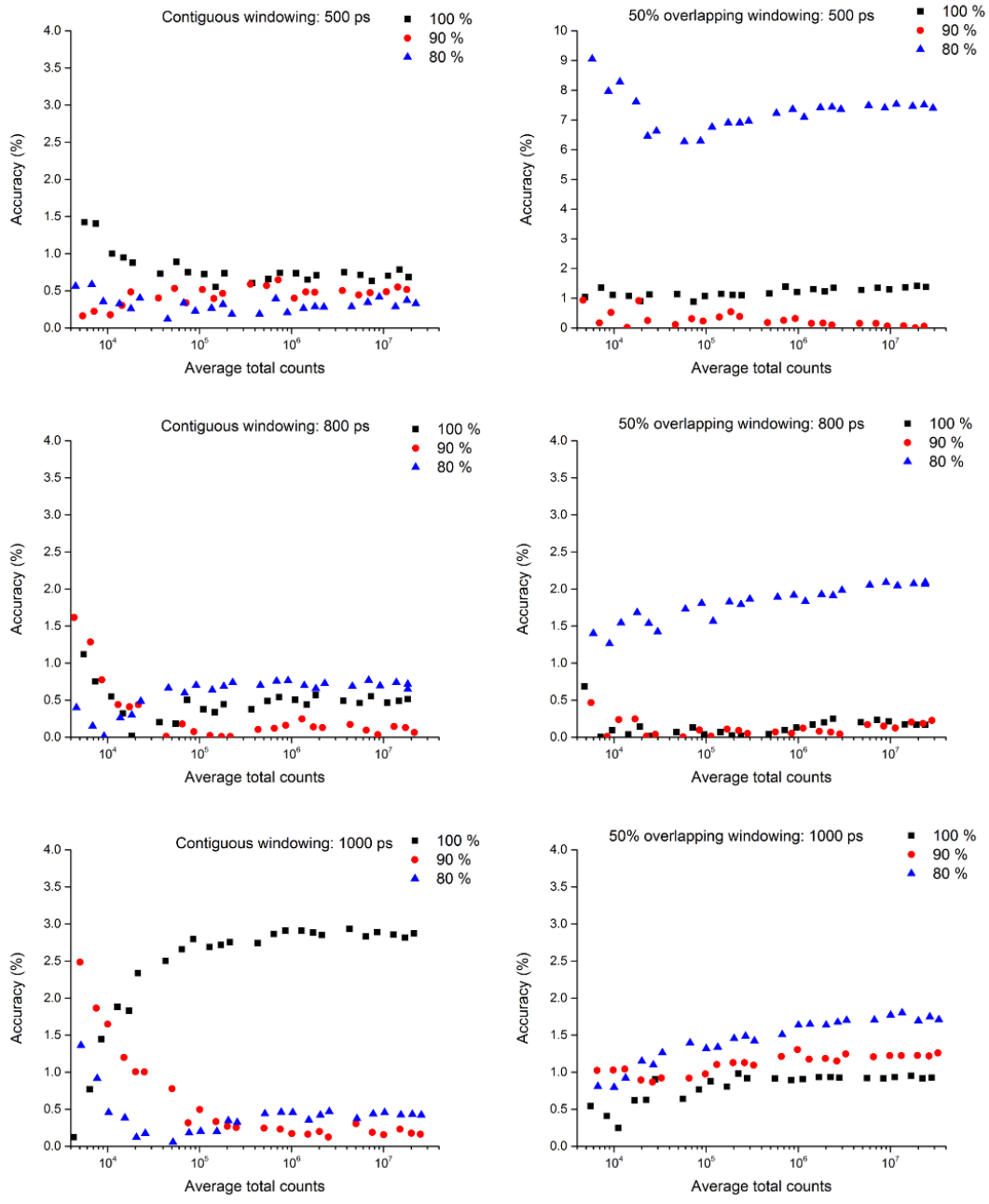

Figure 6.4 – Accuracy of the free to protein-bound ratio calculated by the RLD method (contiguous and 50% overlapping windowing), as function of the total number of counts in the decay and of the laser power, which influences the gating profile. The accuracy is measured by the relative mean error (RME). Data is presented for gate widths of 500, 800 and 1000 ps. Note that the vertical scale on the graph corresponding to the 50% overlapping windowing with a 500 ps gate is different from that on the other graphs.

As Figure 6.4 shows, almost all acquisition schemes allow a very good accuracy of the measured metabolic indicator, with an accuracy error lower than 3%. The only exception occurs when using the 80% power level and the overlapping windowing scheme with the smaller gate width, where the accuracy error is always larger than 6%. For laser powers of 90% and 100%, the overlapping windowing schemes show better performance than the contiguous scheme except for the nominal gate width of 1000 ps.

The precision in the measurement of the free to protein-bound ratio was evaluated using the standard deviation calculated from the 100x100 array of ratio values obtained with the RLD method. In Figure 6.5, this standard deviation is normalized to the standard deviation of the free to protein-bound ratio on the data array representing the sample. Therefore, the plots of Figure 6.5 give the amount of precision degradation resulting from the RLD method.

The precision degradation is almost negligible, being possible to obtain normalized standard deviations lower than 1.1 The best values were obtained for the larger gate widths, using contiguous windowing. The better performance of this acquisition scheme is more evident for TC values below 10^5.

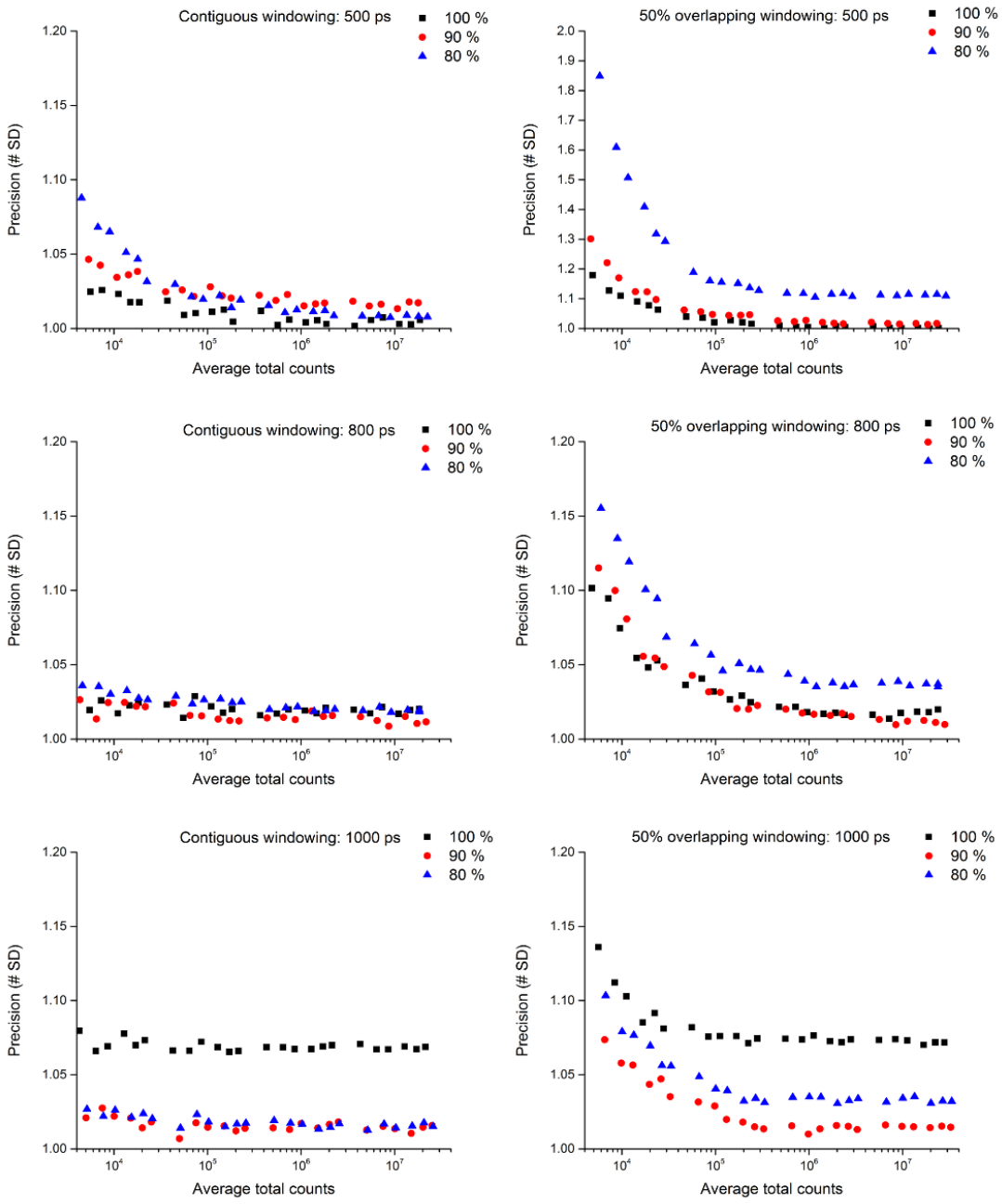

Figure 6.5 - Precision of the free to protein-bound ratio calculated by RLD method (contiguous and 50% overlapping windowing), as function of the total number of counts in the decay and of the laser power, for gate widths of 500, 800 and 1000 ps. The precision is measured by the standard deviation of the calculated free to protein-bound ratio normalized to the standard deviation associated to the sample used in the simulation. Note that the vertical scale on the graph corresponding to the 50% overlapping windowing with a gate of 500 ps is different from that on the other graphs.

It is also worth mentioning that we verified that for Poisson-noise limited images, acquired with ideal rectangular windows from samples without any spatial variability in the decay parameters, the precision in the free to protein-bound ratio varies inversely with the square root of the total number of counts. This result was already presented by Sharman et al (Sharman *et al.*, 1999).

3. TC higher than 10^4: extended noise model

Here we present the results of the simulations concerning the accuracy and precision associated with measurements of FAD decay parameters using a noise model representative of our time-gated fluorescence lifetime microscope. The simulations were done considering the noise contributions from the gated intensified camera, using the values of η, k, E and σ_{CCDrd} already mentioned. Simulation results are presented just for contiguous windowing with gate width of 1000 ps and power level of 90%.

As expected, the accuracy and precision of the decay parameters improves for higher total counts being almost gain independent for TC higher than 10^6. For total counts between 10^4 and 10^5, the accuracy and the precision are better when using lower gains (k values) in the intensified camera. This was also expected due to the contribution from the image intensifier to the image variance.

The simulations show that it is possible to obtain a good accuracy (RME lower than 5.0%) on the free to protein-bound for total counts higher than 10^4, if we restrict the gain k to values equal or lower than 5.2. In this range, the precision on the ratio is basically not degraded, being close to the precision defined in the sample. The accuracy on the fluorescence lifetimes is also adequate with relative mean errors always below 4%. The precision of the shortest lifetime (τ_1) does not degrade beyond 3 times the original standard deviation. For the longest lifetime, the precision degradation is much lower, a result that can be explained by the large standard deviation of the sample (see Table.6.1), which corresponds to 36% of the lifetime value. For lower gains, the initial precision has a larger weight on the measured lifetime precision than the uncertainty introduced by the instrument and the RLD method.

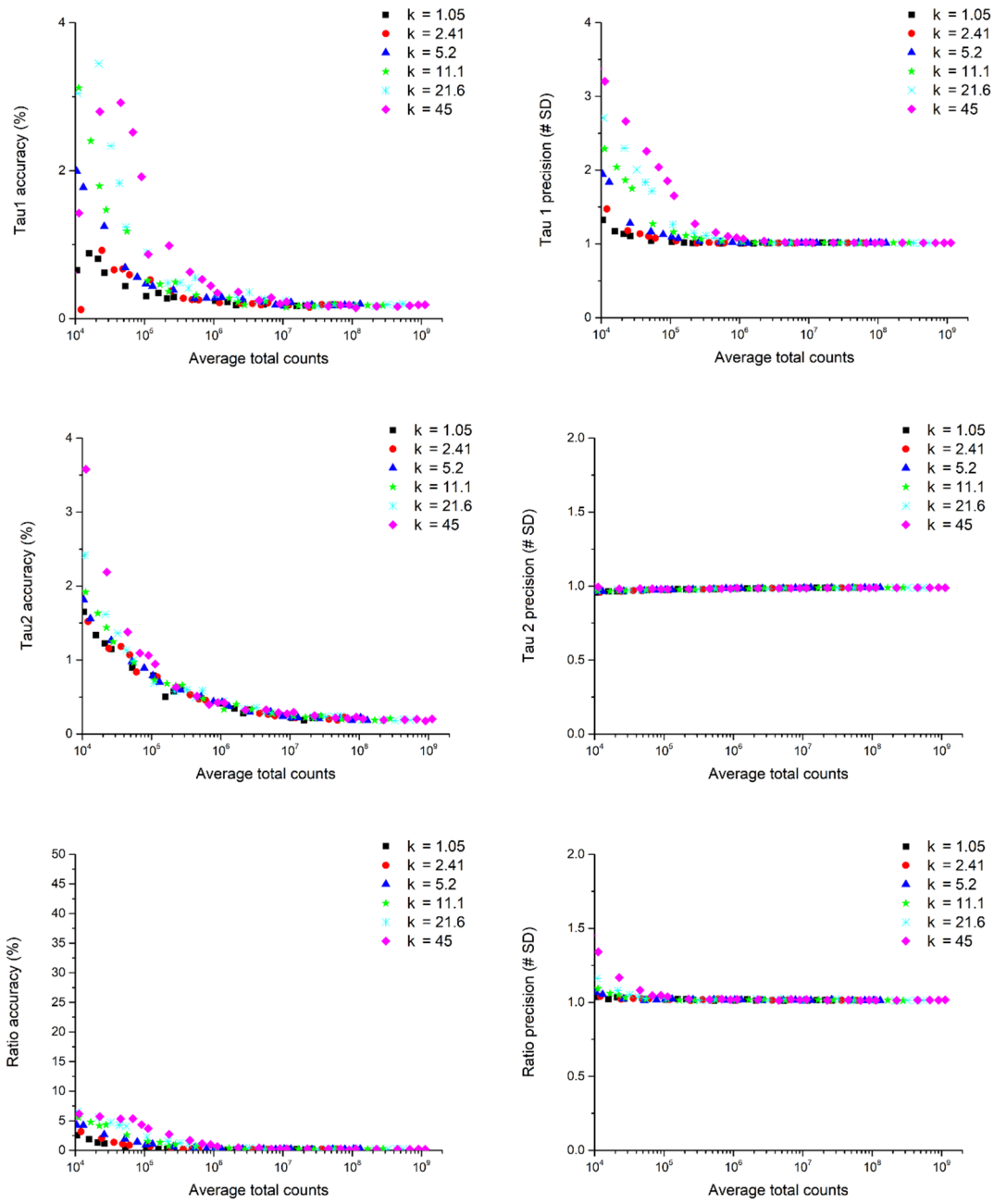

Figure 6.6 – Accuracy and precision of the decay parameters (τ_1, τ_2 and free to protein-bound ratio) calculated by RLD method using the contiguous windowing scheme with a gate width of 1000 ps and a laser power level of 90%.), as function of the total number of counts in the decay and of the number of electrons in the CCD per detected photon. The accuracy is measured by the absolute error to the input decay parameters (sample parameters). The precision is measured by the standard deviation of the calculated decay parameters, normalized to the corresponding standard deviation in the sample.

Once again, we remind that these results imply an operating regime that requires frame summing or binning. The relation between the average total counts and the average counts on the image corresponding to the first integration window depends only on the intensifier gate width and on the profile of the excitation laser pulse, which is determined by the laser power level. For a gate width of 1000 ps and a power level of 90 %, the average counts of the first image amount to 68%

of the average total counts, meaning that 10^4 total counts correspond to an average of 6.8 x 10^3 counts on the first image. As the gated intensified camera has a 12-bits A/D converter, achieving a value of 10^4 total counts will require 2x2 binning, summing at least three frames or a combined acquisition scheme resorting to these two approaches.

4. TC lower than 10^4

Following our simulations for TC values higher than 10^4 and benefiting from several experimental trials on the time-gated fluorescence lifetime microscope, we decided to fix the nominal gate width at 1000 ps and the laser power at 90%. These parameters give the best compromise between higher sensitivity and better accuracy and precision. Therefore, all the simulations for the TC < 10^3 regime were done with these settings.

Using the FAD decay parameters listed in Table.6.1, we simulated RLD measurements for the different k values for studying the influence of the gate separation Δt on the accuracy and precision of the measured decay parameters. Figure 6.7 shows the accuracy and the precision for the fluorescence lifetimes τ_1 and τ_2 for different gains k and gate separations Δt. The accuracy is measured by the relative mean error (RME) and the precision by the relative standard deviation (RSD). Although the value TC depends on the gate spacing, the average counts on the peak image was kept constant and close to the maximum (4094) across all simulations. FiguresFigure 6.7, Figure 6.8, and Figure 6.9 present the obtained results.

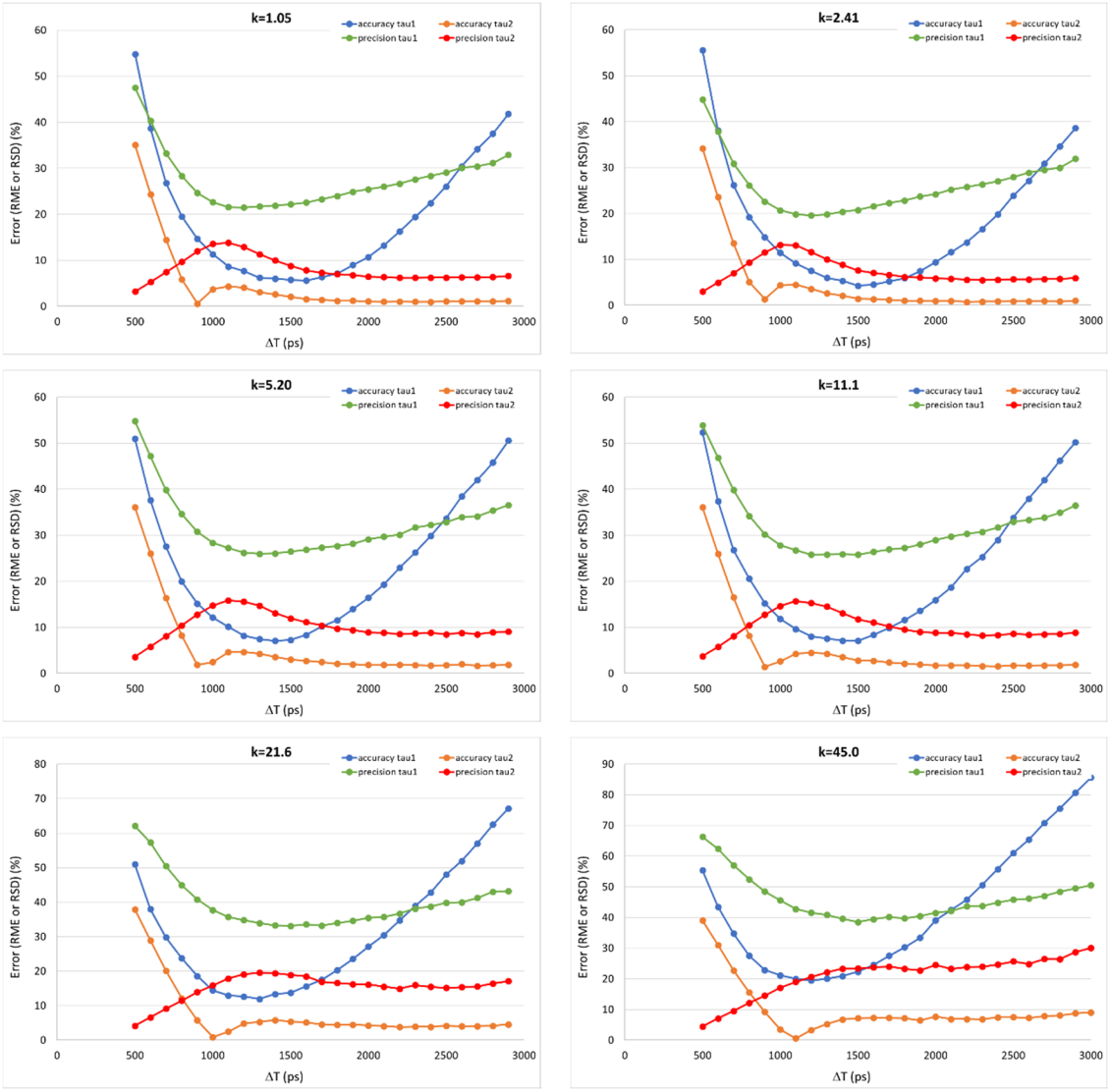

Figure 6.7 – Accuracy and precision of FAD fluorescence lifetimes obtained by simulation as a function of the gate separation Δt, for the different gains of the gated intensified camera (K). The accuracy is measured by the relative mean error (RME) and the precision by the relative standard deviation (RSD).

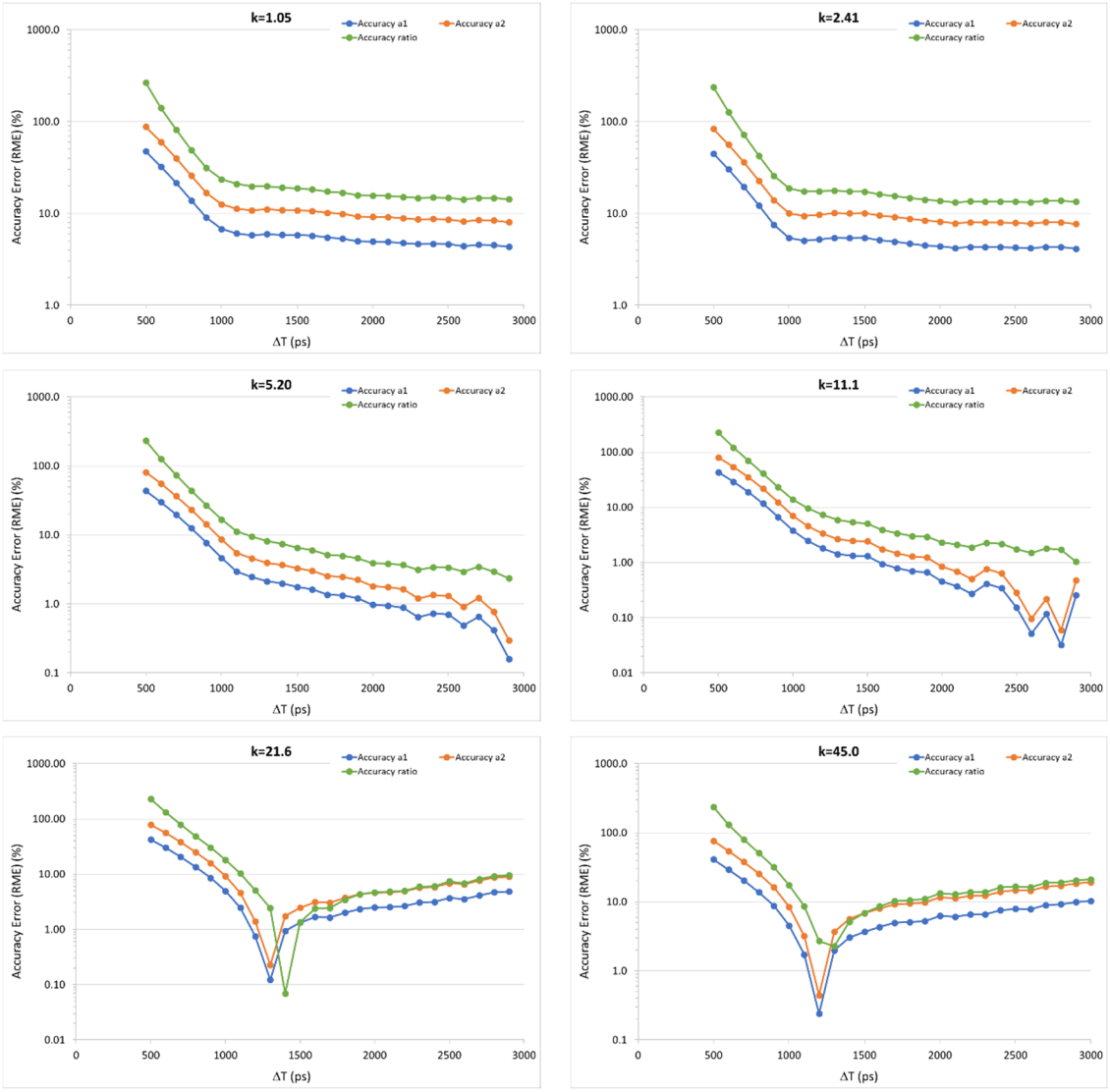

Figure 6.8 – Accuracy of FAD decay parameters α_1 and α_2 and of the metabolic ratio α_2/α_1 obtained by simulation as a function of the gate separation Δt, for the different gains of the gated intensified camera (k). The accuracy is measured by the relative mean error (RME).

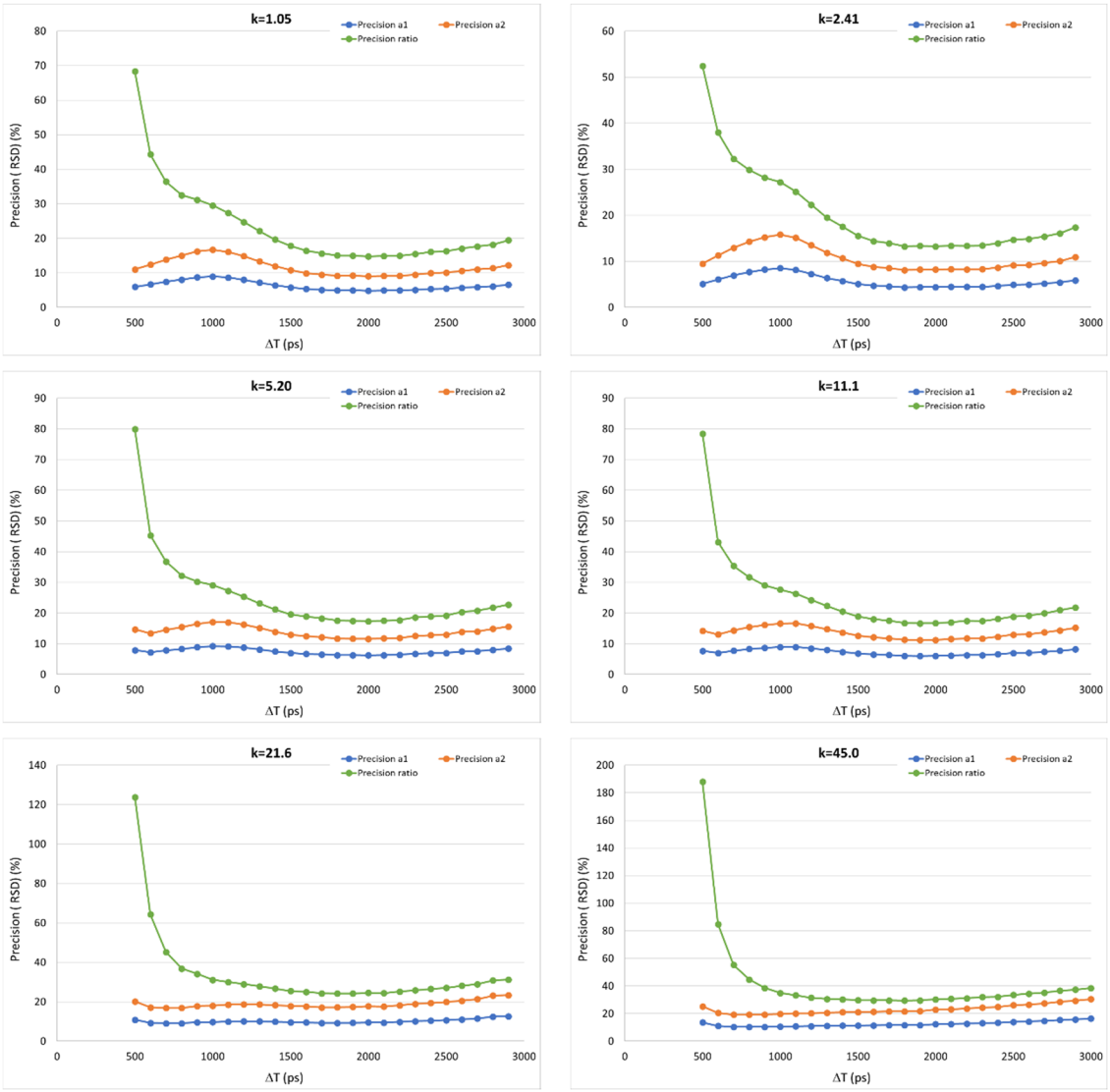

Figure 6.9 – Precision of FAD decay parameters α_1 and α_2 and of the metabolic ratio α_2/α_1 obtained by simulation as a function of the gate separation Δt, for the different gains of the gated intensified camera (K). The precision is measured by the relative standard deviation (RSD).

On the accuracy of the fluorescence lifetimes (Figure 6.7), we can conclude that it is always better for τ_2 than for τ_1. This is an expected result since τ_1 is in the order of 500 ps making its measurement highly affected by the IRF of the time-gated microscope. It is known that when the finite width of the IRF is not at least two orders of magnitude shorter than the measured fluorescence lifetime, the accuracy of the measurement is highly affected. This requirement implies the use of expensive femtosecond lasers when measuring sub-nanosecond fluorescence lifetimes. In the final section of this chapter, we will report on the use of a deconvolution

algorithm to improve the accuracy of fast lifetimes measured by RLD in systems where the IRF width cannot be ignored.

The accuracy of τ_2 is always better than 10% for gate separations higher than 800 ps, with a pronounced minimum for values Δt in the range from 900 to 1100 ps. It is important to note that the gate separation that yields the maximum fluorescence lifetime accuracy (RME near zero) depends highly on the decay parameters. So, tuning the windowing for maximum accuracy is only possible with some *a priori* knowledge on the decay parameters.

The accuracy of τ_1 is clearly better for the lower gains ($k \leq 11.1$). The pattern of variation is similar throughout all camera gains, with an optimal region for gate separations between 1000 and 2000 ps.

The fluorescence lifetime precision also exhibits a variation pattern with a shape that is almost independent from the camera gain. Once again, the performance is better for τ_2 than for τ_1, a result that can also be explained by the effect of the IRF width. The precision of τ_1 is clearly better for low gains ($k \leq 2.41$). There is an optimal region for gate separations between 1000 and 1800 ps, but the RME is only (marginally) lower than 20% for $k = 2.41$.

The precision of τ_2 is less affected by the gate separation Δt. For the lower gains ($k \leq 11.1$), it is always better than 10% for gate separations equal or higher than 1800 ps. The precision error also decreases for low values of gate separation (< 700ps). However, the performance for the other parameters in this region of Δt values is clearly inadequate.

The accuracy of the fractional contributions α_1 and α_2 and of the metabolic ratio α_2/α_1 is presented in Figure 6.8. For gains $k \geq 5.2$ it is possible to identify clear minimums for the accuracy error. The gate separation for which these minimums occur depends on the gain setting. It also depends on the nominal values of the pre-exponential parameters as we will show just ahead. From the point of view of a real application, where *a-priori* knowledge on α_1 and α_2 is not available, it is desirable to operate in a setting range where performance is as stable as possible. For α_1, α_2 and ratio accuracies this is obtained at $k \leq 2.41$ and $\Delta t > 1000$ ps. In this operating region, it is possible to obtain a ratio accuracy error around 15%.

The precision of α_1, α_2 and of the metabolic ratio almost stabilizes for gate separations between 1500 and 2500 ps (see Figure 6.9), for all k values. In this region, the precision of the metabolic ratio is near the limit imposed by error propagation. In fact, the metabolic ratio is not measured directly but calculated from α_1 and α_2. Knowing the variances associated with the pre-exponential factors, it is possible to obtain the precision limit for the metabolic ratio r, given by its variance σ_r^2 – Equation (6.17), where $\sigma_{\alpha_1}^2$ and $\sigma_{\alpha_2}^2$ are the variances associated with α_1 and α_2,

respectively, and $\sigma_{\alpha_1\alpha_2}$ is the covariance between α_1 and α_2, which and can be expressed by Equation (6.18) with ρ the correlation coefficient between α_1 and α_2.

$$\sigma_r^2 \approx \left(\frac{\partial_r}{\partial\alpha_1}\right)^2 \sigma_{\alpha_1}^2 + \left(\frac{\partial_r}{\partial\alpha_2}\right)^2 \sigma_{\alpha_2}^2 + 2\frac{\partial r}{\partial\alpha_1}\frac{\partial r}{\partial\alpha_2}\sigma_{\alpha_1\alpha_2} \tag{6.17}$$

$$\sigma_{\alpha_1\alpha_2} = \rho\sigma_{\alpha_1}\sigma_{\alpha_2} \tag{6.18}$$

If we consider the definition of the metabolic ratio α_2/α_1 and set ρ to its value in the absence of noise $\rho = -1$, we obtain Equation (6.19).

$$\sigma_r^2 = \frac{1}{\alpha_1^2}\left[\left(\frac{\alpha_2}{\alpha_1}\right)^2 \sigma_{\alpha_1}^2 + \sigma_{\alpha_2}^2 + 2\frac{\alpha_2}{\alpha_1}\sigma_{\alpha_1}\sigma_{\alpha_2}\right] = \frac{1}{\alpha_1^2}\left[r^2\sigma_{\alpha_1}^2 + \sigma_{\alpha_2}^2 + 2r\sigma_{\alpha_1}\sigma_{\alpha_2}\right] \tag{6.19}$$

Equation (6.19) is useful as it shows that higher values of the metabolic ratio will have inherently lower precision.

We performed two additional simulations to evaluate the accuracy and precision of the RLD algorithm for different values of metabolic ratio. Both simulations were done for *k*=2.41 since this was the gain value that offered better overall performance on the previous simulations. On the first simulation (results in Figure 6.10), we fixed the gate separation at 1800 ps and varied the α_2 factor from 0.2 to 0.8 in 0.01 steps. This resulted in a range of metabolic ratio values from 0.25 to 4. On the second simulation (Figure 6.11), we limited the same range of metabolic ratio values at 2.846 and varied the gate separation to cover the ranges of stable accuracy and precision identified on the previous simulations.

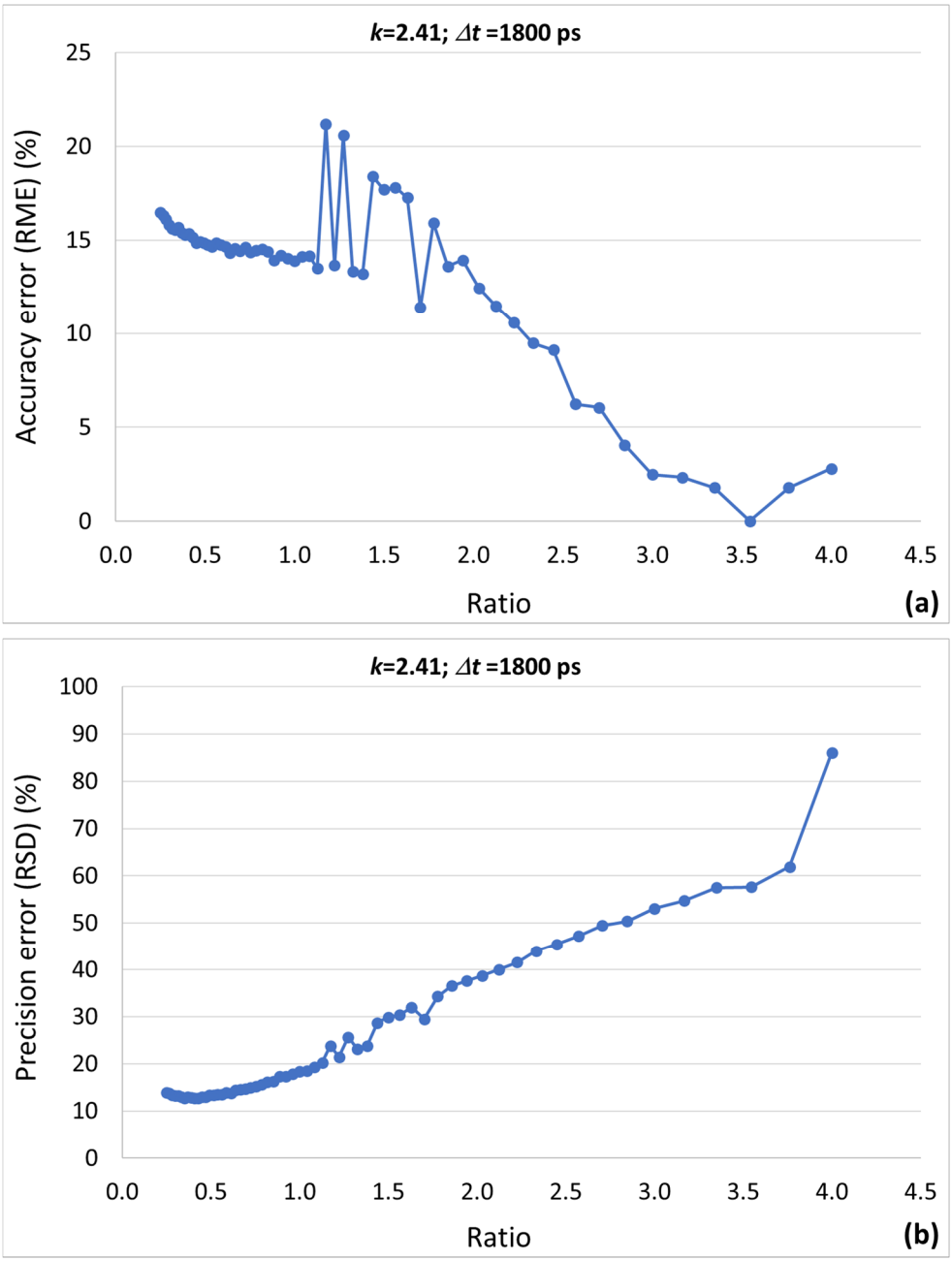

Figure 6.10 – Accuracy and precision of the metabolic ratio α_2/α_1 obtained by simulation for a fixed operating setting (k = 2.41; Δt = 1800 ps). The accuracy and the precision are measured by the RME and the RSD, respectively.

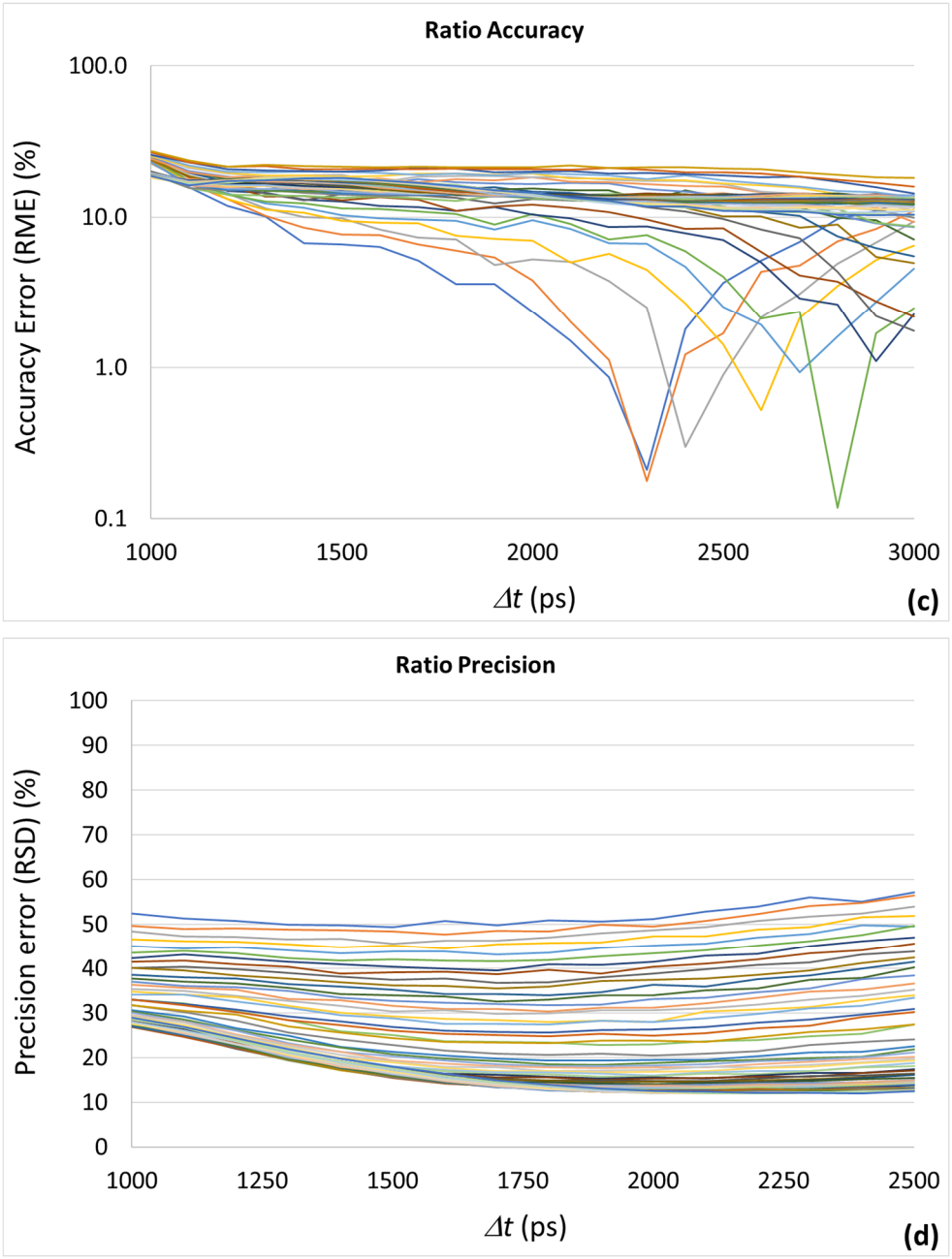

Figure 6.11 – Accuracy and precision of the metabolic ratio α_2/α_1 as a function of gate separation Δt, obtained by simulation for a gain $K = 2.41$. Each line corresponds to a value of metabolic ratio. On the precision graph, the ratio decreases from top to bottom. On the accuracy graph, the sequence of ratio curves is not regular.

Figure 6.10 shows clearly that the accuracy and the precision of the metabolic ratio vary with its mean value, as expected from the previous simulations. These results clearly show that is impossible to find an optimal acquisition setting for the time-gated fluorescence lifetime microscope when using the RLD algorithm, since the quality of the measurement of the metabolic parameter will depend on its value. The precision curve confirms that higher values of metabolic ratio will have worse precision due to the limits imposed by error propagation from the measurements of α_1 and α_2.

Figure 6.11 confirms that no value of gate separation offers measurement performance independent of the ratio value being measured. It also confirms that, for any ratio value, its precision is quite stable for gate separations between 1500 and 2500 ps.

With this set of simulations, it was possible to confirm that the accuracy and the precision associated to the value of the metabolic ratio obtained by RLD algorithm not only depends on the adopted windowing scheme, but also on the nominal value of the ratio. For the ranges of gate separation and metabolic ratio considered, the accuracy error can be as high as 30% and the precision error can reach a value around 60%. Precision errors lower than 10% cannot be obtained.

5. RLD performance with HiLo Microscopy

Here we report our evaluation on the impact of HiLo microscopy on the accuracy and precision of RLD algorithm. We imaged, separately, a capillary filled with a solution of Erythrosine B in MeOH and another capillary filled with a solution of Coumarin 153 in MeOH. Both capillaries were imaged in the wide-field and HiLo modes. The purpose was to compare the lifetime histograms for each imaging mode, to assess an eventual degradation imposed by the HiLo structured illumination method on the fluorescence lifetime measurement through RLD methods.

Table 6.3 shows the obtained results as well as the corresponding reference values, measured with a TCSPC microscope (MicroTime 100, PicoQuant GmbH, Berlin, Germany) equipped with an excitation source equal to the one installed in the time-gated microscope. The measured values show that HiLo processing does not affect the average value of the fluorescence lifetime in both cases under analysis. Differences between the values are less than 2%, meaning that accuracy is not affected by HiLo. On the other hand, it is easy to verify that HiLo degrades the precision of the fluorescence lifetime of the Coumarin solution: its standard deviation increases to more than twice the value obtained with widefield imaging. This degradation of precision is not observed for the Erythrosine solution, which has a much shorter fluorescence lifetime.

Table 6.3 – Reference, epi-fluorescence imaging and HiLo imaging fluorescence lifetimes for Erythrosine B and Coumarin 153 solutions.

SOLUTION	REFERENCE LIFETIME (PS)	EPI-FLUORESCENCE IMAGE LIFETIME (PS)	HILO IMAGE LIFETIME (PS)
Coumarin 153	3959.7	3825.6 ± 198.1	3846.6 ± 463.5
Erythrosine B	490.7	604.2 ± 40.4	613.2 ± 42.0

6. Improving RLD performance: IRF deconvolution

Table 6.3 shows that the fluorescence lifetime measured by RLD, for both imaging methods, for the Erythrosine B in MeOH solution does not agree with its reference value. This deviation, results from the finite width of the time-gated FLIM microscope IRF. Here, we report on a deconvolution procedure for correcting this deviation, improving RLD accuracy for fast fluorescence lifetimes.

The effects of IRF in lifetime measurements were already previously addressed. As mentioned before, when the width of the IRF is not at least two orders of magnitude shorter than the measured fluorescence lifetime, the accuracy of the measurement is highly affected, leading to fluorescence lifetime values higher than the true value. As we described in Chapter 3 , the actual fluorescence decay acquired by a time-domain instrument is the result of the convolution of the real fluorescence decay curve with the IRF of the instrument, as described by Equation (6.20), where $D(t, \tau)$ is the measured fluorescence decay, $IRF(t)$ is the IRF of the instrument and $F(t, \tau)$ is the true fluorescence decay of the sample under analysis.

$$D(t,\tau) = IRF(t) * F(t,\tau) \tag{6.20}$$

Following the formalism presented by (Warren *et al.*, 2013), a single-exponential decay can be described by Equation (6.21), where H(t) is the Heaviside step function, T is the period of the train of excitation pulses and N is a parameter related to the total number of counts on the decay curve.

$$F(t,\tau) = N\left\{\left[H(t) + \frac{1}{\exp(\frac{T}{\tau})}\right]\exp\left(-\frac{t}{\tau}\right)\right\} \tag{6.21}$$

Starting from Equation (6.21), we implemented a different version of RLD, which relies on a deconvolution algorithm. The algorithm starts by using the experimental images (I_{0exp} and I_{1exp}) to calculate an array of lifetimes. By using them and the classical version of RLD an array of lifetimes $\tau_{(i,j)}$, using the standard RLD method. This array will serve to create a new synthetic dataset using Equation (6.21). From this dataset we select the two data arrays (I_{0sim} and I_{1sim}) corresponding to the time positions of the I_{0exp} and I_{1exp} images and normalize them using the image I_{0exp} as reference. Then, we compute the square of the differences $[(I_{1exp} - I_{1sim})^2]$ that will be used as a measure of goodness of the fit between experimental and simulated data. This

procedure is repeated, while decreasing the elements of the array $\tau(i,j)$ until reaching the minimum value of the sum of the square of the differences. Figure 6.12 shows the flowchart for the RLD deconvolution algorithm.

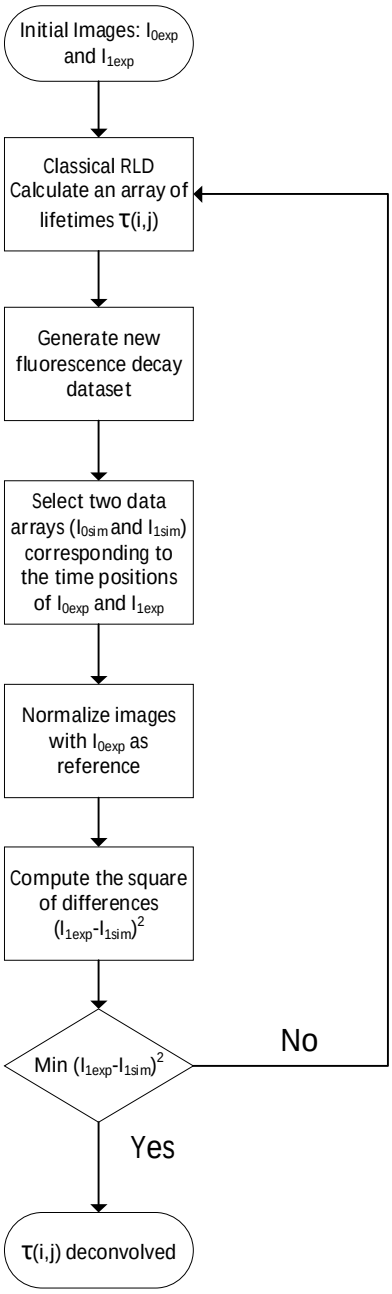

Figure 6.12 – Flowchart for the RLD deconvolution algorithm.

Computational simulations were performed to assess the performance of this new deconvolution RLD approach. From Equation (6.21), different datasets were simulated for several reference lifetimes. Then, standard RLD and RLD deconvolution were applied to each dataset generated and their accuracy was compared. Figure 6.13 describes the results obtained, where it is very easy

to understand the improvement on accuracy when using deconvolution. This improvement is particularly important to shorter lifetimes.

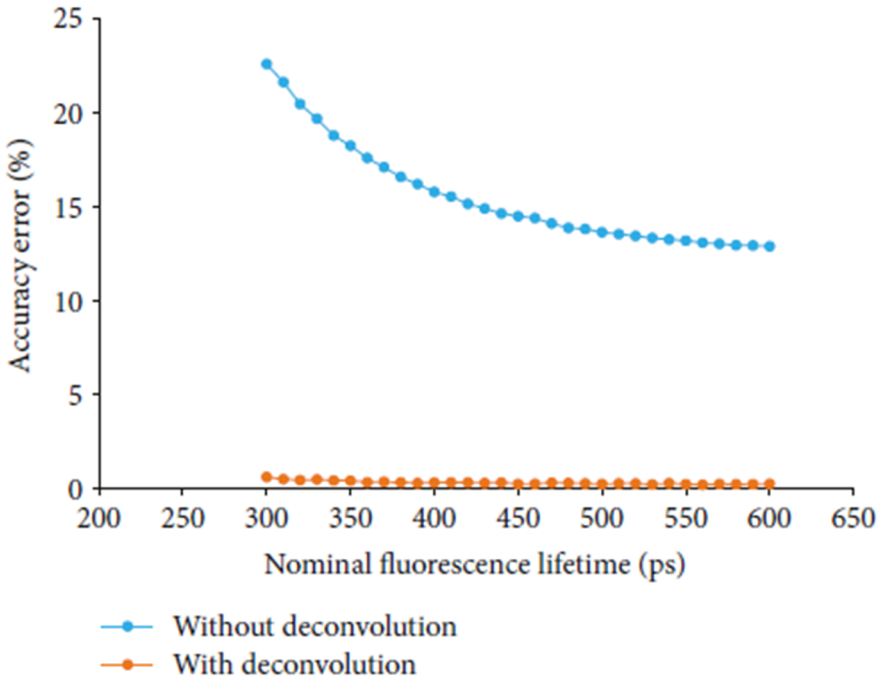

Figure 6.13 – Accuracy error of the fluorescence lifetime calculated by the RLD technique without and with IRF deconvolution, for different values of nominal fluorescence lifetime. The simulations were done considering a gate width of 1000 ps and a laser power level of 90%. The accuracy error corresponds to the relative mean error (RME).

The algorithm was applied on images of capillary tubes filled with Coumarin 153 and Erythrosine B in MeOH solutions, acquired with the developed time-gated microscope. Examples of HiLo images processed with the deconvolution algorithm, along with their lifetime histograms are depicted in the next figure. From them, we can conclude that the accuracy results are quite improved, being very close to the reference expected values.

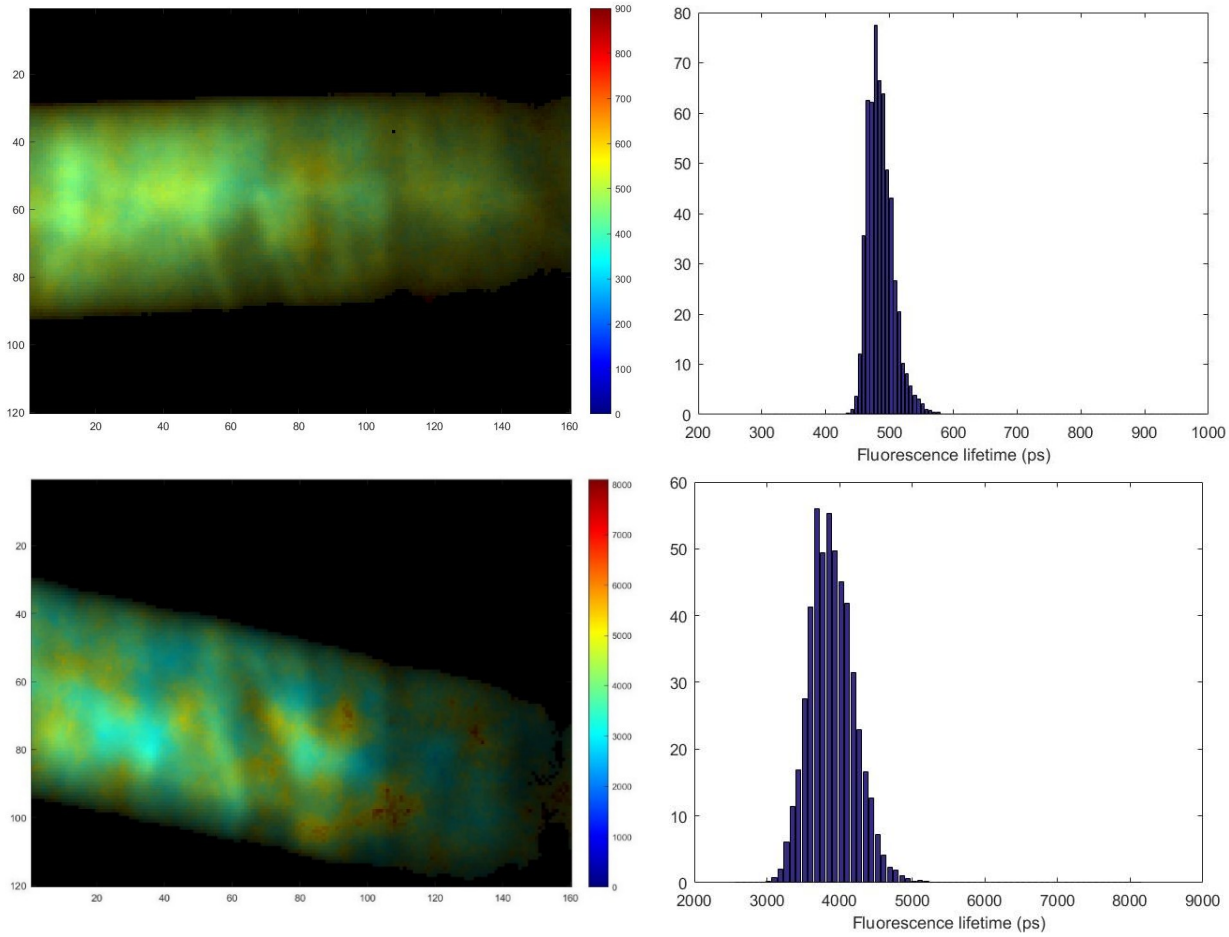

Figure 6.14 – Fluorescence lifetime images and histograms for HiLo processed images of capillary tubes filled with Erythrosine B (top) and Coumarin 153 in MeOH solutions, after running the IRF deconvolution algorithm. By comparing the histograms with the values presented in Table 6.3, it is possible to verify that the IRF deconvolution algorithm improves the accuracy of the fluorescence lifetimes measured with RLD.

Chapter 7 Application to Thick, Transparent Samples: The Cornea

The cornea is a challenging sample given its anatomy and morphology, specially its thickness and transparent nature. In the Introduction section of this thesis, we presented the background and the motivation that supported the orientation of this research project towards corneal metabolic imaging. As was also stated, we were not successful in our efforts to achieve FAD fluorescence lifetime imaging with the Time-Gated microscope. Anyway, we obtained a set of results, which we present in this chapter together with a brief introduction on cornea structural characteristics and the main results obtained with the Time-Gated microscope.

A. Corneal Structure

The cornea is the outmost tissue of the eye. It is a transparent tissue responsible for providing around 70% of the total eye refractive power (43/60 D) (Chalam *et al.*, 2011), while serving as the first major barrier to protect more sensitive ocular tissues. Optically, it is considered a convex-concave lens with elliptical shape, whose longer axis has 12.6 mm and shorter axis has 11.7 mm with an average thickness of 520 μm in the central region and 650μm in periphery (Maurice, 1984). Corneal transparency is guaranteed by the structural organization of the stromal collagen fibers, the absence of a vascular network, the lack of myelin sheath on its nerves and through its capacity of controlling hydration (Quadrado, 2013).

Structurally, cornea is composed by six distinct layers: epithelium, basal membrane, Bowman's layer, stroma, Descemet's membrane and endothelium (Waring *et al.*, 1982; Quadrado, 2013). While not considered a layer, the tear film, located anterior to the corneal epithelium, has a fundamental role in corneal optical power. It is composed of three layers: lipid (or oily), aqueous and mucin and it is estimated to have between 3 to 35 μm in width with a tear volume of around 10 μl (Prydal *et al.*, 1992; King-Smith, Fink and Fogt, 1999; Wang *et al.*, 2003; Chalam *et al.*, 2011; Quadrado, 2013).

The most anterior layer of cornea is the epithelium. It can be divided into three-layers, each of them morphologically defined by different types of cells: superficial, wing and basal cells. Superficial cells are squamous and flattened with polygonal shape and distributed in 2 to 3 different sheets with 40 to 60 μm in diameter and 2 to 6 μm in thickness - Figure 7.1. Ravier wing cells form the intermediate sub-layer of the epithelium. These cells are an intermediate state of differentiation between superficial and basal cells. They have polygonal shape and a great central

ovoid nucleus and are distributed in 2 to 3 layers in the central region while in the periphery the number of these layers increases to 4 or 5 (Nischida and Saika, 2011). Basal cells compound the inner sub-layer of the epithelium and are characterized by being cylindrical cells with around 18 µm in height and 10 µm in width and an ovoid nucleus (Quadrado, 2013). They are the only ones capable to differentiate and proliferate into wing and superficial cells (Nischida and Saika, 2011). Moreover, they have anchor fibrils, made of collagen VII, which go deep into the stroma to form anchors of collagen I. These anchors give the epithelium the capacity to remain linked to the stroma and, with it, to resist to multiple mechanical stresses (Quadrado, 2013). Epithelium is responsible for providing optical transparency, protection and tear stabilization while acting as barrier to the invasion of fluids or microorganisms (Quadrado, 2013).

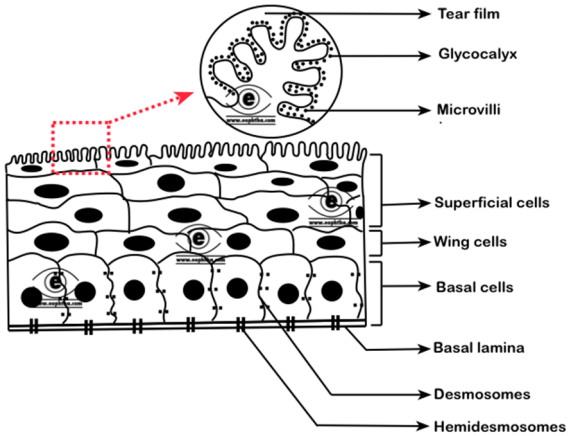

Figure 7.1 – Corneal epithelial cell layers (Quadrado, 2013).

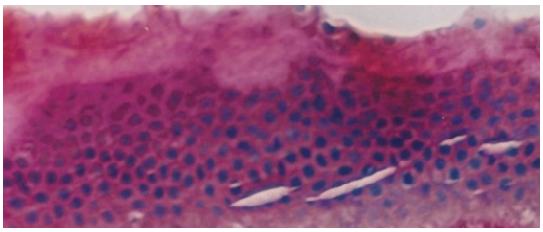

Figure 7.2 - Histological cut of corneal epithelium (image taken from the archive of our research group).

The Bowman's layer is a 10 to 15 µm thick acellular structure located right after the epithelium. It maintains the integrity and epithelial organization while separating the epithelial layer from the stroma (Edelhauser HF and Ubels JL, 2002). Made of a network of collagen I and II fibers and proteoglycans it serves as structural base for epithelial basal cells. Bowman's layer collagen fibers have a shorter diameter than stromal ones. However, with increasing depth they start to enlarge and transforming into stromal fibers (Quadrado, 2013).

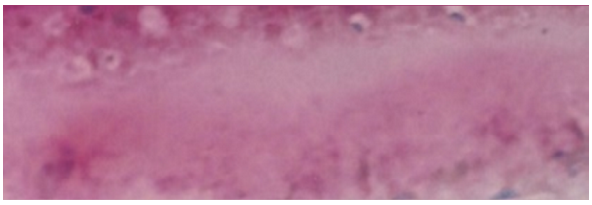

Figure 7.3 - Histological cut of Bowman's layer (image taken from the archive of our research group).

The stroma is the thicker layer of the entire cornea (90% of total corneal width). With 500 to 540 μm in the central region and up to 700 μm in the periphery (Nischida and Saika, 2011), it is composed of connective tissue, keratocytes, collagen lamellae and fundamental substance (Klyce and Beuerman, 1998). Keratocytes are the only cellular structures present in stroma and represent 3 to 5% its volume (Nischida and Saika, 2011). These large, flattened cells are placed between the collagen lamellae with extensions from the cellular body in a star pattern. These extensions have the same orientation that collagens lamellae and are connected to other keratocytes through gap junctions (Ueda *et al.*, 1987). These cells are responsible for the synthesis of proteoglycans and collagen that maintain the collagen lamellae and extracellular matrix structure. Upon injury on the stromal layer, quiescent keratocytes move to the affected zone to repair the damaged structures (Nischida and Saika, 2011). While so, they are transformed into mirofibroblasts - cells that produce extracellular matrix, collagens degradation enzymes and metalproteins and cytokins. They also have a contraction capacity that is essential in the scar process. Collagen fibers are present in different types in the stromal structure. The majority is of type I (75%), but types III, V and VI are also present in reduced amounts. Collagens fibers diameter has typically 22.5 to 35 nm (Giraud *et al.*, 1975). This reduced diameter is what most contributes to maintain corneal transparency. Fibers are also predisposed at an uniform distance between them, around 42 nm (Nischida and Saika, 2011).

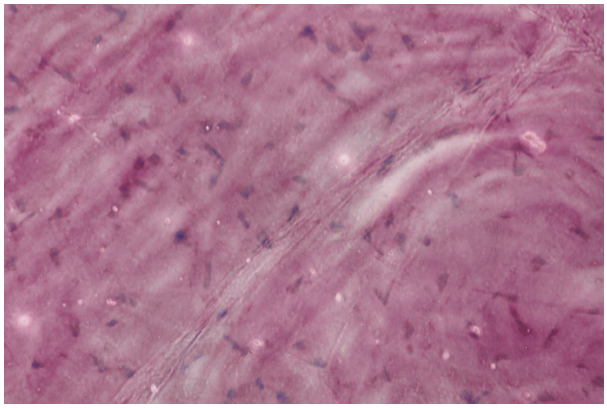

Figure 7.4 - Histological cut of the stromal layer (image taken from the archive of our research group).

The Descemet's membrane is placed between the endothelium and the stroma and serves as basal membrane for the endothelium. It is a homogeneous thin layer connected to the stroma that is constantly growing throughout the human life. At birth Descemet's has typically around 3 μm in width and it grows around 1 μm each decade mainly in the posterior region (Edelhauser HF and Ubels JL, 2002). This layer is also acellular and mainly composed of collagen IV, VIII, fibronectin and glicoproteins. It has great elasticity and resistance to traumatic and inflammatory injuries. Upon rupture, it is covered by endothelial cells without regeneration capacity, which contributes to the enlargement of the Descemet's membrane.

Finally, endothelium is the most inner layer of the entire corneal structure. It can be described as a mono layer of cubic, contiguous cells that form a hexagonal pavement. These cells have a spherical nucleus (occupying almost the entire cell structure), numerous mitochondria, endoplasmic reticulum and Golgi apparatus. They are typically involved in molecular synthesis and energy production. This layer is very thin, with 4 to 6 μm width and its cells have high metabolic activity. In the endothelial layer, there are no intercellular spaces. Cells are linked through gap junctions to allow the transference of small molecules and electrolytes between them. Despite the increased metabolic activity, endothelial cells do not have renewing capacity. Throughout the human life, the endothelium thickness and cell density decrease and its permeability increases. The main function of the endothelium is to control the penetration of substances from the aqueous humor to ensure the normal hydration of stroma (Quadrado, 2013).

Confocal microscopy is the standard method to image the different corneal layers and correspondent cells and structures. Examples of corneal confocal images are depicted in Figure 7.5. With this type of imaging system, all the layers can be easily distinguished and the different morphology of the cells easily identifiable.

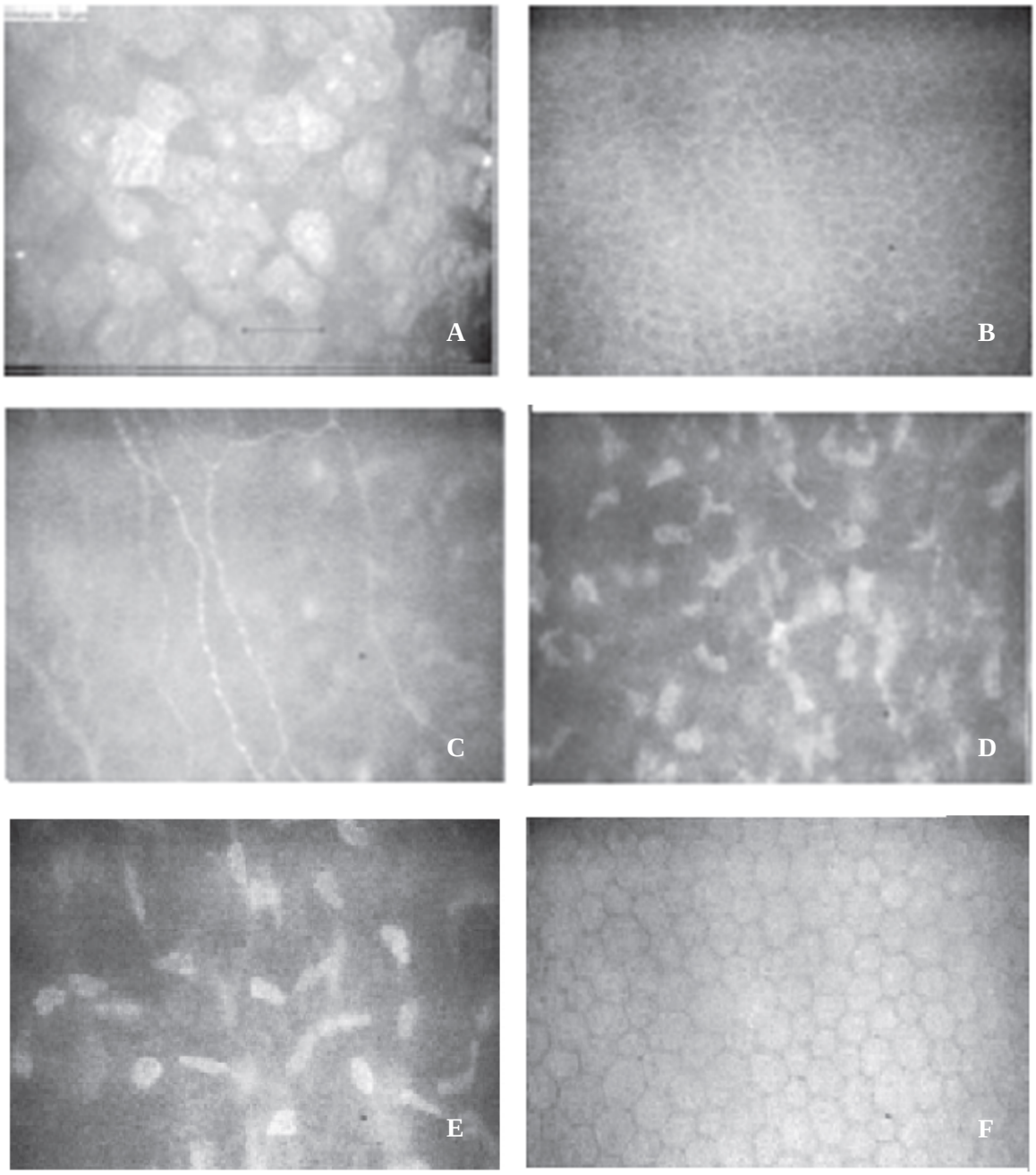

Figure 7.5 - Corneal confocal microscopic images. A - Superficial epithelial cells. B - Basal epithelial cells; C – Bowman's Layer with sub-basal nerve plexus; D – Anterior Stroma; E – Posterior Stroma; F - Endothelium (Tavakoli et al, 2008).

B. Imaging trials on animal corneas

Here, we report on our efforts on corneal imaging using whole corneal buttons from animals.

We started by trying to image bovine corneas collected in a local slaughterhouse. Bovine corneas have around 1000 µm in thickness, with an average value around 29.8 mm for the horizontal meridian and around 23.9 mm for the vertical meridian. Multiphoton microscopy on bovine corneas was already achieved, using the signal from NADH fluorescence to image cellular

morphology and second harmonic generation to image collagen fibers (Lai and Tang, 2014). Together with the large availability of samples from slaughterhouses, this suggested that bovine corneas could be the perfect candidate to test the system.

However, although FAD fluorescence signal was detectable, structurally it was impossible to distinguish between corneal layers. Structured illumination was also hard to implement since the out-of-focus contributions were too high and pattern contrast was very low. Bovine cornea is a very thick sample. It has 5 layers as the human cornea, but around twice the thickness (Doughty, Petrou and Macmillan, 1995). This made impossible to identify structural features, since more out-of-focus contributions degraded completely the image contrast and made impossible the implementation of optical sectioning through structured illumination. Therefore, we quit using bovine corneas and chose to use samples from a different animal with thinner corneas.

Chicken corneas were selected as an adequate alternative to bovine corneas. Despite not being from mammalian origin, chicken cornea is similar to human cornea, presenting the same layer structure and without great discrepancies in size and thickness. It was used as model to study corneal pathologies specially in the corneal wound healing field (Fowler *et al.*, 2004; Ritchey *et al.*, 2011). Chicken cornea has a total thickness of 405 ± 10 µm, which is inferior to that of the human cornea (500 µm). However, the thicknesses of their layers are very close to those of human corneas, when considered in relative terms, as percentage of the total corneal thickness, as Table 7.1 (Fowler *et al.*, 2004).

Table 7.1 - Comparison of chicken and human corneal anatomy (Fowler et al., 2004).

	THICKNESS (µm)		THICKNESS (% OF TOTAL)	
	Chicken	**Human**	**Chicken**	**Human**
Epithelium	35 ± 1	50-52	9	10
Bowman's layer	5.2 ± 0.3	8-10	1.3	1.7
Stroma	355 ± 10	~470	88	~87
Descemet's membrane	3.2 ± 0.1	~7 (3-12)	0.8	1.3
Endothelium	4.0 ± 0.2	4-6	1	1
Total	405 ± 10	520-540	~100	~100

First trials concerned the imaging of corneal epithelial cells using the reflectance mode of the microscope. We were only able to image the epithelial basal cells, probably for being anterior to the diopter corresponding to the interface between epithelium and Bowman's membrane. Once again, structured illumination could not be applied because the projected sinusoidal pattern did not have enough contrast to be detected by the structured illumination algorithms. The reflectance wide-field mode made possible to image functional alterations on the basal cells. An example is presented in Figure 7.6 where images A and B were acquired with a difference of 8 hours. It is visible that the cells contrast is reduced, due to increased scattering on the second acquisition. Corneal opacity increases with increasing post-mortem time and explains the observed contrast reduction.

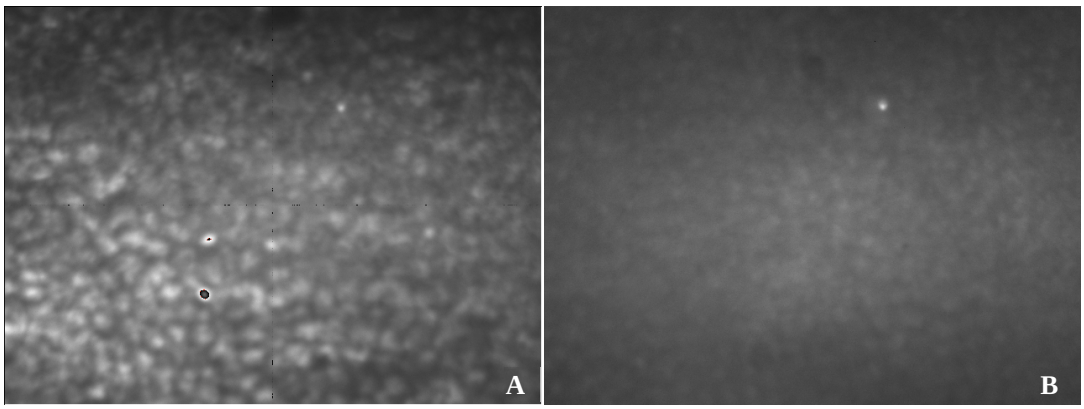

Figure 7.6 - Epithelial basal cells, reflectance images 2 and 8 hours post-mortem.

It was very hard to achieve FAD fluorescence imaging of basal epithelial cells imaging. We were never able to achieve structured illumination of corneal samples on fluorescence mode. Chicken cornea still has around 400 micrometers in thickness and although being transparent, fluorescence blurring from the out of focus planes prevented the projection of the sinusoidal pattern with enough contrast on deep layers. However, it was possible to image corneal epithelial cells in fluorescence widefield mode. Although this result was not repeatable in every cornea tested. Figure 7.7 andFigure 7.8 are examples of images of corneal basal epithelial cells acquired in fluorescence wide-field mode.

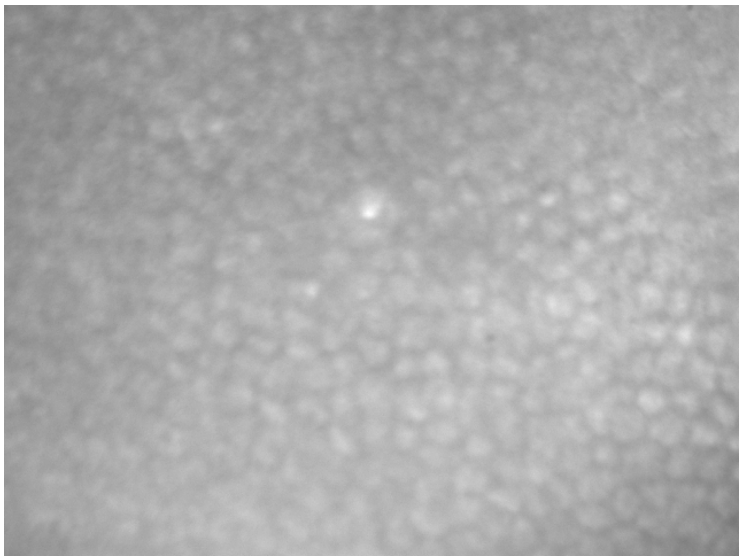

Figure 7.7 - Epithelial basal cells, image acquired in fluorescence mode with Zeiss Achroplan 40Wx objective.

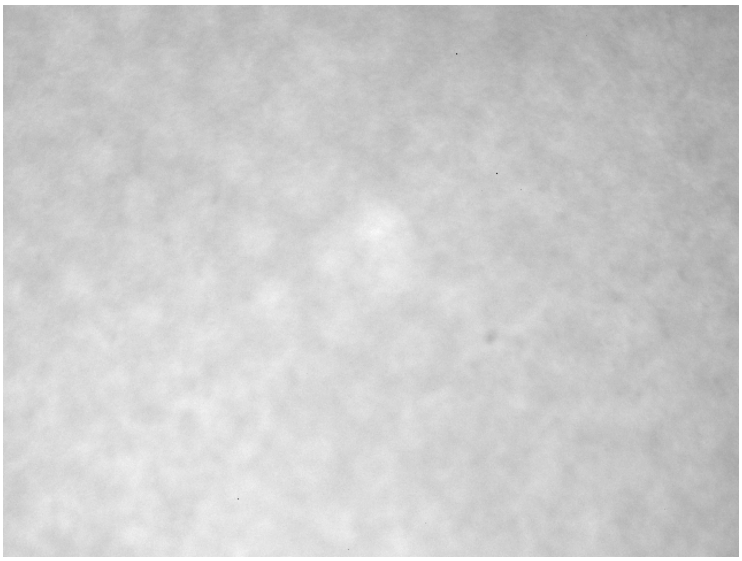

Figure 7.8 - Image of corneal epithelial cells acquired in fluroescence mode using widefield illumination and with Olympus 60Wx objective.

It was also possible to image corneal endothelial cells in widefield fluorescence mode. This was not done by imaging from the anterior side, but instead by flipping the sample and imaging directly from the posterior side. Once again, this result was not achieved in every cornea tested and structured illumination imaging could not be performed due to the reasons previously described. Examples of images acquired from the endothelial layer of the cornea are depicted in Figure 7.9.

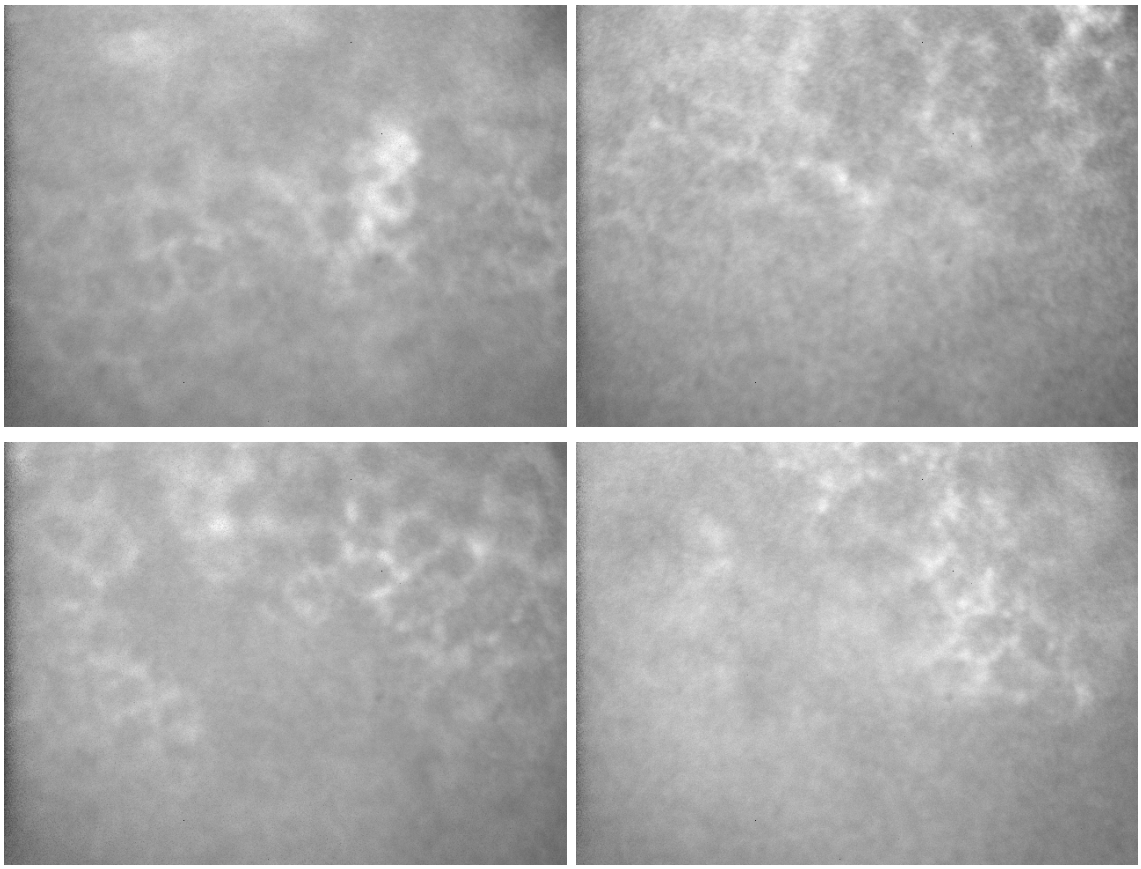

Figure 7.9 - Images of corneal endothelial cells acquired in fluorescence mode with widefield illumination.

To obtain the images depicted in Figure 7.2 to Figure 7.4, the exposure time and the MCP gain had to be increased to very high levels. As already pointed out in studies with multiphoton microscopy (Batista, Hans G. Breunig, *et al.*, 2018), FAD concentration in corneal cells is much lower than expected, making difficult to obtain enough fluorescence signal to acquire a fluorescence decay curve with adequate SNR, even with two-photon excitation. Moreover, and as a consequence of this low signal, fluorescence from other structures of corneal affects this measurement. Collagen, as pointed out by Schweitzer et al (Schweitzer *et al.*, 2007), has a fluorescence excitation and emission spectra very close that of FAD in cells. Due to the high concentration of collagen in corneal stroma, fluorescence coming from this structure affects the measurements of corneal epithelial and endothelial cells. Figure 7.10 represents the fluorescence image of a transversal cut of an unstained human cornea imaged under the time-gated microscope. The stroma and the epithelium are visible, which indicates that there is some fluorescence emission from both structures. Although, epithelium is brighter than stroma, this confirms that fluorescence coming from collagen degrades the isolation of FAD fluorescence, creating a strong background of fluorescence when epithelial and endothelial layers are focused. The presence of collagen fluorescence may also be one of the causes that complicated the application of structured

illumination. This strong background degraded pattern projected contrast and rendering it impossible to apply.

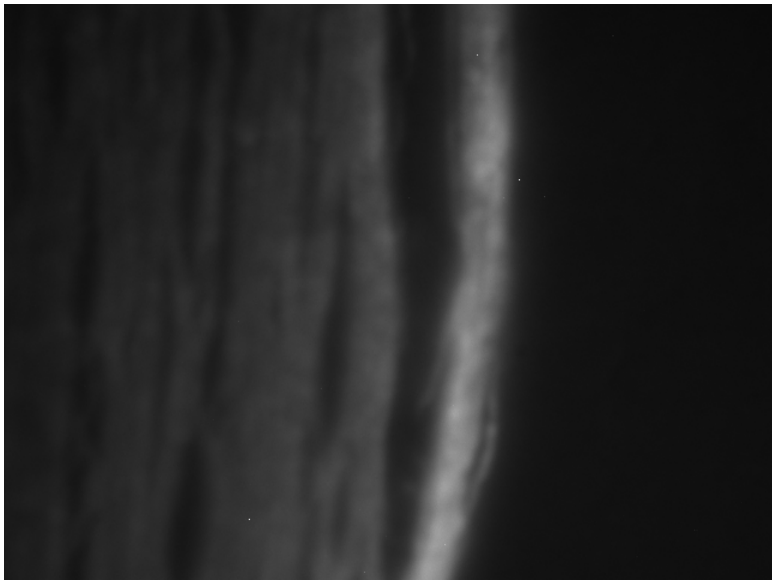

Figure 7.10 - Fluorescence Image of Stroma and Epithelium.

Additionally, the high exposure times required to image FAD in cells causes fluorescence photobleaching. This phenomenon involves a photochemical modification of the fluorophore that results in irreversible loss of its ability to emit fluorescence and affects the fluorescence intensity images that will present lower signal and, consequently, reduced SNR. Fluorescence lifetimes are not directly affected by photobleaching. However, photobleaching interferes with lifetime measurement by the time-gated technique whenever all the delayed acquisition windows are not acquired in the same excitation cycle. In our instrument only one acquisition window is active per excitation cycle. So, the final acquisition windows will deal with a photobleached sample of fluorophores that will emit a lower fluorescence signal by the natural fluorescence decay. Therefore, when acquiring sequentially gated fluorescence intensity images it is highly likely that the curve obtained under these conditions will have a different decay rate than what was expected, affecting the accuracy of the lifetime measurement.

This effect was verified on a few trials to measure the fluorescence decay curve of corneal samples, either with or without visible cells on the image.

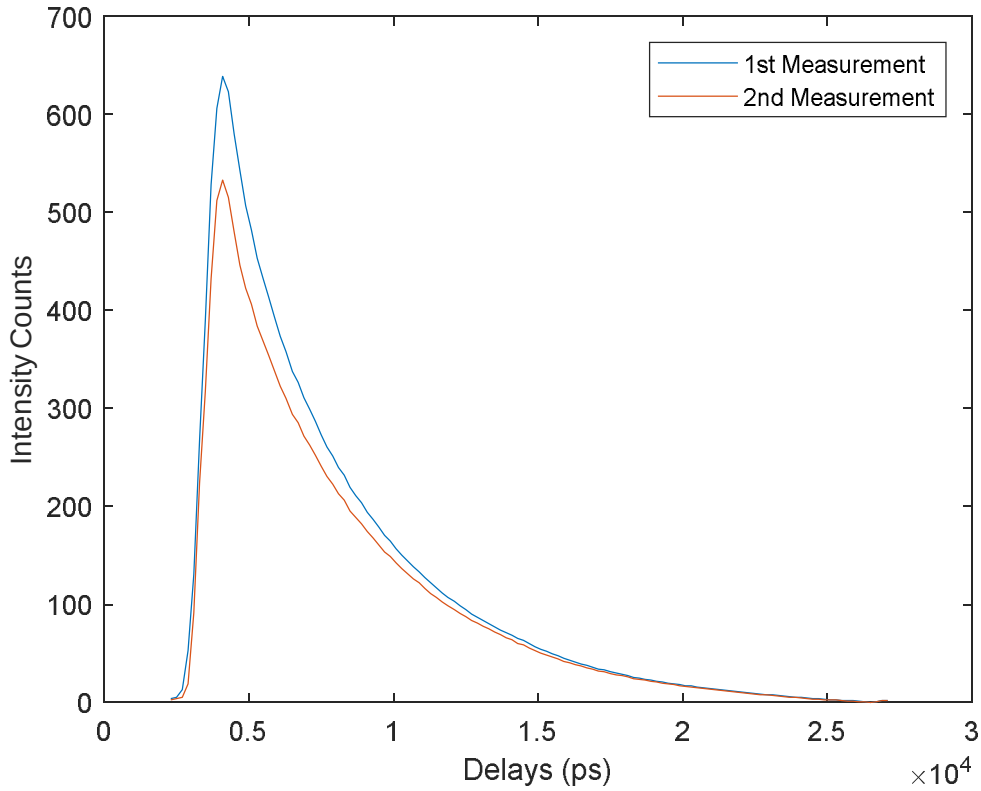

Figure 7.11 – Two consecutive fluorescence lifetime decays of chicken corneas in which each gated image has an exposure time of 5120 ms, taking 10.66 minutes to acquire an entire scan.

Figure 7.11 represents two consecutive average fluorescence decay curves acquired from the epithelial side of a chicken cornea. Each gated image has an exposure time of 5120 ms with a total scan time of 10.66 minutes. It is visible that the intensity of the fluorescence decay curve peak decreases from the first measurement to the second one. When normalizing the curves - Figure 7.12, it is also visible that their shape and decay rates are different. This can be explained by the effects of the photobleaching.

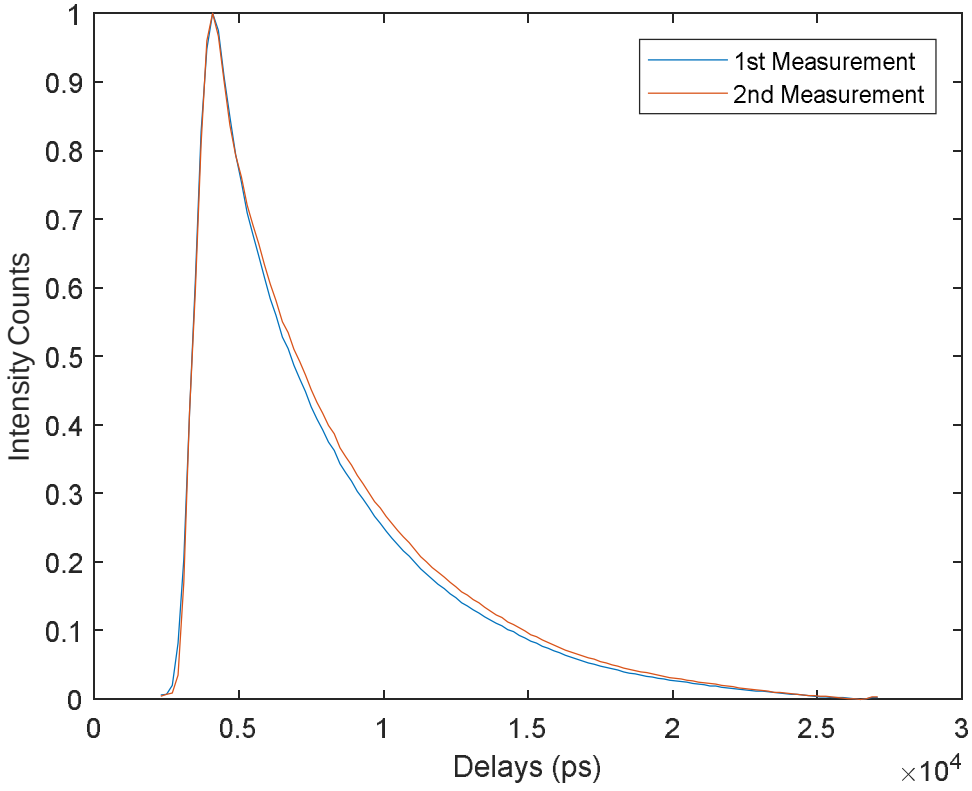

Figure 7.12 – The fluorescence decays represented in Figure 7.11, but normalized to the measured maximum value.

Nevertheless, some measurements of fluorescence lifetime were still performed with both epithelial and endothelial sides of the chicken corneas. The analysis was performed with FLIMfit and the obtained results are summarized in Table 7.2. Although the lifetime values are completely different from the ones reported with multiphoton studies (see Table.6.1 and (Batista *et al.*, 2016)), particularly in what τ_1 is considered, we were able to identify a double-exponential decay curve with more presence of short-lifetime components, as expected.

Table 7.2 – Fluorescence decay parameters obtained from analysis of fluorescence decay curves obtained in both epithelium and endothelium of chicken corneas.

CORNEAL LAYER	τ_1	τ_2	α_1	α_2	MEAN T	CHI-SQR
Epithelium	4468 ps	442 ps	0.23	0.77	1358 ps	1.77
Endothelium	4467 ps	417 ps	0.1	0.9	828 ps	2.17

Chapter 8 Final Discussion and Conclusions

As stated in the Introduction section of this document, the main objective of this project was to evaluate the performance and suitability of the wide-field time-gated fluorescence lifetime microscopy technique for metabolic assessment of thick tissues. This evaluation had to be done having in mind the conditions required by *in vivo* image acquisition.

For accomplishing this main objective, it was deemed necessary:

- To design, setup and characterize a time-gated fluorescence lifetime microscope for widefield imaging of FAD fluorescence.
- To evaluate the performance of optical sectioning methods for widefield microscopy.
- To determine the limits of accuracy and precision of the RLD algorithms in the intended operating conditions of the instrument.

The first tasks of the project concerned the design and the setup of the time-gated microscope hardware and its supporting software applications and the testing and characterization of its performance. Regarding this, it can be concluded that the final instrument obtained and described in Chapter 4 fulfilled the optical parameters required for acquiring FAD fluorescence from cells, particularly the field of view and the lateral resolution. The developed microscope also complies with the timing requirements to measure the fluorescence decay parameters usually associated with FAD fluorescence emission from cells, as long as standard IRF deconvolution techniques are used. As expected, lifetime determination of short lifetimes is more challenging than for longer lifetimes, a common observation working with fluorescence lifetime systems that resent enlarged IRFs. Measurement comparisons between the developed time-gated microscope and a commercial TCSPC microscope, demonstrated that our instrument measures accurately fluorescence lifetimes within the tested range of values. Measurement precision for short decay lifetimes is worse than that obtained with the TCSPC. This is an expected result in face of the much better counting statistics obtained with the TCSPC microscope.

The second partial objective defined above concerned the evaluation of optical sectioning methods for widefield imaging, particularly structured illumination methods. This objective deals with a very important aspect of the project, since optical sectioning is a mandatory requirement for imaging multilayer tissues with cellular resolution. During this work, we did several experiments with structured illumination using test samples like capillaries filled with fluorescent solutions and thick biological tissues, namely corneal samples. On the test samples, we could verify that the optical sectioning measured for both implemented techniques (3-phase and HiLo)

fulfills the project requirements and meets the optical sectioning performance commonly found in confocal microscopes. Moreover, when images from samples with components in-focus and out-of-focus with similar fluorescence intensities are processed, the out-of-focus contribution is easily eliminated. On the other hand, this is only true if processed images have a high SNR. When the noise level is close to the signal level, optical sectioning techniques start to fail, and the out-of-focus components remain present in the processed images. Another case where the tested wide-field optical sectioning techniques did not perform adequately is when different fluorescence species are being imaged and those in-focus are dimmer than the ones located out-of-focus. In this case, the ability of the algorithms to eliminate the out-of-focus components is also limited. These observations can be explained by the high dependence of the structured illumination algorithms on the contrast of the pattern projected into the in-focus components. High performance implies a very high value of contrast, limiting their applicability to images with very high SNR. This limitation has a large impact on the possibility of imaging thick biological samples, as discussed later in this chapter,

It was also important to evaluate if the structured illumination algorithms degraded the accuracy and the precision of the measures obtained for the fluorescence decay parameters. The results we presented in Chapter 6 show that while HiLo algorithm did not affect the accuracy of the fluorescence lifetime measurements, it degraded their precision. This is a direct consequence of the noisier images that result from HiLo processing and emphasizes the importance of acquiring images with a high SNR when using structured illumination techniques for optical sectioning.

It is important to note that the structured illumination algorithm has to be applied in all the acquired images. The performance of the algorithm will be more affected by the images corresponding to larger delays relatively to the excitation pulse. Let us consider a 12-bit camera like the one installed on our time-gated microscope and the acquisition of just 4 images in accordance with the RLD algorithm. A simple calculation for the FAD decay parameters leads to an average pixel value around 900 for the fourth image, when using the maximum dynamic range on the first image. This result, obtained for contiguous windowing with a nominal gate width of 1000 ps, corresponds to 6300 electrons in the CCD. For this signal level, the best SNR possible, considering just Poisson shot noise associated with photon detection, is close to 38 dB. This is the best possible solution and it is implied that the use of the whole dynamic range on the first image is possible within an acceptable gate exposure, a condition that is not easy to meet for weakly emitting samples. Therefore, we could conclude that is difficult to make compatible the SNR requirement posed by the successful application of the structured illumination algorithms with the requirement of not using frame summing from the image acquisition time constraints associated to *in vivo* applications.

A critical part of this project was the assessment of the application of the time-gated microscope to biological samples imaging. As explained on the Introduction section, this project was designed in the sequence of an existing research line on corneal imaging methods and instrumentation. At start, the corneas were an adequate candidate for metabolic imaging based on wide-field time-gated fluorescence lifetime measurement. Its anatomical location, as the most exterior structure of the human eye, provides easy accessibility without being hampered by scattering in anterior tissues. Its lack of vascular network decreases substantially the absorption effects and eases the task of isolating the FAD signal. The main concerns were related to its challenging thickness and transparency that would pose a demanding test on the limits of wide-field optical-sectioning techniques. As we already explained, since the microscope is based on one-photon excitation, we chose to detect only FAD signals since NADH spectra would require UV-excitation, raising laser safety issues. The detection of FAD signal from corneas with the developed microscope proved to be a very difficult task. First, as it was recently proved on a collaborative project, involving our research group, using multiphoton excitation techniques (Batista, Hans G. Breunig, *et al.*, 2018), FAD signal is much weaker than expected in corneal cells, making its detection very difficult and reliant on high MCP gains and long exposure times. On the other hand, and again due to the low FAD signal, the projection of the sinusoidal patterns required by the structured illumination techniques was practically impossible. The contrast was always too low to even apply the algorithms. Therefore, it was not possible to obtain optical sectioned images of corneal tissues. Moreover, the long exposure times required to acquire a complete fluorescence decay curve degraded the fluorescence signal resulting in large accuracy error, as the measured lifetime values were never similar to those reported by studies with multiphoton microscopy. Considering this, we must conclude that Time-Gated microscopy with optical sectioning through structured illumination techniques is not adequate to image FAD in whole corneas. The developed time-gated microscope can be used to image other biological samples that have higher concentrations of fluorophores within its range of excitation and detection, allowing easier applications of structured illumination and operation with shorter exposure times and lower MCP gains.

Regarding the studies on RLD accuracy and precision, we focused our efforts on the FAD decay parameters since this was our target molecule. Initial simulations dealt with “softer” conditions, namely Poisson noise limited images with a high number of counts, not representative of the actual operating conditions that we wished to analyze. These simulations guided us in the design of the following round of simulations that considered not only the influence of the IRF of the time-gated microscope but also a realistic model of noise on gated intensified cameras. The simulations for counts higher than 10^4 demonstrated that, as expected, the accuracy and precision of the decay parameters improves for higher total counts being almost independent of the camera gain for counts higher than 10^6. For total counts between 10^4 and 10^5, the accuracy and the

precision are better when using lower gains in the intensified camera, a result explained by the contribution from the image intensifier to the image variance. More important, those simulations showed that it is possible to obtain a good accuracy (RME lower than 5.0%) on the free to protein-bound ratio for total counts higher than 10^4, if we restrict the gain k to values equal or lower than 5.2, and that the ratio precision is not degraded by the measurement, being close to the precision defined in the sample. The accuracy on the fluorescence lifetimes is adequate (RME always below 4%). The only significant precision degradation occurs for the shortest lifetime (τ_1).

The results stated above were obtained with a standard windowing scheme: contiguous windowing with a nominal gate width of 1000 ps. Although the determination of the optimal gating scheme for RLD usage requires the *a priori* knowledge of the lifetime values of the sample, our results show that is not difficult to obtain adequate values of accuracy and precision, provided that the total number of counts under the sampled decay curve is adequate. These results validate the use of RLD algorithm for FAD metabolic imaging whenever the acquisition conditions allow a TC value higher than $10^{4.}$ It was particularly important to verify the accuracy and precision associated with the metabolic ratio since the RLD performance on measuring this metabolic indicator is not addressed in the published literature.

It is important to note that, if necessary, *a priori* knowledge on the fluorescence decay parameters for setting optimal gating schemes, can be obtained with thorough studies using other techniques of lifetime analysis (such as non-linear least squares deconvolution). This is often the case when setting up a new application based on lifetime analysis of fluorescence decays.

The objectives of this project required the evaluation of the RLD performance on the much more demanding regime of total counts lower than 10^4. We carried out several simulations of FAD fluorescence decay measurement through RLD. Our results show that the measurement accuracy is always better for the longer lifetime, τ_2, a result that reflects the influence of the system IRF, which is not considered when applying the standard RLD algorithm. The shorter lifetime τ_1 is in the order of 500 ps, a value that is not two orders of magnitude shorter than the IRF width, since the laser pulse alone has a width ranging from 63 to 190 ps. Improving the accuracy on the value of the shorter wavelength would require the use of expensive femtosecond lasers or the modification of the RLD algorithm to account for and correct the effect of the IRF width.

As expected, the gate separation that yields the maximum fluorescence lifetime accuracy (RME near zero) depends highly on the decay parameters. Please note that, although we do not present these results, we confirmed the literature reports stating that the gate separation has a much higher impact of the performance of RLD than the gate width. We could conclude that the accuracy of τ_2 is always better than 10% for gate separations higher than 800 ps and that the accuracy of τ_1 is

clearly better for gains equal or lower than $k \leq 11.1$, with an optimal region for gate separations between 1000 and 2000 ps.

Concerning precision, the performance for τ_1 is clearly better for low gains ($k \leq 2.41$), with an optimal region for gate separations between 1000 and 1800 ps. However, the precision error is almost always higher than 20%. The performance of τ_2 is better, with RSD values better than 10% for gate separations equal or higher than 1800 ps at low gains ($k \leq 11.1$).

From these observations, it is possible to define an optimal region for FAD fluorescence lifetime accuracy and precision: gate separations around 1800 ps and low gains (1.05 or 2.41).

Our simulations revealed that the accuracy of the fractional contributions α_1 and α_2 and of the metabolic ratio α_2/α_1 remains rather stable for $k \leq 2.41$ and Δt>1000 ps. This is an important result since, contrary to what happens for the fluorescence lifetimes, *a priori* knowledge on α_1 and α_2 is not easy to obtain, because the values of these parameters depend highly on the cells' metabolic state. Therefore, it is advisable to operate the instrument on a regime where the measurement performance is as independent as possible from the adopted windowing scheme. For the mentioned operating region, it is possible to obtain a ratio accuracy error around 15%.

The results also show that the precision of α_1, α_2 and of the metabolic ratio almost stabilizes for gate separations between 1500 and 2500 ps, for all k values. In this operating region, the precision of the metabolic ratio is near the limit posed by error propagation. The best precisions are obtained for $k = 2.41$. However, the ratio precision is always worse than 10%. These precision results are compatible with those related to the accuracy, allowing to define the same optimal region.

Finally, we studied the RLD performance for a range of values of the metabolic ratio, fixing the operating conditions on the optimal region determined by our previous simulations. We also ran simulations where we varied the gate separation value to cover the ranges of stable accuracy and precision previously identified. The results clearly demonstrate the impossibility of finding an optimal acquisition setting for the time-gated fluorescence lifetime microscope when using the RLD algorithm, since the quality of the measurement of the metabolic ratio depends on its value: higher values of metabolic ratio will have worse precision and better accuracy. Moreover, no value of gate separation offers measurement performance independent of the ratio value being measured, although, for any ratio value, its precision is quite stable for gate separations between 1500 and 2500 ps.

So, the final conclusion is that the accuracy and the precision associated to the value of the metabolic ratio obtained using RLD on a time-gated fluorescence lifetime microscope not only depends on the adopted windowing scheme, but also on the nominal value of the ratio. For the ranges of gate separation and metabolic ratio we considered, the accuracy error can be as high as

30% and the precision error can reach a value around 60% Precision errors lower than 10% cannot be obtained.

This raises the question of whether metabolic imaging through fluorescence lifetime imaging should rely on the RLD algorithm for measuring the decay parameters: the answer depends highly on the application, namely on the expected range of metabolic ratio values. Applications where the range of expected ratio values lies between 0.25 and 1.22 yield precision errors between 13.5% and 25% for TC values lower than 10^4. These precision errors can be acceptable for certain applications.

Our results show that RLD must be always an option to consider since it offers fast image acquisition capabilities. If high precision is mandatory, the solution is to increase the total number of counts either by summing frames or using pixel binning. The simulation results show that RLD performance improves a lot for TC higher than 10^4, which, allied with its acquisition speed, can make RLD quite advantageous for imaging biological samples.

In theory, the effect of the IRF of the microscope in the measurement accuracy can be corrected by deconvolution the IRF from the acquired data. Although this was never proposed for the RLD method, we demonstrated its benefits on accuracy improvement for single-exponential decays. So far, we were not able to produce an adequate deconvolution method for the four gate RLD algorithm. While for single-exponential decays, the RLD deconvolution was relatively straightforward to implement, since the decay equation is easily linearized, and the lifetime deviation always occurs in the direction of higher lifetimes, the same does not apply to double-exponential decays. Here, the four decay parameters can deviate for increased or decreased values and the deconvolution problem becomes an ill-poised problem. Like what happens when deconvoluting the IRF from TCSPC data, the deconvolution process is in fact a sequence of convolution operations between a decay function proposal and the IRF curve followed by fitting to the experimental data. In RLD, this approach is rather difficult since we only have four data points (four gates) per decay curve. The search for a RLD deconvolution method for double-exponential decays is a research theme still being pursued at our group.

While using the developed time-gated microscope to try to obtain metabolic maps of chicken cornea cells, we were able to identify the weak points of this microscope and to update the requirements to obtain a solution for metabolic imaging of cornea with one-photon excitation. The results obtained by our group with multiphoton microscopy also helped in determining these requirements. Considering the incapacity of applying structured illumination methods on corneal tissues, a different method of optical sectioning should be selected. Therefore, the most suitable candidate is confocal microscopy. The great majority of confocal microscopy applications with fluorescence lifetime detection relies on TCSPC acquisition. This could be a possible solution,

since fluorescence images based on FAD signal were imaged with this type of microscope. However, to maintain the scope of this work and use Time-Gated detection, a possible solution would be to reuse the DMD to implement the confocal pinholes or the confocal slits (the two architectures are possible, the second is only truly confocal in the direction of the smaller dimension of the slit but has the advantage of much higher light throughput) and transform the time-gated microscope into a confocal microscope. This type of DMD implementation for confocal microscopy was already successfully applied (Wang *et al.*, 2016). However, maintaining the used laser source in this new setup would not be the best solution since DMD implementations imply great losses of optical power, limiting the final power that would reach the cornea. Moreover, due to the low FAD fluorescence signal detected with our experiments and confirmed by the multiphoton imaging measurements, basing the metabolic imaging on the single excitation of this molecule would not be the best option. Adding an UV source for allowing the detection of NADH fluorescence and increasing the laser power to account for the losses implied by the DMD and other optical elements required would be a possible solution. Nevertheless, the use of UV excitation sources needs to be carefully addressed since with this type of sources, biological tissues can suffer damage through photochemical interactions. A laser safety study to evaluate the feasibility and the limits of their use would be mandatory. On the other hand, while considering a confocal Time-Gated approach, the RLD methods studied and described in Chapter 6 on this thesis would still be applied, helping to achieve faster acquisition times compatible with the application of these techniques to *in vivo* specimens.

References

Abraham, H. and Lemoine, J. (1899) ‘Disparition instantanée du phénomène de Kerr. Comptes Rendus Hebdomadaines des Seances de Academie des Sciences’, *Sciences Naturelles*, 129, pp. 206–208.

Abraham, H. and Lemoine, J. (1900) ‘Nouvelle méthode de mesure des durées infinitesimals. Analyse de la disparition des phénomènes électro-optiques’, *Ann Chim*, 20, pp. 264–287.

Ballew, R. and Demas, J. (1989) ‘An error analysis of the rapid lifetime determination method for the evaluation of single exponential decays’, *Analytical Chemistry*, pp. 30–33. Available at: http://pubs.acs.org/doi/pdf/10.1021/ac00176a007 (Accessed: 27 October 2013).

Ballew, R. M. and Demas, J. N. (1991) ‘Error analysis of the rapid lifetime determination method for single exponential decays with a non-zero baseline’, *Analytica Chimica Acta*, 245(C), pp. 121–127. doi: 10.1016/S0003-2670(00)80210-X.

Batista, A. *et al.* (2016) ‘Two-photon spectral fluorescence lifetime and second-harmonic generation imaging of the porcine cornea with a 12-femtosecond laser microscope.’, *Journal of biomedical optics*, 21(3), p. 36002. doi: 10.1117/1.JBO.21.3.036002.

Batista, A., Breunig, H. G., *et al.* (2018a) ‘Assessment of Human Corneas Prior to Transplantation Using High-Resolution Two-Photon Imaging’, *Investigative Opthalmology & Visual Science*. The Association for Research in Vision and Ophthalmology, 59(1), p. 176. doi: 10.1167/iovs.17-22002.

Batista, A., Breunig, H. G., *et al.* (2018) ‘Assessment of the metabolism and morphology of the porcine cornea, lens and retina by 2-photon imaging’, *Journal of Biophotonics*. Wiley-Blackwell, 11(7), p. e201700324. doi: 10.1002/jbio.201700324.

Batista, A., Breunig, H. G., *et al.* (2018b) ‘High-resolution, label-free two-photon imaging of diseased human corneas’, *Journal of Biomedical Optics*. International Society for Optics and Photonics, 23(03), p. 1. doi: 10.1117/1.JBO.23.3.036002.

Batista, A. (2018) *Two-photon imaging of the cornea using femtosecond laser microscopes and tomographs*. Saarland University - Saarbrücken.

Becker, W. (1993) ‘Verfahren und Vorrichtung zur Messung von Lichtsignalen durch Einzelphotonenz{ä}hlung mit zeitlicher und r{ä}umlicher Aufl{ö}sung Method and apparatus for measuring light signals by single photon counting with temporal and spatial resolution’. Google Patents. Available at: http://www.google.com.na/patents/DE4339787C2?cl=en.

Becker, W. (2005) *Advanced Time-Correlated Single Photon Counting Techniques, Journal of Microscopy*. doi: 10.1007/3-540-28882-1.

Becker, W. (2015) *Springer Series in Chemical Physics 111: Advanced Time- Correlated Single Photon Counting Applications*. doi: 10.1007/978-3-319-14929-5.

Becquerel, E. (1867) 'La lumière, ses causes et ses effets'. Paris: Firmin Didot frères, fils et cie. Available at: http://catalog.hathitrust.org/Record/011601769.

Bird, D. K. *et al.* (2005) 'Metabolic Mapping of MCF10A Human Breast Cells via Multiphoton Fluorescence Lifetime Imaging of the Coenzyme NADH', *Cancer Research*. United States, 65(19), pp. 8766–8773. doi: 10.1158/0008-5472.CAN-04-3922.

Bollinger, L. M. and Thomas, G. E. (1961) 'Measurement of the Time Dependence of Scintillation Intensity by a Delayed-Coincidence Method', *Review of Scientific Instruments*, 32(9).

Braslavsky, S. E. (2007) 'Glossary of terms used in photochemistry, 3rd edition (IUPAC Recommendations 2006)', *Pure and Applied Chemistry*, 79(3), pp. 293–465. doi: 10.1351/pac200779030293.

Brody, S. S. (1957) 'Instrument to Measure Fluorescence Lifetimes in the Millimicrosecond Region', *Review of Scientific Instruments*, 28(12), pp. 1021–1026.

Bueno, J. M. *et al.* (2011) 'Multiphoton microscopy of ex vivo corneas after collagen cross-linking', *Investigative Ophthalmology and Visual Science*, 52(8), pp. 5325–5331. doi: 10.1167/iovs.11-7184.

Chalam, K. *et al.* (2011) *Fundamentals and Principles of Ophtalmology, Basic and clinical science course ; 2011-2012, section 2*. American Academy of Ophtahalmology - The Eye M.D. Association.

Chance, B. *et al.* (1962) 'Intracellular Oxidation Reduction States in Vivo', 137(3529), pp. 499–508.

Chance, B. *et al.* (1979) 'Oxidation-reduction ratio studies of mitochondria in freeze-trapped samples. NADH and flavoprotein fluorescence signals.', *Journal of Biological Chemistry*, 254(11), pp. 4764–4771.

Chance, B. and Lieberman, M. (1978) 'Intrinsic fluorescence emission from the cornea at low temperatures: evidence of mitochondrial signals and their differing redox states in epithelial and endothelial sides.', *Experimental eye research*, 26(1), pp. 111–117. doi: 10.1016/0014-4835(78)90159-8.

Chang, C.-W. (2009) *Improving Accuracy and Precision in Biological Applications of Fluorescence Lifetime Imaging Microscopy*. University of Michigan.

Chang, C.-W. and Mycek, M.-A. (2010) 'Enhancing precision in time-domain fluorescence lifetime imaging.', *Journal of biomedical optics*, 15(5), p. 056013. doi: 10.1117/1.3494566.

Chorvat, D. and Chorvatova, A. (2009) 'Multi-wavelength fluorescence lifetime spectroscopy: a new approach to the study of endogenous fluorescence in living cells and tissues', *Laser Physics Letters*. WILEY-VCH Verlag, 6(3), pp. 175–193. doi: 10.1002/lapl.200810132.

Christensen, T. M., Hurn, A. S. and Lindsay, K. A. (2008) 'The Devil is in the Detail: Hints for Practical Optimisation', *Economic Analysis and Policy*. Elsevier, 38(2), pp. 345–368. doi: 10.1016/S0313-5926(08)50025-7.

Cole, M. J. *et al.* (2000) 'Whole-field optically sectioned fluorescence lifetime imaging.', *Optics letters*, 25(18), pp. 1361–1363. doi: 10.1364/OL.25.001361.

Cole, M. J. *et al.* (2001) 'Time-domain whole-field fluorescence lifetime imaging with optical sectioning.', *Journal of microscopy*, 203(Pt 3), pp. 246–257. doi: 10.1046/j.1365-2818.2001.00894.x.

Cooper, G. M. and Hausman, R. E. (2007) *The Cell - A Molecular Approach*. 4th edn. Sunderland: Sinauer Associates.

Cova, S., Bertolaccini, M. and Bussolati, C. (1973) 'The measurement of luminescence waveforms by single-photon techniques', *physica status solidi (a)*. WILEY-VCH Verlag, 18(1), pp. 11–62. doi: 10.1002/pssa.2210180102.

Cubeddu, R. *et al.* (1995) 'Tumor detection in mice by measurement of fluorescence decay time matrices', *Opt. Lett.*, 20(24), pp. 2553–2555. doi: 10.1364/OL.20.002553.

Cubeddu, R., Taroni, P. and Valentini, G. (1993) 'Time-gated imaging system for tumor diagnosis', *Optical Engineering*, 32(2), pp. 320–325. doi: 10.1117/12.60754.

Cunha-Vaz, J., Domingues, J. P. and Correia, A. C. M. B. (2000) 'Ocular fluorometer'. US.

Dan, D. *et al.* (2013) 'DMD-based LED-illumination super-resolution and optical sectioning microscopy.', *Scientific reports*, 3, p. 1116. doi: 10.1038/srep01116.

Domingues, J. P., Branco, I. and Morgado, A. M. (2010) 'Corneal quantitative fluorometry - A slit-lamp based platform', in *IFMBE Proceedings*. Springer, Berlin, Heidelberg, pp. 475–478. doi: 10.1007/978-3-642-13039-7_119.

Doughty, M. J., Petrou, S. and Macmillan, H. (1995) 'Anatomy and morphology of the cornea of

bovine eyes from a slaughterhouse', *Canadian Journal of Zoology*, 73(11), pp. 2159–2165. doi: 10.1139/z95-253.

Dowling, K. *et al.* (1998) 'Fluorescence lifetime imaging with picosecond resolution for biomedical applications', 23(10), pp. 810–812.

Dupuis, G. *et al.* (2013) 'Time-resolved wide-field optically sectioned fluorescence microscopy', *SPIE BiOS*, (FEBRUARY 2013), p. 85890H–85890H–8. doi: 10.1117/12.2003966.

Eberhardt, E. H. (1979) 'Gain model for microchannel plates.', *Applied optics*. United States, 18(9), pp. 1418–1423.

Edelhauser HF and Ubels JL (2002) 'Cornea and Sclera', in Kaufman, P. and Alm, A. (eds) *Adler's physiology of the eye*. Mosby, pp. 47–117.

Elson, D. S. *et al.* (2002) 'Wide-field fluorescence lifetime imaging with optical sectioning and spectral resolution applied to biological samples', *Journal of Modern Optics*, 49(5–6), pp. 985–995. doi: 10.1080/09500340110109377.

Elson, D. S. *et al.* (2004) 'Real-time time-domain fluorescence lifetime imaging including single-shot acquisition with a segmented optical image intensifier', *New Journal of Physics*, 6, pp. 1–13. doi: 10.1088/1367-2630/6/1/180.

Ferreira, A., Morgado, A. M. and Silva, J. S. (2010) 'Corneal nerves segmentation and morphometric parameters quantification for early detection of diabetic neuropathy', in, pp. 264–267. doi: 10.1007/978-3-642-13039-7_66.

Fowler, W. C. *et al.* (2004) 'A new paradigm for corneal wound healing research: the white leghorn chicken (Gallus gallus domesticus)', *Curr Eye Res*, 28(4), pp. 241–250. Available at: http://www.ncbi.nlm.nih.gov/pubmed/15259293.

Fukano, T. and Miyawaki, A. (2003) 'Whole-field fluorescence microscope with digital micromirror device: imaging of biological samples', *Applied Optics*, 42(19), p. 4119. doi: 10.1364/AO.42.004119.

Galletly, N. P. *et al.* (2008) 'Fluorescence lifetime imaging distinguishes basal cell carcinoma from surrounding uninvolved skin', *British Journal of Dermatology*, 159(1), pp. 152–161. doi: 10.1111/j.1365-2133.2008.08577.x.

Gaviola, E. (1926) 'Die Abklingungszeiten der Fluoreszenz von Farbstofflösungen', *Annals der Physik*, 386, pp. 681–710.

Georgakoudi, I. and Quinn, K. P. (2012a) 'Optical Imaging Using Endogenous Contrast to Assess Metabolic State', *Annual Review of Biomedical Engineering*, 14(1), pp. 351–367. doi:

10.1146/annurev-bioeng-071811-150108.

Georgakoudi, I. and Quinn, K. P. (2012b) 'Optical Imaging Using Endogenous Contrast to Assess Metabolic State', *Annual Review of Biomedical Engineering*, 14(1), pp. 351–367. doi: 10.1146/annurev-bioeng-071811-150108.

Ghukasyan, V. V and Kao, F.-J. (2009) 'Monitoring Cellular Metabolism with Fluorescence Lifetime of Reduced Nicotinamide Adenine Dinucleotide', *The Journal of Physical Chemistry C*, 113(27), pp. 11532–11540. doi: 10.1021/jp810931u.

Giraud, J. P. *et al.* (1975) 'Statistical morphometric studies in normal human and rabbit corneal stroma', *Experimental Eye Research*. Academic Press, 21(3), pp. 221–229. doi: 10.1016/0014-4835(75)90092-5.

Golub, G. and Pereyra, V. (2003) 'Separable nonlinear least squares: the variable projection method and its applications', *Inverse Problems*, 19(2), pp. R1–R26. doi: 10.1088/0266-5611/19/2/201.

Gustafsson, M. G. L. *et al.* (2008) 'Three-dimensional resolution doubling in wide-field fluorescence microscopy by structured illumination.', *Biophysical journal*, 94(12), pp. 4957–70. doi: 10.1529/biophysj.107.120345.

H. Sun (2015) *A Practical Guide to Handling Laser Diode Beams*. Springer.

Jablonski, A. (1935) 'Über den Mechanismus der Photolumineszenz von Farbstoffphosphoren', *Zeitschrift für Physik*, 94(1), pp. 38–46. doi: 10.1007/BF01330795.

Kerr, J. (1875) 'A new relation between electricity and light: Dielectrified media birefringent', *Philosophical Magazine Series 4*. Taylor & Francis, 50(332), pp. 337–348. doi: 10.1080/14786447508641302.

King-Smith, P. E., Fink, B. A. and Fogt, N. (1999) 'Three interferometric methods for measuring the thickness of layers of the tear film.', *Optometry and vision science : official publication of the American Academy of Optometry*, 76(1), pp. 19–32. Available at: http://www.ncbi.nlm.nih.gov/pubmed/10030612 (Accessed: 14 September 2017).

Kinoshita, S., Ohta, H. and Kushida, T. (1981) 'Subnanosecond fluorescence-lifetime measuring system using single photon counting method with mode-locked laser excitation', *Review of Scientific Instruments*, 52(4).

Klyce, S. and Beuerman, R. (1998) 'Structure and function of the cornea', in Kaufman, H. (ed.) *The Cornea*. New York: Churchill Livingstone, pp. 3–50.

Knemeyer, J. P., Marme, N. and Sauer, M. (2000) 'Probes for detection of specific DNA

sequences at the single-molecule level.', *Analytical chemistry*. UNITED STATES, 72(16), pp. 3717–3724.

Koenig, K. (2012) 'Hybrid multiphoton multimodal tomography of in vivo human skin', *IntraVital*. Karsten Koenig, 1(1), pp. 11–26. doi: 10.4161/intv.21938org/10.4161/intv.21938.

Lai, T. and Tang, S. (2014) 'Cornea characterization using a combined multiphoton microscopy and optical coherence tomography system', *Biomedical Optics Express*, 5(5), pp. 1494–1511. doi: 10.1364/BOE.5.001494.

Lakowicz, J. R. *et al.* (1992) 'Fluorescence lifetime imaging of free and protein-bound NADH.', *Proceedings of the National Academy of Sciences*, 89(4), pp. 1271–1275. doi: 10.1073/pnas.89.4.1271.

Lakowicz, J. R. (2006a) *Principles of fluorescence spectroscopy*. Third Edit. Springer.

Lakowicz, J. R. (2006b) *Principles of fluorescence spectroscopy*, *Principles of Fluorescence Spectroscopy*. doi: 10.1007/978-0-387-46312-4.

Laptenok, S. *et al.* (2007) 'Journal of statistical software.', *The journal of statistical software*. [UCLA Statistics], 18(8), pp. 1–20. Available at: http://library.wur.nl/WebQuery/wurpubs/361379 (Accessed: 26 August 2018).

LaVision (2007a) 'La Vision Datasheet', in.

LaVision (2007b) 'LaVision User Manual'.

Lazarev, G. *et al.* (2012) 'LCOS spatial light modulators: Trends and Applications', *Optical Imaging and Metrology: Advanced Technologies*, pp. 1–29. doi: 10.1002/9783527648443.ch1.

Lee, B. (2013) 'DMD 101 : Introduction to Digital Micromirror Device (DMD)', *Application Report*, (October), pp. 1–11.

Leskovar, B. *et al.* (1976) 'Photon counting system for subnanosecond fluorescence lifetime measurements', *Review of Scientific Instruments*, 47(9).

Lévêque-Fort, S. *et al.* (2004) 'Fluorescence-lifetime imaging with a multifocal two-photon microscope.', *Optics letters*, 29(24), pp. 2884–2886. doi: 10.1364/OL.29.002884.

Lewis, C. *et al.* (1973) 'The Measurement of Short-Lived Fluorescence Decay Using the Single Photon Counting Method', *Review of Scientific Instruments*, 44(2).

Lim, D. *et al.* (2011) 'Optically sectioned in vivo imaging with speckle illumination HiLo microscopy.', *Journal of biomedical optics*, 16(1), p. 016014. doi: 10.1117/1.3528656.

Lim, D., Chu, K. K. and Mertz, J. (2008) 'Wide-field fluorescence sectioning with hybrid speckle and uniform-illumination microscopy.', *Optics letters*, 33(16), pp. 1819–1821. doi: 10.1364/OL.33.001819.

Marcu, L. *et al.* (2004) 'Fluorescence Lifetime Spectroscopy of Glioblastoma Multiforme¶', *Photochemistry and Photobiology*, 80, pp. 98–103. doi: 10.1111/j.1751-1097.2004.tb00055.x.

Marcu, L. (2010) 'Fluorescence lifetime in cardiovascular diagnostics.', *Journal of biomedical optics*, 15(1), p. 011106. doi: 10.1117/1.3327279.

Marcu, L., French, P. M. W. and Elson, D. S. (eds) (2014) *Fluorescence Lifetime Spectroscopy and Imaging - Principles and Applications in Biomedical Diagnostics*. CRC Press.

Maurice, D. (1984) 'The cornea and sclera', in Davison, H. (ed.) *The Eye*. 3rd edn. Orlando: Academic Press.

McGinty, J. *et al.* (2009) 'Signal-to-noise characterization of time-gated intensifiers used for wide-field time-domain FLIM', *Journal of Physics D: Applied Physics*, 42(13), pp. 1–9. doi: 10.1088/0022-3727/42/13/135103.

Mertz, J. and Kim, J. (2010) 'Scanning light-sheet microscopy in the whole mouse brain with HiLo background rejection.', *Journal of biomedical optics*, 15(1), pp. 016027-1–7. doi: 10.1117/1.3324890.

Michael W. Davidson (2018) *Resolution | MicroscopyU*. Available at: https://www.microscopyu.com/microscopy-basics/resolution (Accessed: 26 August 2018).

Morgado, A. M. L. S. (2003) 'Fluorometria ocular não-invasiva : técnicas e instrumentação'. Available at: https://estudogeral.sib.uc.pt/handle/10316/1840 (Accessed: 26 August 2018).

Muro, E. *et al.* (2011) 'Single-shot optical sectioning using two-color probes in HiLo fluorescence microscopy.', *Biophysical journal*. The Biophysical Society, 100(11), pp. 2810–9. doi: 10.1016/j.bpj.2011.03.047.

Mycek, M.-A. and Pogue, B. W. (eds) (2003) *Handbook of Biomedical Fluorescence*. New York: CRC Press. doi: 10.1201/9780203912096.

National Cancer Institute (2017) *National Cancer Institute*. Available at: https://www.cancer.gov/publications/dictionaries/cancer-terms?cdrid=44126 (Accessed: 10 May 2017).

Neil, M. a, Juskaitis, R. and Wilson, T. (1997) 'Method of obtaining optical sectioning by using structured light in a conventional microscope.', *Optics letters*, 22(24), pp. 1905–1907. Available at: http://www.ncbi.nlm.nih.gov/pubmed/18188403.

Nelson, D. and Cox, M. (2005) 'Lehninger: Principles of Biochemistry', *Biochemistry and Molecular Biology Education*, 33(1), pp. 74–75. doi: 10.1002/bmb.2005.494033010419.

Nischida, T. and Saika, S. (2011) 'Cornea and Sclera: Anatomy and Physiology', in Krachmer, J., Mannis MJ, and Holland, E. (eds) *Cornea*. St Louis. Mosby, pp. 3–24.

Nocedal, J. and Wright, S. J. (1999) *Numerical Optimization, Global Change Biology*. Springer. doi: 10.5194/bgd-11-12733-2014.

O'Holleran, K. and Shaw, M. (2014) 'Optimized approaches for optical sectioning and resolution enhancement in 2D structured illumination microscopy', *Biomedical Optics Express*, 5(8), p. 2580. doi: 10.1364/BOE.5.002580.

OIA (2011) *Spectra at UA*. Available at: http://www.spectra.arizona.edu/ (Accessed: 30 August 2018).

Oida, T., Sako, Y. and Kusumi, A. (1993) 'Fluorescence Lifetime Imaging Microscopy (FLIM)', *Biophysical journal*, 64(March), pp. 676–685.

Otel, I. *et al.* (2013) 'Diabetic peripheral neuropathy assessment through corneal nerve morphometry', in *2013 IEEE 3rd Portuguese Meeting in Bioengineering (ENBENG)*. IEEE, pp. 1–6. doi: 10.1109/ENBENG.2013.6518436.

Periasamy, A. *et al.* (1996) 'Time-resolved fluorescence lifetime imaging microscopy using a picosecond pulsed tunable dye laser system', *Review of Scientific Instruments*, 67(10), p. 3722. doi: 10.1063/1.1147139.

Picoquant (2014) *Time-Correlated Single Photon Counting Wiki*. Available at: http://www.tcspc.com/doku.php/glossary:irf (Accessed: 30 November 2017).

PicoQuant (2016) *PicoQuant*. Available at: https://www.picoquant.com/products/category/picosecond-pulsed-sources/ldh-series-picosecond-pulsed-diode-laser-heads.

Popper, M. *et al.* (2004) 'Corneal Cell Density Measurement in vivo by Scanning Slit Confocal Microscopy: Method and Validation', *Ophthalmic Research*, 36(5), pp. 270–276. doi: 10.1159/000081207.

Popper, M. *et al.* (2005) 'Subbasal Nerves and Highly Refelective Cells in Corneas of Diabetic Patients: In vivo Evaluation by Confocal Microscopy', *Investigative Ophthalmology & Visual Science*. C.V. Mosby Co, 46(May 13), p. 879. Available at: https://iovs.arvojournals.org/article.aspx?articleid=2400615 (Accessed: 29 August 2018).

Prydal, J. I. *et al.* (1992) 'Study of human precorneal tear film thickness and structure using laser

interferometry', *Investigative Ophthalmology and Visual Science*. C.V. Mosby Co, 33(6), pp. 1996–2005. Available at: http://iovs.arvojournals.org/article.aspx?articleid=2161128 (Accessed: 14 September 2017).

Qian, J. *et al.* (2015) 'Full-color structured illumination optical sectioning microscopy.', *Scientific reports*. Nature Publishing Group, 5, p. 14513. doi: 10.1038/srep14513.

Quadrado, M. J. *et al.* (2006) 'Diabetes and Corneal Cell Densities in Humans by In Vivo Confocal Microscopy', *Cornea*, 25(7), pp. 761–768. doi: 10.1097/01.ico.0000224635.49439.d1.

Quadrado, M. J. (2013) *Avaliação Microestrutural da Córnea por Microscopia Confocal In Vivo*. University of Coimbra.

van Resandt, R. W. W., Vogel, R. H. and Provencher, S. W. (1982) 'Double beam fluorescence lifetime spectrometer with subnanosecond resolution: Application to aqueous tryptophan', *Review of Scientific Instruments*, 53(9).

Ritchey, E. R. *et al.* (2011) 'The chicken cornea as a model of wound healing and neuronal re-innervation.', *Molecular vision*, 17, pp. 2440–54. Available at: http://www.ncbi.nlm.nih.gov/pubmed/21976955 (Accessed: 28 August 2018).

Santos, S. *et al.* (2009) 'Optically sectioned fluorescence endomicroscopy with hybrid-illumination imaging through a flexible fiber bundle.', *Journal of biomedical optics*, 14(3), pp. 030502-1-030502-3. doi: 10.1117/1.3130266.

Schneckenburger, H. *et al.* (2004) 'Autofluorescence lifetime imaging of cultivated cells using a UV picosecond laser diode', *Journal of Fluorescence*, 14(5), pp. 649–654. doi: 10.1023/B:JOFL.0000039351.09916.cc.

Schneckenburger, H. and König, K. (1992) 'Fluorescence decay kinetics and imaging of NAD(P)H and flavins as metabolic indicators', *Optical Engineering*, 31(7), pp. 1447–1451. doi: 10.1117/12.57704.

Schwartz, A. *et al.* (2008) 'Method and apparatus for measuring quantity of a fluorochrome in a biological environment.' Available at: https://patents.google.com/patent/US20080129961A1/en (Accessed: 29 August 2018).

Schweitzer, D. *et al.* (2004a) 'In vivo measurement of time-resolved autofluorescence at the human fundus.', *Journal of biomedical optics*. United States, 9(6), pp. 1214–1222. doi: 10.1117/1.1806833.

Schweitzer, D. *et al.* (2004b) 'In vivo measurement of time-resolved autofluorescence at the human fundus.', *Journal of biomedical optics*, 9(6), pp. 1214–1222. doi: 10.1117/1.1806833.

Schweitzer, D. *et al.* (2007) 'Towards metabolic mapping of the human retina', in *Microscopy Research and Technique*. Wiley Subscription Services, Inc., A Wiley Company, pp. 410–419. doi: 10.1002/jemt.20427.

Shah, A. T. *et al.* (2014) 'Optical Metabolic Imaging of Treatment Response in Human Head and Neck Squamous Cell Carcinoma', *PLoS ONE*. Edited by I. V. Lebedeva, 9(3), pp. e90746-1–10. doi: 10.1371/journal.pone.0090746.

Sharick, J. *et al.* (2018) 'Personalized neoadjuvant treatment planning using optical metabolic imaging', *Cancer Research*. American Association for Cancer Research, 78(4 Supplement), pp. P5-01-01-P5-01–01. doi: 10.1158/1538-7445.SABCS17-P5-01-01.

Sharman, K. K. *et al.* (1999) 'Error analysis of the rapid lifetime determination method for double-exponential decays and new windowing schemes.', *Analytical chemistry*, 71(5), pp. 947–952. doi: 10.1021/ac981050d.

Sing Po Chan *et al.* (2001) 'Optimized gating scheme for rapid lifetime determinations of single-exponential luminescence lifetimes', *Analytical Chemistry*, 73(18), pp. 4486–4490. doi: 10.1021/ac0102361.

Skala, M. C., Riching, K. M., Bird, D. K., *et al.* (2007) 'In vivo multiphoton fluorescence lifetime imaging of protein-bound and free nicotinamide adenine dinucleotide in normal and precancerous epithelia.', *Journal of biomedical optics*. United States, 12(2), p. 24014. doi: 10.1117/1.2717503.

Skala, M. C., Riching, K. M., Gendron-Fitzpatrick, A., *et al.* (2007) 'In vivo multiphoton microscopy of NADH and FAD redox states, fluorescence lifetimes, and cellular morphology in precancerous epithelia.', *Proceedings of the National Academy of Sciences of the United States of America*, 104(49), pp. 19494–19499. doi: 10.1073/pnas.0708425104.

Skala, M. and Ramanujam, N. (2010) 'Multiphoton Redox Ratio Imaging for Metabolic Monitoring In Vivo', in *Methods in molecular biology (Clifton, N.J.)*, pp. 155–162. doi: 10.1007/978-1-60761-411-1_11.

Spring, K. R. and Davidson, M. W. (2017) *Nikon - MicroscopyU - Field of view*. doi: 10.1016/j.tripleo.2009.04.001.

Stanford Computer Optics (2018a) *Image Intensifier for ICCD Cameras*. Available at: https://stanfordcomputeroptics.com/technology/image-intensifier.html (Accessed: 25 August 2018).

Stanford Computer Optics (2018b) *The Phosphor Screen of the Image Intensifier*. Available at: https://stanfordcomputeroptics.com/technology/image-intensifier/phosphor-screen.html (Accessed: 25 August 2018).

Stokes, G. G. (1852) ‘On the Change of Refrangibility of Light’, *Philosophical Transactions of the Royal Society of London*, 142(0), pp. 463–562. doi: 10.1098/rstl.1852.0022.

Straub, M. and Hell, S. W. (1998) ‘Fluorescence lifetime three-dimensional microscopy with picosecond precision using a multifocal multiphoton microscope’, 73(13), pp. 1769–1771.

Suhling, K. *et al.* (2015) ‘Fluorescence lifetime imaging (FLIM): Basic concepts and some recent developments’, *Medical Photonics*, 27, pp. 3–40. doi: 10.1016/j.medpho.2014.12.001.

Sun, Y. *et al.* (2009) ‘Fluorescence lifetime imaging microscopy: in vivo application to diagnosis of oral carcinoma’, *Optics letters*, 34(13), pp. 2081–2083. doi: 10.1364/OL.34.002081.

Sun, Y. *et al.* (2010) ‘Fluorescence lifetime imaging microscopy for brain tumor image-guided surgery.’, *Journal of biomedical optics*, 15(5), p. 056022. doi: 10.1117/1.3486612.

Tadrous, P. J. *et al.* (2003) ‘Fluorescence lifetime imaging of unstained tissues: early results in human breast cancer’, *The Journal of Pathology*, 199(3), pp. 309–317. doi: 10.1002/path.1286.

Texas Instruments (2012) ‘DLP LightCrafter Evaluation Module’, in.

Ueda, A. *et al.* (1987) ‘Electron-microscopic studies on the presence of gap junctions between corneal fibroblasts in rabbits*’, *Cell Tissue Res*, 249, pp. 473–475. Available at: https://link.springer.com/content/pdf/10.1007/BF00215533.pdf (Accessed: 14 September 2017).

Venugopal, V., Chen, J. and Intes, X. (2010) ‘Development of an optical imaging platform for functional imaging of small animals using wide- field excitation’, *Biomedical Optics Express*, 1(1), pp. 143–156. doi: 10.1364/BOE.1.000143.

Wahl, M. (PicoQuant G. (2014) ‘Time-correlated single photon counting’, *Technical Note*, pp. 1–14. doi: 10.1016/0022-2313(89)90051-3.

Walsh, A. J. *et al.* (2013) ‘Optical metabolic imaging identifies glycolytic levels, subtypes, and early-treatment response in breast cancer’, *Cancer Research*, 73(20), pp. 6164–6174. doi: 10.1158/0008-5472.CAN-13-0527.

Walsh, A. J. *et al.* (2014) ‘Quantitative optical imaging of primary tumor organoid metabolism predicts drug response in breast cancer’, *Cancer Research*, 74(18), pp. 5184–5194. doi: 10.1158/0008-5472.CAN-14-0663.

Walsh, A. J. and Skala, M. C. (2015) ‘Optical metabolic imaging quantifies heterogeneous cell populations’, *Biomedical Optics Express*, 6(2), p. 559. doi: 10.1364/BOE.6.000559.

Wang, J. *et al.* (2003) ‘Precorneal and pre- and postlens tear film thickness measured indirectly with optical coherence tomography’, *Investigative Ophthalmology and Visual Science*. The

Association for Research in Vision and Ophthalmology, 44(6), pp. 2524–2528. doi: 10.1167/iovs.02-0731.

Wang, Q. *et al.* (2016) 'Parallel detection experiment of fluorescence confocal microscopy using DMD', *Scanning*, 38(3), pp. 234–239. doi: 10.1002/sca.21265.

Waring, G. O. 3rd *et al.* (1982) 'The corneal endothelium. Normal and pathologic structure and function.', *Ophthalmology*. United States, 89(6), pp. 531–590.

Warren, S. C. *et al.* (2013) 'Rapid Global Fitting of Large Fluorescence Lifetime Imaging Microscopy Datasets', *PLoS ONE*, 8(8). doi: 10.1371/journal.pone.0070687.

Webb, S. E. D. *et al.* (2002) 'A wide-field time-domain fluorescence lifetime imaging microscope with optical sectioning', *Review of Scientific Instruments*, 73(4), pp. 1898–1907. doi: 10.1063/1.1458061.

Wood, R. W. (1921) 'The Time Interval between Absorption and Emission of Light in Fluorescence', *Proceedings of the Royal Society of London A: Mathematical, Physical and Engineering Sciences*, 99(700), pp. 362–371. Available at: http://rspa.royalsocietypublishing.org/content/99/700/362.abstract.

van Zandvoort, M. A. M. J. *et al.* (2002) 'Discrimination of DNA and RNA in cells by a vital fluorescent probe: lifetime imaging of SYTO13 in healthy and apoptotic cells.', *Cytometry*. United States, 47(4), pp. 226–235.